SCUOLA DI DOTTORATO
UNIVERSITÀ DEGLI STUDI DI MILANO-BICOCCA

Department of Materials Science
PhD program in Materials Science and Nanotechnology
Cycle XXXIV

Insight into ZnO luminescence to engineer nanoparticles for X-Ray based cancer treatment

Candidate:
Roberta Crapanzano 776027

Supervisor:
Professor Anna Vedda

Co-supervisor:
Doctor Irene Villa

Coordinator:
Professor Marco Bernasconi

Academic Year 2020/2021

To my grandpa Mario.

You always said I was your "Mascotte",
well, it turns out you are mine.

Contents

Abstract

Nanoparticles disclose unique properties that enable their applications in different fields, such as energy, catalysis, opto-electronics, and medicine. At the nanosize, the surface-to-volume ratio is increased, leading to the formation of defects that influence the resultant features, *e.g.* the catalytic and optical behaviours of the systems. Moreover, the high surface area and reactivity of nanoparticles allow their functionalization with several ligands, enhancing their versatility, especially in the biomedical field. Indeed, the accuracy and efficiency of several diagnoses and treatments may improve by implementing traditional strategies with targeted nano-agents. Among the nanomedicine researches, heavy nanoparticles are promising for the innovation of radiotherapy and for the development of novel oncological procedure, such as X-Ray induced photodynamic therapy, that exploits the combination of nanoscintillators and photosensitizers.

In this context, ZnO is of particular interest. Indeed, ZnO is a wide band gap semiconductor that displays emissions in the visible region of the spectrum, surface reactivity, and biocompatibility. Moreover, upon X-Ray exposure, ZnO can generate cytotoxic species both directly, due to its catalytic activity, and indirectly, by activating the close photosensitizers, due to its ability to down-convert X-Ray photons into visible ones.

This thesis focuses on the study of ZnO NPs for the innovation of X-Ray based cancer therapies. In detail, a fundamental investigation of the optical and catalytic properties of several ZnO samples is performed and used as background to design and develop ZnO based multicomponent nanosystems.

Namely, the optical features of ZnO samples with different sizes (nanometric, micrometric, and bulk) and growth conditions are investigated by photoluminescence and radioluminescence techniques aiming at deepening the comprehension of the impact of morphology on the material defectiveness. A Gaussian reconstruction of all the spectra identifies in ZnO luminescence as many as five emission bands (one related to excitons and four to defects), whose spectral shapes and time decays vary with the dimensionality and the synthesis procedure. Moreover,

the test of the ability of various nanosized ZnO sample to promote the production of different cytotoxic species unveils that their radio-catalytic activity is affected by the type and concentration of occurring point defects. Thus, by controlling the synthesis parameters and the morphology (size, shape, interfaces) of ZnO nanostructures, its defectiveness can be engineered to tune its optical and catalytic properties.

Then, to realize a nano-agent for X-Ray induced photodynamic therapy, ZnO nanoparticles, supported onto nanosized silica substrates with different porosity, are functionalized with various concentrations of porphyrins. The study of their optical properties reveals that, under light excitation, the dye luminescence is activated only by a rather poor re-absorption mechanism. Differently, upon X-Ray exposure, the porphyrin emission sensitization is enhanced, especially at low concentrations and high energy of the ionizing beams, by the locally augmented energy deposition favoured by ZnO, as also confirmed by Monte Carlo simulations. These findings highlight the synergic role of X-Ray and functionalization, paving the way for further studies on the impact of nano-agent design on its performances.

This PhD project has been performed at the Department of Materials Science of the University of Milano-Bicocca, in collaboration with the NanoMat@Lab for the samples preparation and with Dr Anne-Laure Bulin of the Synchrotron Radiation for Biomedicine Group at the University of Grenoble-Alpes, INSERM, for the computational analysis.

Riassunto

Le nanoparticelle possiedono proprietà uniche che permettono il loro utilizzo in diversi settori, come la catalisi, l'opto-elettronica e la medicina. A livello nanometrico, il rapporto superficie-volume è alto, portando alla formazione di difetti che influenzano le proprietà del sistema, ad esempio le risposte catalitiche e ottiche. Inoltre, le elevate aree e reattività superficiali delle nanoparticelle consentono la loro funzionalizzazione con diversi leganti, incrementando la loro versatilità, soprattutto nell'ambito medico. L'accuratezza e l'efficacia di diagnosi e terapie può migliorare implementando le strategie tradizionali con nano-agenti. Tra i campi di ricerca in nanomedicina, nanoparticelle con alto numero atomico sono promettenti per innovare la radioterapia e per sviluppare nuove procedure oncologiche, come la terapia fotodinamica indotta dai raggi X, che sfrutta nanoscintillatori combinati a fotosensibilizzatori.
In questo ambito, ZnO è di grande interesse. ZnO è un semiconduttore che mostra emissioni nello spettro del visibile, reattività superficiale e biocompatibilità. Inoltre, esposto ai raggi X, ZnO può generare specie citotossiche sia direttamente, grazie alla sua attività catalitica, sia indirettamente, attivando i vicini fotosensibilizzatori, grazie alla sua abilità di convertire i fotoni X in visibili.
Questa tesi concerne lo studio di nanoparticelle di ZnO per l'innovazione di terapie oncologiche attivate dai raggi X. In dettaglio, un'analisi fondamentale delle proprietà ottiche e catalitiche di diversi campioni di ZnO è condotta e usata come base per progettare nanosistemi multicomponente a base di ZnO.
In particolare, le proprietà ottiche di campioni di ZnO con diverse dimensioni (nanometriche, micrometriche e massive) e condizioni di crescita sono studiate con tecniche di fotoluminescenza e radioluminescenza con l'obiettivo di approfondire la comprensione del ruolo della morfologia sulla difettualità. L'analisi numerica di tutti gli spettri identifica nella luminescenza di ZnO un massimo di cinque bande di emissione (una attribuita agli eccitoni e quattro ai difetti), le cui forme spettrali e tempi di vita variano con la dimensione e la procedura di sintesi. Inoltre, lo studio dell'abilità di diversi campioni nanometrici di ZnO di

produrre specie citotossiche rivela che la sua attività radio-catalitica dipende dal tipo e dalla concentrazione dei difetti di punto. Quindi, il controllo dei parametri di sintesi e della morfologia (dimensione, forma, interfacce) potrebbe permettere l'ingegnerizzazione sia dei difetti che delle proprietà ottiche e catalitiche.
Per realizzare un nano-agente per la terapia fotodinamica indotta dai raggi X, nanoparticelle di ZnO, supportate su substrati nanometrici di silice con diversa porosità, sono funzionalizzate con varie concentrazioni di porfirine. Lo studio delle loro proprietà ottiche rivela che, sotto eccitazione ottica, la luminescenza della porfirina è attivata solo da un meccanismo di riassorbimento con efficienza limitata. Invece, sotto radiazione ionizzante, l'emissione della porfirina è ben sensibilizzata, specialmente a basse concentrazioni e alte energie del fascio di raggi X, grazie al locale aumento del deposito di energia favorito dalle nanoparticelle di ZnO, come confermato dalle simulazioni. Questi risultati evidenziano il ruolo sinergico dei raggi X e della funzionalizzazione, aprendo a ulteriori studi sull'impatto della progettazione del nano-agente sulle sue prestazioni.
Questo progetto è stato condotto nel Dipartimento di Scienza dei Materiali dell'università di Milano-Bicocca e in collaborazione con il NanoMat@Lab per la preparazione dei campioni e con la Dottoressa Anne-Laure Bulin dell'università di Grenoble-Alpes per l'analisi computazionale.

List of abbreviations

APTES	(3-Aminopropyl)triethoxysilane
ATR	Attenuated total reflection
BET	Brunauer-Emmett-Teller
CHNS	Elemental analysis of carbon, hydrogen, nitrogen, and surfur
CCD	Charge-coupled device
CM-H_2DCFDA	5-(and-6)-chloromethyl-2',7'-dichlorodihydro-fluorescein diacetate, acetyl ester
CT	Computed tomography
CTAB	Cetyltrimethylammonium bromide
CW	Continuous wave
DABCO	(1,4-diazabicyclo[2.2.2]octane)
DMF	Dimethylformamide
DNA	Deoxyribonucleic acid
EMA	European Medicines Agency
EPL	Pulsed diode laser
EPLED	Pulsed diode light emitting device
ET	Energy transfer
FTIR	Fourier transformer infrared resonance
FWHM	Full width at half maximum
HI	Hot injection
HRTEM	High-resolution transmission electron microscopy
MRI	Magnetic resonance imaging
MTCP	Meso-tetra (4-carboxyphenyl) porphyrin
NPs	Nanoparticles
ODA	Octadecylamine
PBS	Phosphate-buffered saline
PDT	Photodynamic therapy
PL	Photoluminescence

PpIX	Protoporphyrin IX
PXRD	Powder X-Ray diffraction
PS	Photosensitizer
QDs	Quantum dots
RL	Radioluminescence
ROS	Reactive oxygen species
RT	Radiotherapy
SA	Stearic acid
SEM	Scanning electron microscopy
SG	Sol-gel
SOSG	Singlet oxygen sensor green
SSA	Specific surface area
TCPP	5,10,15,20-(tetra-4-carboxyphenyl) porphyrin
TCSPC	Time correlated single photon counting
TEM	Transmission electron microscopy
TGA	Thermogravimetric analysis
TRES	Time resolved emission spectroscopy
TRPL	Time resolved photoluminescence
UCNPs	Upconverting nanoparticles
UV	Ultraviolet
VIS	Visible
X-PDT	X-Ray induced photodynamic therapy

Introduction

Nanoparticles (NPs), defined as inorganic and/or organic structures with size ranging from few nanometers to few hundreds of nanometers, [1] are promising materials for several applications due to their tuneable and unique properties, often novel with respect to those of their bulk counterparts. [2, 3] Indeed, in the last decades, the development of various easy and cost-effective synthesis routes and post-synthesis modifications, such as surface functionalization, has allowed to realize a plethora of NPs with different chemical, physical, and biological features, [4,5] leading to advances in nanotechnologies, [6] that are the use of nanosized materials for targeted purposes. Nanostructures applications include the energy and cosmetics sectors as well as the opto-electronics and medicine fields. [7]

In particular, luminescent inorganic NPs are of great interest for the innovation of light-emitting diodes, energy-harvesting devices, and medical procedures. [8,9] In fact, the possibility of engineering the optical properties of nanosystems by varying their shapes, size, and surface features represents an unique tool to match the material performances with the application requirements. For instance, NPs have been proposed for the development of photonic devices emitting in the UV/blue range and working at room temperature, [10] flexible detectors, [11] fluorescent agents for medical imaging and/or light-activated cancer treatments. [12,13] Often, the physical properties of inorganic nanomaterials, *e.g.* the optical, electrical, and catalytic features, are determined by their high surface-to-volume ratio that can modulate the NPs surface reactivity, allowing their functionalization with different ligands, as well as the NPs defectiveness, defined as the type and concentration of point defects. In fact, at the material interfaces, modifications with respect to the bulk occur in the positions and in the bonding of lattice atoms, generating defective surface states, whose impact on the final properties increases by scaling down the size down. At the nanoscale, the nature of these defects plays a role in determining the nanostructures optical features: they can dissipate non-radiatively the excitation causing a decrease in the luminescence efficiency or

introduce additional energy levels in the material forbidden energy gap, leading to new emission bands. Moreover, the conductivity as well as catalytic activity of NPs depends on the nature of the surfaces states.

Besides the applications of NPs in photonics and catalysis, due to the feasibility of functionalization of their surfaces and the engineering of their defects, the attractiveness for the use of nanostructures in the field of medicine is continuously increasing. [9] Indeed, NPs offer several unique advantages to enhance the accuracy and the efficiency of both diagnostic and therapeutic strategies: they can be internalized in cells, due to their nanometric size, [14] targeted towards specific sites in the human body, due to their easiness of functionalization, [5] and properly triggered by an external stimulus, such as light, heat or even a magnetic field, and hence contribute actively to the medical procedure. [15]

Notably, NPs have been studied to implement and innovate the oncological treatments. [1, 16, 17] In fact, nowadays, the leading cause of morbidity and death, especially in the developed countries, is cancer. [18] Despite several strategies have been developed to treat cancer patients, *e.g.* surgery, chemotherapy, radiotherapy, immunotherapy, and hormonal therapy, their outcomes are still affected by drawbacks and side effects, mainly caused by the difficulty to kill all the cancer cells without affecting the healthy tissues. [19] For instance, radiotherapy (RT) is widely used to treat deep tumours thanks to the ability of X-Ray to both penetrate the human body up to 40 cm and to induce deoxyribonucleic acid (DNA) damages, [20] but it requires high doses to promote a good therapeutic effect and it lacks the tissue selectivity. [21] In this context, heavy inorganic NPs, whose interaction with the ionizing radiation is more efficient than that of the human body, are promising tools to improve the results of traditional RT. Depending on their atomic number and their catalytic properties, dense nanosystems can passively enhance the energy release of the high energy radiation in the malignancy proximity [22] and/or actively generate cytotoxic radical species through oxidation/reduction of the water and oxygen moieties present in the human tissue, [23] promoting the RT effects also at lower doses.

Furthermore, a novel oncological treatment, called X-Ray induced photodynamic therapy (X-PDT), that relies on the combined use of ionizing radiation and heavy NPs functionalized with organic photosensitizers, has been proposed. [16] This therapy aims at exploiting the ability of scintillating nanostructures to down-convert the high energy radiation into UV/VIS photons for triggering the photophysical process of the photosensitizers to produce the cytotoxic free radical, especially singlet oxygen with the most effective DNA damages. [24] Although the

potentialities of this oncological approach have been already proven by different *in vitro* and *in vivo* studies, [20,25,26] the achievement of solid comprehension in the design and control of the photochemical properties of multicomponent nanosystems, as well as in the luminescence and scintillation phenomena occurring in this class of NPs, deserve further investigations. In particular, the understanding of the energy deposition mechanisms deriving from the interaction of the ionizing radiation with the nanosized structure and the biological environment in correlation to the beneficial outcomes on both RT mediated by NPs and X-PDT is an open issue. To address this topic, computational analyses represent a useful tool to evaluate the spatial distribution of energy release in a biological environment loaded with NPs upon high energy radiation exposure and also to relate it with the nanomaterials features, such as size and composition, and the ionizing radiation parameters, such as energy and direction. [21,27]

In this frame, nanosized ZnO have great potentiality thanks to its various and interesting properties and consequently its application versatility. [28,29] Indeed, its optical, electrical, and mechanical features make ZnO a promising material for transparent thin-film transistors, photonics and optoelectronic devices, [30,31] its high surface reactivity for catalysis and sensing, [32,33] its biocompatibility and anti-cancer and anti-bacterial effects for nanomedicine, [23,34] and its radiation hardness and scintillating properties for X-Ray applications. [35]

In detail, ZnO is a semiconductor with a direct and wide band gap (∼3.4 eV), [36] whose large exciton binding energy (∼60 meV) [37] allows exciton emission also at room temperature. On the other hand, different studies have already observed that ZnO optical properties are strongly affected by its defectiveness, that in turn is related to several factors, *e.g.* the growth parameters, the synthesis precursors, morphology, [38–40] as well as the environmental conditions. [41] In fact, ZnO typically exhibits, together with the near UV exciton luminescence at ∼3.4 eV, several defect-related emissions along the whole visible region: the most commonly reported bands are at ∼1.9 eV (orange-red), ∼2.3 eV (yellow-green), ∼2.6 eV (blue), and ∼3.0 eV (violet). [29,39] Anyhow, their attribution is controversial due to the complexity of ZnO defectiveness, especially at the nanometric size. Since the topic is broad and complex, an exhaustive comprehension of the role of ZnO morphological and surface features is pivotal for the development of ZnO nanostructures with optimized optical properties. Additionally, the surface related defectiveness of ZnO has been associated to its reactivity, and hence its catalytic properties, upon both light and X-Ray exposure. In particular, correlations between the ZnO catalytic performances, the surface-to-volume

ratio, and the occurrence of quenching channels and points defects have been observed. [36, 42, 43]
In this context, ZnO NPs have been proposed as agents for the degradation of environmental pollutants and for the generation of cytotoxic species to promote the death of infective pathogens or cancer cells. [23, 42] For instance, different *in vitro* studies have reported the killing rate of cells incubated with ZnO NPs is higher than that of cells alone under both light and X-Ray irradiation, demonstrating the photo- and radio- induced catalytic production of free radicals by ZnO NPs. [44, 45] Many multicomponent nanosystems for X-PDT, that exploit ZnO nanostructures as scintillators and porphyrin derivatives as photosensitizers, have been studied. [46, 48] Despite these works attest the potentiality of these functionalized NPs as anti-cancer agents, they also reveal that the resultant performances of multicomponent nanosystems are strongly related to the functionalization step and its impact on the interaction mechanism under X-Ray exposure. Hence, a deep understanding of the processes triggered by ionizing radiation in the X-PDT agent is required to optimize its design and hence its therapeutic efficiency.

In this work, an accurate investigation of the spectroscopic properties of nano-sized ZnO with different morphologies and surface functionalizations is presented in detail.
Chapter 1 and Chapter 2 report the background and the state of art of the studied topics, aiming to both remark their fundamental starting point and to highlight their main open issues. A general overview of the broad variety of developed nanoparticles and nanotechnology, with a particular focus on medical procedures exploiting nanometric materials and ionizing radiation is provided in Chapter 1. A brief description of ZnO physical properties and of its main applications, especially in X-Ray activated nanomedicine, is given in Chapter 2.
In Chapter 3, the materials and methods used in this work are presented. In detail, for each examined ZnO samples, its synthesis procedure and morphological characterization is provided. Moreover, the methods of the experimental and numerical analyses are described.
The results and the discussion of this PhD project are presented in Chapter 4 and Chapter 5. Firstly, a detailed investigation of the optical and catalytic properties of ZnO samples with dimensions from the bulk to the nano-size is presented and then the obtained findings are used to design and develop porphyrin functionalized ZnO nanosystems for possible use in X-PDT.
Namely, Chapter 4 discloses that the ZnO luminescence and catalytic activity

are strongly related to its surface properties, hence to its defectiveness. Indeed, this work clearly evidences that the size and interfaces as well as the growth parameters concur in defining the type and concentration of point defects in ZnO samples, especially at the nanometric scale. For instance, a decrease in the luminescence efficiency and an increase in the generation of free radicals have been observed, under X-Ray exposure, scaling down the size. A deep comprehension of the correlations between material defectiveness and the resultant optical and/or catalytic properties may pave the way for the defect engineering of inorganic nanoparticles, thus enhancing their applicability. The results and the discussion of the spectroscopic analysis of the various ZnO samples has been also reported in a publication. [49]

Chapter 5 unveils that the final performances of the X-PDT agents depend on the interaction efficiency and mechanism between the inorganic and organic part of the multicomponent nanosystems, that in turn are affected by the spatial distribution and the concentration of the photosensitisers on the scintillating NPs. In particular, the highest enhancement in the porphyrin luminescence has been observed in the sample functionalized with the lowest concentration of dye aggregates and upon exposure with X-Ray photons of 10.0 keV mean energy, optimized for energy release in ZnO, as confirmed by the simulations. Hence, this study shows that the porphyrin emission sensitization under ionizing radiation exposure is boosted by the promotion of energy deposition in the heavy NPs and it is favoured by the close proximity of the ZnO NP with properly dispersed dye molecules.

Lastly, in Conclusions and Perspectives (pp. 136), the results of the PhD project are summarized and outlooks for further research activities are provided.

This PhD project has been performed at the Department of Materials Science of the University of Milano-Bicocca, also in collaboration with the NanoMat@Lab headed by Professor Scotti for the materials preparation and morphological characterization. The computational analysis has been performed in collaboration with Dr Anne-Laure Bulin of the Synchrotron Radiation for Biomedicine Group at the University of Grenoble-Alpes, INSERM.

Chapter 1

Nanoparticles for advances in medicine

In this chapter, nanometric materials and their properties will be introduced. Then, an overview of their applications in the field of nanomedicine, with a focus on X-Ray activated cancer therapies, will be provided.

1.1 Nanoparticles

NPs are defined as structures whose size ranges from 1- to 100 nm made by organic and/or inorganic materials. [1] Examples of organic nanosystems are micelles, dendrimers, and polymersomes: [2] common types of inorganic NPs are clusters formed by few metal atoms, semiconductors quantum dots (QDs), and fullerenes. [3, 13] Moreover, hybrid nanomaterials made by a combination of inorganic and organic moieties, such as metal organic frameworks and core-shell systems, have been studied. [50] NPs are often classified by their dimensionality as zero-dimensional, one-dimensional, two-dimensional, and three-dimensional.
The various approaches of NPs synthesis can be categorized into *top-down* and *bottom-up* methods. The emphtop-down approach relies on the reduction of a bulk material into nanometric particles by, for example, mechanical milling or laser ablation; [3] differently, in the *bottom-up* procedures, synthetic chemistry (as hot-injection and sol-gel routes) and self-organization are exploited to build-up materials from atoms or molecules. [4, 51] Therefore, a plethora of NPs with different compositions and morphologies (hence sizes, shapes, crystallinities, surface charges, and interfaces properties) can be obtained in a controlled matter (Figure 1.1).

Remarkably, nanomaterials, with respect to their bulk counterparts, disclose

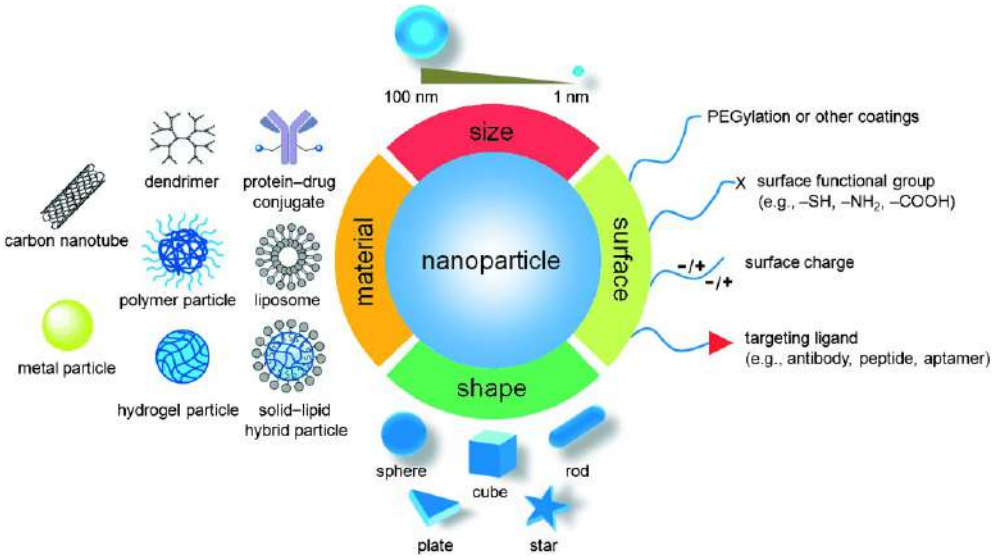

Figure 1.1: A summary of main features of nanoparticles (material, shape, surface, and size) together with a schematic representation of different types of nanomaterials. Picture taken from [1].

novel and unique physical, chemical, and biological features, which strongly depend on the structural and morphological properties and, especially, on the high surface-to-volume ratio. The possibility of designing and engineering NPs by tuning their features through synthesis routes and post-synthesis modifications has aroused great interest in the scientific community because it paves the way for their application in several fields. Indeed, in the last decades, the attractiveness of nanotechnology (defined by the European Medicines Agency, EMA, as the use of structures with size less then 1000 nm and designed with specific properties) is continuously increasing: [6] it has been proposed to exploit NPs in almost all kind of sectors, such as cosmetics, food, construction, opto-electronics, catalysis, medicine, energy, and environment. [7]
The following sub-Section will be focused on three-dimensional inorganic nanomaterials - *i.e.* the NPs type studied in this thesis - and their properties.

1.1.1 Inorganic nanoparticles

The study and the development of inorganic NPs, that include metal, semiconductor, and insulator systems, are widespread and ongoing in the scientific community because of their unique optical, electrical, mechanical, catalytic, and magnetic properties as well as their stability and surface reactivity. The high surface-to-volume ratio plays a key role in many of physical features of inorganic NPs. In nanosystems, a significant fraction of the atoms, that consequently are

under-coordinated, lies on the surface, leading to dramatic changes with respect to the material bulk counterparts, as, for example, the melting point lowering and the reactivity enhancement. Moreover, the material defectiveness is strongly affected by the NPs large surface areas, often inducing an increase of the NPs hardness and generally altering their luminescence and conductivity.
Interestingly, inorganic nanomaterials with different compositions disclose characteristic physical properties. In metal particles (*e.g.* Au, Ag, Pt NPs), whose sizes are comparable or smaller than the wavelength of the incident light, surface plasmons are confined and their excitation generates an effect called "localized surface plasmon resonance". [52] As a consequence, the electric fields near the NPs surfaces are hugely enhanced and their optical absorption is maximum at the plasmon resonance frequency, that depends on the refractive index. Due to these unique opto-electrical properties, metal NPs have been exploited to develop surface-enhanced Raman spectroscopy, to cause light-induced local heating in photothermal cancer treatments, and in sensing applications. [52, 53]
Remarkably, in semiconductor QDs - e.g. CdSe, GaAs, Si QDs -, due to the quantum confinement of the free charges, the energy levels are discrete and the energy bad gap is size-dependent. Hence, by varying the QDs dimensions, the absorption and the corresponding emission energies can be tuned from the violet to the near infra-red region, leading to a plethora applications, such as light-emitting devices, photovoltaics, and medical imaging. [13, 54]
On the other hand, the quantum confinement effects are usually negligible in metal oxide NPs with wide energy band gap (*e.g.* ZnO, TiO_2, HfO_2 NPs) because their Bohr radii is quite small (less than few nanometers). Therefore, in these nanosystems, some physical properties, such as the optical features, depend significantly on the material defectiveness, defined as the concentration and types of intrinsic and extrinsic points defects (Figure 1.2). At the nanoscale level, intrinsic defects include atomic vacancies, interstitials, anti-sites, surface defects, such as under-coordinated atoms, dangling bonds, hydroxo-, and peroxo-linkages. Extrinsic defects are dopants, that are external element intentionally introduced in the NPs, and impurities deriving from the synthesis, that, anyhow, being rather easy to control for nanometric materials, allows generally to reach excellent samples purity. The luminescence and conductivity properties as well as the reactivity of the material surfaces are greatly affected by the points defects type and concentrations, that in turn depend on the synthesis route and the material morphology. Hence, the possibility to control these parameters permits to tune the optical, electrical, and catalytic properties of wide bandgap metal ox-

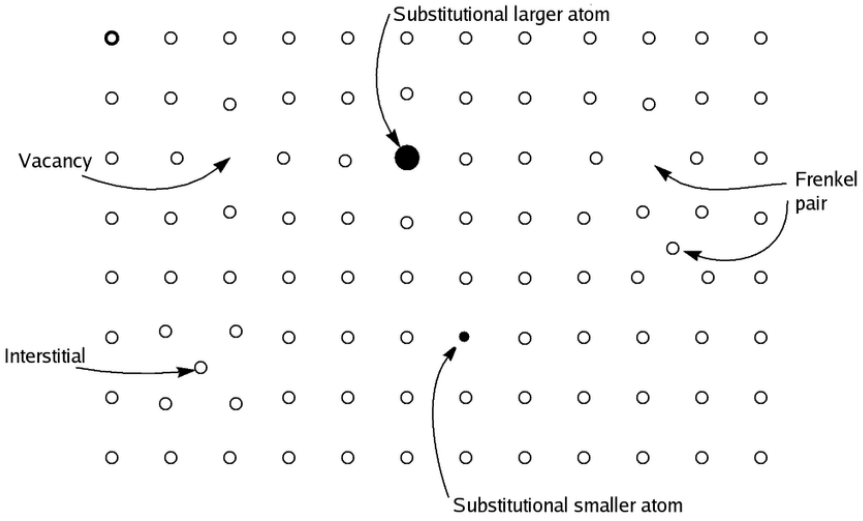

Figure 1.2: Schematic illustration of some point defect types in a monoatomic solid. From Wikipedia Commons.

ide NPs, paving the way for several applications, such as light-emitting devices, transistors, sensing, catalysis, and medicine. [8, 55] Inorganic metal and metal oxide NPs containing magnetic elements, such as iron, nickel and cobalt, disclose often novel physical properties, such as superparamagnetisism, and have great potentiality for biological and medical applications. [56]
As already mentioned, with respect to their bulk counterparts, the high surface-to-volume ratio of inorganic NPs enhances their surface activity, enabling the occurrence of chemical reactions at the interfaces. Using different strategies, the surface functionalization of nanomaterials with a variety of ligands (*e.g.* organic and bio- molecules, surfactants, and polymers) can be been effectively and easily performed with several improvements in the nanosystems stability and compatibility with host materials and/or biological environment, leading to a great increase in their possible applications. [1, 5] A thorough discussion of the features and potentiality of functionalized inorganic NPs in the biomedical field will be provided in the following sections.

1.2 Nanomedicine

Nanomedicine comprises, as defined by EMA, all applications of nanotechnology for medical purpose such as diagnostics, therapies, and theranostics - *i.e.* the simultaneous patient monitoring and treatment. [9] The nanoscale dimensions and versatility of NPs play a major role in making them promising tools to implement and advance health care methods. Thanks to their nanometric size, nanomaterials

can, after entering the human body and the systemic circulation via direct injection, inhalation, and oral intake, be up-taken by cells, enhancing the diagnosis and/or therapy accuracy. [14] Moreover, the tunability of NPs physical and chemical properties, which depends on nanosystems parameters (*e.g.* the composition, morphology, interfaces), allows to engineer them for several medical applications, that include fluorescent/contrast agents for imaging techniques, targeted carriers for drug delivery, and sensitizers for cancer therapies. In particular, NPs large surfaces can be adapted due to their modifiable features, like shape, size, and surface charge, [5] to accommodate functional groups or hydrophobic molecules. The main aims of surface functionalization are both the enhancement of solubility and biocompatibility, that leads to improved stability and retention time in body fluids, [57] and the targeting towards the malignancy and illness sites in the patients' body, enabling the specificity of their diagnostic and therapeutic activity. [1] Passive targeting relies on the different physiological conditions developed by some malignancies, like tumours, with respect to normal tissue, that cause the nanomaterials tendency to accumulate in their location. Anyhow, to increase the accuracy and to extend the use of targeted medicine to chronic illness and pathogens, active targeting has been studied: this strategy requires to graft on the NPs surface ligands, such as antibodies, peptides, aptamers, able to recognize and bind only to specific receptors expressed by abnormal cells. [5]

Despite nanomedicine could realize countless benefits and remarkable advances in both diagnosis and therapeutics, the NPs administration in patients could be potentially harmful, leading, for instance, to systemic toxicity and accumulation in vital organs. [58] Local delivery protocols as well as rapid clearance routes from the human body after the treatments are strategies currently under study to overcome these drawbacks and further increment the beneficial effects of NPs use for bio-medical applications. [34, 59]

Nanomedicine is a complex field that includes several topics (from the NPs synthesis to the clinicals trial) and necessitates the collaboration of the chemical, physical, biological, and medical communities. In this thesis, the impact of NPs design on their chemical and physical properties will be discussed in relation to the requirements of innovative medical protocols.

In the following sub-Section, imaging techniques, drug delivery modalities, and oncological therapies that exploit inorganic NPs will be briefly presented. X-Ray based cancer treatments, that are the possible applications proposed for the nanosystems studied in this thesis, will be accurately discussed in Section 1.3.

1.2.1 Inorganic nanoparticles for biomedical applications

During recent years, ongoing researches by the scientific communities have been carried out on the possibility to use inorganic NPs with the aim of implementing and innovating medical diagnostics, therapies, and theranostics.
Currently, the diagnostic tools in use in healthcare rely on bio-sensing and imaging methods, like optical imaging, radiography, magnetic resonance imaging (MRI), and computed tomography (CT); [2, 12] to overcome their drawbacks, in the last decades, various inorganic NPs have been studied. For instance, to surpass conventional diagnosis of infectious diseases, that usually require expensive and time-consuming bacterial cultures, the development of portable devices based on assays of targeted nanosystems to sense pathogens is of great interest. [53] Moreover, in imaging techniques, iron oxide NPs and AuNPs have been proposed as contrast agents to enhance the sensitivity of MRI and CT, respectively; whereas QDs and rare-earth doped nano-oxides have been investigated as probes to increase the limited penetration depth of optical imaging. [12] Moreover, thanks to the ease of NPs surface functionalization, all the standard imaging methods can be implemented to perform in molecular imaging modality, that is the quantitative and non-invasive imaging of targeted biomolecules combined with the monitoring of related biological processes. [60]
Furthermore, ceaseless efforts have been put in applying nanotechnologies in medical treatments, especially in drug delivery and cancer therapies, to fulfil the need of improving the efficiency and accuracy of treatments, and at the same time of reducing their adverse effects. Today, the innovation of oncological techniques is more and more compelling since cancer is one of the main causes of morbidity and death worldwide. Established cancer treatments - *e.g.* surgery, chemotherapy, radiotherapy, immunotherapy, and hormonal therapy - have enabled an active fight against cancer assuring long-term survival and quality of life for several malignancies in oncological patients, but their broad use has been always associated to several drawbacks and side effects. Surgery, that is the only oncological invasive procedure, does not always guarantee the complete removal of cancer cells leading to the need of combined therapeutic protocols to avoid tumours recurrence. [61] The main drawback of chemo- and radio-therapy is the difficulty to kill the malignant cells without affecting healthy tissues: the low specificity and poor tumour accumulation of chemotherapeutic drugs results in high toxicity, damages of healthy cells, as well as systemic side effects; [62] whereas the maximum cumulative radiation dose allowed in radiation therapy is limited to avoid significant injuries to the surrounding tissues or organs. [19] The advances of nanotechnolo-

gies have promoted the overcoming of low specificity of chemotherapy mainly through the chemotherapeutic medicine administration in drug delivery modality. Efficient drug delivery systems require to supply an active pharmaceutical ingredient to a specific location in a stable and controlled manner. [63] Several studies on targeted inorganic NPs, for instance on mesoporous silica NPs capped with ZnO, AuNPs, and carbon nanotubes, have shown that these systems offer the advantage to control both the drug transport and release, whose activation and rates can be regulated by enzymatic, thermal or pH factors. [15] A further implementation is the design and development of theranostics nanomaterials able to provide valuable information on the drug delivery rate and efficiency opening up the possibility to move toward personalized therapeutic interventions. [9] In addition to chemotherapy, drug delivery mediated by nanomaterials is a promising modality for several efficient and targeted medical treatments, like chronic disease, gene therapy, antibiotics, and vaccines administration. [15, 64–66]
Recently, also novel and non-invasive cancer treatments, such as hyperthermia therapy and photodynamic therapy (PDT), have been combined with nanotechnology: their implementation with NPs offer the possibility to localize the treatment by tumour cells targeting and to control the activation of their cytotoxic activity by an external source. In hyperthermia method, upon stimulation, the nanomaterials generate heat in the tumour tissues that destroys cells, if the local temperature is higher than 47 °C, or that renders the cells more susceptible to chemo- or radio-therapy, if the local temperature is between 41 °C and 47 °C. Among the nanostructures, AuNPs and carbon-based nanosystems activated by near-infrared laser, magnetic NPs stimulated by an alternating magnetic field, QDs under non-ionizing radiofrequency exposure have been proposed as hyperthermia agents. [67] Differently, in PDT, the photoexcitation of photosensitizers (PS), like metals containing structures or carbon-based nanostructures, as well as polymeric PSs and small organic moieties, is exploited to induce the generation of cytotoxic reactive oxygen species (ROS) - *e.g.* hydrogen peroxide, hydroxyl radicals, superoxide ions, singlet oxygen, peroxyl radicals - and cause cancer cell death. After interaction with light, the PS is excited from the ground state (S_0) to an unstable singlet excited state. Then, the first excited state (S_1) may be converted into a more stable excited triplet state (T_1) with longer lifetime ($\sim \mu s$) through intersystem crossing. Triplet states of PS can then produce ROS by interacting with water and molecular oxygen: the first interaction generates free radicals, while the second one produces singlet oxygen ($^1O_2$) moieties. Typically, for organic PSs, the second reaction is the most efficient and thus highly reactive

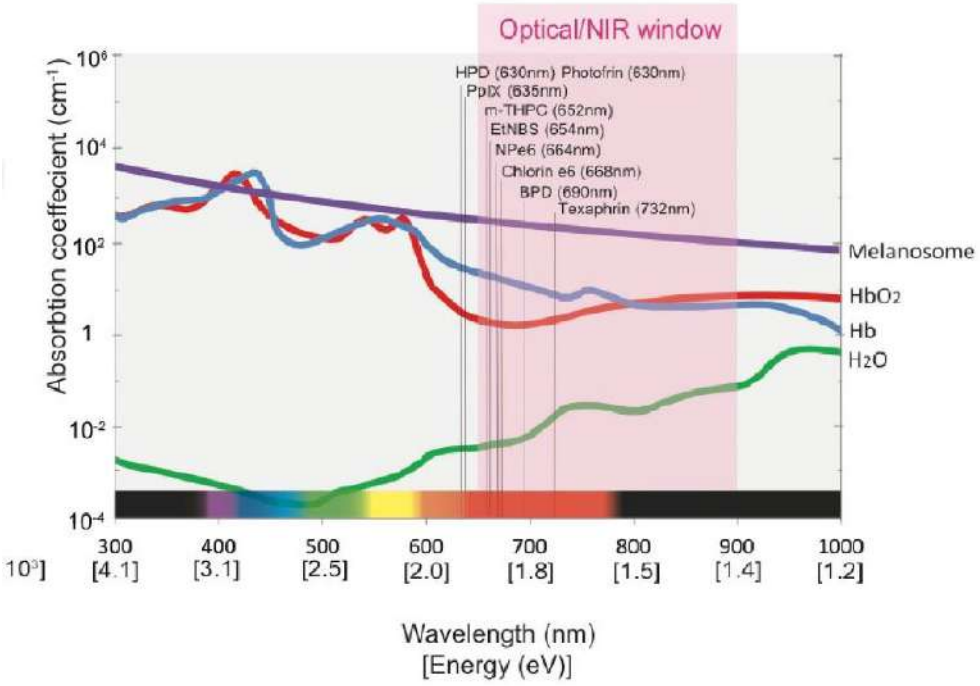

Figure 1.3: Absorption spectrum of physiological chromophores - melanosome, deoxygenated hemoglobin (HbO_2), oxygenated hemoglobin (Hb) - and water (H_2O) in the visible and near-infrared (NIR) spectral range. The optical window region where absorption of is low is evidenced in pink; the absorption peaks of most commonly used photosensitizers for photodynamic therapy are also reported (black lines). Picture taken from [69].

$^1O_2$ is the primary cytotoxic species in PDT. [68] However, this procedure is limited to superficial diseases, since the most common PSs can be excited by UV or VIS light and in this range the human tissues are not transparent (Figure 1.3). [69] The enhancement of tumour selectivity can be achieved by grafting PSs on properly targeted NPs; while, to increase the treatment penetration, the combination of PSs with upconverting luminescent NPs (UCNPs), that typically are ceramic materials doped with rare-earth or transition metals, such as $NaYF_4$:Er^{3+}, has been investigated. [70] UCNPs absorb light in the near-infrared region, where biological tissues present a transparency window, and then via an anti-Stokes emission process convert it into visible light that can activate the PSs through radiative and/or non-radiative energy transfer mechanisms.

1.3 X-Ray based cancer treatments mediated by nanomaterials

In this section, firstly the protocols and mechanism of traditional radiotherapy will be described. Then, the use of dense nanoparticles and multicomponent nanosystems in innovative X-Ray activated cancer strategies will be presented. Lastly, the ionizing radiation energy deposition processes in nanosized materials will be discussed.

1.3.1 Conventional radiotherapy

Radiotherapy is one of the most effective and widely used cancer therapeutic modalities. About 50% of cancer patients are treated with RT for curative and palliative purposes both as single therapeutic modality and in combination with other treatment methods. [19] In conventional RT, the ionizing radiation, usually from external beams with energy between 6 and 20 MeV, is exploited to stop the rapid proliferation of cancer cells aiming at delivering the maximum dose to the target tumour tissue while sparing the surrounding normal tissue. [24] In typical launched protocols, patients are treated through fractionated regime with a dose of 1.8-3 Gy delivered every few days over the course of 4-8 weeks up to 50-70 Gy total dose [71] to limit toxicity to normal tissues, but in advanced therapeutic protocols, different treatment schedules are used. In hyperfractionated RT, small doses (1.2-2 Gy) per fraction with an increased number of fractions are delivered two or more times a day aiming at increasing the total dose, and hence the success probability. [18] Differently, in hypofractionated RT, patients, who would not tolerate surgical resection, are treated with few doses of about 15-20 Gy over a short period of time (2-3 weeks). [72] In the RT mechanism, the killing of tumour cells is induced by the high energy radiation that directly damages the DNA and the molecular structure leading to the termination of cell division and proliferation, and even to cell necrosis or apoptosis; alternatively, RT can indirectly form ROS upon interaction with the cellular aqueous environment. [19]

The first interaction of with biological tissues can occur by photoelectric effect, Compton effect, and pair production, according to the energy of the external X-Ray source; the deposit of their energy occurs gradually through a cascade of secondary photoelectrons and Auger electrons, [73] stimulating all the radiobiological effects depicted above. The interaction between ionizing radiation and matter through each of the primary three mechanisms depends on the atomic number of the material (Z) and on the energy of the incident beam (E_i), as dis-

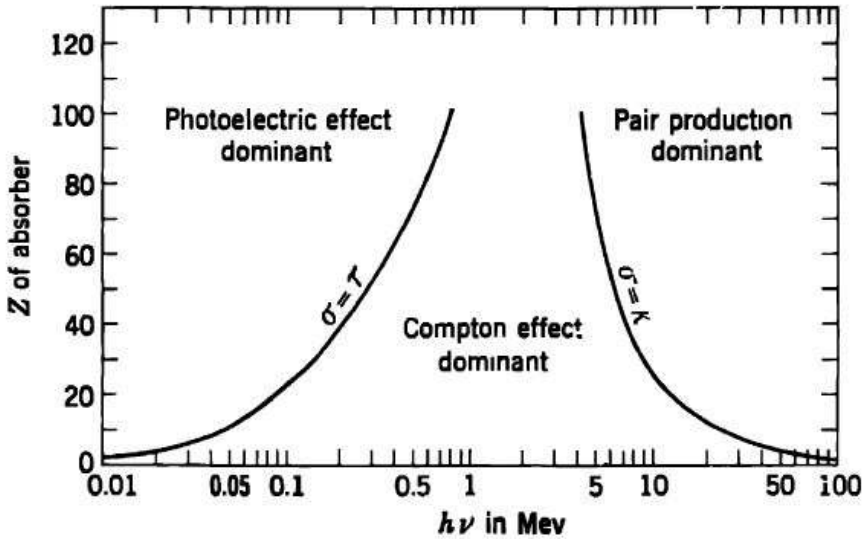

Figure 1.4: Relative importance of the three primary mechanism of X-Ray interaction. The lines show the values of the atomic number (Z) and the photon energy ($h\nu$) for which the two neighbouring effects are just equal. Picture taken from [74].

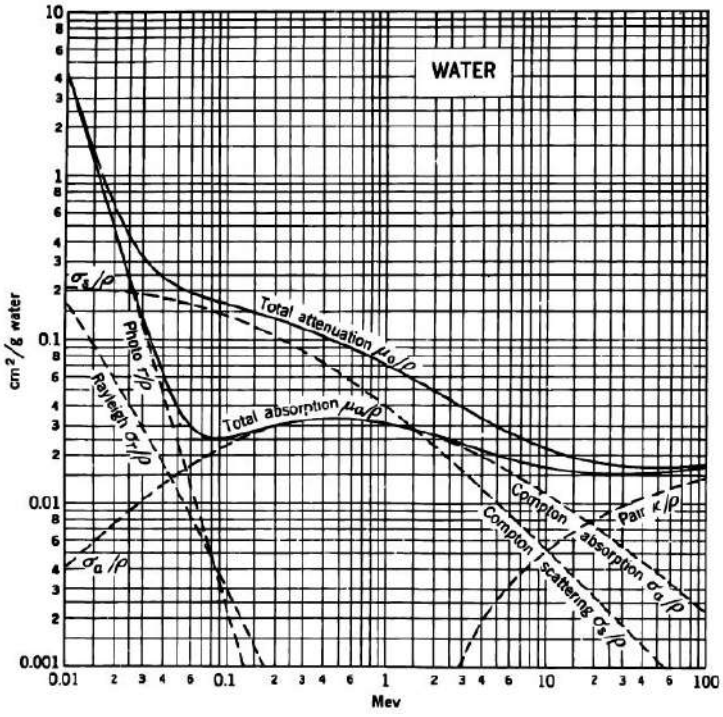

Figure 1.5: Mass attenuation and absorption coefficients for photons in water. Picture taken from [74].

played in Figure 1.4. [74] For all the three mechanisms, the interaction probability raises for higher Z values. The photoelectric and Compton effects are dominant for E_i lower than tens of MeV and their probability decreases as E_i increases, whereas the pair production is allowed only for energy photons exceeding 1.02 MeV, that correspond to the sum of the rest mass of an electron and a positron, hence is the minimum energy required to generate an electron-positron pair. As an example, Figure 1.5 reports the mass attenuation and absorption coefficients of the three primary interaction mechanism for X-Ray photons in water. It is worth highlighting that the decrease of the total attenuation and absorption coefficients as E_i increases is related to the higher penetration depth of MeV photons than of keV ones in matter. [73] These relationships between E_i, Z, and penetration depth are crucial to both address the RT requirements, such as the release of an amount of energy adequate to start the biochemical ROS production to destroy the proliferation of the malignant cells and the need of high energy primary beams enabling the penetration of the radiation in deep tumours, and to surpass its main drawback, that is the lack of tissue selectivity, hindering the discrimination between the tumour and the heathy cells.

1.3.2 High density nanoparticles in radiotherapy

The implementation of nanotechnologies with RT aims at both enhancing and localizing the therapeutic effect, in order to reduce the local dose to be delivered and the toxicity towards normal surrounding tissues, and consequently to improve the quality of life of the patient during and after the radiological treatments. In particular, the most advanced strategies propose to use dense NPs in radiotherapy as passive enhancers of energy deposition or as active ROS generators. Passive nanomaterials include high density systems (for instance, metal containing nanoparticles), able to efficiently stop the ionizing radiation and significantly increase the local energy release within the tissues, thanks to the difference in Z value between the biological environment and the NPs, and thus to boost the RT effects at lower doses. Several studies on metals (Au, Gd, Pt NPs) and metal oxides (HfO_2, Ta_5O_2) nanostructures have already highlighted the great potentiality of this innovative RT procedure. [22] Differently, active ROS generating NPs are inorganic catalysts, that possess lower Z than the passive NPs but can sensitize the RT effects by producing, thanks to their reactive surfaces, an excess of ROS in cells upon X-Ray exposure and by causing ROS-dependent functional disorder/cell death/apoptosis. For instance, TiO_2 and ZnO have been proved to create free radicals as well as $^1O_2$ after oxidation of superoxide radical

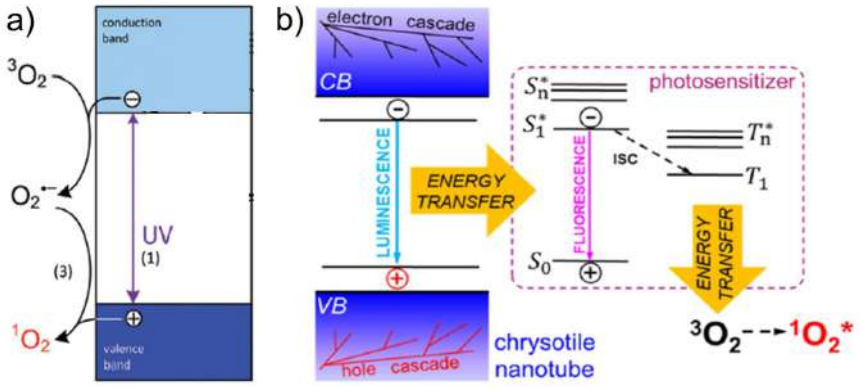

Figure 1.6: Photophysical mechanisms of the induced singlet oxygen generation at the surface of an inorganic catalyst NPs under UV exposure (**a**) and by multicomponent nanosystems, as X-PDT agents, under X-Ray irradiation (**b**). Picture adapted from [75] and [25].

ions (Figure 1.6a) under both light and ionizing radiation [23, 75, 76] excitation, and therefore to be suitable for X-Ray based oncological treatments. [44, 77] The catalytic process that leads to ROS sensitization by these nanosized semiconductors will be described in Section 2.3. Nevertheless, the classification of dense inorganic nanomaterials into passive and active RT agents is not strict: generally, both types of NPs disclose the ability to favour the release of the energy of the ionizing radiation and to produce ROS, but typically with different efficiencies. Thus, this classification considers as passive NPs the nanomaterials with high probability of interaction with the ionizing radiation and low catalytic activities and *vice versa* for active NPs.

1.3.3 Multicomponent nanosystems for X-PDT

Another advanced oncological strategy that exploits inorganic NPs is X-Ray induced photodynamic therapy. In fact, as mentioned in sub-Section 1.2.1, traditional PDT, in which the PS is activated by UV/VIS light, is ineffective for deep-tissue treatment: irradiation using ionizing radiation, thanks to its high penetrability, offers an effective solution for adapting this treatment to deep tumours. [16] X-PDT mechanism relies on an inorganic/organic multicomponent nanosystem: [20] PSs therapeutic agents are grafted on scintillating nanoparticles, able to convert the ionizing radiation into UV/VIS light through a three-stage scintillation process roughly described as- conversion, transport, and luminescence. [78] These functionalized NPs can be targeted towards the malignancy where the absorption of X-Ray by the inorganic part leading to energy

deposition in its proximity - *i.e.* the biological surrounding - can occur. Afterwards, the energy can be transferred to the PSs through multiple radiative emission/reabsorption processes and/or through efficient energy transfer mechanisms, activating the photophysical processes required for free radicals (especially $^1O_2$) generation (Figure 1.6b). Moreover, high-energy beam can deposit energy in the cellular aqueous environment with the consequent excitation of the NPs and then the activation of PSs nearby and also the organic molecules can interact with the primary beam by themselves. In order to employ energy transfer from the nanoscintillators to the PSs for triggering the ROS production, the organic moieties absorption spectrum should be resonant with the NPs emission.
Many inorganic nanomaterials like oxides, fluorides, silica-based nanostructures, and semiconductor nanocrystals have been combined with organic photosensitizers towards X-PDT applications. [25, 26, 46, 47] For example, a previous study has shown that chrysotile scintillating nanotubes functionalized by an ionic self-assembly strategy with porphyrins as PSs sensitize $^1O_2$ production under ionizing radiation and induce cell killing even at low doses (2 Gy), [25] opening the possibility to effectively reduce the high-energy radiation exposure of patients during oncological therapies. Moreover, this work discloses that the $^1O_2$ generation is strongly affected by the X-PDT agents design and hence their synthesis should be optimized to avoid PSs aggregation on the nanoscintillators surfaces and to increase the NPs dispersibility in the physiobiological environment.
In particular, the employment of conjugated organic molecules, such as porphyrins, as PSs can be effective because of their high singlet oxygen production yield, but their tendency to form aggregates, [79] that quench the excitation, can strongly limit their ability to generate cytotoxic species. [80] The rate of this self-association, driven by electrostatic interaction between the molecules aromatic central rings [81] depends on the temperature of the functionalization step and on the PSs concentration, leading to aggregates with different lengths (from dimers and trimers to multi-monomers chains) and super-molecular structures (from disordered to highly ordered configurations). [82] Among them, the ordered assemblies, *i.e.* J-aggregates and H-aggregates, in which the monomers are arranged in head-to-tail and face-to-face alignment, respectively, are of particular interest due to their peculiar electronic and spectroscopic properties, different from the ones of conjugated single molecules. [81, 83] For instance, the absorption and emission spectra of J-aggregates and H-aggregates are shifted to lower and higher energies, respectively, compared to the single molecule; [82] furthermore, the non-radiative rate of aggregates is higher compared to that of the monomer,

thus hindering the PSs photophysical processes pivotal for ROS generation. [84]

1.3.4 The effect of nanosized materials on X-Ray energy deposition

In conventional RT as well as in innovative X-Ray cancer therapies mediated by nanomaterials, the effective result of RT and the estimation of the dose deposited in the malignancy environment depend on the interactions in tissue involving both primary and secondary events. In any case, the processes occurring within the nano-sized material after the interaction with the ionizing radiation require a deep comprehension. Indeed, the reduced material dimension is critical in the presence of high energy beams as the migration distance of secondary charges generated in the NPs along the track from the point of the ionizing event (relaxation mechanisms) are significantly larger than the nanometric radius of the NPs. In nanomedicine, open issues concern the estimation of the effective energy release within the nanomaterials embedded in the biological surrounding, the radiation dose-enhancement in the vicinity of the malignancy due to the presence of high-Z/dense NPs, and the radiobiological consequences. Moreover, the microscopic processes involved in X-PDT are also under debate: besides the mechanisms due to the presence of high-Z nanoscintillators, the effect of the photo-toxicity of the PSs grafted on their surface should be considered, together with the possible interactions of the high energy beam directly with the PSs. [24]
In this context, Monte Carlo simulations are powerful tools that enable to evaluate the spatial energy distribution resulting from the interaction between the high energy radiation and the NPs, [27] which drives the RT efficiency enhancement and the activation of PSs in X-PDT. For instance, in a theoretical dosimetric work the irradiation of a brain tumour phantom in the presence of high Z iodine agents has been simulated for several X-Ray energies (from 30 keV to 6 MeV); it has been observed that the major dose deposition enhancement and accuracy are obtained for a medium energy beam (80 keV), despite its lower penetration depth with respect to MeV ones. [85] Furthermore, these computational models are useful to relate the release of secondary particles after the first ionization event with the physical, chemical, and structural properties of the nanomaterials. Moreover, an interesting computational work reported that, even if the primary interactions occur mainly in the aqueous surroundings, a significant fraction of the beam energy is transferred in the NPs by the secondary particles and that the amount of energy deposited in the NPs depends on the particle energy as well as on the nanomaterial size and composition. [86]

Chapter 2

Zinc oxide properties - from bulk to nano-size

In this chapter, the properties and applications of bulk and nanosized zinc oxide will be introduced. Then, an insight on the optical and catalytic properties of ZnO as well as an overview of its possible uses in nanomedicine will be provided.

2.1 Introduction

Zinc oxide is a semiconductor, widely studied since the beginning of the 20^{th} century for various potential applications due to its unique properties and the availability of high-quality bulk crystals as well as of a plethora of nanostructures. [28,29] Indeed, its optical, electrical, and mechanical properties make ZnO a good candidate for transparent thin-film transistors, photonics and optoelectronic devices, and in spintronics. [30,31] Moreover, the development of novel nanosized ZnO-based systems promoted both the opportunity of studying stimulated emissions and nonlinear optics in nanometric samples, [29] and the exploration of new applications in the field of catalysis, [32] photocatalysis, [87] gas sensing, [33] and nanomedicine. [23] In particular, the attractiveness for the biomedical applications of ZnO relies on its biocompatibility and stability together with the anti-cancer and anti-bacterial activities displayed by this material at the nanosize. [34]

ZnO is a II-IV compound that can crystallize in three forms: hexagonal wurtzite, cubic zinc blende, and rocksalt. [28] At ambient conditions, the thermodynamically stable phase is wurtzite (Figure 2.1a), characterized by a mixed ionic and covalent bonding: indeed, each ion (Zn^{2+} and O^{2-}) is tetrahedrally coordinated with the other ion through *sp3* hybrid orbitals. [36] Due to the low symmetry of

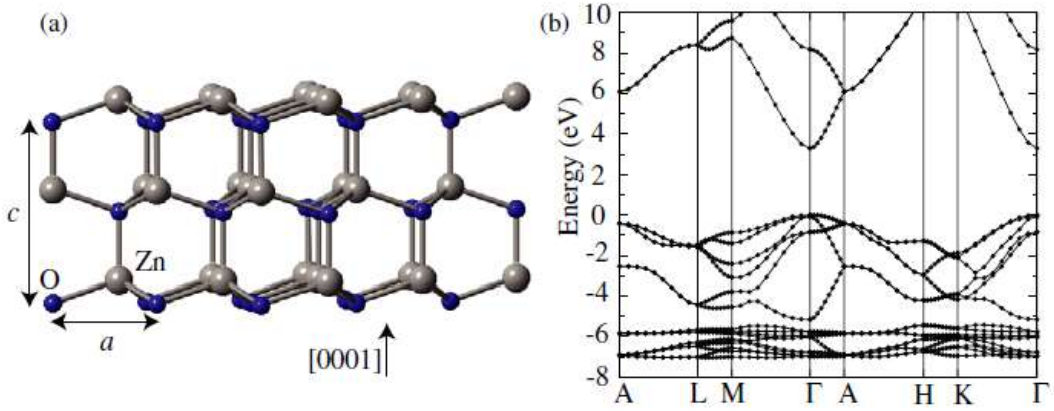

Figure 2.1: The wurtzite crystal structure of ZnO with the lattice parameters a and c indicated in (**a**), and the calculated band structure of ZnO in (**b**). The energy of the valence-band maximum is set to zero. Picture taken from [30].

the wurtzite crystal structure together with a large electromechanical coupling, ZnO discloses strong piezo- and pyro-electric properties. [28] Besides, ZnO is stable up to 1000 °C and exhibits high heat capacity and thermal conductivity, that are properties advantageous for heat dissipation applications. [30]

Furthermore, ZnO direct wide band gap of about ∼3.4 eV [36] (Figure 2.1b) with a large excitonic binding energy of approximately 60 meV, [37] determines its electrical and optical properties, which are also strongly affected by its defectiveness, *i.e.* the concentration and types of intrinsic and extrinsic points defects (as mentioned in sub-Section 1.1.1). Remarkably, ZnO excitons are stable and consequently their processes occur even at room temperature, since their binding energy is about 2.4 times higher than thermal energy (k_BT) at 298 K. Anyway, the role of native defects and impurities on ZnO electrical conductivity and luminescence has still to be unveiled. [30] For instance, the development of ZnO based devices with stable and reproducible p-type conductivity has been not yet achieved and its control requires a deeper understating of the material defectiveness. [55] Likewise, luminescence emission includes, in addition to the near-UV excitonic emission at ∼3.4 eV, several emission bands in the VIS region of the spectrum, associated to defect states, whose energy levels lie inside ZnO forbidden energy gap and whose origin has no unique consensus in the literature. [28, 29, 37] Moreover, the impact of defectiveness on ZnO electrical and optical properties has been boosted by the possibility to synthesize nanosized ZnO-based systems. [49] In fact, the advances of nanotechnologies have opened the possibility of realizing ZnO NPs with a variety of morphologies and hence with several points defect types and concentrations by easy, cost-effective, and

low-energy consuming routes. [4,88] Additionally, the large surface area combined with the great surface activity of ZnO NPs have further improved their ability to promote catalysis, photocatalysis, and the formation of environmentally persistent free radicals as well as anti-bacterial and anti-cancer effects. [34,36,38,42]

2.2 Optical properties

As already mentioned, ZnO is a promising material for several optoelectronics and photonics applications, such as laser diodes, light emitting diodes, photodetectors and photovoltaics, due to both its near-UV exciton emission at ∼3.4 eV and VIS defect-related luminescences. [30] In particular, ZnO excitonic emission persisting even at room temperature is of great interest for photonic applications in the UV and blue spectral range. Moreover, ZnO is also known as a scintillating material with great radiation hardness. [35,89,90]
The development of engineered ZnO-based nanosystems for both optical devices and ionizing radiation applications requires further comprehension of the role of defectiveness and morphology on its luminescence properties. [91] In the last decades, several studies have been devoted to the investigation of ZnO excitonic and defect emission bands. [28,29,37,39]
The ZnO UV peak has been studied by temperature-resolved photoluminescence to discriminate the bound and free exciton optical features. [92] The bound excitons emission is progressively suppressed by temperature increase and it is completely quenched between 50 and 150 K; [31] at variance, the luminescence of free excitons is still present at room temperature and its peak position shifts to lower energies as temperature increases. [29]

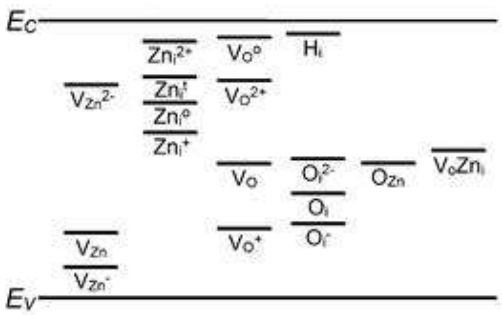

Figure 2.2: Schematic representation of ZnO energy gap and points defect energy levels. Picture taken from [55].

Moreover, ZnO defect emissions in the VIS range (orange-red ∼1.9 eV, yellow-

green ∼2.3 eV, blue ∼2.6 eV, and violet ∼3.0 eV) have been widely investigated, but their attribution is still matter of debate (Figure 2.2). In oxygen-rich samples, the luminescence in the orange-red spectral region is usually reported: an enhancement of the red emission at ∼1.9 eV has been observed in ZnO NPs after annealing in air [93] and in ZnO nanorods after sulfur hexafluoride plasma treatment. [94] The VIS luminescence detected between 2.2 and 2.4 eV, defined as the yellow-green band, is the most commonly observed [55] and the most controversial. Its origin has been associated to the singly ionized oxygen vacancies: [95] in fact, the ZnO green emission has been observed in samples that also disclose an electron paramagnetic resonance signal at g=1.96, [96] whose assignment to these defect species has reached a wide consensus in the scientific community. [97] Nevertheless this attribution is still under debate. [98–100] Several others hypotheses have been proposed, among which a recombination mechanism that involves electrons trapped in shallow levels with holes trapped in deep levels, [101] and surface defects. [102] Indeed, a previous work on ZnO/SiO_2 systems suggests that the green luminescence is related to surface defects. [38] Moreover, in hydrothermal crystals, the yellow-green band has been attributed to a defect related to the presence of Li ions. [28, 30] Indeed, bulk crystals grown with this method are affected by the presence of metal impurities, such as Li, K, Al, [103] that can introduce localized energy levels in the ZnO forbidden energy gap. [104, 105] Emissions in the blue (∼2.6 eV) and violet (∼3.0 eV) spectral regions are generally attributed to zinc interstitials (Zn_i) and/or vacancies (V_{Zn}): [29] the former is a shallow donor that lies at ∼0.3 eV below the conduction band, while the latter is a shallow acceptor that lies at ∼0.3 eV above the valence band. [30] The violet emission has been associated almost unambiguously to the radiative decay of photogenerated electrons from the Zn_i levels to the valence band. [106] Differently, two mechanisms have been proposed for the blue luminescence: it could occur either due to radiative recombination of electrons between the Zn_i and the V_{Zn} levels [107] or between Zn_i states, that due to lattice disorder are deeper than simple Zn_i states, and the valence band. [108]

Moreover, as observed for other nanomaterials [109–111], the optical properties of ZnO have demonstrated a high sensitiveness to several features, such as morphology, [38, 112] growth parameters, presence of precursors, [39, 40] as well as environmental conditions. [41, 113] Indeed, ZnO defectiveness is strongly related to all these parameters.

2.3 Photo- and radio-catalytic properties

In the last years, the use of ZnO as a catalyst has attracted great interest, especially because of the possibility to activate its high surface reactivity upon light or X-Ray exposure. [36, 44] In particular, catalytic effects have been investigated for the degradations of organic pollutants from the environment by converting them into benign products as well as for triggering toxicity towards infective pathogens and cancer cells by ROS generation and release. [23, 42]
For nanosized semiconductors, such as ZnO and TiO_2, the photo- and radio-catalysis phenomenon, displayed in Figure 2.3, can be described as a three step process: i) absorption of high energy ionizing radiation or light source with energy larger than the energy gap of the material; ii) generation of an excited electron e^- in the conduction band and of a hole h^+ in the valence band; iii) migration of of e^-/h^+ charges toward the materials surface to rapidly (in the sub-nanosecond time range) initiate reduction and/or oxidation reactions with molecules adsorbed at the nano-catalyst surface with subsequent formation of radical species. In an aqueous environment, the photo- or radio-generated carriers trigger ROS production: electrons at the nanomaterial interfaces reduce molecular oxygen, forming superoxide radical anion; hydroxyl radicals and hydrogen peroxide molecules are induced by the holes, oxidizing water molecules and hydroxide ions. In addition, singlet oxygen can be generated by the oxidation of superoxide radical anions by holes in the valence band. [76]

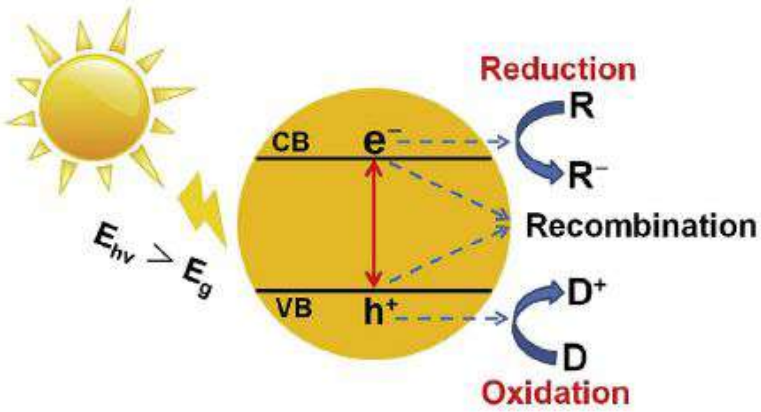

Figure 2.3: Basic mechanism of photocatalysis in ZnO. E_{hv} is the irradiated photon energy, E_g is the energy gap, R is the electron acceptor, and D is the electron donor. Picture taken from [42].

The efficiency of the catalysis process is strongly related to the diffusion step

(step iii): indeed, the recombination of the generated e^-/h^+ is an alternative relaxation pathway, that decreases the number of carriers able to reach the nano-catalyst surfaces. Moreover, since the catalysis reactions occur at material interface with the environment, the surface properties, such as area and defectiveness, play a key role in defining the catalytic properties. Several studies have reported the enhancement of the catalytic efficiency upon reduction of the material size. [36] The effect of points defects type and concentration on the free carriers processes (generation, migration, and recombination) has also been widely investigated. [42] For instance, it has been observed that under light excitation the catalytic efficiency is restrained by the occurrence of quenching channels in ZnO NPs, [114] whereas it is favoured by the intentional inclusion of vacancies and interstitials in crystalline ZnO nanorods. [43] Indeed, to enhance the performances of ZnO as a nano-catalyst, several strategies based on the engineering of surface defects have been proposed: additional defects states can be created by altering the synthesis procedure towards non-equilibrium growth conditions [115] or by doping, that introduce an impurity in the ZnO lattice and consequently alter its crystal structure. [116]

2.4 ZnO nanosystems for oncological applications

Nanoparticles of ZnO, recognized as safe by the Food and Drug Administration due to their noticeably low toxicity, are attractive materials for biomedical applications. [117] ZnO NPs have been widely explored for anticancer, antidiabetic, antibacterial, antifungal, and anti-inflammatory activities, as well as for imaging and drug delivery applications. [34] Especially, ZnO NPs have been proposed as active ROS generators and PSs carriers in both light and X-Ray induced oncological protocols (*e.g.* PDT, enhanced radiotherapy, and X-PDT) since their anticancer action relies on the ability to trigger ROS generation and apoptosis mechanisms under external excitations. [16, 20, 44, 46, 48, 118, 119] Moreover, the loading of anticancer drug into the ZnO nanoparticles results in an augmented cytotoxicity effect of the cancer therapy, due to the synergism produced by the combination of chemotherapeutic drug and the lethal ROS production activated by ZnO. [120, 121] Although ZnO anti-bacterial and anti-cancer effects are generally induced by ROS generation, also other mechanisms have been proposed for the killing of pathogens and tumours cells. [34] For instance, electrostatic interactions between ZnO NPs and cell walls can result in the loss of cells integrity

and in the malfunction of their permeability barrier, [23] whereas the release of Zn^{2+} ions from ZnO NPs can lead to cell unbalanced metabolism and death. [42] In the following, the most significant and promising examples of ZnO-based nanosystems proposed for applications in light and X-Ray induced cancer therapies will be described.

In a previous work, the therapeutic behaviour in cancer treatment of ZnO NPs with different average diameters (20, 60 and 100 nm) under UV irradiation has been proved on human hepatocarcinoma cell lines by comparing cells survival after light exposure with and without NPs. [45] The authors also note an increase of the suppression of cell proliferation as the UV triggered ZnO NPs size decreases, thus supporting the correlation between surface reactivity and cytotoxic species production. More recently, further *in vitro* analyses on the molecular mechanism activated by ZnO NPs upon UV exposure indicate the triggering of cell death through mainly caspase-dependent apoptosis. [122]

Moreover, the potentiality of ZnO coated by a silica layer (ZnO/SiO_2), with an average diameter of 80-100 nm, to promote the radiation-induced killing effect has been studied under X-Ray irradiation (200 kVp) on prostate adenocarcinoma cell lines. [44] By evaluating cells survival after RT with and without NPs, a 2-fold augmented killing rate in presence of ZnO based nanosystems is observed; the findings show the active response to ionizing radiation of ZnO/SiO_2 and thus the radio-catalytic mechanisms occurring at its surface. Moreover, the radiation-induced cytotoxicity sensitized by ZnO NPs with 100 nm diameter has been validated on human head and neck squamous cell carcinoma under 6 MV X-Ray irradiation. [119] In particular, the authors report a significant increase of the cell oxidative stress, due to ROS generation, only in cells both incubated with the ZnO NPs and exposed to the ionizing radiation.

Furthermore, due to their ability to promote ROS production, ZnO NPs have been proposed as PSs coupled with rare-earth doped nanoscintillators for X-PDT. [16, 20] For instance, $LiYF_4:Ce^{3+}@SiO_2$ @ZnO-PEG nanostructures have been developed aiming at exploiting the scintillating core ($LiYF_4:Ce^{3+}$) to convert X-Ray energy into UV fluorescence, able in turn to excite the semiconductor shell (ZnO) and consequently initiate its catalytic process. [123] The findings indicate that hydroxyl radical is the primary cytotoxic species produced by ZnO, at variance with what occurs using organic molecules as PSs that induce mostly singlet oxygen, paving the way to overcome the PDT efficiency dependence on oxygenation of cancer tissue.

Finally, in the last decade, ZnO has been loaded with different organic PSs to

realize synergic PDT or X-PDT agents. [16, 46, 118] In fact, the absorption of UV light or ionizing radiation by ZnO NPs can both promote ROS production and trigger the excitations of the dyes, thanks to optical interaction between the inorganic and organic part, leading to the activation of the PDT process. The mechanisms of both PDT and X-PDT have been already described in Section 1.2.1 and 1.3.3, respectively. Several *in vitro* studies have demonstrated the increased toxicity of ZnO nanosystems conjugated with porphyrins compared to the killing effect of the inorganic and organic part alone under UV exposure. [117] In a recent work, ZnO NPs with sizes ranging from 3 to 26 nm coupled with meso-tetra (4-carboxyphenyl) porphyrin (MTCP) and CuMTCP has been investigated for both PDT and X-PDT applications. [48] Photoluminescence analyses evidence the quenching of the high energy component of ZnO emission upon the conjugation of the inorganic nanomaterials with porphyrins, suggesting the occurrence of energy transfer between them. Cytotoxicity tests report an excellent killing effect towards human prostate and breast cancer cell lines of the functionalized nanosystems upon UV activation, but, interestingly, cell death is induced only by bare ZnO NPs under X-Ray exposure. To explain this finding, the authors propose that, under ionizing radiation, the optical interaction between the inorganic and organic part of the nanosystems fails and consequently ROS production is inhibited. Differently, in a current study on ZnO NPs doped with Ga^{3+} and coated with a SiO_2 shell loaded with PpIX porphyrins (ZnO:Ga^{3+}@SiO_2-PpIX), an efficient energy transfer both under light and X-Ray excitation between the nano-scintillating cores and the PSs has been observed. [46] In particular, time-resolved photoluminescence measurements performed by monitoring the PpIX emission in the functionalized nanosystems display that the dye luminescence is indeed activated upon ZnO excitation in its band gap, also evidencing the presence of porphyrin aggregates. Nevertheless, the evaluation of singlet oxygen generation upon ionizing radiation promoted by ZnO:Ga^{3+}@SiO_2-PpIX discloses a rather poor sensitization effect, probably related to the formation of PpIX aggregates, that are detrimental for the dye ability to generate cytotoxic species, as already discussed in sub-Section 1.3.3. In conclusion, the need for a further optimization of the multicomponent nanosystems synthesis is a key open issue in the development of porphyrin coupled ZnO nanostructures for X-PDT.

Chapter 3

Materials and methods

In this chapter, the synthesis approaches and the experimental procedures used to analyse the ZnO-based samples are presented together with their morphological characterization. In particular, Section 3.1 describes the material preparation and characterization of ZnO systems with different morphology with a focus on the dimensionality, that scales from the bulk to the nano-size. Section 3.2 illustrates the functionalization of ZnO/SiO_2 nanosystems with porphyrins, their morphological properties as well as the used experimental and computational methods. The synthesis together with the structural and morphological analyses of all the ZnO-based nanostructures have been realized in collaboration with the NanoMat@Lab of the Department of Materials Science. The computational analyses have been performed in collaboration with Dr Anne-Laure Bulin of the Synchrotron Radiation for Biomedicine Group at the University of Grenoble-Alpes, INSERM. The results and the discussion of the ZnO-based systems are reported in Chapter 4 and 5, respectively.

3.1 ZnO samples with different morphologies

In this section, the synthesis and methods characterization together with the morphological features of four sets of ZnO, comprising two types of nanoparticles, a commercial micrometric powder, and an industrial bulk single crystal are provided. The micrometric and bulk samples are studied to accurately compare the optical properties of ZnO with different dimensions and morphologies.

3.1.1 Samples preparation

Synthesis of ZnO/SiO_2 nanosystems: ZnO/SiO_2 are prepared by a two-step procedure, according to ref. [38]. First, an SG method reported elsewhere [124, 125] is exploited to synthesize shape-controlled silica NPs, *i.e.* SS or SR having different aspect ratios (1, 5, respectively). Successively, silica NPs are used as suitable matrix to grow nanometric ZnO NPs through a method reported, [126, 127] in which the hydrolysis and condensation of zinc acetate dihydrate is carried out to get homogeneously distributed ZnO NPs anchored onto the surface of the two supports (N05-SG-SS and N05-SG-SR, respectively). All the reagents are purchased from Merck Life Science. The reactant amounts are chosen in order to get a nominal ZnO loading on silica equal to 12 wt%.

Synthesis of isolated ZnO NPs: ZnO nanometric powders are synthesized using a standard air-free Schlenk technique. In a three necks flask (25 mL), solution A is prepared by dissolving 1 mM of zinc acetate dihydrate ($Zn(CH_3COO)_2$*$2H_2O$, $\geq$ 98%), 4 mM of stearic acid (SA) ($C_18H_{36}O_2$, 95%) and 10 mM of 1,2-dodecanediol ($CH_3(CH_2)_9CH(OH)CH_2OH$, 90%) in 20 mL of 1-octadecene (90% tech.). In another flask, 4 mM of octadecylamine (ODA) ($C_{18}H_{39}N$, 90% tech.,) are dissolved in 4 mL of 1-octadecene (90% tech) (solution B). Both the solutions are degassed at 100 °C for 30 minutes under vigorous stirring, and two clear solutions are obtained. SA and ODA are employed as capping agents with a molar ratio 1:1, as optimal molar ratio to get homogeneously shaped and sized ZnO NPs. [128, 129] All the reagents are purchased from Merck Life Science and used as received.
Solution A is then heated up to reflux (270 °C) under a nitrogen atmosphere, until its coloring turned orange. Under reflux conditions, solution B is quickly added to solution A through a syringe (hot injection method) and left under stirring at 270 °C for a suitable time (5 minutes for N05-HI, 20 minutes for N22-HI). Then, the mixture is cooled down to room temperature and the NPs are separated by adding acetone as antisolvent through centrifugation (octadecene:acetone volume ratio equal to 1:1). At last, the solid precipitate is washed twice with fresh hexane (5 mL) and again reprecipitate with acetone (hexane:acetone volume ratio 1:1) and eventually stored in hexane (5 mL).

Micrometric ZnO powder: Zinc Oxide, Puratronic, ~325 mesh (~44 μm) powder with a purity of 99.999% (metal basis) is purchased from Alfa Aesar by Thermo Fisher. The sample is labelled as MP.

ZnO bulk single crystal: A ZnO single crystal (BC), grown by hydrothermal method, with purity 99.99% (metal basis), orientation 0001 and two sides polished is purchased from Alineason Materials Technology. The crystal dimensions

are 10 mm x 1 mm x 1 mm.

3.1.2 Structural and morphological characterization

Diffraction experiment: Powder X-Ray diffraction (PXRD) patterns are collected with a Rigaku MiniFlex 600 diffractometer with 0.154 nm Cu Kα radiation). The measurements are performed in the range 30-80° 2θ (2θ step 0.02°, 1°min^{-1} scan rate).

Electron microscopy: Scanning electron microscopy (SEM) is used to study the morphological features of the three nanometric samples (N05-SG-SS, N05-SG-SR, N22-HI), whereas for N05-HI high-resolution transmission electron microscopy (HRTEM) is employed. SEM measurements are performed by a VEGA TS5136 XM TESCAN microscope in a high-vacuum configuration (electron beam excitation = 30 kV, beam current = 25 pA, working distance = 12 mm). SEM analysis is further employed to verify the size of ZnO particles in a MP micrometric sample. Prior to SEM analysis, the samples have been gold-sputtered, to increase their conductivity. HRTEM images of ZnO NPs are collected on a FEI Tecnai Transmission Electron Microscope equipped with a Gatan OneView camera operating at 200 kV. ZnO NPs have been deposited onto carbon coated Cu TEM mesh grids by drop-casting a dilute NPs dispersion in hexane. The size of ZnO NPs is determined by manually measuring 100 particles randomly chosen in each sample.

Infrared spectroscopy: Fourier transformer infrared resonance (FTIR) is employed to assess the nature of residual capping agents on the surface of N05-HI and N22-HI. The analysis is performed with a Perkin Elmer Spectrum 100 instrument by a single reflection attenuated total reflection (ATR) method (1 cm^{-1} resolution spectra, 650-4000 cm^{-1} region, 16 scans).

Thermogravimetric analysis: The quantification of surface ligands on N05-HI and N22-HI is performed through a thermogravimetric analysis (TGA). TGA analyses are carried out using a TGA/DCS1 STARe SYSTEM at constant air flux (50 mL min^{-1}), measuring the sample weight loss between 150 and 1000 °C ($\Delta W_{150-1000°C}$) at increase furnace temperatures (temperature range 30-1000 °C), heating rate 10 °C min^{-1}, applying two isotherms at 150 °C and 1000 °C both of 15 minutes. In these conditions a complete SA combustion is achieved.

3.1.3 Structural and morphological properties

The structural features of both micrometric and nanometric ZnO materials are analyzed by PXRD.

For all samples, PXRD spectra (Figure 3.1) indicate the presence of the hexagonal ZnO wurtzite crystal phase (JCPDS no. 36-1451). The nanometric average size of crystalline ZnO NPs is validated by the lower relative intensity and higher width of the (100) and (101) reflections of the nanometric samples prepared by the HI method (N05-HI, N22-HI). Differently, sharp peaks are obtained for the microcrystalline MP sample. The size of ZnO NPs estimated by the Scherrer equation results (8.9±1.3) nm and (15.9±2.4) nm for N05-HI and N22-HI, respectively, in agreement with the average diameters of NPs estimated by TEM images. Besides, the SG procedure leads to slightly lower crystallization degree of ZnO NPs, especially in N05-SG-SS, as disclosed by the reduction in the relative intensity of (100) and (101) ZnO reflections in N05-SG-SS and N05-SG-SR. Due to the presence of amorphous SiO_2 NPs, PXDR spectra of N05-SG-SS and N05-SG-SR show an additional broad peak at $2\theta = 22°$.

The morphology of ZnO particles in all samples is investigated by electron microscopy. First, SEM of N05-SG-SS and N05-SG-SR confirms that the developed synthetic procedure promotes the anchoring of nanometric ZnO NPs (∼5 nm) onto the surface of porous SiO_2 NPs having different aspect ratios (average diameter of SiO_2 spheres ∼ 80 nm in N05-SG-SS, average length of SiO_2 rod-like particles ∼ 400 nm in N05-SG-SR, Figure 3.2).HRTEM and SEM corroborate the nanometric size of N05-HI and N22-HI, by showing almost spherical NPs with a size of (5±1) nm and (22±5) nm, respectively (Figure 3.3). Lastly, the SEM micrographs of MP (Figure 3.4) reveal the occurrence of micrometric agglomerates of particles very inhomogeneous both in shape and dimensions, which range from 100 nm to 2 μm.

FTIR spectra of N05-HI and N22-HI evidence the presence of SA molecules, used as capping agent in the HI synthesis procedure, on the surface of ZnO NPs (Figure 3.5), as demonstrated by: i) the asymmetric and symmetric stretching of CH_2 groups at 2916 and 2860 cm^{-1}, ii) the asymmetric and symmetric stretching of the carboxylate groups (-COO-) at 1538 and 1398 cm^{-1}, characteristic of the coordination of SA molecules with Zn atoms onto the surface of ZnO NPs. By TGA technique (Figure 3.6), the amount of SA organic ligand, corresponding to the measured weight loss between 150 and 1000 °C ($\Delta W_{150-1000°C}$), results 80 wt% for N05-HI and 20 wt% for N22-HI, in agreement with the higher surface/volume ratio and surface energy of ZnO NPs in N05-HI, compared to N22-HI.

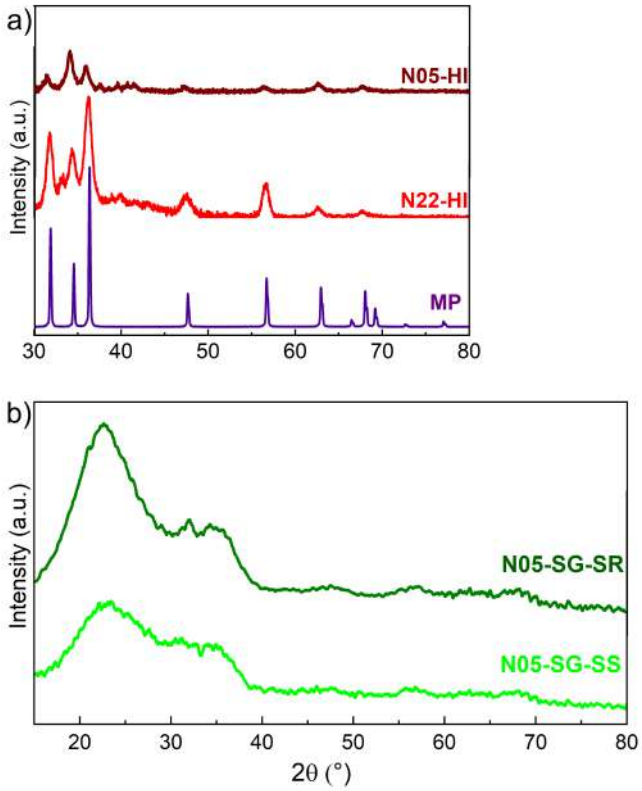

Figure 3.1: PXRD spectra of ZnO NPs prepared by **a**) hot injection method (N05-HI and N22-HI, in comparison to MP) and **b**) supported onto SiO_2 NPs (N05-SG-SS and N05-SG-SR).

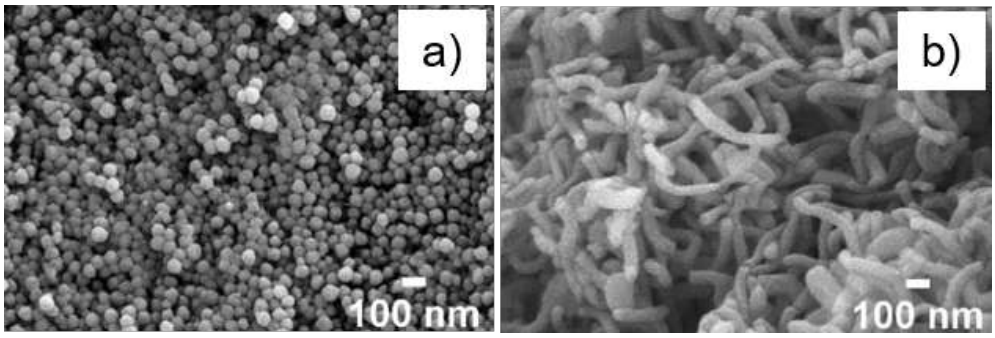

Figure 3.2: SEM of N05-SG-SS (**a**) and N05-SG-SR (**b**), respectively. SS: spherical, SG: sol–gel method, SR: rod-like.

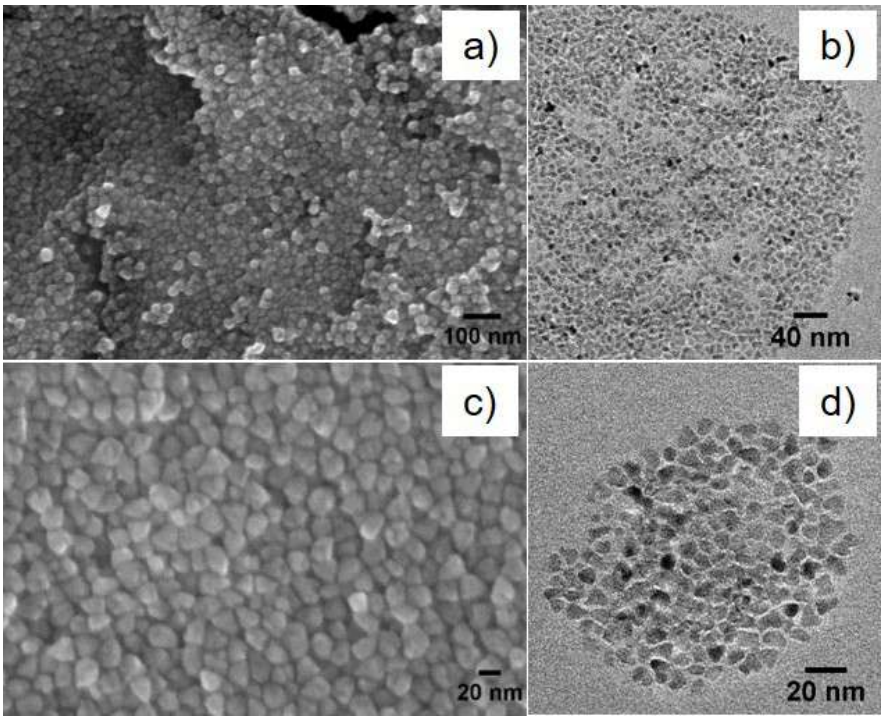

Figure 3.3: SEM images of N22-HI (**a,c**) and HRTEM of N05-HI (**b,d**).

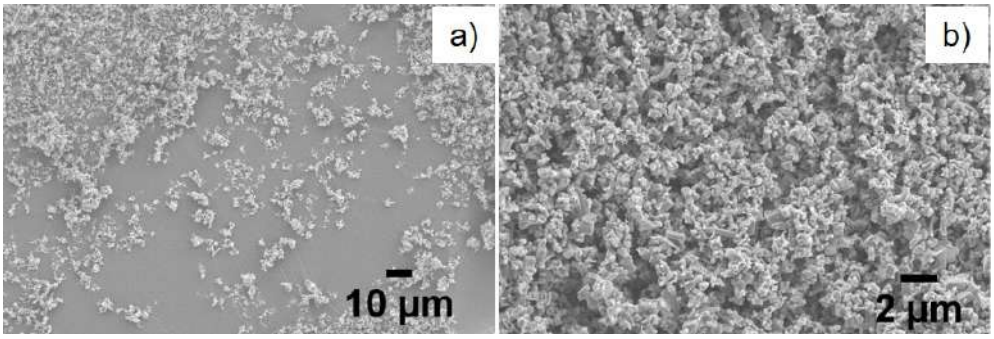

Figure 3.4: SEM images of MP.

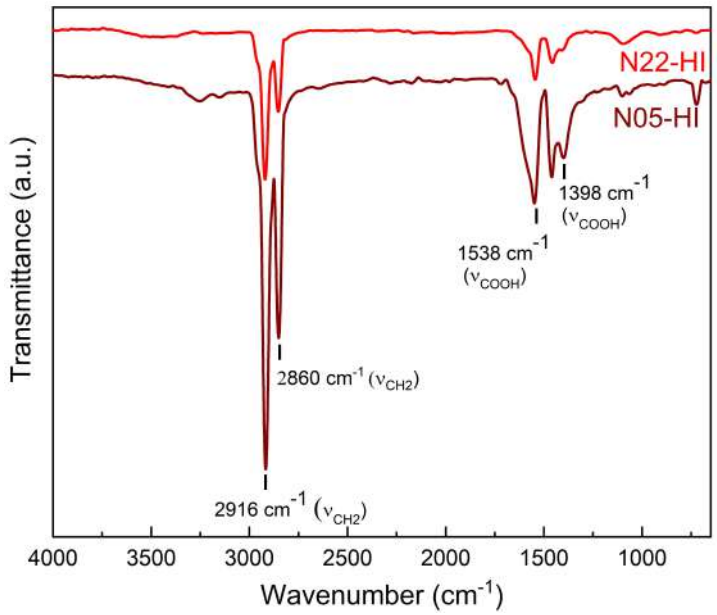

Figure 3.5: ATR-FTIR spectra of ZnO NPs synthesized through the hot injection method (N05-HI and N22-HI)

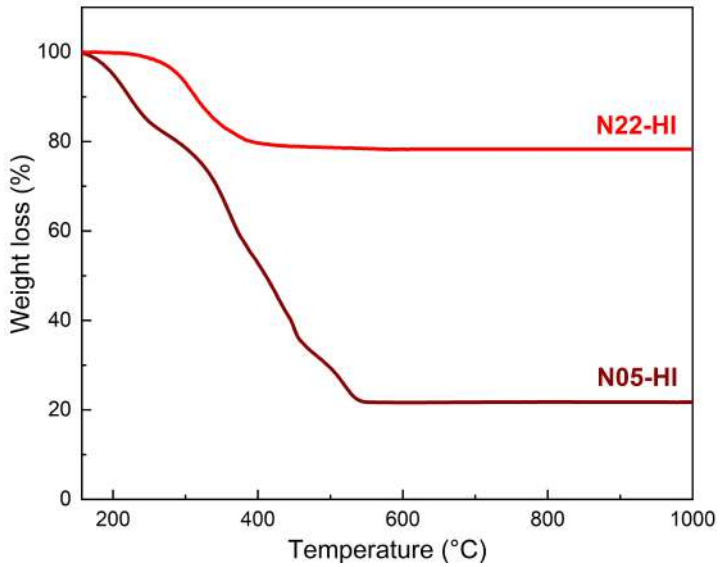

Figure 3.6: TGA profile of ZnO NPs prepared by hot injection. The weight loss ($\Delta W_{150-1000°C}$) is connected to the combustion of the surface ligands.

3.1.4 Spectroscopic and catalytic characterization

Steady state photoluminescence analysis: Steady state photoluminescence (PL) spectra are measured by a continuous wave (CW) Xenon lamp as excitation source coupled to a double monochromator Jobin-Yvon Gemini 180 with 1200 grooves/mm gratings and recorded through a nitrogen cooled, back illuminated, UV enhanced, CCD (charge-coupled device) detector coupled to a monochromator Jobin-Yvon Micro HR with a 150 grooves/mm grating. All the spectra, recorded as a function of nanometers, are firstly corrected for the spectral response of the detector and subsequently converted into spectra as a function of energy.

Time resolved photoluminescence measurements: Time resolved photoluminescence (TRPL) measurements are carried out in time correlated single photon counting (TCSPC) mode using a FLS 980 spectrofluorometer. TRPL spectra of N05 and N22 monitored at 1.8 eV, of N05-HI, N22-HI, and SA at 2.8 eV, of N05-SG-SS at 2.1 eV, of N05-SG-SR at 2.3 eV, and of BC at 2.2 eV are collected using a pulsed diode light emitting device (EPLED) emitting at 3.6 eV as excitation source with a pulse width of ∼950 ps while TRPL decay of N05-SG-SR monitored at 2.7 eV and of MP at 2 eV are recorded exploiting a pulsed diode laser (EPL) emitting at 3.1 eV with pulse width of ∼75 ps.

TRPL data analysis: The time resolved PL spectra of all the samples has been reproduced with an analytically multi-exponential function:

$$I(t)_{PL} = y_0 + \sum_{1}^{i} A_i \; e^{\frac{-t}{\tau_i}} \tag{3.1}$$

where y_0 represents a constant background, A_i the amplitude of the component at t=0, τ_i the decay times, and i the number of decay times. [130] The weight of each component of the TRPL decay, that represents the fractional contribution, has been computed using:

$$w_i = \frac{A_i \, \tau_i}{\sum_1^i A_i \, \tau_i} \tag{3.2}$$

where the terms $A_i \, \tau_i$ are proportional to the area under the decay curve for each decay time. Then, the average PL lifetime $\overline{\tau}$ has been calculated as the weighted average of the characteristic decay time for each exponential function i using:

$$\overline{\tau} = \frac{\sum_1^i w_i \, \tau_i}{\sum_1^i w_i} \tag{3.3}$$

Radioluminescence measurements: Steady state room temperature radioluminescence (RL) measurements are carried at using a homemade apparatus featuring, as a detection system, CCD Jobin-Yvon Syncerity coupled with a spectrograph Jobin-Yvon CP140-1825 operating in the 200-1100 nm range. All spectra are detected at a pressure of 10^{-3} mbar to avoid the RL emission from molecules present in the air. RL excitation is obtained by X-Ray irradiation through a Be window, using a Philips 2274 X-Ray tube with tungsten target operated at 20 kV and 20 mA (beam mean energy of ∼6.6 keV). For voltages of few tens of kV, continuous X-Rays spectrum is produced mainly by a bremsstrahlung mechanism superimposed to the L and M transitions, [131] due to the impact of electrons generated through thermionic effect and accelerated onto a tungsten target. At the used working conditions, the dose rate evaluated with an ionization chamber in air is 0.273±0.005 mGy/(mA*s). RL measurements as a function of the temperature are carried out in the 10-300 K interval by using the same instrumentation and a closed-cycle He Cryogenic Technologies Inc. cryocooler, whose working conditions require an ultra-high vacuum (10^{-7} mbar). Only for N05-SG-SS, N05-SG-SR and N05-HI, RL measurements, as a function of the temperature, are carried out exploiting a different detection system made by a CCD Jobin-Yvon Spectrum One 3000 coupled with a spectrograph Jobin-Yvon Triax 180 operating in the 200-1100 nm range. All the room and low temperature RL spectra, recorded as a function of nanometers, are firstly corrected for the spectral response of the detector and subsequently converted into spectra as a function of energy.
Singlet Oxygen and ROS Relative Concentration Measurement: The optical probes 5-(and-6)-chloromethyl-2',7'-dichlorodihydrofluorescein diacetate, acetyl ester (CM-H_2DCFDA) and Singlet Oxygen Sensor Green (SOSG) are purchased from Thermo Fisher Scientific and used as received; the solvents dimethyl sulfoxide (DMSO, 99 %) and phosphate-buffered saline (PBS) are purchased from Merck Life Science. The CM-H_2DCFDA and SOSG powders are diluted in a 1:10 solution of DMSO and PBS, respectively. 1,4-diazabicyclo[2.2.2]octa- ne (DABCO) powder, purchased from Fluorochem and used as received, is dispersed in milli-Q water to realize solutions with concentration 0.01, 0.1, and 1 M. To test the ROS and $^1O_2$ generation, ZnO NPs are dispersed in CM-H_2DCFDA and SOSG solutions, respectively; whereas to evaluate the probes sensitivity towards singlet oxygen moieties, ZnO NPs are mixed in solutions 1:1 of probe (CM-H_2DCFDA or SOSG) and DABCO solutions at different concentration. All the ZnO dispersions are exposed continuatively to ionizing radiation for 10 minutes and simultaneously the

intensity of the CM-H_2DCFDA or SOSG fluorescence, which increases coherently with the raise of the concentration of ROS and $^1O_2$ in the environment, [132] respectively, has been monitored under CW laser light excitation at 2.6 eV. All the above measurements are carried out in the RL apparatus depicted above, exploiting the Philips 2274 X-Ray tube operating at 20 kV and 20 mA as excitation source, and CCD Jobin-Yvon Symphony II coupled with a spectrograph Jobin-Yvon Triax 180, as detection system.

3.2 Porphyrin functionalized ZnO/SiO_2 nanosystems

In this section, the synthesis of ZnO NPs grown onto either highly porous or non-porous spherical silica support are presented together with the functionalization process of these nanosystems. Different loading levels of both amino-silane moieties, used as surface functionalizing agent, and porphyrins are considered. Then, the methods and results of the morphological characterization of the nanostructures are reported. Lastly, the methods of the optical investigation and the parameters of the developed computational models are described.

3.2.1 Samples preparation

For both porous and non-porous ZnO/SiO_2 systems synthesis all the reagents are purchased from Merck Life Science. For the functionalization with porphyrin: (3-aminopropyl)triethoxysilane ($H_2N(CH_2)_3$ $Si(OC_2H_5)_3$, APTES, 98%), N,N-dimethylformamide (DMF, 99%) and toluene (99%) are purchased from Alfa Aesar; 5,10,15,20-(tetra-4-carboxyphenyl) porphyrin (TCPP, 98%) is used as received from PorphyChem SAS.

Synthesis of SiO_2 NPs: Highly porous SiO_2 NPs (SS) are synthesized through a sol-gel method, by using cetyltrimethylammonium bromide (CTAB) templating agent for the control of pores growth according to ref [125] (Figure 3.7a, step I). Non-porous SiO_2 NPs (SS_{np}) are synthesized according to [133]. Briefly, 100 mL of ethanol are mixed with water (C H_2O = 6M) and ammonium hydroxide, (NH_4OH, C NH_4OH = 0.40 M) and sonicated at room temperature for 10 minutes. Then, tetraethyl orthosilicate (TEOS) is added quickly (C TEOS = 0.28 M) and the reaction is left under vigorous magnetic stirring overnight. The powder is recovered through centrifugation (9000 rpm, 30 minutes), washed with fresh ethanol twice and dried overnight at 60°C (Figure 3.7b, step I).

Synthesis of ZnO/SiO_2 nanosystems: To prepare the two sets of ZnO/SiO_2 nanosystems (ZS and ZS_{np}), as previously reported in ref. [38], ZnO NPs are grown onto the surface of both porous and non-porous SiO_2 NPs (SS and SS_{np}, respectively) by the hydrolysis and condensation of zinc acetate dihydrate [126,127] in ethanol, to get ZnO NPs attached to SiO_2 through the Zn interaction with SiO_2 surface hydroxyl groups (Figure 3.7, step II). It is worth mentioning that ZS corresponds N05-SG-SS, introduced in Section 3.1 and analysed in Chapter 4; anyhow in this Section and in Chapter 5, the sample label is changed to align it with the herein used nomenclature. The reactant amounts are chosen in order to get a nominal ZnO loading on both porous and non-porous silica equal to 12 wt%. The reaction yield is of about 80 % for ZS and 60 % for ZS_{np}, coherently with the higher surface area available for the ZnO NPs growth on/into the porous substrate. Consequently, the ZnO resultant loadings of ZS and ZS_{np} are of about 10.0 and 6.6 wt% and correspond to about 328 and 215 ZnO NPs for every SiO_2 NP, respectively.

Decoration of ZnO/SiO_2 nanosystems with amino-silane moieties: As anchors for the coupling of the ZnO/SiO_2 nanosystems with porphyrins, APTES is anchored to SiO_2, employing its surface hydroxyl group. For the porous nanosystems, 2.0 g of both ZS are dispersed in 48 mL of toluene at 120 °C; then, increasing volumes of APTES (16, 80 or 400 μL) are added to the SiO_2 suspension in order to get a surface functionalization agent loading equal to 0.2, 1.0, 5.0 wt% (Figure 3.7, step III). The reactions are left under stirring for 24 hours under reflux. The powders are filtrated, washed two times with fresh toluene and dried overnight at 100 °C. These sample are labelled ZS-A, ZS-A5 and ZS-A25, accordingly with their relative increment of APTES content. For the non-porous nanosystems, the same procedure is exploited to anchor the lowest APTES amount equal to 0.2 wt% of APTES on SiO_2 surfaces (ZS_{np}-A).

Functionalization of ZnO/SiO_2 nanosystems with porphyrin: TCPP is covalently supported onto the nanosystems by exploiting the amino groups of APTES able to react with the -COOH groups of TCPP. Different TCPP amounts are loaded onto ZS-A, ZS-A5, ZS-A25 and or ZS_{np}-A (Figure 3.7, step IV). Firstly, for the porous nanosystems with different APTES loading (namely ZS-A, ZS-A5, ZS+A25), 0.5 g of each sample is dispersed separately in 25 mL for ZS-A, 160 mL for ZS-A5, and 780 mL for ZS-A25 of DMF at room temperature and specific amounts of TCPP are added in order to have for each NPs an APTES:TCPP molar ratios equal to 1:1 determining a consequent dye loading equal to 2.7 wt% on ZS-A, 13.5 wt% on ZS-A5, and 67.5 wt% on ZS-A25. After 18 hours, the products are

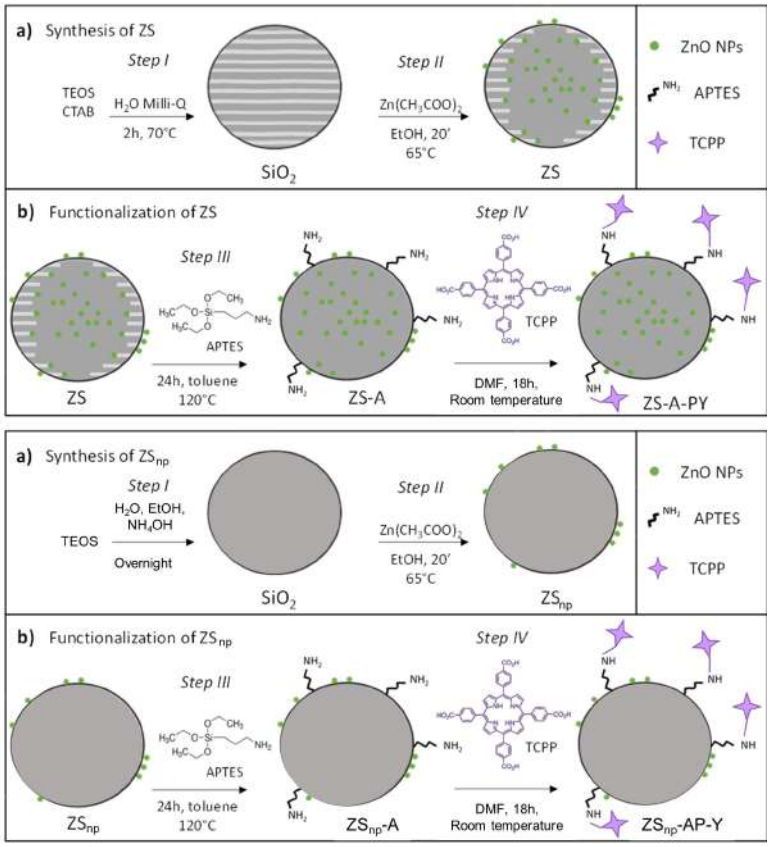

Figure 3.7: Reaction path used for the synthesis of the porous (**a**) and non-porous (**b**) ZnO/SiO_2 functionalized nanosystems. For each step, a schematic representation of the morphological features (as observed by TEM analysis, that will be reported in Section 3.2.3) is also depicted.

isolated by centrifugation, washed two times with fresh DMF and dried overnight at 80°C. The obtained TCPP coupled NPs are labelled ZS-AP-1, ZS-A5P-1, ZS-A25P-1, respectively. Then, for both the porous and non-porous nanosystems with an APTES loading of 0.2 wt% (namely ZS-A and ZS_{np}-A), by employing the same protocol, increasing amounts of TCPP are added (APTES:TCPP molar ratios equal to 1:1, 1:0.5, 1:0.25, 1:0.1) in order to get a dye loading equal to 2.7, 1.4, 0.7, 0.3 wt%, respectively. The final TCPP functionalized NPs are labelled ZS-AP-Y or ZS_{np}-AP-Y, where Y is the APTES:TCPP molar ratio used during the synthesis.

Mechanical mix: To further investigate the role of TCPP-ZnO proximity through the covalent bonding, a homogenous mix, called ZS-A+P-0.5, is obtained by mechanically mixing 98.6 mg of bare ZS-A with 1.4 mg of TCPP, in order to have a TCPP amount equal to 1.4 wt%.

3.2.2 Structural and morphological characterization

Electron microscopy: The morphological analysis is carried out on all samples through TEM. TEM images are collected by using a JEOL JEM-2100Plus TEM operating with an acceleration voltage of 200 kV, equipped with an 8-megapixel Gatan Rio^{TM} complementary metal-oxide-semiconductor camera. The samples are deposited onto carbon coated Cu TEM mesh grids by drop-casting dilute NPs dispersions in ethanol. The size of SiO_2 and ZnO NPs are determined by manually measuring 100 particles randomly chosen.
Diffraction experiment: The structural features are investigated with PXRD, with a Rigaku MiniFlex 600 diffractometer with 0.154 nm Cu Kα radiation. The measurements are performed in the 2θ range 20-70° (2θ step 0.02°, 1° min^{-1} scan rate).
Specific surface area analysis: The porosity of the porous SiO_2 NPs in the substrate alone, in ZnO/SiO_2 nanosystems before and after the functionalization steps is studied by nitrogen physisorption using a Micromeritics ASAP 2020 HD analyser, after degassing the samples at 100°C under vacuum. Specific surface area (SSA) values are obtained using the Brunauer–Emmett–Teller (BET) model.
Infrared spectroscopy: The functionalization with both APTES and TCPP is qualitatively studied with the FTIR in ATR mode, by using a Thermo Fisher Scientific Nicolet iS20, wavenumber range between 4000 cm^{-1} and 600 cm^{-1}, resolution spectra 4 cm^{-1}, 32 scans.
Thermogravimetric analysis: The amount of the organic substituents is quantified with a TGA on a Mettler Toledo TGA/DSC1 STAR e System (30 °C-1000 °C, heating rate of 10 °C min^{-1}, constant air flux of 50 mL/min^{-1}) and further confirmed with the Elemental Analysis (CHNS), performed on an Elemental VarioMICRO analyser (temperature of the combustion column = 1150 °C, reduction column = 850 °C).
TGA data elaboration: From the thermal profiles measured during TGA, the weight loss between 150 and 1000 °C ($\Delta W_{150-1000°C}$) is used to calculate i) the amount of APTES in ZS-A, ZS-A5, ZS-A25, and ZS$_{np}$-A, ii) the amount of TCPP in ZS-AP-Y, ZS-A5P-1, ZS-A25P-1, and ZS$_{np}$-AP-Y samples (TCPP amount, wt%), respectively, and iii) the ratio between APTES and TCPP molecules distributed over SiO_2 surface (number of molecules/nm^2 SiO_2). In the APTES decorated nanosystems, $\Delta W_{150-1000°C}$ is attributed to two main components by using a simplified model where APTES is bonded to SiO_2 through three covalent bonds at low APTES loadings: i) combustion of the -$CH_2CH_2CH_2NH_2$ groups anchored to SiO_2 NPs after the reaction with APTES; ii) water desorption from the resid-

ual surface silanol groups, assuming that three surface OH groups are replaced by each APTES bonded to SiO_2. In the porphyrin functionalized nanosystems, an additional contribution due to TCPP has to be considered. The contributions to the weight loss $\Delta W_{150-1000°C}$ in the dye coupled NPs are reported in the following equation:

$$\begin{aligned}\Delta W_{150-1000°C} = & \, n_{APTES} \cdot MW_{APTES} \\ & + \frac{1}{2} \cdot (n_{OH} \cdot w_{SiO_2(1000°C)} - 3n_R) \cdot MW_{H_2O} \\ & + n_{TCPP} \cdot MW_{TCPP}\end{aligned} \tag{3.4}$$

where n_{APTES} and n_{TCPP} represent the APTES and TCPP moles on SiO_2, respectively; MW is the molecular weight (APTES: -$CH_2CH_2CH_2NH_2$ groups = 58.0 g mol^{-1}; TCPP = 790.8 g mol^{-1}); n_{OH} is the moles number of OH surface groups of bare SiO_2; $w_{SiO_2(1000°C)}$ is the weight of residual SiO_2 at 1000°C. Then, the APTES amount (wt%) is calculated by deriving n_R from Equation 3.4. For the porphyrin functionalized nanosystems, considering that the APTES amount remains constant from the NPs decorared only with APTES and those also loaded with the dye, the only difference in the measured $\Delta W_{150-1000°C}$ came from the TCPP contributions. Thus, from Equation 3.4 the TCPP amount (wt%) can be calculated using the following equation:

$$\begin{aligned}TCPP\ amount = & \, \Delta W_{150-1000°C}\ (TCPP\ and\ APTES\ coupled\ NPs) \\ & - \Delta W_{150-1000°C}\ (APTES\ coupled\ NPs)\end{aligned} \tag{3.5}$$

and compared to the nominal TCPP amounts. From the obtained TCPP amounts (wt%) and APTES amount (wt%), the number of TCPP and APTES molecules anchored onto SiO_2 surface is calculated:

$$\frac{n.molecules}{surface(nm^2)} = \frac{m_{species} \cdot N_A}{1g_{SiO_2} \cdot MW_{species} \cdot SSA_{BET} \cdot 10^{18}} \tag{3.6}$$

where $m_{species}/1g_{SiO_2}$ is the mass of TCPP or APTES anchored on 1.0 gram of SiO_2 (calculated from TCPP or APTES amount), N_A the Avogadro number, S_{BET} is the specific surface area of SiO_2 (that is 109 m^2/g for ZS and 66 m^2/g for ZS_{np}).

Centrifugation process: To test the stability of ZS-AP-1, ZS-A5P-1, and ZS-A25P-1 in an biological environment, PBS dispersions of the samples with ZnO concentration of 10^{-3} M are centrifugated for 15 minutes at 9000 revolutions per minutes (rpm) using a Hettich Universal 320 centrifuge and then the products

isolated from the solutions are washed with fresh PBS. This process is repeated for an overall of three times and subsequentially the obtained powders are dried overnight at 80°C.

Absorption measurement: Absorption spectra from 200 to 800 nm are collected with a double beam Perkin Elmer Lambda 950 spectrometer with a spectral resolution of 1.0 nm using Suprasil quartz cuvettes with a 0.1 cm optical path length. For the evaluation of stability in a biological environment, the absorption measurements are performed on PBS dispersion of TCPP, ZS-AP-1, ZS-A5P-1, and ZS-A25P-1, while for the determination of TCPP concentration, on DMF dispersion of the dye alone and of all the porphyrin functionalized samples.

Absorption data analysis: A calibration curve is obtained by measuring the absorption spectra of TCPP solution in DMF at known concentrations (in the range: 10^{-6} M – 7*10^{-5} M, data not shown) and by exploiting the Lamber-Beer equation:

$$Abs_\lambda = \epsilon_\lambda \cdot d \cdot C \tag{3.7}$$

where Abs_λ is the absorbance at a given wavelength, ϵ_λ is molar extinction coefficient at a given wavelength, d the optical path length, and C the concentration. [134] In the used concentration range, the best linear regression of the TCPP absorbance as a function of its content is obtained at 520 nm (∼2.4 eV) correspondent to the first peak of the Q-bands; whereas the calibration results non reliable at 410 nm (∼3.0 eV) due to the occurrence of spectral shape distortions in the Soret band (data not shown). Thus, the molar excitation coefficient is derived at 520 nm (ϵ_{520}) and resulted about 8900 M^{-1} cm^{-1}. Then, for all the dye coupled NPs, the TCPP concentration is calculated from Equation 3.7 using the evaluated ϵ_{520} and the measured Abs_{520}.

3.2.3 Structural and morphological properties

The morphology of all samples is investigated by TEM analyses. TEM images of porous SiO_2 (SS, Figure 3.8a) confirm the formation of almost spherical SiO_2 NPs, with an average size of 80 nm and ordered mesoporous channels of few nanometers diameter (∼average diameter 3±1 nm), generated by the self-assembly of the CTAB, used as templating agent, during SiO_2 growth. Subsequently, the interaction of the zinc precursor in a basic ethanol solution with the -OH surface groups of SiO_2 is exploited to grow ZnO NPs of 4-6 nm diameter onto the silica support (ZS). Anyway, the TEM images (Figure 3.8b) disclose that ZnO NPs are

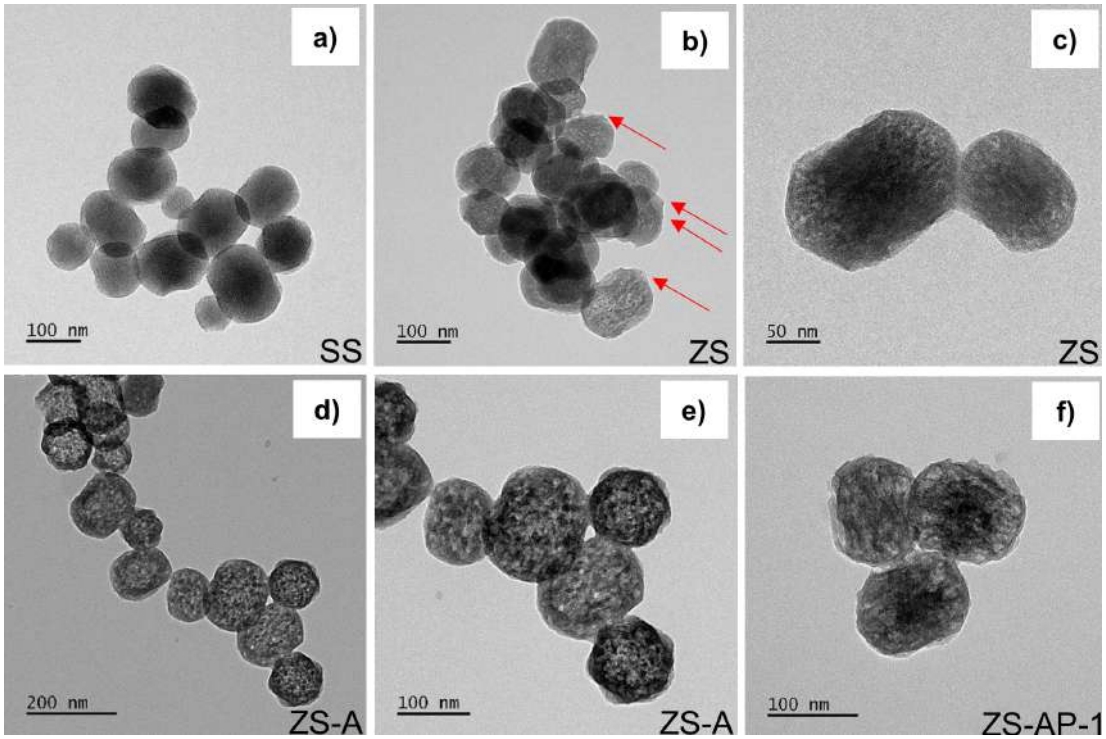

Figure 3.8: TEM images of porous SiO_2 NPs (SS, **a**), of the porous ZnO/SiO_2 nanosystems (ZS in **b,c**), and of the porous ZnO/SiO_2 nanosystems upon APTES (**d,e**) and TCPP functionalization (**f**): as examples, ZS-A in **d,e** and ZS-AP-1 in **f** are reported. The red arrows in **b** indicate the ZnO NPs grown on the external SiO_2 surface.

attached both on the external SiO_2 surface (red arrows) and in the SiO_2 mesopores; in fact, the long-range order given by the pristine SiO_2 channels is partially depleted due to a contrast reduction in the images, caused by the presence of the high-atomic number Zn element in the core of SiO_2 NPs (Figure 3.8c). This observation can be explained considering that the zinc precursor is reasonably able to penetrate the mesoporous channels of SiO_2, mainly due to the high available surface area inside the SiO_2 pores (SSA = 1100 m^2g^{-1} as reported in [125]) and may lead to the formation of ZnO NPs inside the SiO_2 mesoporosity. This hypothesis is further confirmed by the nitrogen physisorption analysis performed on SiO_2 after ZnO growth: in fact, ZS shows a severe reduction of SSA value (109 m^2g^{-1}) compared to bare SiO_2, suggesting that the formation of ZnO NPs strongly affects the SiO_2 mesoporosity and that a considerable portion of ZnO NPs may be located onto the SiO_2 pores. A schematic representation of ZnO distribution in ZS is reported in Figure 3.7a.

After the functionalization of ZS with APTES, a further modification of SiO_2 morphology is evidenced, regardless of its loading level (namely, for ZS-A, ZS-

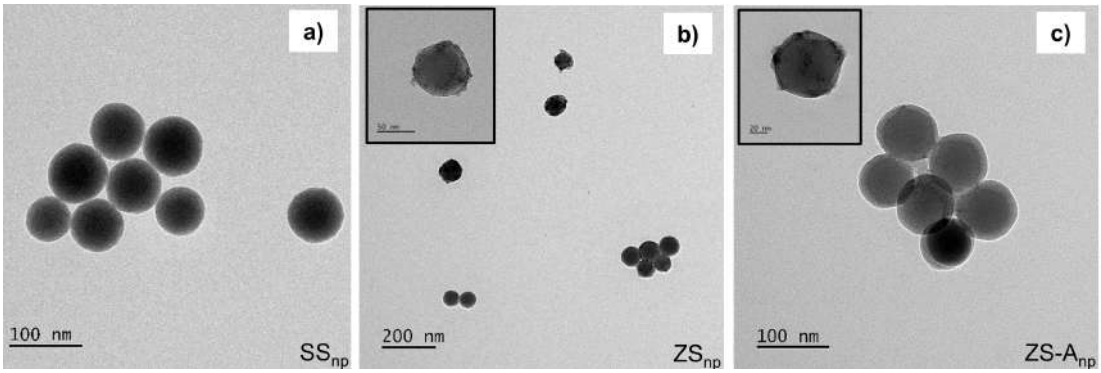

Figure 3.9: TEM images of non-porous SiO_2 NP (SS_{np}, **a**), of the non-porous ZnO/SiO_2 nanosystems before (ZS_{np}, **b**) and after APTES functionalization (ZS_{np}-A, **c**). Insets are TEM images zoomed on only one nanoparticle.

A5, and ZS-A25). Thus, as an example, only TEM images of ZS-A are reported (Figure 3.8d,e). The TEM analysis discloses that the overall typical SiO_2 mesoporosity is not detectable, suggesting that also APTES molecules may partially penetrate the available SiO_2 pores and may condensate mainly as silica-based species in the pores. Moreover, spotted areas of high and low contrast, with a growing amorphous character appear in the SiO_2 core structure. Lasty, for all the APTES decorated samples, these morphological features are not altered by the porphyrin addition, regardless of the used TCPP content. As an example, for the porous dye functionalized NPs (ZS-AP-Y, ZS-A5P-1, and ZS-A25P-1), a TEM image of ZS-AP-1 is reported in Figure 3.8f.

TEM images of non-porous SiO_2 (SS_{np}, Figure 3.9a) validate the formation of almost spherical silica NPs with an average size of 75 nm. After the growth of ZnO NPs, ZnO NPs of 4-6 nm diameter and small aggregates on the external surface of SiO_2 NPs are detected (ZS_{np}, Figure 3.9b), corroborating the formation of ZnO NPs randomly distributed onto the support.After the functionalization of the non-porous ZnO/SiO_2 (ZS_{np}) with only APTES and subsequently also with TCPP, no further modifications of the sample morphological features are observed. As an example, TEM images of ZS_{np}-A are reported in Figure 3.9c.

From the structural point of view, PXRD analysis of the porous nanosystems (SS and ZS) unveils the amorphous character of both SiO_2 and ZnO NPs, as suggested by the only presence of a broad peak centred at $2\theta = 22°$ due to the amorphous SiO_2 (Figure 3.10a). The same structural properties are evidenced in the non-porous nanosystems (SS_{np} and ZS_{np}), even though a slightly increased ZnO crystallinity is observed as demonstrated by the appearance of the small diffraction peaks due to the wurtzite ZnO phase (Figure 3.10b). No other peaks are detectable in all the porous and non-porous nanosystems upon both APTES

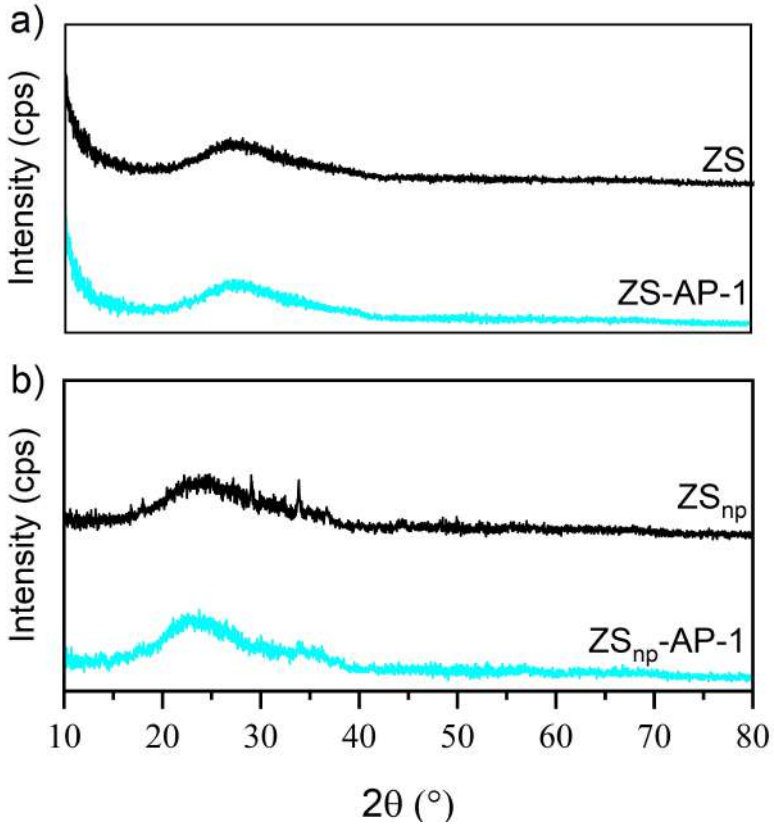

Figure 3.10: PXRD spectra of porous (**a**) and non-porous (**b**) ZnO/SiO_2 nanosystems with no functionalization (ZS and ZS_{np}) and upon APTES-TCPP loading (as examples ZS-AP-1 and ZS_{np}-AP-1 are reported).

and TCPP functionalization (ZS-A, ZS_{np}-A, ZS-A5, ZS-A25, ZS-AP-Y, ZS_{np}-AP-Y, ZS-A5P-1, and ZS-A25P-1), implying that no crystalline structures are formed and no porphyrin aggregation into crystalline domains occurrs (Figure 3.10). [135] To validate both APTES and TCPP functionalization, ATR-FTIR measurements are performed. Figure 3.11 displays the spectra of six different porous samples and TCPP alone to investigate the surface modifications of the nanosystem upon each step of the synthesis process, reported as examples for both porous and non-porous systems. First, in the ATR-FTIR spectrum of the ZS compared to the silica substrate (Figure 3.11a), the absence of the peak at 958 cm^{-1}, attributed to the surface -OH groups of SiO_2 confirms the ZnO anchoring on SiO_2 surface, due to their partial replacement with Si-O-Zn bonds. [127] Moreover, comparing the ATR-FTIR spectrum of the ZS before and after the APTES anchoring (Figure 3.11a), two new peaks at 2930 cm^{-1} and 2860 cm^{-1} are observed at all APTES content and assigned to the asymmetric and symmetric stretching of -CH_2 groups (υ_{as} and υ_a) of the propyl APTES chains. These two peaks are similarly evident in the dye coupled NPs, validating the stability of these samples in DMF, used

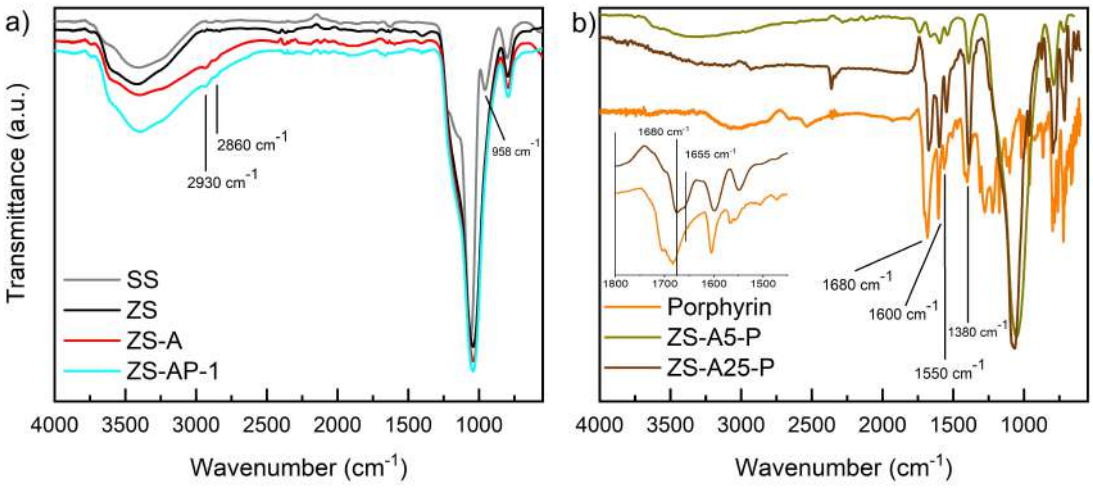

Figure 3.11: **a**) ATR-FTIR spectra of SS after each synthetic step to obtain ZS-AP-1, according to the synthetic procedure. **b**) ATR-FTIR of two samples at high APTES and TCPP content and of TCPP alone.

both as reaction solvent for the TCPP interaction and for the PL measurements. For all the porphyrin functionalized nanoscintillators, the intensity of the typical peaks due to TCPP, that are observed in the range from 1800 to 1300 cm^{-1} (Figure 3.11b) and are in agreement with the literature, [136, 137] decreases coherently with the dye amounts used in the synthesis. Indeed, no strong signals due to TCPP are detected in the ATR-FTIR spectra of ZS-AP-Y and ZS_{np}-AP-Y (Figure 3.11a), due to the low TCPP content ($<$ 3wt%, as calculated from TGA analysis); whereas several peaks are observed in both ZS-A5P-1 and ZS-A25P-1 in the 1800-1300 cm^{-1} range due to TCPP (Figure 3.11b). In particular, the signals at 1600, 1550, and 1380 cm^{-1} are attributed to the vibrational stretching of C=C in phenyl configuration, C=C in the pyrrolic ring, and C=N, respectively, while the peak at 1680 cm^{-1} to the stretching of the carbonyl group (C=O) of the -COOH pendant groups. It is worth mentioning that the peaks observed in the TCPP coupled NPs are shifted towards lower wavenumbers with respect to the dye alone, [136] suggesting the interaction between TCPP and the APTES functionalized ZS system. The possible interaction between the terminal amino groups of APTES ($-NH_2$) and carboxy groups of TCPP (-COOH) is further suggested by the presence of a small additional peak located at 1655 cm^{-1}, as a shoulder of the more intense peak at 1680 cm^{-1} (Inset in Figure 3.11b), likely ascribable to the formation of an amide bond between the two species.

The quantification of APTES and TCPP is realized through the TGA thermal profiles of all the functionalized samples, by comparing them to either the bare ZS or ZS_{np} (Figure 3.12, for details please refer to sub-Section 3.2.2). The weight loss

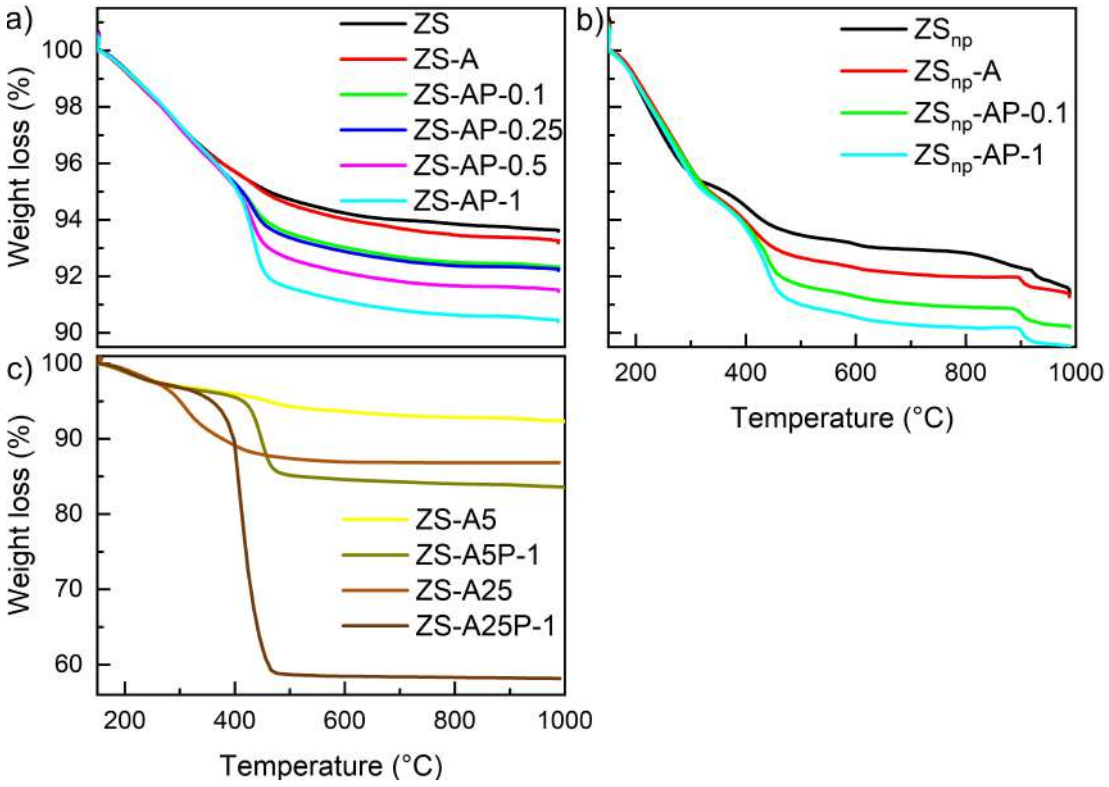

Figure 3.12: TGA profiles in the temperature range 150-1000 °C of all the bare and functionalized ZnO/SiO_2 nanosystems.

$\Delta W_{150-1000°C}$ increases from the only inorganic nanoscintillators (ZS and ZS_{np}) to the APTES functionalized NPs (ZS-A, ZS_{np}-A, ZS-A5, and ZS-A25) and the dye coupled nanosystems (ZS-AP-Y, ZS_{np}-AP-Y, ZS-A5P-1, ZS-A25P-1), due to the presence of APTES and TCPP covalently bonded to the SiO_2 surface. Besides, the highest $\Delta W_{150-1000°C}$ are measured by increasing both the APTES and the TCPP amounts in the functionalized samples. From $\Delta W_{150-1000°C}$ values (reported in Table 3.1) both the amount of APTES and TCPP for the loaded samples are calculated close to the nominal ones. Besides, the calculated ratios between TCPP and APTES molecules over SiO_2 are similar to the expected nominal values (reported in Table 3.1), suggesting that the anchoring of TCPP to SiO_2 is carried out under high controlled conditions. The only exceptions are represented by the samples with the highest TCPP loading (ZS-A5-P1 and ZS-A25-P1), where the TCPP amounts are lower than the nominal ones, possibly due to the high steric hindrance of TCPP that leads to reduced reaction yields at high TCPP content. TGA results are further validated by the elemental CHNS analyses, where the increased N% of the APTES and APTES-TCPP coupled samples compared to either the porous or non-porous bare ZnO/SiO_2 nanosystems is assigned to the nitrogen contributions given by both APTES and TCPP

Sample	TGA results				CHNS results	
	$\Delta W_{150-1000°C}$ (%)	TCPP amount (wt%)	Nominal TCPP (wt%)	Ratio TCPP / APTES (n molecules)	N% nominal	N% measured
ZS	6.4	-	-	-	-	0.15
ZS-A	6.7	-	-	-	0.05	0.21
ZS-A5	7.7	-	-	-	0.24	+0.23
ZS-A25	13.2	-	-	-	1.28	+1.10
ZS-AP-0.1	7.7	1.0	0.3	0.3	0.07 (+0.02)	+0.03
ZS-AP-0.25	7.8	1.1	0.7	0.4	0.10 (+0.05)	+0.09
ZS-AP-0.5	8.5	1.8	1.4	0.6	0.15 (+0.10)	+0.15
ZS-AP-1	9.6	2.9	2.7	1.1	0.24 (+0.19)	+0.20
ZS-A5P-1	16.4	8.7	13.5	0.7	1.2 (+0.96)	+0.94
ZS-A25P-1	41.7	28.5	67.5	0.4	6.05 (+4.84)	+2.34
ZS_{np}	8.5	-	-	-	-	0.50
ZS_{np}-A	8.7	-	-	-	0.05	+0.05
ZS_{np}-AP-0.1	9.5	0.8	0.3	0.3	0.07 (+0.02)	+0.09
ZS_{np}-AP-1	10.8	2.1	2.7	0.8	0.24 (+0.19)	+0.2

Table 3.1: For both the porous and non-porous sets of samples, amount of APTES and TCPP anchored over SiO_2 calculated from TGA results (according to Equations 3.4-3.6) and increment of the nitrogen content from CHNS analysis of the APTES decorated nanosystems compared to the bare ZnO/SiO_2 ones and of the APTES-TCPP functionalized nanosystems compared to the APTES decorated ones.

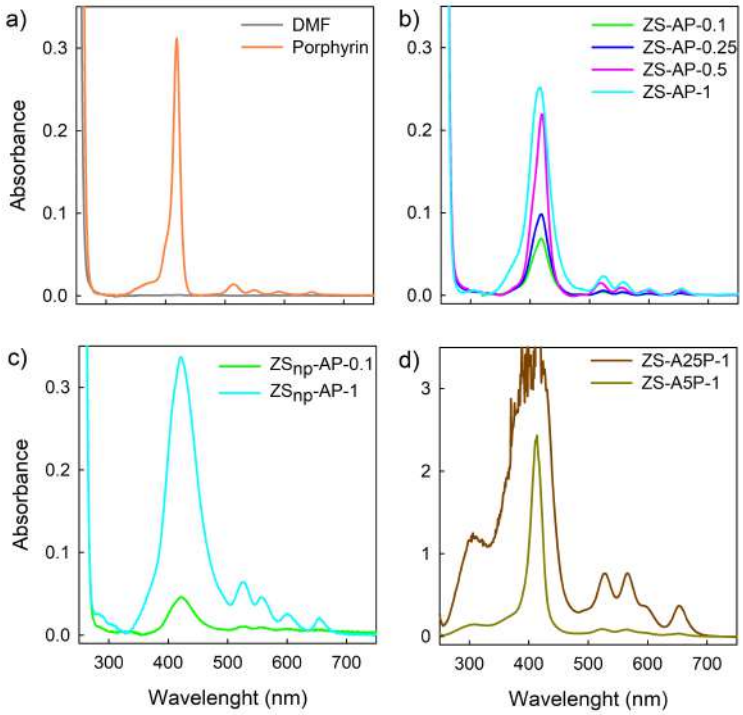

Figure 3.13: Absorption spectra of DMF solution of TCPP alone (10^{-5} M) and of all the porous and non-porous porphyrin functionalized (ZnO concentration of 10^{-5} M), compared to DMF alone.

molecules. As observed for TGA analysis, the N% increased by increasing the APTES and TCPP amount and the results confirmed the previous TGA quantification (Table 3.1).

At last, absorption spectra of all the porous and non-porous porphyrin coupled NPs dispersed in DMF are compared to the dye alone, in order to investigate the TCPP absorption features upon anchoring on the inorganic nanoscintillators and to estimate the dye amount in the samples (Figure 3.13). All the spectra disclose the characteristic porphyrin absorption features: the Soret band at ∼3.0 eV (∼413 nm) and the Q-bands between 1.8 eV (∼700 nm) and 2.5 eV (∼500 nm), related to $S_0 \rightarrow S_2$ and $S_0 \rightarrow S_1$ transitions, [138] respectively. However, the wide Soret band, whose broadening progressively increments with the TCPP concentration, observed in the TCPP coupled samples with respect to the sharp peak of the dye alone unveils the occurrence of dye aggregates and the dependence of their formations probability on the porphyrin content. [82,83] For all the TCPP functionalized NPs, the spectra (recorded at constant ZnO amount = 10^{-3} M) showed that the absolute value of the absorbance scales coherently with the dye content, that is also estimated by Equation 3.7 considering the main Q-band

	C_{TCPP} [M] at Abs_{520}
ZS-AP-0.1	$4.9 * 10^{-6}$
ZS-AP-0.25	$6.5 * 10^{-6}$
ZS-AP-0.5	$1.5 * 10^{-5}$
ZS-AP-1	$2.6 * 10^{-5}$
ZS_{np}-AP-0.1	$6.1 * 10^{-6}$
ZS_{np}-AP-1	$3.6 * 10^{-5}$
ZS-A5P-1	$1.3 * 10^{-4}$
ZS-A25P-1	$1.4 * 10^{-3}$

Table 3.2: Porphyrin concertation in the functionalized nanoscintillators calculated from the absorption spectra with Equation 3.7

(∼520 nm). Generally, the TCPP amounts measured (Table 3.2) from the absorption measurements are consistent with TGA and CHNS results (Table 3.1), even if they disclose slight discrepances for the nanosystems with the lowest and highest porphyrin loading (ZS-AP-0.1, ZS_{np}-AP-0.1, ZS-A5P-1 and ZS-A25P-1), probably because their too small and too big absorbance, respectively, limits the accuracy of the Lambert-Beer law.

3.2.4 Spectroscopic characterization

Steady-state photoluminescence analysis: Steady state excitation-emission luminescence measurements are carried out using the experimental apparatus already described in sub-Section 3.1.4. PL spectra are detected exciting at ∼3.7 eV for TCPP, ZS, ZS-A, and ZS-AP-Y as well as SS_{np}, ZS_{np}, ZS_{np}-A, and ZS_{np}-AP-Y, and at ∼3.1 eV only for TCPP, ZS-AP-Y and ZS_{np}-AP-Y samples. Photoluminescence excitation (PLE) spectra are detected monitoring the TCPP emission at ∼1.9 eV for TCPP, ZS-AP-Y and ZS_{np}-AP-Y samples; ZnO emission at ∼2.3 eV for ZS, ZS-A, ZS-AP-Y as well as ZS_{np}, ZS_{np}-A, and ZS_{np}-AP-Y. All the spectra are corrected for the spectral response of the system.
TRPL measurements: TRPL measurements are performed in TCSPC mode thought a FLS 980 spectrofluorometer by Edinburgh Photonics using Suprasil quartz cuvettes with a 0.1 cm optical path length. TRPL spectra collected at 2.3 eV with a band-width of 10 nm are collected using a EPLED emitting at 3.6 eV as excitation source with a pulse width of ∼950 ps; TRPL decays monitored at 1.9 eV with a band width of 5 nm are obtained exploiting a EPL emitting at 2.4 eV with pulse width of ∼280 ps. The TRPL data are analysed following the numerical procedure described in sub-Section 3.1.4.

Time resolved emission spectroscopy: Time resolved emission spectroscopy (TRES) is also used: the emission spectra are recorded both immediately after the pulse and with 0.2 ms delay exciting at ∼3.7 eV with a Xenon flash lamp with pulse duration of 0.1 ms by an Agilent Cary Eclipse fluorimeter using Suprasil quartz cuvettes of 1 cm optical path length.
PL, PLE, TRPL as well as TRES optical analyses are performed at room temperature and atmospheric pressure in DMF solutions for all the samples.
Radioluminescence: RL measurements are carried using the experimental apparatus described in sub-Section 3.1.4. In particular, for the sets of samples that will be investigated in Section 5.1 (*i.e.* ZS, ZS-A, ZS-A5, ZS-A25, ZS-AP-1, ZS-A5P-1, and ZS-A25P-1), the Philips 2274 X-Ray tube is operating at 20 kV and 20 mA and, as a detection system, a CCD Jobin-Yvon Sincerity coupled with a spectrograph Jobin-Yvon CP140-1825 operating in the 200 - 1100 nm range is exploited. For the sets of samples that will be analysed in Sections 5.2 and 5.3 (i.e. TCPP, ZS, ZS-A, ZS-AP-Y, SS_{np}, ZS_{np}, ZS_{np}-A, and ZS_{np}-AP-Y), the X-Ray tube is operated at 20 mA and 10 / 20 / 30 kV and, as a detection system, a CCD Jobin-Yvon Symphony II coupled with a spectrograph Jobin-Yvon Triax 180 operating in the 200 - 1100 nm range is used. At these working conditions, the beam mean energy are of ∼3.3 / 6.6 / 10.0 keV and the dose rate evaluated with an ionization chamber in air are of 0.048±0.001 / 0.273±0.005 / 0.68±0.01 mGy/(mA*s), respectively. All spectra are detected on powders at room temperature and at a pressure of 10^{-3} mbar to avoid any RL emission from molecules present in the air and corrected for the spectral response of the detection system.

3.2.5 GEANT4 based Monte Carlo simulations

Monte Carlo simulations based on the GEANT4 toolkit (version 4.10.6 patch 03) are employed to investigate the spatial distribution of energy deposition in non-porous ZnO/SiO_2 nanosystems (ZS_{np}). To evaluate the role of both the ZnO concentration and the X-Ray energy beam on the deposited energy profile, two codes (A and B, respectively) are developed. The geometries used in code A and B are different, yet the irradiation conditions are similar and they both rely on the same models to describe the cross-section of each physical processes. All these parameters are selected to mimic the sample and the experimental conditions whenever the computational capacity allowed, while in the other cases, appropriate approximations are chosen; as detailed below.
Geometry parameters of code A: The geometry of this code is optimized to compute the relative contribution of SiO_2 and ZnO in the energy deposition in ZS_{np}

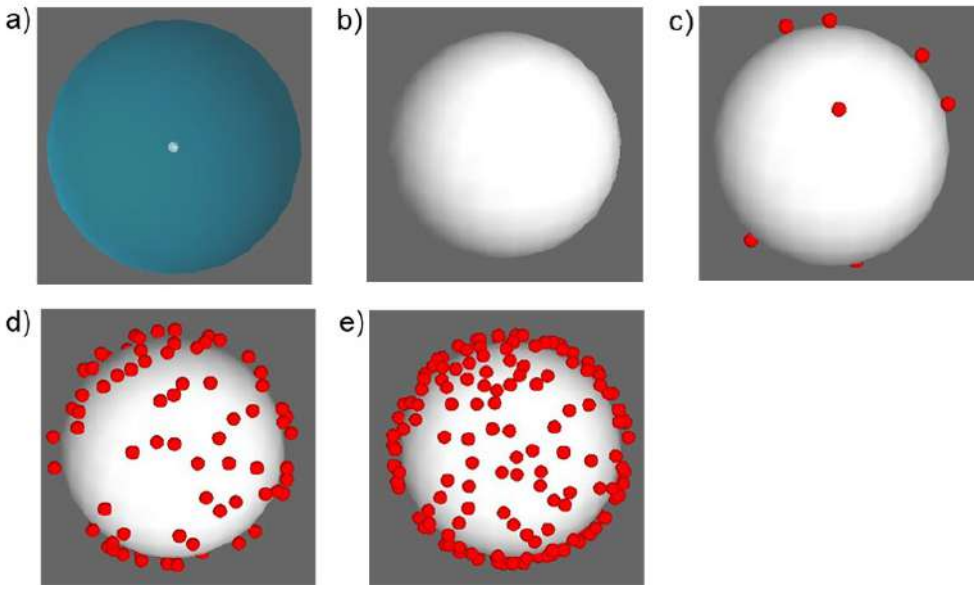

Figure 3.14: **a**) Visualization of the geometry simulated in code A: **a**) one SiO_2 NP (white) is placed at the centre of the *environment* (dark blue) located at the centre of the *world* (grey); **b-f**) Visualization of the SiO_2 NP (white) with 0 (**b**) / 10 (**c**) / 100 (**d**) / 215 (**e**) ZnO NPs (red) randomly distributed on its external surfaces.

due to the primary interaction with the X-Ray beam. The volume in which the interactions between the ionizing radiation and the matter occur, also called the *environment* is a sphere of 2 μm diameter filled with air. The sphere is placed at the centre of the whole physical space, referred to as the *world*, that consists in an empty box with dimensions of 150 cm. At the centre of the *environment*, one spherical SiO_2 NP of 80 nm in diameter is placed (Figure 3.14a). Lastly, the code is implemented with the possibility of randomly distributing on the silica surface a given number of distinct ZnO NPs of 5 nm diameter. In particular, four cases are considered: 0 / 10 / 100 / 215 ZnO NPs, corresponding to a ZnO concentration of 0.0 / 0.3 / 3.0 / 6.6 wt% (Figure 3.14b-e). Because performing the simulations with the actual dimensions of the experimental setup is not doable computation-time wise, both the *environment* and *world* size are scaled down, keeping at least a difference of about three orders of magnitude between the dimensions of the nanosystems, the *environment*, and *world*.

Geometrical parameters of code B: The goal of this code is to estimate the spatial distribution of energy profile in the ZnO/SiO_2 nanosystems in geometrical conditions similar to the experimental ones. In the RL measurements, a cylindrical sample holder of diameter of ∼8.5 mm and height of ∼1 mm is filled with ZS_{np} powders. The ratio between the volumes of the sample holder and the nanosys-

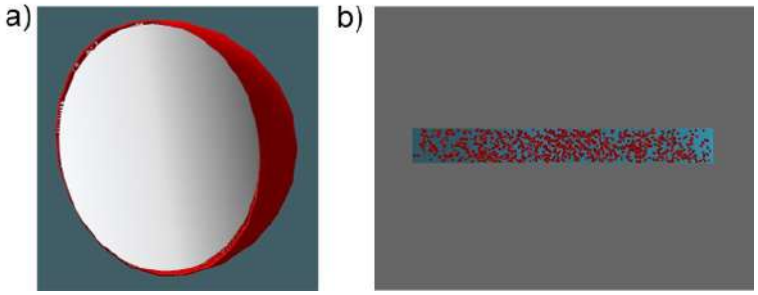

Figure 3.15: **a**) Approximation of the ZnO/SiO_2 NP geometry: each SiO_2 NP is covered with a thin layer of ZnO (red); **b**) Visualization of the geometry simulated in the code B: several SiO_2 NPs covered with the thin layer of ZnO (red) are randomly placed in the *environment* (blue) positioned at the centre of the *world* (grey).

tems provides the number of SiO_2 and ZnO NPs contained in the sample. These numbers are equal to $1.8*10^{14}$ and $3.9*10^{16}$, respectively (since 215 ZnO NPs are gattached to each SiO_2 support). However, thse values are far above the computational capacity. Consequently, to limit the overall amount of particles, the following approximation are used: i) the size of the sample holder is scaled down to the micro-meters range, ii) the number of nanosystems is lowered to $5*10^4$ so that their mean inter-distance (∼50 nm) is sufficiently long to allow a fast particle placement and small enough to study the energy deposition in neighbouring NPs, and iii) for every SiO_2 NP, the 215 ZnO NPs are replaced by a spherical shell of thickness of ∼0.4 nm placed around the silica support. The thickness of the ZnO layer is calculated to provide a volume of ZnO that is equivalent to that of 215 NPs of 5 nm diameter (Figure 3.15a). Hence, to recreate the geometry of the used RL sample holder, the *environment* is defined as a cylinder with a diameter of 4.25 μm and a height of 1 μm. This cylinder is filled with air and located at the centre of the *world*, that is depicted as an empty box with dimensions of 150 cm. Then, $5*10^4$ SiO_2 NPs with a diameter of 80 nm and coated with a 0.4 nm-thick shell of ZnO are randomly placed in the *environment* (Figure 3.15b).

Physical process modelling: The Low Energy Electromagnetic Physics-Livermore package is used because it allows to describe and compute the interactions of electrons and photons with inorganic materials down to about 250 eV, with proper accuracy. The cutting step, *i.e.* the threshold below which no secondary charges are generated, is set to 1 nm.

Irradiation conditions: To mimic the RL experimental setup, the incident radiation is represented by a beam of 10^8 parallel X-Ray photons with a mean beam energy of 3.3 / 6.6 / 10.0 keV and generated at a distance of 15 cm and with a

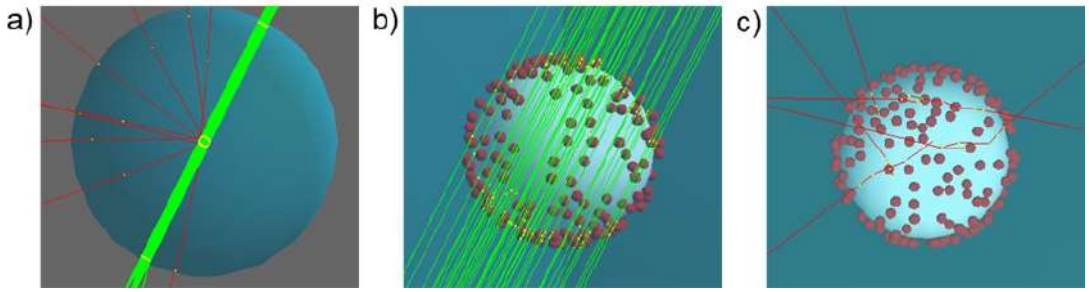

Figure 3.16: Visualization of the simulated energy deposition computed by operating code A when X-Ray photons with a mean energy of 6.6 keV are irradiating a target sample made of 215 ZnO NPs attached to one SiO_2 NP): **a**) depicts the whole geometry and all the occuring physical processes, while **b**) and **c**) are enlargement that display only the incoming X-Ray (**b**) or the production of secondary carries (**c**), respectively. The *world* is depicted in grey, the *environment* in blue, the SiO_2 NP in white, and the ZnO NPs in red; the green lines are the incoming X-Ray, the yellow dots are the interaction points between the ionizing radiation and the nanosystems and/or the *environment*, the red lines are the generated secondary carriers.

tilt angle of 26° with respect to the geometrical centre - *i.e.* where the interacting matter is placed. As an example, Figure 3.16 displays the visualization of the evaluated energy deposition computed by operating code A in the case of one SiO_2 NPs covered with 215 ZnO NPs exposed to X-Ray mean energy beam of 6.6 keV. In detail, in Figure 3.16a, upon the irradiation with ionizing radiation (green lines) of the ZnO/SiO_2 nanosystem, some interactions occur statistically both in the nanosystem and in the *environment* (yellow dots) leading to the possible deposition of energy and generation of secondary charges (red lines). Figure 3.16b and 3.16c show solely the NP exposed to X-Ray and the subsequent energy release and secondary charges production, respectively.

Chapter 4

ZnO samples with different morphologies

As introduced in Chapter 2, ZnO-based nanostructures are promising for the development of performant and innovative photonics and opto-electronics devices as well as for novel interesting applications, especially in the biomedical field. In particular, the attractiveness of ZnO NPs relies on the possibility of varying its physical and chemical properties by controlling the dimensions, shape, and interfaces. All these parameters contribute in defining the defectiveness, *i.e.* concentrations and types of point defects of ZnO and its resultant features, such as the luminescence and the catalytic activity. Nevertheless, the impact of ZnO morphological and surface properties is still an open issue in the scientific community and its comprehension represents a key point to promote the development of engineered ZnO nanostructures for optical and medical applications.
Aiming at providing a significant contribution in this matter, this chapter presents a detailed study on the influence of the points defects on the optical and catalytic properties of ZnO. ZnO luminescence is studied through a systematic spectroscopic approach involving seven ZnO samples with different growth conditions, interfaces, and dimensions (from bulk to nano-size) and different excitations, from optical sources to ionizing radiation. This optimized experimental procedure results to be a powerful and useful tool to deepen the understanding of the correlations between ZnO luminescence, morphology, and defectiveness, that may go beyond the material itself. Moreover, the role of surface properties and reactivity is carefully addressed by testing the ability of nanometric ZnO with different sizes and interfaces, and hence surface area and defects, to sensitize the production of radical species, such as ROS and singlet oxygen, in an biological environment under ionizing radiation. Thus, this study is also a crucial proof of

concept of the possible use of ZnO NPs as active ROS generator to implement conventional radiotherapy.

In the following, first, the structural and morphological properties of four sets of ZnO NPs together with those of industrial micrometric powders and of a commercial single bulk crystal is described. Then, the findings of an accurate spectroscopical analysis performed on all the samples are presented and discussed in relation to the role of the excitation energy, of the dimensionality as well as of the growth parameters and interfaces. Lastly, tests and results of ROS and $^1O_2$ generation upon X-Ray exposure of the four ZnO NPs are reported.
As a guideline to the reading of this chapter, a schematic description of the herein analysed ZnO-based systems (for synthesis details please refer to sub-Section 3.1.1) is provided in Table 4.1.

Sample	Size	Synthesis	Interfaces	Shape	Form and colour
N05-HI	5 nm	Hot Injection	Capped with stearic acid	Spherical	White powder
N22-HI	22 nm	Hot Injection	Capped with stearic acid	Spherical	White powder
N05-SG-SS	5 nm	Sol-Gel	Supported onto spherical SiO_2 NPs	Spherical	White powder
N05-SG-SR	5 nm	Sol-Gel	Supported onto rod-like SiO_2 NPs	Spherical	White powder
MP	100-2000 nm	Unknown (commercial)	Unknown (commercial)	Not homogeneous	White powder
BC	10 cm x 10 cm x 1 mm	Hydrothermal growth (commercial)	Two sides polished	Parallelepiped	Yellow crystal

Table 4.1: Schematic description of the investigated samples.

4.1 Optical properties - from bulk to the nano-size

4.1.1 Radio- and photoluminescence

The luminescence properties of all ZnO samples are investigated at room temperature under both ionizing radiation and optical excitation (Figure 4.1). The former analysis is performed exploiting low energy X-Ray in rotary vacuum condition (10^{-3} mbar), to avoid the RL signal caused by air molecules ionization. For photoluminescence, the excitation energy is selected from a continuous wave Xenon lamp. Each sample reveals peculiar optical features with emissions from defects and/or excitonic states.

Figure 4.1a displays the absolute RL intensities of the nanometric samples, the micrometric commercial specimen, together with the bulk crystal, while Figure 4.2 reports the absolute RL spectra of silica NPs (a), *i.e.* the N05-SG-SS and N05-SG-SR substrates, and of the stearic acid (b), *i.e.* N05-HI and N22-HI capping agent. All the spectra are collected under the same experimental conditions and normalized to the ZnO weight percent to ensure an accurate comparison between their amplitudes. Under X-Ray excitation, SiO_2 NPs and SA molecules display a very weak and absent signal, respectively, proving that the optical properties observed in all the nanometric powders are completely attributable to ZnO. The overall emissions of the nanometric powders are about 10 and 70 times weaker than that of the micrometric one for the silica supported N05-SG-SS and N05-SG-SR NPs and for the bare N05-HI and N22-HI NPs, respectively. The RL efficiency of the bulk sample is about 250 times weaker with respect to that of the micrometric powders. In this regard, it has to be remarked that the BC is transparent and yellowish, while the other specimens white powders (Figure 4.3). Consequently, the comparison between crystal and powders must take into account the effect of different morphologies on light collection: the detection of light emitted from crystal can be affected by the waveguide effect, [139] at variance in highly scattering white powder systems, the luminescence is more effectively conveyed into the collection angle.

Figure 4.1b shows the RL spectra normalized to their maximum. The relative intensity of the UV exciton luminescence with respect to the defects bands decreases by scaling down the sample size. In fact, the excitonic emission is evident in the crystal, it is still noticeable in the micrometric sample, while it is very weak or absent in the nanometric powders. The shape of VIS defect-related lu-

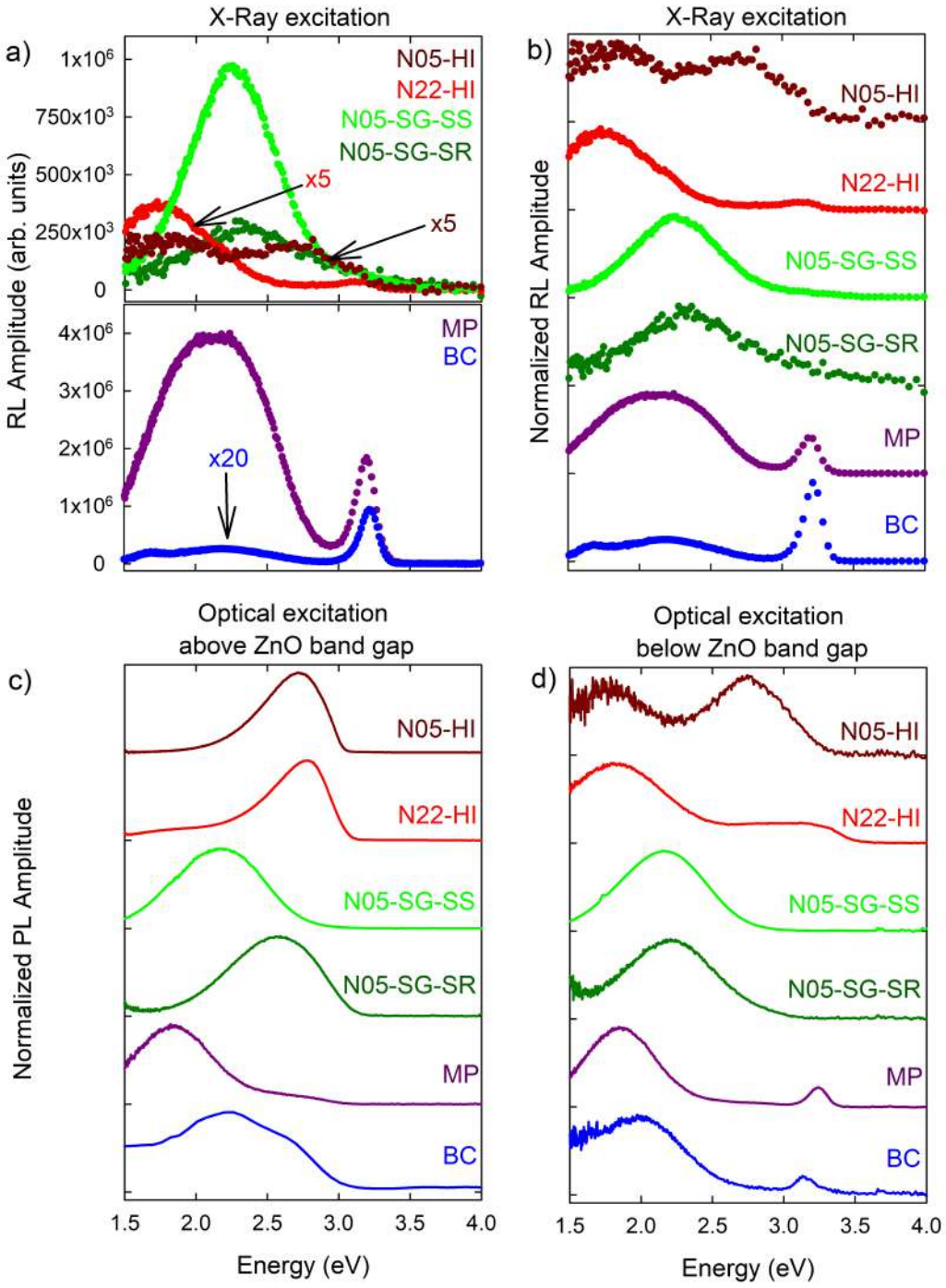

Figure 4.1: **a,b**) Room temperature RL intensities and normalized RL spectra under X-Ray irradiation, respectively; for all samples the spectra are measured at 300 K and 10^{-3} mbar, operating the X-Ray tube at 20 kV and 20 mA; **c**) Normalized PL spectra of all samples recorded under CW excitation at 3.5-3.6 eV (above ZnO band gap) with the use of a long-pass filter with cutting wavelength at 370 nm (3.4 eV); **d**) Normalized PL spectra of all samples recorded under CW excitation at 3.1-3.2 eV (below ZnO band gap) with the use of a long-pass filter with cutting wavelength at 418 nm (3.0 eV).

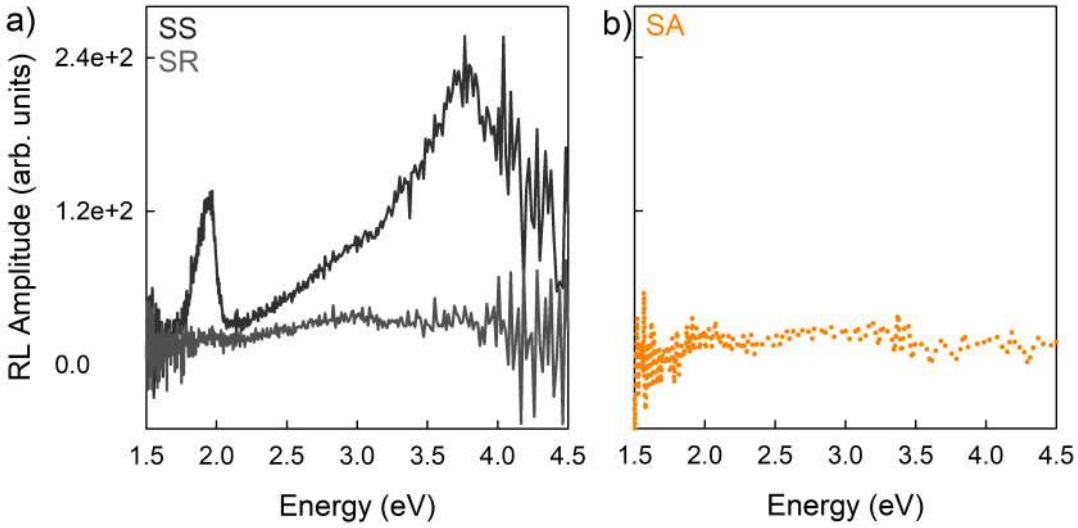

Figure 4.2: **a**) RL of spherical (SS) and rod-like (SR) silica NPs; **b**) RL of stearic acid (SA).

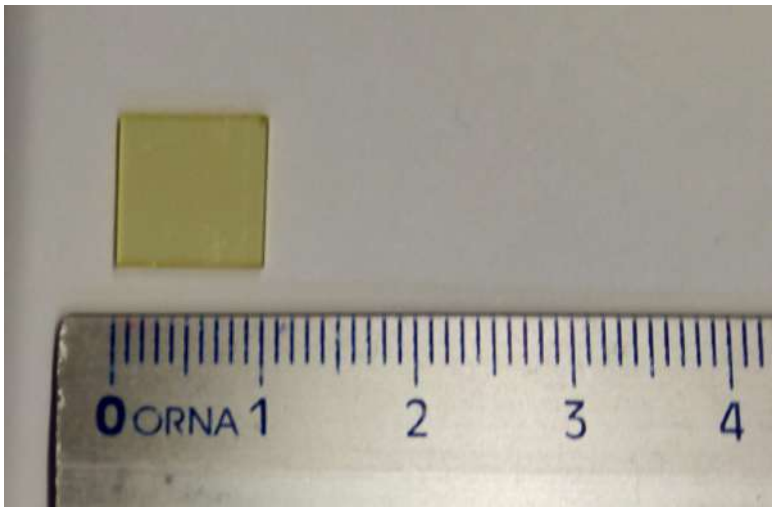

Figure 4.3: Photograph of commercial ZnO bulk single crystal (BC) purchased from Alineason.

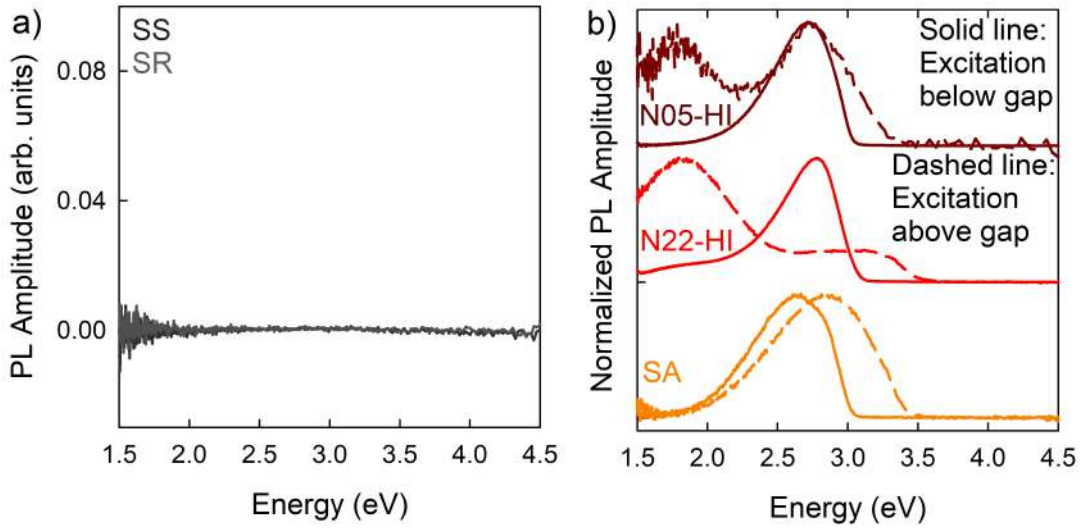

Figure 4.4: **a**) PL spectra of spherical (SS) and rod-like (SR) silica NPs measured at 3.8 eV excitation; **b**) b) PL spectra measured above (3.5-3.6 eV) and below (3.1-3.2 eV) ZnO band gap of bare ZnO NPs (N05-HI and N22-HI) and of SA.

minescence varies throughout the specimens: BC and MP samples display broad composite emissions extending from 1.5 eV to almost 2.9 eV, while the nanometric systems present distinct peaks in the green (N05-SG-SS and N05-SG-SR), red (N05-HI and N22-HI) and blue (N05-HI) region of the spectrum. A detailed analysis of the RL spectral components of all the samples emissions will be carried out in sub-Section 4.1.2.

Figures 4.1c and 4.1d show the normalized PL emission spectra of all ZnO systems acquired under light excitation above (3.5-3.6 eV) and below (3.1-3.2 eV) the ZnO band gap, with the use of a long-pass filter with a cutting wavelength at 370 nm (3.4 eV) and at 418 nm (3.0 eV), respectively. Only BC and MP present the exciton luminescence, excited solely above ZnO band gap, whose intensity ratio with those of the defect emissions is lower with respect to the one under X-Ray excitation (Figure 4.1c). Exciting above the ZnO band gap, the defect-related emission of each sample is analogous to the one detected in RL. Differently, when the excitation energy is smaller than the ZnO band gap, variations in the spectral shape are observed expect that for the N05-SG-SS emission (Figure 4.1d). BC and MP systems exhibit a slight modification in the PL spectra, due to an enhancement of the emission intensities in the green and blue region of the spectrum. Otherwise, three nanometric specimens (N05-SG-SR, N05-HI and N22-HI) show a significant change of their luminescence since bright blue emission is observed. To complete the spectroscopic analysis of the nanometric samples, PL

measurements are performed on the silica substrates and of the SA molecules are investigated. The results indicate that SS and SR are non-luminescent (Figure 4.4a), whereas the capping agent shows an emission peaked at around 2.8 eV that matches the bright luminescence observed in N05-HI and N22-HI upon excitation at energies lower than the ZnO band gap (Figure 4.4b). Consequently, further analyses are necessary to unequivocally assign the origin of this blue component either to defect species or to the SA molecules.

4.1.2 Analysis of spectral components

RL spectra are collected a function of temperature from 10 to 300 K on all the ZnO systems to deepen the investigation on the features of exciton and defect emissions. To lower the sample temperature, a closed-cycle He cryo-cooler operating in high vacuum conditions (10^{-7} mbar) is used, differently than in the previous RL experimental procedure in which higher pressures (10^{-3} mbar) are adequate. A pressure-sensitive behavior under ionizing radiation is displayed by nanometric N05-SG-SS and MP samples (Figure 4.5). Varying the pressure from 10^{-7} mbar to 10^{-3} mbar, a decrease in the exciton luminescence intensity with respect to the defect one is observed in the micrometric MP specimen. Moreover, the RL spectral shape of N05-SG-SS is also slightly affected by the change pressure, since an additional broad emission, extending from approximately 2.5 eV to 3.2 eV, is detected under high vacuum conditions.

Figure 4.6 displays the Gaussian deconvolutions of the room temperature RL spectra of all the ZnO samples: overall five bands are identified, one associated to excitonic transition and four to defect centers. To perform the fit procedure, two main guidelines are followed: i) to use the minimum number of bands necessary to achieve a satisfactory spectrum reproduction for each sample, ii) to consider, the energy bands values reported in the literature for ZnO emissions as fit starting values, whenever possible. The outcome of the numerical analysis shows that the UV excitonic emission, labelled as band E, is centered at 3.27 eV with an uncertainty of 4%, whereas the VIS defect-related luminescence components are peaked in the red (band A centered at 1.83 eV with an uncertainty of 3%), green (band B centered at 2.29 eV with an uncertainty of 6%), blue (band C centered at 2.68 eV with an uncertainty of 4%), and violet (band D centered at 3.05 eV with an uncertainty of 7%) region of the spectrum. The set of all the parameters of the numerical analysis, together with their percentage weight at 300 K, are reported in Table 4.2.

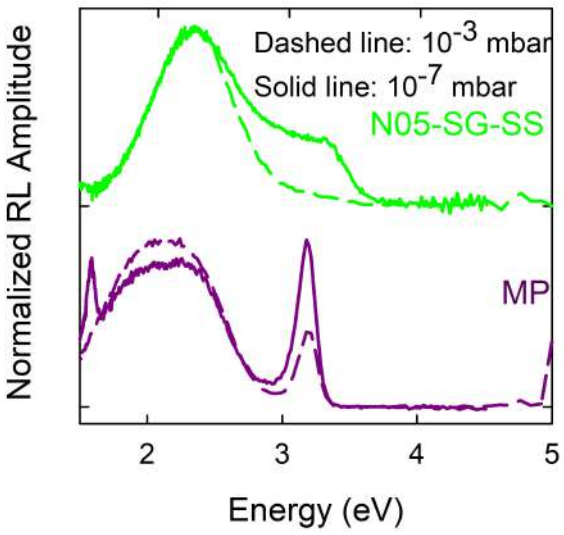

Figure 4.5: Normalized RL spectra of one nanometric sample (N05-SG-SS) and the micrometric powder (MP) recorded at 300 K in high rotary vacuum (10^{-3} mbar, dashed line) and high vacuum (10^{-7} mbar, solid line) condition. The peak at 1.6 eV observed in the micrometric sample is caused by the diffraction second order of the exciton emission generated by the spectrograph of the detection system.

The sets of ZnO nanostructure synthesized through the same procedure exhibit similar spectral components, disclosing nevertheless slight differences. Isolated N05-HI and N22-HI NPs share the same defect bands, A and C, while only in N22-HI the excitonic one, labelled as E, is present (Figure 4.6a and 4.6b). As already mentioned, the spectra of N05-SG-SS recorded in rotary and high vacuum conditions (Figure 4.5) differ from each other: at 10^{-3} mbar, two spectral components, B and E, are identified (Figure 4.7), whereas at 10^{-3} mbar, a supplementary band, D, is necessary (Figure 4.6c). The RL emission of N05-SG-SR is similar to the N05-SG-SS one at 10^{-3} mbar (4.6d). Instead, the reconstruction of the RL spectrum of the micrometric powder required all the five spectral components (Figure 4.6e). In the bulk crystal, two defect spectral components, A and B, together with the exciton one (E) are recognized (Figure 4.6f). In the bulk and micrometric sample, the peak detected at 1.6 eV is just the second order of the exciton emission. The analysis of the Full Width at Half Maximum (FWHM) parameters of the Gaussian deconvolutions of RL spectra reveals that the emission bands of nanometric powders are broader than those of the micrometric sample and of the bulk one (Table 4.2). The broadening of the bands widths in nanoscale materials can be due to the inhomogeneous structural distortions in

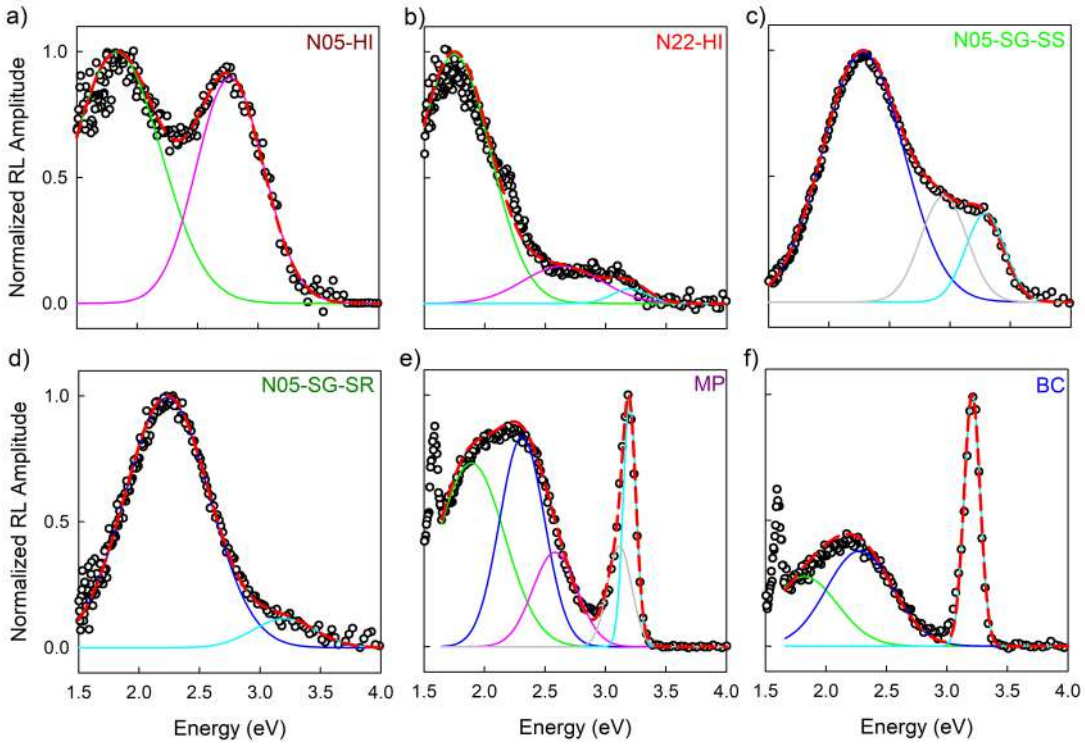

Figure 4.6: Gaussian deconvolution of normalized RL spectra of different ZnO samples at 300 K and 10^{-3} mbar. Gaussian components (green, blue, pink, light blue, and grey solid lines) obtained by numerical fit are shown together with experimental curves (black empty circle lines). The curve representing the whole numerical fit (red dashed line) is superimposed to the experimental data. The sets of all parameters of the deconvolution are listed in Table 4.2.

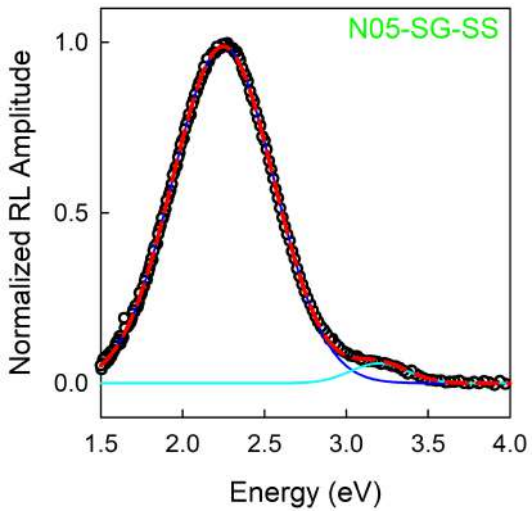

Figure 4.7: Gaussian deconvolution of RL emission recorded at 300 K and 10^{-3} mbar of one nanometric sample (N05-SG-SS). The fit parameters are listed in Table 4.2.

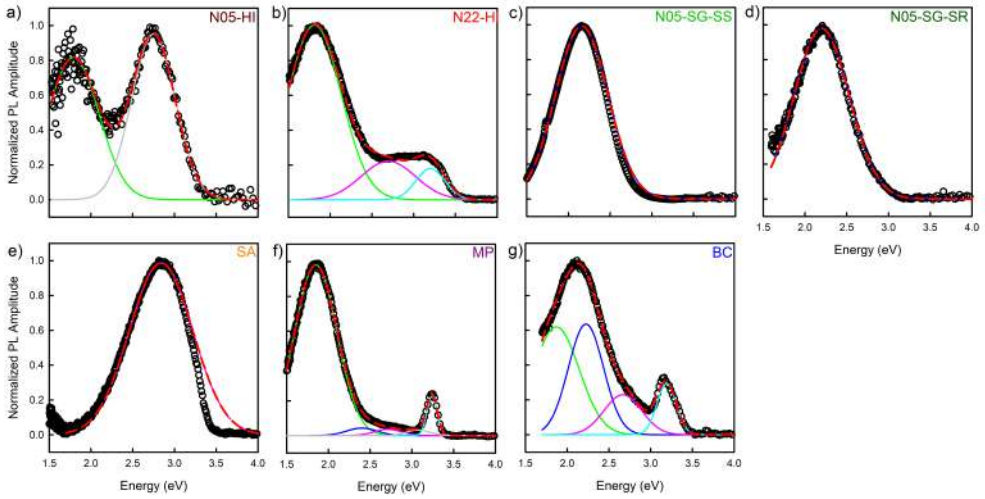

Figure 4.8: Gaussian deconvolution of normalized PL spectra of all ZnO samples and stearic acid (SA) recorded at room temperature under CW excitation at 3.5-3.6 eV (above ZnO band gap) with the use of a long-pass filter with cutting wavelength at 370 nm (3.4 eV). Gaussian components (green, blue, pink, light blue, and grey solid lines) obtained by numerical fit are shown together with experimental curves (black empty circle lines). The curve representing the whole numerical fit (red dashed line) is superimposed on the experimental data. The sets of all parameters of the deconvolution are listed in Tables 4.3.

the surroundings of optically active centres that generate a distribution of their energy level. [134]

Furthermore, the Gaussian deconvolution procedure is performed also on PL spectra of all the samples recorded exciting both above and below the ZnO band gap, (Figures 4.8 and 4.9, Tables 4.3 and 4.4). Interestingly, five components, corresponding exactly to the bands identified in the RL emissions, are required for satisfactory spectra reproduction. The use of a different detection system in the RL and PL measurements can account for the slight discrepancies in the energy peak positions and in the FWHM.

To provide an overview of the RL shapes and intensities variation as a function of the temperature, Figure 4.10 shows the RL spectra recorded at 10, 150, 300 K normalized to their total area at 300 K. The lower defect bands relative intensity in the green–blue region of the VIS spectrum at 300 K than at 10 K is responsible for the modification in the RL spectral shape of BC, N05-SG-SS and N05-HI (Figure 4.10). Moreover, Figure 4.10 clearly displays the shift of excitonic peak (band E) position towards higher energies together with its broadening as the temperature increases, in accordance with the suppression of bound excitons and the characteristics of the free ones. [29,31] The overall light output decreases

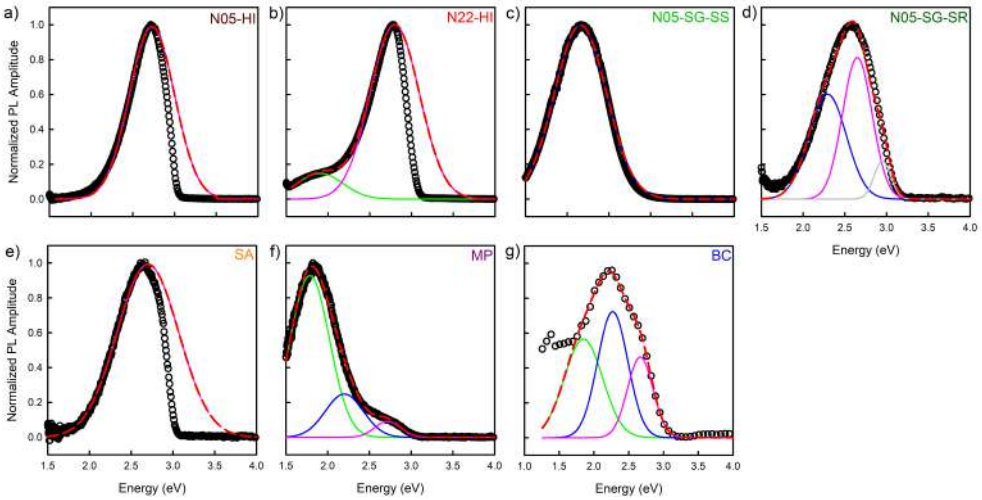

Figure 4.9: Gaussian deconvolution of normalized PL spectra of all ZnO samples and stearic acid (SA) recorded at room temperature under CW excitation at 3.1-3.2 eV (below ZnO band gap) with the use of a long-pass filter with cutting wavelength at 418 nm (3.0 eV). Gaussian components (green, blue, pink, light blue, and grey solid lines) obtained by numerical fit are shown together with experimental curves (black empty circle lines). The curve representing the whole numerical fit (red dashed line) is superimposed on the experimental data. The sets of all parameters of the deconvolution are listed in Table 4.4.

as the temperature increases, due to thermal quenching, in all ZnO systems except for N05-SG-SR, whose emission efficiency is almost constant. For all ZnO samples, the evolution of their RL properties is investigated by performing the Gaussian deconvolutions of spectra recorded at different temperatures: the results of the numerical analysis disclose that all the RL spectra could be fitted in a coherent way for all the temperature by the sum of the spectral components identified at 300 K (Figure 4.11). Panel a of Figure 4.11 reports for all the ZnO systems the integrated RL of each component, normalized to the area of the total light output at 300 K, whereas panels b-f of Figure 4.11 display the integrated RL, normalized to their value at 10 K and as a function of temperature, of the five bands. In Figure 4.11, the RL intensities are displayed in logarithmic scale. The obtained data enlighten a weaker temperature dependence in the nanometric powders luminescence with respect to the bulk and micrometric sample. The activation energy of the thermal quenching (E_a) of the exciton luminescence for all the three systems (bulk, micrometric powder and NPs) and of band A, B, and C for the nanometric samples is determined from the RL intensity dependence

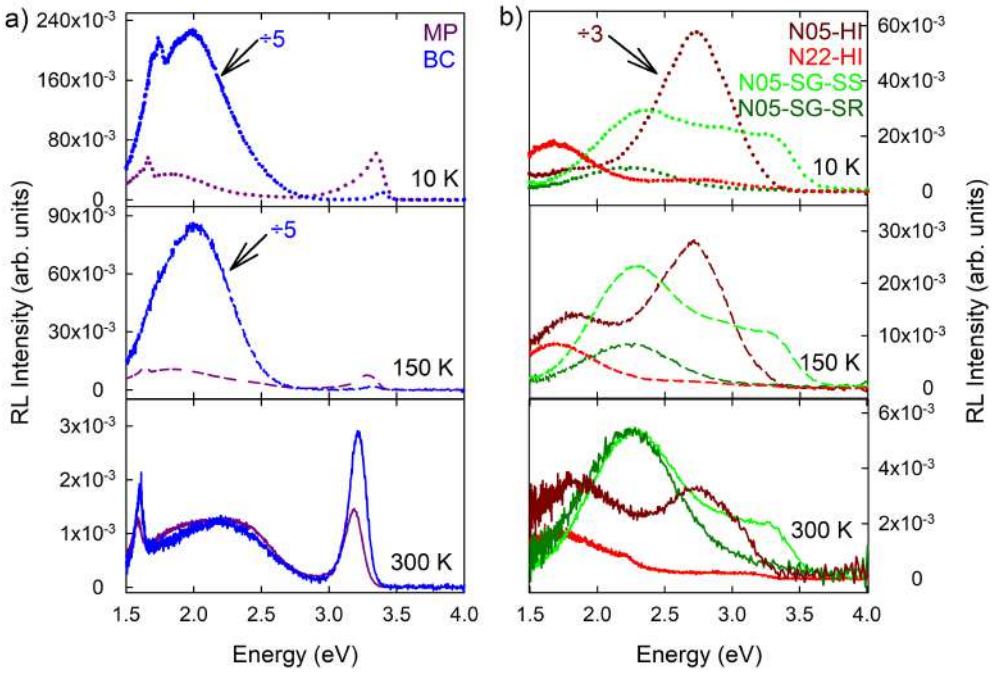

Figure 4.10: RL intensities recorded at 10^{-7} mbar and at 300 K (solid line), 150 K (dashed line) and 10 K (dotted line) normalized to the total area at 300 K of bulk single crystal (BC) and micrometric powder (MP) (**a**) and of the nanometric samples (N05-HI, N22-HI, N05-SG-SS, N05-SG-SR) (**b**).

on the temperature (Figure 4.11) according to the following equation:

$$I(t) = \frac{I_0}{1 + \alpha\, e^{\frac{-E_a}{k_B T}}} \tag{4.1}$$

where k_B is the Boltzmann's constant, α is a constant parameter, and I_0 is the luminescence intensity at 0 K. The analysis is performed on the range 100 K-300 K and, since the intensity of the bands is approximately constant at low temperatures, I_0 is considered as the RL intensity at 50 K. [140] In agreement with the literature, [141, 142] the mean value of the thermal activation energy of the exciton luminescence results of ∼40 meV for all the three systems (bulk, micrometric powder and NPs). The analysis of the defect emissions temperature dependence of the nanometric samples reports an activation energies of ∼70 meV for band B (detected in N05-SG-SS and N05-SG-SR) and of ∼40 meV for band A and of ∼50 meV for band C (detected in N05-HI and N22-HI). Previous works reported similar activation energies for defect-related luminescence in ZnO nanosystems. [143, 144]

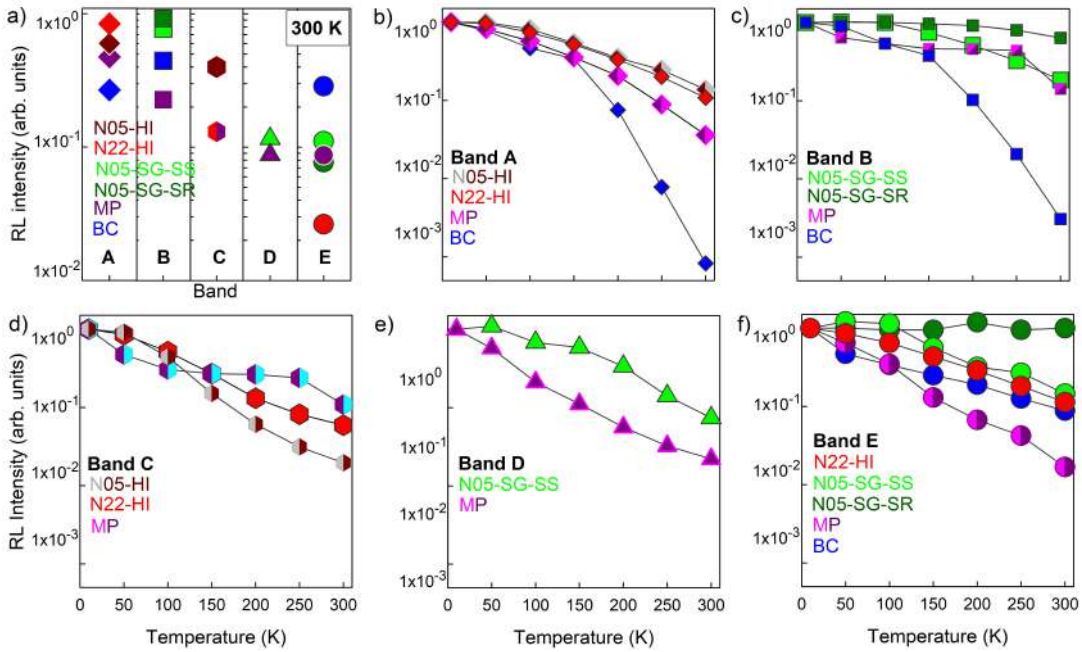

Figure 4.11: Temperature influence on RL spectral components of different ZnO samples: **a**) Integrated RL intensities, displayed on a logarithmic scale, at 300 K of band A (diamond), B (square), C (hexagon), D (triangle), E (circle). For each sample, the integrated RL of a single component is normalized to the total RL intensity at 300 K. **b-f**) Integrated RL, displayed on a logarithmic scale, versus temperature of the five spectral components. For each component, the integrated RL is normalized to its integrated RL recorded at 300 K.

		N05-HI	N22-HI	N05-SG-SS	N05-SG-SR	MP	BC
Band A (green line)	Energy (eV)	1.84±0.02	1.73±0.01	-	-	1.85±0.04	1.90±0.04
	FWHM (eV)	0.86±0.02	0.68±0.05	-	-	0.62±0.03	0.56±0.06
	Weight (%)	60	84	-	-	48	27
Band B (blue line)	Energy (eV)	-	-	2.30±0.04	2.22±0.01	2.33±0.03	2.23±0.04
	FWHM (eV)	-	-	0.78±0.03	0.82±0.01	0.42±0.02	0.57±0.06
	Weight (%)	-	-	77	92	23	45
Band C (pink line)	Energy (eV)	2.73±0.02	2.63±0.04	-	-	2.65±0.06	-
	FWHM (eV)	0.63±0.02	0.68±0.06	-	-	0.42±0.02	-
	Weight (%)	40	13	-	-	12	-
Band D (grey line)	Energy (eV)	-	-	2.97±0.02	-	3.13±0.03	-
	FWHM (eV)	-	-	0.50±0.04	-	0.29±0.03	-
	Weight (%)	-	-	12	-	9	-
Band E (light blue line)	Energy (eV)	-	3.22±0.04	3.30±0.04	3.23±0.03	3.28±0.06	3.31±0.06
	FWHM (eV)	-	0.34±0.02	0.36±0.03	0.64±0.02	0.14±0.01	0.14±0.02
	Weight (%)	-	3	11	8	8	28

Table 4.2: Fit parameters of the Gaussian deconvolution of the RL spectra of different ZnO sample recorded at 300 K and 10^{-3} mbar. The energy and FWHM parameters are calculated also for the RL spectra recorded as a function of the temperature and no discrepancies are observed.

		N05-HI	N22-HI	SA	N05-SG-SS	N05-SG-SR	MP	BC
Band A (green line)	Energy (eV)	1.79±0.02	1.81±0.01	-	-	-	1.85±0.04	1.87±0.04
	FWHM (eV)	0.72±0.02	0.77±0.07	-	-	-	0.59±0.03	0.65±0.06
	Weight (%)	50	75	-	-	-	88	43
Band B (blue line)	Energy (eV)	-	-	-	2.16±0.04	2.20±0.04	2.34±0.03	2.23±0.04
	FWHM (eV)	-	-	-	0.74±0.03	0.78±0.04	0.45±0.04	0.50±0.06
	Weight (%)	-	-	-	100	100	3	35
Band C (pink line)	Energy (eV)	2.75±0.02	2.70±0.07	2.84±0.09	-	-	2.71±0.06	2.67±0.05
	FWHM (eV)	0.62±0.04	0.77±0.07	0.89±0.02	-	-	0.39±0.02	0.53±0.07
	Weight (%)	50	17	100	-	-	3	13
Band D (grey line)	Energy (eV)	-	-	-	-	-	3.07±0.03	-
	FWHM (eV)	-	-	-	-	-	0.29±0.03	-
	Weight (%)	-	-	-	-	-	2	-
Band E (light blue line)	Energy (eV)	-	3.20±0.03	-	-	-	3.24±0.05	3.19±0.06
	FWHM (eV)	-	0.41±0.02	-	-	-	0.12±0.01	0.27±0.03
	Weight (%)	-	8	-	-	-	4	9

Table 4.3: Fit parameters of the Gaussian deconvolution of the PL spectra of different ZnO samples and of stearic acid SA recorded at room temperature exciting above ZnO band gap.

		N05-HI	N22-HI	SA	N05-SG-SS	N05-SG-SR	MP	BC
Band A (green line)	Energy (eV)	-	1.90±0.06	-	-	-	1.79±0.04	1.85±0.04
	FWHM (eV)	-	0.65±0.07	-	-	-	0.55±0.03	0.65±0.06
	Weight (%)	-	12	-	-	-	75	39
Band B (blue line)	Energy (eV)	-	-	-	2.16±0.04	2.29±0.05	2.20±0.03	2.27±0.04
	FWHM (eV)	-	-	-	0.74±0.03	0.53±0.12	0.54±0.04	0.51±0.06
	Weight (%)	-	-	-	100	45	19	40
Band C (pink line)	Energy (eV)	2.73±0.02	2.80±0.07	2.70±0.09	-	2.65±0.05	2.72±0.06	2.67±0.04
	FWHM (eV)	0.64±0.04	0.69±0.07	0.87±0.02	-	0.42±0.09	0.36±0.02	0.43±0.07
	Weight (%)	40	13	-	-	12	-	
Band D (grey line)	Energy (eV)	-	-	-	-	2.95±0.06	-	-
	FWHM (eV)	-	-	-	-	0.20±0.05	-	-
	Weight (%)	-	-	-	-	47	-	-
Band E (light blue line)	Energy (eV)	-	-	-	-	-	-	-
	FWHM (eV)	-	-	-	-	-	-	-
	Weight (%)	-	-	-	-	-	-	-

Table 4.4: Fit parameters of the Gaussian deconvolution of the PL spectra of different ZnO samples and of stearic acid SA recorded at room temperature exciting below ZnO band gap.

4.1.3 Time resolved luminescence

The time decay of the bands identified through the Gaussian reconstruction of the emission spectra is also investigated to deepen the analysis of the ZnO optical properties. In all the ZnO samples that exhibit the exciton luminescence (corresponding to band E), the TRPL measurements are tentatively carried out. By the outcomes, the lifetime of the ZnO excitonic band results faster than the instrumental response (tens of picoseconds), indicating that it is in the sub-nanosecond range, in agreement with the literature. [28] For the time decay of ZnO VIS defect-related emissions, solely the signals originated from bands that could be clearly isolated are collected aiming at evaluating the time decay of specific defect centers. The results of the PL numerical analysis (Figures 4.8 and 4.9) are used to choose the bands and the samples to investigate by TRPL technique. In particular, the TRPL selected measurements to be performed are: i) for the red luminescence (band A), on N05-HI, N22-HI NPs and of MP, ii) for the green emission (band B), on N05-SG-SS and N05-SG-SR, iii) for the blue component (band C), on N05-HI, N22-HI samples and, for comparison, on their capping agent. Lastly, since the violet band (D) strongly overlaps with the others, preventing the exclusive collection of its signal, the investigation of its time decay is not carried out. Moreover, the recorded TRPL signal are reproduced with an analytically multi-exponential function by the fit procedure described in sub-Section 3.1.4.

The TRPL measurements on the red luminescence (band A) are performed monitoring the signal at 1.8 eV (exciting at 3.6 eV) and at 2 eV (exciting at 3.1 eV) for nanometric N05-HI and N22-HI NPs and for MP, respectively. Since exciting both at above and below the ZnO band gap, the defect emission of the MP sample is similar (Figure 4.1c,d), the experimental condition with the better signal to noise ratio is chosen. Remarkably, the fastest lifetime of the red spectral component (band A) is observed in the smallest ZnO system: by performing a multi-exponential fit, average lifetimes of the order of tens and thousands of nanoseconds, for N05-HI, N22-HI and for MP samples, respectively (Figures 4.12a-c, Table 4.5) are disclosed. Additionally, for a satisfactory reconstruction of MP TRPL, a constant background is also required: this outcome hints that the time dynamic of the collected luminescence is even slower.
For the green luminescence (band B), the TRPL signals of N05-SG-SS and N05-SG-SR are recorded at 2.1 and 2.3 eV, respectively. Their decays are fitted with three-exponential functions (Figure 4.12d, Table 4.5) and the average lifetimes, both of the order of hundreds of nanoseconds, are shorter for N05-SG-SR than

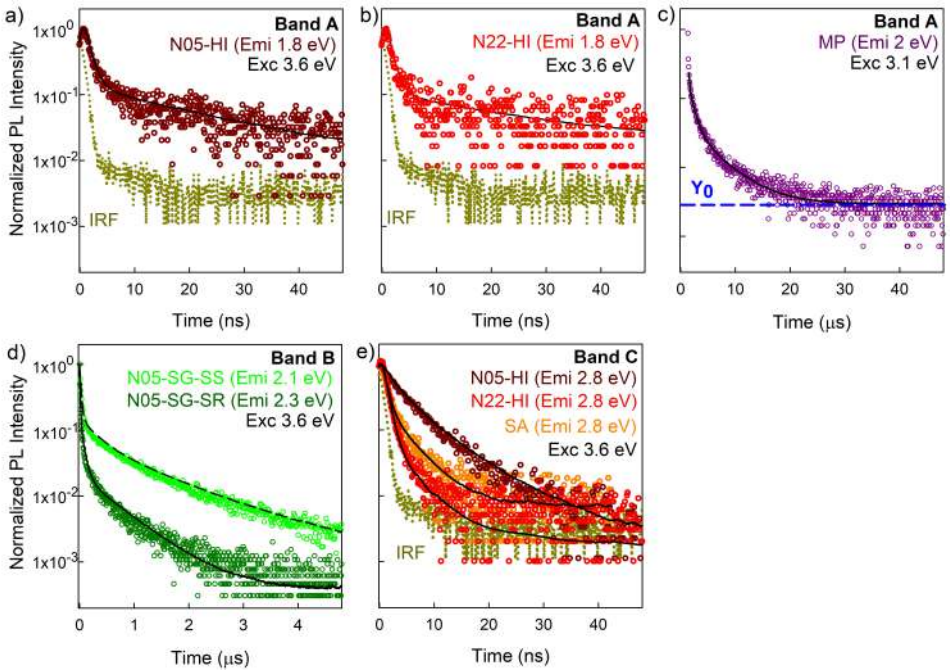

Figure 4.12: Time dynamics of excitonic and defect emissions in different ZnO samples: **a,b**) PL time decays of bare ZnO NPs (N05-HI and N22-HI, respectively) at 1.8 eV (corresponding to band A) under pulsed excitation at 3.6 eV; **c**) PL time decays of micrometric powder (MP) at 2 eV (corresponding to band A) under pulsed excitation at 3.1 eV **d**) PL time decays of ZnO NPs grown on silica substrates (N05-SG-SS, N05-SG-SR) at 2.1 eV and 2.3 eV, respectively (corresponding to band B), under pulsed excitation at 3.6 eV; **e**) PL time decays of the bare ZnO NPs (N05-HI, N22-HI), and their capping agent (stearic acid, SA) at 2.8 eV (corresponding to band C) under pulsed excitation at 3.6 eV. In panels (**a, b, d**), the instrument response functions (IRF) are also shown (mustard dotted line). From (**a**) to (**e**), the signal decays are fitted as multiexponential functions (black solid lines). In (**c**) a constant parameter (y_0) as backgrounds is also used. The sets of all parameters used to model the PL decay are reported in Table 4.5.

for N05-SG-SS.

To study the time dynamics of the blue emission (band C), the TRPL measurements are carried out on bare N05-HI, N22-HI NPs and their capping agent under excitation at 3.6 eV and collecting the emission at the PL maximum intensity peaked at 2.8 eV. Time decays of the two ZnO samples both fitted by a bi-exponential curve differ: average lifetimes are of the order of few of nanoseconds and are faster for N22-HI than for N05-HI (Figure 4.12e, Table 4.5). Interestingly, the time decay of SA and of N22-HI are similar (Figure 4.12e, Table 4.5). Hence, taking into account the RL and PL features of these two specimens, we hypothesized that the emission peak at 2.8 eV originates from defect centers in N05-HI,

while it is mainly due to the stearic acid in N22-HI. In fact, under X-Ray excitation, the capping agent is not luminescent (Figure 4.2b) and the blue spectral component (band C), detected both in N05-HI and N22-HI, is more intense in the smallest NPs (Figure 4.1a,b), suggesting that the concentration of the defect species emitting at 2.8 eV is higher in N05-HI than in N22-HI. These observations are in agreement with TRPL measurements. In N05-HI, because of the occurrence of a high content of defect centers emitting at 2.8 eV, their emission prevails and consequently its decay time is different from that of SA. On the other hand, due to the lower concentration of blue emitting defect species in N22-HI, the SA emission overcomes the one from ZnO, as also the similar time dynamics of N22-HI and SA validate. For all the multi-exponential PL decays, the complete data set of the obtained decay components with corresponding weights is reported in Table 4.5.

	N05-HI	N22-HI	MP	N05-SG-SS	N05-SG-SR	N05-HI	N22-HI	SA
Emission energy (eV)	1.8 (Band A)	1.8 (Band A)	2.0 (Band A)	2.1 (Band B)	2.3 (Band B)	2.8 (Band C)	2.8 (Band C)	2.8 (Band C)
Excitation energy (eV)	3.6	3.6	3.1	3.6	3.6	3.6	3.6	3.6
τ_1 (ns)	1.04±0.04	0.94±0.04	136±6	25±1	10±1	2.4±0.1	0.85±0.02	0.85±0.03
Weight$_1$ (%)	45	52	4	18	33	38	87	62
τ_2 (ns)	1.92±1.2	20.7±2.8	934±25	305±6	70±1	7.2±0.2	4.7±0.4	4.4±0.2
Weight$_2$ (%)	55	48	36	21	27	62	13	38
τ_3 (ns)	-	-	5100±130	1280±10	660±5	-	-	-
Weight$_3$ (%)	-	-	60	61	40	-	-	-
y_0	-	-	0.003	-	-	-	-	-
$\langle\tau\rangle$ (ns)	11±1	11±3	1300±200	850±20	290±10	5.4±0.3	1.5±0.4	2.2±0.2

Table 4.5: TRPL fit parameters for red (band A), green (band B) and blue (band C) emissions of the nanometric samples and the capping agent (SA) under excitation at 3.6 eV and for micrometric powder red emission (band A) under excitation at 3.1 eV.

4.2 Correlations between morphology, defectiveness, and luminescence

4.2.1 Role of excitation energy

The optical properties of all ZnO systems are investigated upon excitation with three different energies: 1) ∼6.5 keV (X-Ray mean energy) in RL measurements exciting from deep core bands to high energy electron levels with the production of a cascade of free carries 2) 3.5–3.6 eV in the PL ones exciting from valence to the conduction band, and 3) 3.1–3.2 eV in the PL ones exciting from valence band to intragap states in PL ones (Figure 4.1). RL and PL techniques uses different excitation sources: ionizing radiation and light, respectively, leading to significantly different excitations pathways and, consequently, different relaxation mechanisms. In RL, X-Ray, by causing the ionization of electrons from the core bands of the analyzed material, are converted into high energy electron–hole pairs that in turn, due to a cascade multiplication process, create free carriers that thermalize towards the edges of the conduction and valence bands. The generated electrons and holes can then migrate within the delocalized bands and their relaxation can occur through different pathways, such as prompt radiative recombination, non-radiative energy losses, and trapping by traps. Hence, the RL technique is useful to investigate the effect of carriers migration and the role of traps on the sample luminescence, but because of its high energy excitation, which involves core levels, it does not allow selectivity towards optically active recombinations, either of excitonic or of defect origin. Differently, in PL measurements, the excitation energy, which is close to or even lower than the energy band gap, can be properly chosen, enabling the monitoring of transitions between valence bands and intra-gap electronic levels, or between intra-gap states.
The spectral shapes of the room temperature RL and PL emissions recorded as exciting just above the ZnO band gap are generally similar for all the ZnO samples, suggesting that events of charge carriers trapping on defects are not relevant in the RL carrier migration. [145, 146] Noticeably, the relative intensities of excitonic and defect emissions differs: the former one is more intense under X-Ray excitation. An incident UV photon generates one electron and one hole in PL measurements, whereas numerous carriers are created upon down-converting of the high energy radiation in the RL. Then, in both techniques, the free carrier thermalization and the subsequent recombination through defect centers, or excitons (coupled electron–hole pairs) formation can occur. Hence, in RL, the exciton

emissive processes are more probable upon X-Ray irradiation, because of the high concentration of generated charges, than upon above band gap light excitation, even in very defective samples. On the other hand, exciting with energy lower than the ZnO energy gap, defect-related luminescences in the green (band B) and blue (band C) region of the spectrum are boosted with respect to above gap excitation, especially in nanometric systems.

4.2.2 Role of dimensionality

Various luminescence features related to nanometric dimensions are disclosed. Nevertheless, it is worth remarking that the estimated ZnO Bohr radius (∼2 nm) [31] is smaller than the ZnO sample sizes herein examined and consequently quantum confinement effect could be neglected in this analysis. The ZnO dimensionality impacts on the overall efficiency of luminescence, as Figure 4.1a unveils. This finding indicate that non-radiative dissipation of excitation energy is enhanced in NPs as also validated by TRPL outcomes. Indeed, the defect bands decay dynamics are strongly accelerated with the reduction of dimensions (Figure 4.12a-c): the time decays of the red luminescence (band A) of bare N05-HI and N22-HI NPs are of about tens of nanoseconds, whereas, in micrometric powders, the same band A lifetime is at least in the order of microseconds, in agreement with those reported in the literature for defect emission of ZnO crystals and ceramics. [28,37] Additionally, previous studies already observed complex decay behaviors with fast time dynamics of the defect emissions in ZnO nanostructures. [107, 147] As evidenced in sub-Section 1.1.1, nanometric systems are characterized by a significant degree of defectiveness mainly because of their high surface-to-volume ratio. Interfaces increase disorder, leading to the formation of surface related defect centers, like dangling bonds, hydroxo or peroxo linkages. The smaller the system, the higher the probability that the excitons reach the surface and interact with its defects, leading to both radiative and non-radiative recombination. On the basis of Monte Carlo simulations, it has been reported that, in spherical ZnO nanocrystals, the percentage of excitations that decay on the surface, and of these, the ones that undergo non radiative annihilation, increases scaling down the size: in particular almost all the generated excitons reach the surface and recombine non radiatively in nanosystems with a radius of a few nanometers. [148] Thus, surface states often act as quenching channels, [149] causing a decrease in the decay time of radiative transitions. [130] Consequently, ZnO NPs typically display a time decay acceleration as the size is reduced. [147] Also, the intensity ratio between the excitonic (UV) and defect (VIS) emissions

is compromised when scaling down the size (Figure 4.1). This observation can be accurately examined by focusing on the room temperature RL spectra and their Gaussian deconvolutions (Figure 4.6 and Table 4.2): the lower ratio between the exciton and defect luminescence is observed in nanometric powders, and then it becomes higher in the micrometric one and further increases in the bulk crystal. Interestingly, only the Gaussian deconvolution of one bare nanometric N05-HI sample does not require the excitonic band to obtain an accurate spectrum reconstruction, even if the NPs diameter (5 nm) is the same as that of the ZnO NPs grown on SiO_2, (Table 4.2). These findings are consistent with previous works in which it has been reported, under ionizing radiation, a lower intensity of the ZnO excitonic peak than the defect one in ceramics and powders, while it is enhanced in in mono and poly-crystals. [35,89,90] This study clearly highlights that the exciton emission decreases by scaling down the size of the system. Since the point defects concentration increases, reducing the dimensions, this result confirms that the intensity of the exciton luminescence is significantly related to the occurrence of defect states. Moreover, the probability of interaction between the excitation and the defects could be further increased by the reabsorption within the sample of the excitonic emission, that is almost resonant with the ZnO band gap. [150, 151] All these considerations suggest that, in nano-systems, the probability that the excitations transfer their energy non-radiatively to emissive defects or quenching centers (rather than undergoing radiative relaxation) is higher than in micrometric and bulk samples, which typically are affected by a lower degree of defectiveness.

Moreover, the observed variations in RL spectral shape of the micrometric powder and of a nanometric N05-SG-SS sample (Figure 4.5), lowering the pressure from 10^{-3} mbar to 10^{-7} mbar, evidence that both ZnO UV excitonic and VIS defect-related emissions are pressure and moisture sensitive. Previous works have observed that the exposure of ZnO quantum dots to humid air suppresses the excitonic luminescence [113] and the annealing of ZnO single crystals in an O_2 atmosphere quenches both the exciton and the green emission. [152] Thus, possibly, gaseous molecules, still present in a rotary vacuum, quench the exciton peak, especially due to the H_2O adsorbed on the samples surface, while in a high vacuum, after their release, it is restored. This interpretation could be further validated by the observation (not reported) that the exciton emission of MP is progressively enhanced under continuous X-Ray irradiation; indeed, the increase in RL efficiency after prolonged irradiation ("bright burn" effect) is a known phenomenon in scintillators and it is generally due to the progressive filling of traps

in the forbidden energy gap. [153] Hence, the observed "bright burn" of the MP exciton peak suggests that its surface states, when they are already occupied by the constantly pumped electrons, cannot act anymore as carrier traps.
The decrease of the luminescence efficiency of all bands is decreased by increasing the temperature unveils the occurrence of thermal quenching (Figure 4.10). The most common process that concurs in this phenomenon is the triggering of non-radiative multi-phonon relaxation, as a consequence of the temperature increase. [140] Other mechanisms contribute to the luminescence temperature dependence, among which the competition between radiative and non-radiative recombination centres, whose effects raise with increases in temperature [154] or the thermally activated depopulation of emissive defect levels near the conduction band edge, [155] which allows the excitations to migrate, reach the surface and relax non-radiatively or be re-trapped by other defect centres. This study also discloses that in nanometric systems the exciton emissions are less intense than the defect ones even at low temperatures (Figure 4.10b); therefore, defects are the main radiative recombination centres in NPs, regardless of the temperature, because of the high degree of defectiveness and the small size. As Figure 4.11 reveals, the optical properties of nanometric powders are less affected by temperature variation than those of the micrometric sample and of the single crystal. This observation corroborates that that the effects of the limitation of carrier's migration, caused by the decrease in thermal energy, are less significant in nanosystems than in bulk and micrometric samples.

4.2.3 Role of growth conditions and interfaces

The Gaussian deconvolution analysis identified a maximum of four defect bands in the VIS luminescence of various ZnO samples, all already observed in the literature [28, 29]: band A and B match the red and yellow–green emissions, respectively, whereas C and D match the blue and violet ones. Also, it is worth recalling that the origin of the visible emissions is linked to intrinsic defect species in the nanometric and micrometric powders, while for the single crystal, grown by the hydrothermal method, the occurrence of metal impurities, especially Li, which can influence the ZnO luminescence, should be also taken into account. [103] As Figure 4.6 displays, bands A and B are the more common and intense throughout the samples. Except for N05-HI, bands C and D contribute less to the overall light output but are necessary for an accurate spectrum reproduction. Similar efficiency at room temperature (Figure 4.1) as well as the same spectral components are detected in NPs synthetized by the same procedure, corroborating

the influence of growth conditions on the final point defects type and concentration. The differences in the PL features of ZnO NPs grown on two different silica substrates, having spherical (in N05-SG-SS) or rod-like (in N05-SG-SR) shapes, further highlight the crucial role of morphology and interfaces. The occurrence of inequivalent defect species in these samples is disclosed by their different PL spectra under excitation at energies lower than the ZnO band gap: N05-SG-SS exhibits solely the green luminescence (band B), whereas the PL spectrum of N05-SG-SR include the green (band B), blue (band C), and violet (band D) Gaussian components (Figure 4.9c,d). Moreover, a higher concentration of quenching centers in N05-SG-SR with respect to N05-SG-SS is revealed by the acceleration of the green emission time dynamics of N05-SG-SR (Figure 4.12d). Thus, just by changing the substrate morphology, *i.e.* spherical (in N05-SG-SS) or rod-like (in N05-SG-SR), the surface properties and, consequently, the optical features are affected. Regarding the isolated NPs, the PL features of the bare N05-HI and N22-HI NPs indicate that the stearic acid anchored on the nanostructures do not introduce novel defect centers or surface states in ZnO structures. Hence, the ZnO intrinsic defectiveness is not modified, but the ligand itself can be emissive in certain excitation conditions altering the final luminescence of the nanosystems, as also evidenced by TRPL results. Hence, this spectroscopical analysis clearly points out the impact of synthesis conditions on the optical properties. Moreover, despite that the NPs crystallinity degree changes significantly with the synthesis process (HI or SG) and the morphology of the silica substrates (Figures 3.1 and 3.2), striking correlations with the luminescence features are not observed. In Figure 4.13, the chromaticity diagram created by the Commission internationale de l'éclairage in 1931 (CIE1931), a powerful visualization tool, reports the coordinates of the room temperature RL of all the ZnO samples: the emitted lights of BC and MP samples are green–yellow, while the color outputs of the nanometric powders cover different regions of the spectrum (green for N05-SG-SS, bright blue for N05-SG-SR, violet for N05-HI, and orange for N22-HI), corroborating the influence of point defects on the luminescent properties.

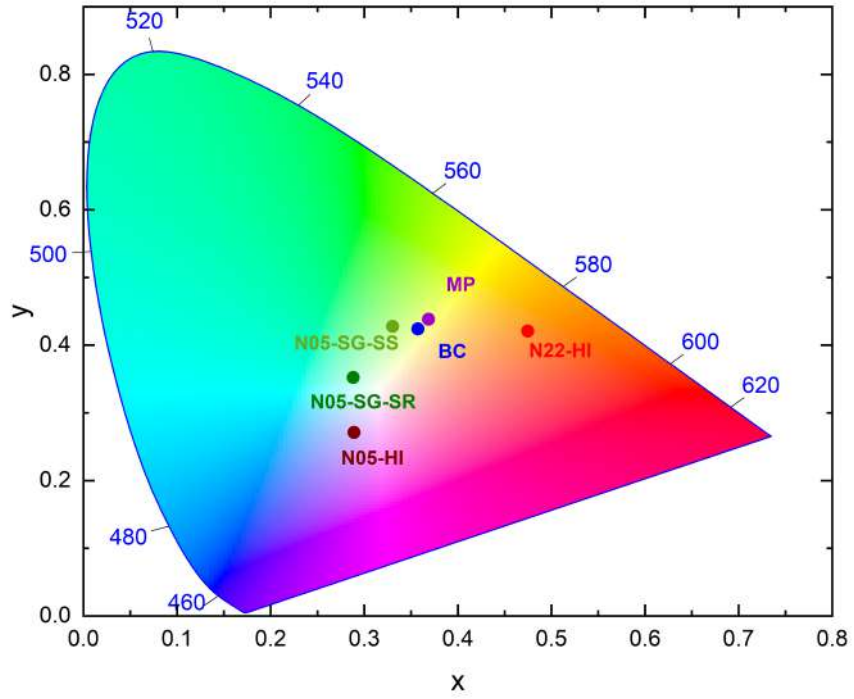

Figure 4.13: Color output of all ZnO samples: CIE1931 chromaticity diagram reporting the coordinates of room temperature RL emissions of N05-HI (dark red circle), N22-HI (red circle), N05-SG-SS (green circle), N05-SG-SR (dark green circle), MP (purple circle), and BC (blue circle).

4.3 Radio-catalytic properties

In this section, the radio-induced catalytic activities of the four nanometric ZnO samples are investigated: firstly, as a preliminary and yet critical analysis, the stability in air of all the nanosized ZnO particles upon continuous exposure to ionizing radiation is evaluated (Figure 4.14) and then their ability to radio-sensitize cytotoxic ROS and singlet oxygen is tested in PBS dispersions at atmosphere pressure, *i.e.* in water and oxygen rich environment, to mimic the cellular conditions (Figure 4.15).

Figure 4.14 displays the normalized RL intensity of the four ZnO nanosystems, recorded in air, as a function of time under and after continuative X-Ray irradiation up to a total accumulated dose of 3.3 Gy. Upon this prolonged exposure, the RL efficiency of all the samples slightly increases ("bright burn" effect, please refer to sub-Section 4.2.2): a similar enhancement of ∼7% is observed for both the bare N05-HI and N22-HI, whereas it differs for ZnO NPs grown onto silica substrates with spherical (SS) and rod-like (SR) morphology varying from ∼8% for N05-SG-SS to ∼2% for N05-SG-SR. More interestingly, these results unveil that ZnO luminescence does not decrease under continuous X-Ray irradiation in air, indicating that the nanosystems do not degrade and that their optical and chemical properties are stable throughout the whole irradiation time. These observations suggest that ZnO NPs are suitable for X-Ray mediated medical applications. After the irradiation shutdown, for the four ZnO NPs, no RL signal is detected, demonstrating the absence of delayed carrier recombination and subsequent long-time phosphorescence. These findings suggest that, in the RL mechanism of all the nanometric ZnO specimens, the role of trap states is rather small, consistently with previous observations (reported in sub-Section 4.2.1).

The evolution of ROS and $^1O_2$ concentration in PBS dispersions of the ZnO nanosystems both with and without simultaneous X-Ray irradiation, reported in Figure 4.15, is monitored *in situ*, exploiting CM-H_2DCFDA and SOSG, respectively (for details, please refer to sub-Section 3.1.4) as optical probes (Figures 4.16-4.19). Both these molecules include fluorescein moieties, whose luminescence is activated by oxidation from specific radical species, upon which they are selective. [156] CM-H_2DCFDA reacts with almost all ROS, but with peculiar detection sensitiveness: its highest reported fluorescence responses are towards hydroxyl radical and peroxynitrite anion; [132] at variance, SOSG is highly specific for $^1O_2$. [157] Consequently, in the absence of ROS and $^1O_2$, CM-H_2DCFDA and SOSG, respectively, disclose a weak emission, whereas, in the presence of ROS and $^1O_2$, the probes exhibit a green luminescence at ∼2.3 eV upon light excita-

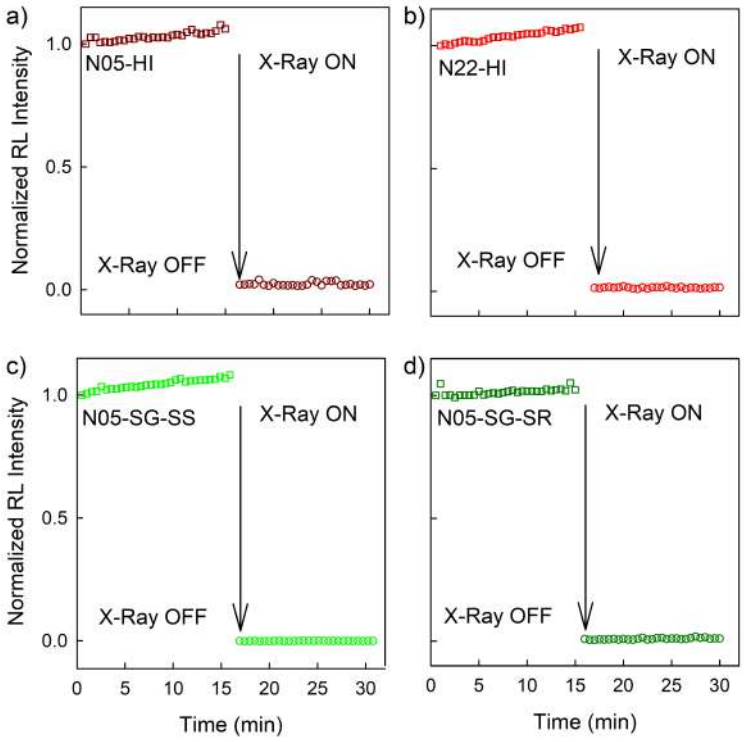

Figure 4.14: Normalized RL intensity of the isolated ZnO NPs (N05-HI, N22-HI) and of silica supported ZnO nanosystems (N05-SG-SS, N05-SG-SR) as a function of irradiation time. The RL emission of ZnO nanometric samples has been monitored in air under continuous X-Ray irradiation (open squares) and after the shutdown of the excitation source (open circles). At the used X-Ray tube working conditions (20 kV and 20 mA), the total accumulated dose is of 3.3 Gy.

tion at 2.6 eV, due to the fluorescein moieties optical triggering, whose intensity increases as the concentration of oxidized sensors molecules, and hence of peculiar radical species, increases. [158] However, it is worth noticing that optical probes suffer from self-oxidation induced by exposure to heat and light. [156, 157] Moreover, it has been reported that SOSG is activated in the presence of X-Ray beam due to the spontaneous ionization of air and water present in the environment upon interaction with the high energy radiation. [159] As a result, a quantitative or absolute determination of the ROS and $^1O_2$ radio-induced production could be not reliable. Thereafter, aiming at an accurate comparative analysis of the relative radio-catalytic activity of the ZnO NPs, the following guidelines are used to develop a consistent experimental procedure: i) the CM-H_2DCFDA or SOSG fluorescence is monitored on ZnO NPs dispersions and, for comparison, on solutions of the probe alone; ii) for each analysed sample, the percentage increment of ROS or $^1O_2$ concentration ($\%\Delta_X\ (t)$) is estimated as the difference between

the probe emission intensity at a given time (I_i) and at t_0 (I_0), normalized to I_0:

$$\%\Delta_X(t) = \frac{I_i - I_0}{I_0} \cdot 100 \tag{4.2}$$

iii) the ROS or $^1O_2$ relative increment of the four sets of ZnO NPs is corrected to their ZnO weight percent.

After 600 s, the enhancement of both ROS and $^1O_2$ concentration is about one/two order of magnitude higher in the ZnO dispersions under continuous X-Ray exposure with respect to those of the irradiated solutions of the probe alone and to those of the non-irradiated samples (Figure 4.15). These findings clearly point out the crucial effect of the presence of nanosized ZnO systems under X-Ray exposure on the sensitization of the cytotoxic species, validating the ZnO radio-catalytic properties. Moreover, the lowest sensitization efficiency both toward ROS and singlet oxygen is observed for N22-HI, the biggest examined nanostructures, corroborating the key role of interfaces in the catalysis phenomenon. Remarkably, scaling down the NPs diameters (from 22 to 5 nm), the increase of the surface-to-volume ratio matches the measured enhancement in the ROS ($^1O_2$) production: both are increased by about 4 times. Among the smallest NPs, similar generation yields of both the cytotoxic species are disclosed for the bare N05-HI and for the silica supported N05-SG-SR, whereas N05-SG-SS exhibits a different catalytic activity. These findings suggest that the radio-catalytic properties are more dependent on the sample final surface defectiveness than on its growth conditions. Indeed, as highlighted in sub-Section 4.2.3, despite the silica supported nanosystems are grown by the same synthesis route, the use of two substrates morphology, *i.e.* spherical (in N05-SG-SS) or rod-like (in N05-SG-SR), influenced the ZnO NPs surface features leading to the occurrence of inequivalent defect species: N05-SG-SR, at variance with N05-SG-SS and similarly to N05-HI, displays a higher concentration of quenching channels and exhibits a blue luminescence (band C), upon light excitation with energy lower than ZnO band gap. In particular, the detected ZnO NPs catalytic activities indicate that, despite the RL signal of the defect species (probably Zn_i and/or V_{Zn}) emitting in the blue region of the spectrum is weak or absent (Figure 4.1), the diffusion of the radio-generated free carriers is affected by their occurrence.

Moreover, the measured sensitization efficiency of N05-HI and N05-SG-SR is higher toward singlet oxygen with respect to that of N05-SG-SS, while the opposite effect is observed for ROS production. As introduced in Section 2.3, ROS are generated by one reduction or oxidation reaction at the nanomaterial surfaces,

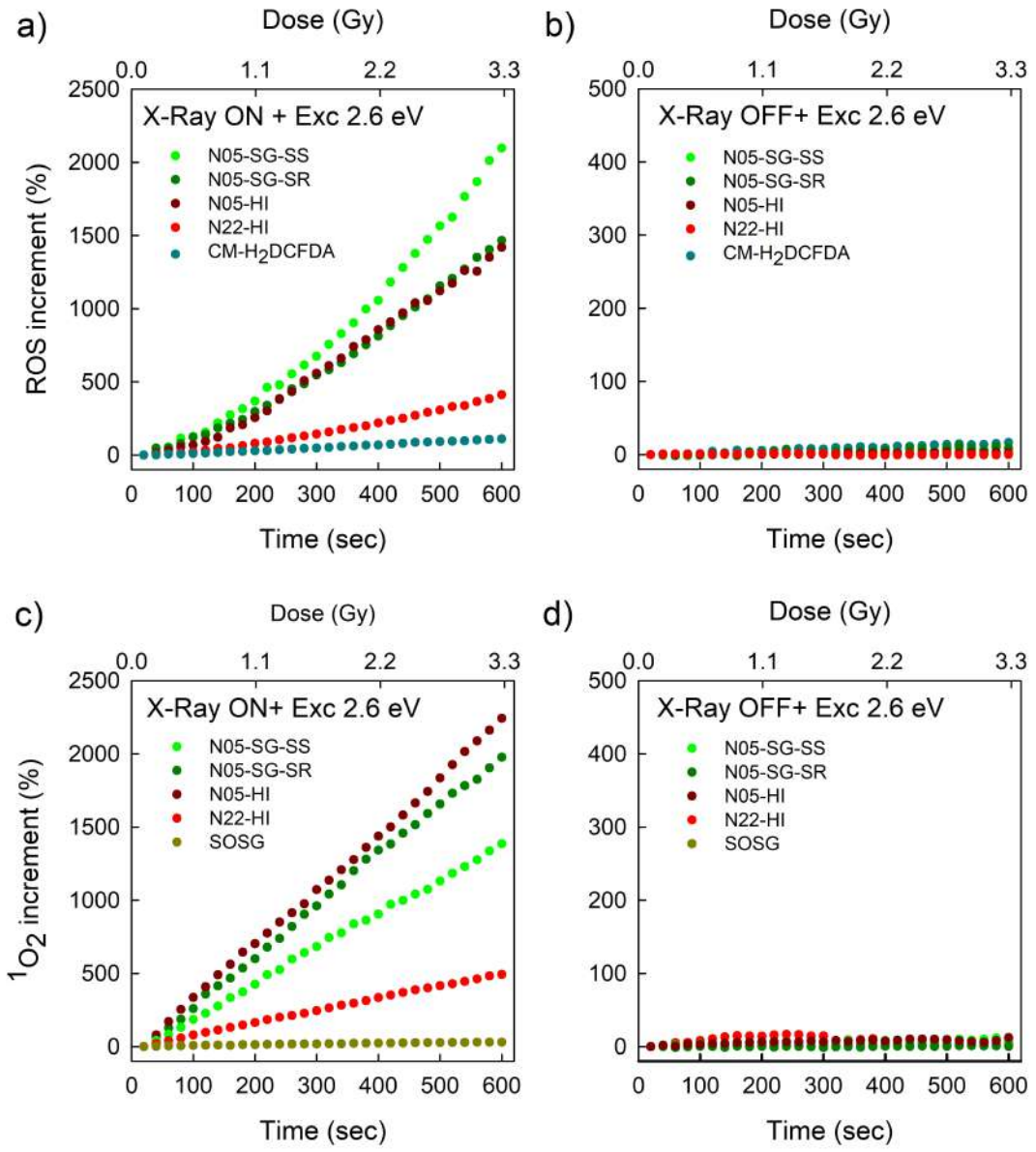

Figure 4.15: ROS (**a,b**) and singlet oxygen ($^1O_2$) (**c,d**) relative increment as a function of time both with (**a,c**) and without (**b,d**) concomitant X-Ray exposure for the probe alone (CM-H_2DCFDA and SOSG, respectively) and for the PBS dispersions of the four nanometric ZnO specimens, corrected to their ZnO weight percent. All the spectra are recorded in air, under laser excitation at 2.6 eV (to monitor the probe fluorescence). In (**a**) and (**c**), the X-Ray tube is operated at 20 kV and 20 mA and the total accumulated dose is of 3.3 Gy. From (**a-d**), the measurements performed on each sample are reported in Figures 4.16-4.19.

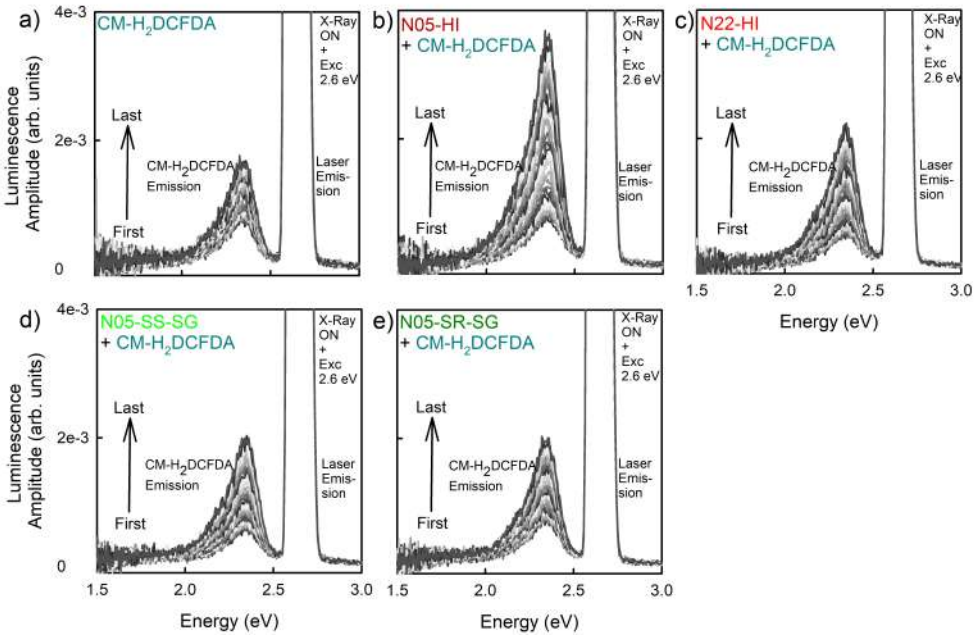

Figure 4.16: Spectra of CM-H_2DCFDA and of the four ZnO NPs in PBS dispersions recorded in air, under both X-Ray irradiation and laser excitation at 2.6 eV (to monitor the probe fluorescence). For each panel, the arrow shows the evolution of the probe signal. The relative ROS increment for each sample is reported in Figure 4.15a.

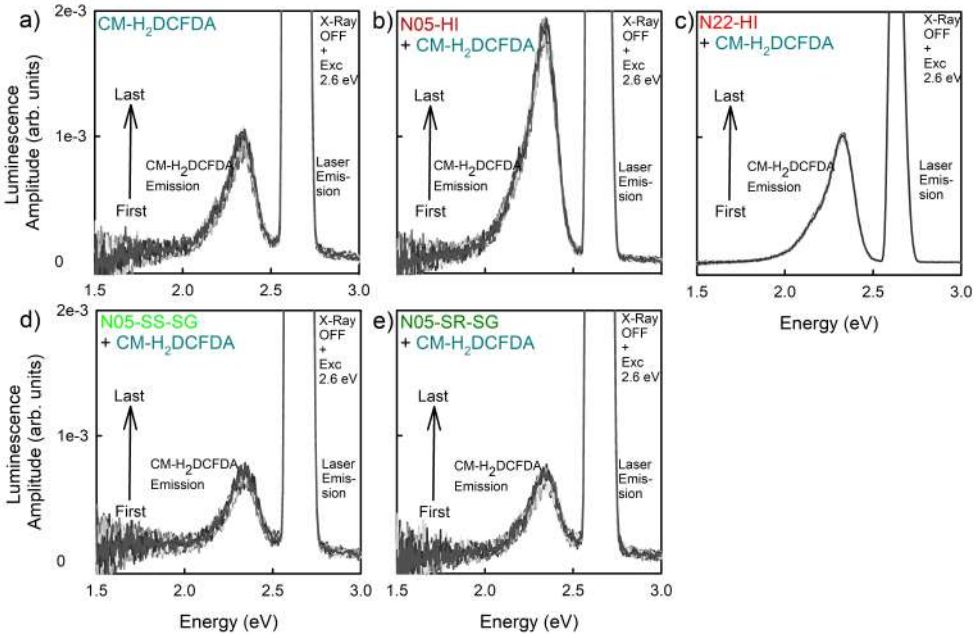

Figure 4.17: Spectra of CM-H_2DCFDA and of the four ZnO NPs in PBS dispersions recorded in air, without X-Ray irradiation and under laser excitation at 2.6 eV (to monitor the probe fluorescence). For each panel, the arrow shows the evolution of the probe signal. The relative ROS increment for each sample is reported in Figure 4.15b.

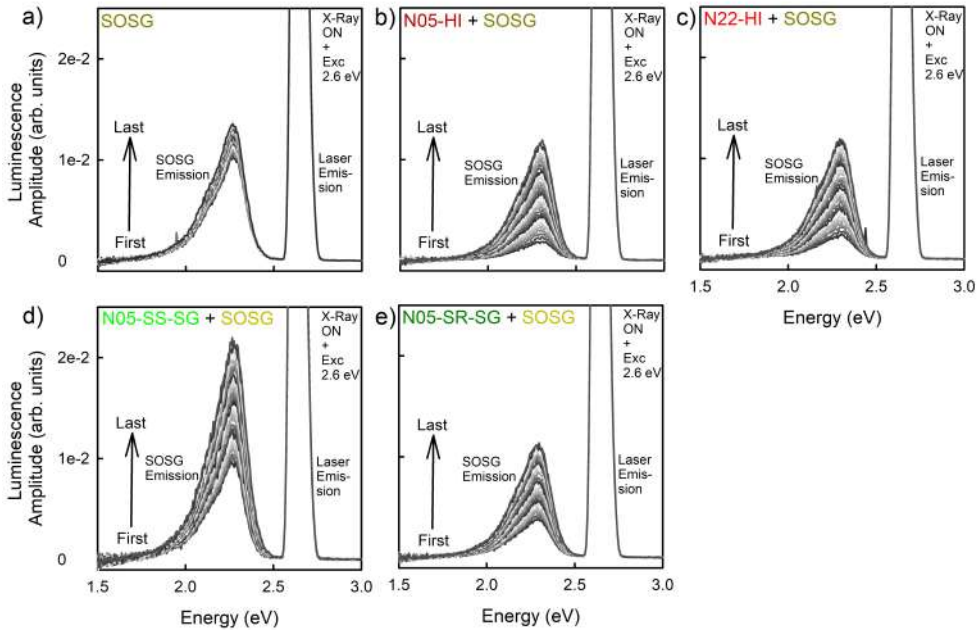

Figure 4.18: Spectra of SOSG and of the four ZnO NPs in PBS dispersions recorded in air, under both X-Ray irradiation and laser excitation at 2.6 eV (to monitor the probe fluorescence). For each panel, the arrow shows the evolution of the probe signal. The relative $^1O_2$ increment for each sample is reported in Figure 4.15c.

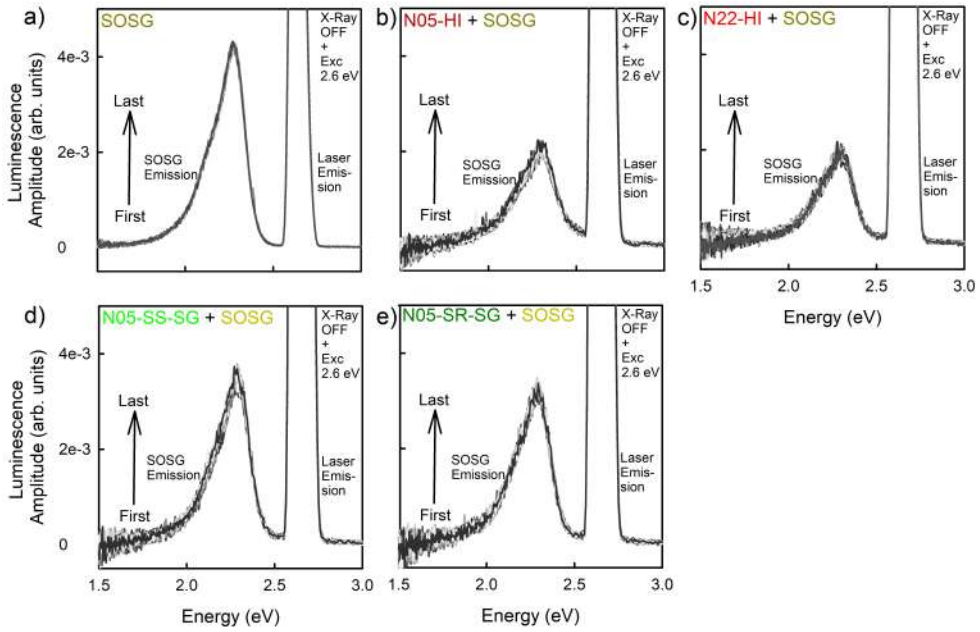

Figure 4.19: Spectra of SOSG and of the four ZnO NPs in PBS dispersions recorded in air, without X-Ray irradiation and under laser excitation at 2.6 eV (to monitor the probe fluorescence). For each panel, the arrow shows the evolution of the probe signal. The relative $^1O_2$ increment for each sample is reported in Figure 4.15d.

whereas $^1O_2$ production requires a two-step process in which oxygen molecules are converted by electron reduction into superoxide radical anions (step i) that are subsequently oxidized upon interaction with a hole in the valence band (step ii). Possibly, a low probability of excitation quenching on the nanosystems surfaces is beneficial for direct ROS production, but, on the other hand, it favors the radiative recombinations limiting the two-step $^1O_2$ generation. Hence, the control of ZnO surface defectiveness by changing the synthesis route as well as its nanometric size is pivotal for the improvement and the engineering of its catalytic activities for the degradation of specific adsorbants or the generation of targeted radical species.

Additionally, to deepen this analysis of the radio-catalytic properties of the four nanometric ZnO specimens and to improve its accuracy, the sensitiveness of SOSG and CM-H_2DCFDA toward singlet oxygen moieties is tentatively measured (Figure 4.20). To accomplish this goal, DABCO molecules dispersed in PBS solution are employed as singlet oxygen scavengers. Indeed, it is noticed that $^1O_2$ is deactivated rapidly and efficiently by DABCO, [160] probably by a charge transfer mechanism. [161] Firstly, the singlet oxygen generation yield under continuous X-Ray exposure of one nanometric ZnO NPs, N05-SG-SS, used as a test specimen, is evaluated using SOSG as optical probe, in the presence of DABCO solutions with different concentrations (0.01, 0.1, and 1 M), to verify its quenching effect (Figure 4.20a and 4.21b-d). Moreover, for sake of comparison, the evolution of the probe alone is monitored with and without 1 M DABCO solution (Figure 4.20a and 4.21a). Surprisingly, the $^1O_2$ radio-sensitization of the ZnO NPs at the lowest DABCO concentration is enhanced compared to that in its absence; whereas, as expected, it decreases progressively, until it is hardly detected, increasing the DABCO content, confirming the almost total SOSG specificity toward singlet oxygen molecules. Furthermore, in the literature, it has been reported that tertiary aliphatic amine moieties (present in DABCO molecular structure) decompose under irradiation with ionizing radiation and that the occurrence of this degradation in aqueous environment leads to the formation of radical amine and water derivates. [162, 163] This observation suggests that a fraction of DABCO molecules is indeed decomposed by the high energy radiation and, as a consequence, the additional generated radicals cause the $^1O_2$ production. Nevertheless, this effect is dominant only at the lowest DABCO content; differently, by increasing the DABCO amount in the solutions, the probability of degradation for a specific molecule decreases, allowing the depletion of the generated $^1O_2$ by the non-decomposed quenchers.

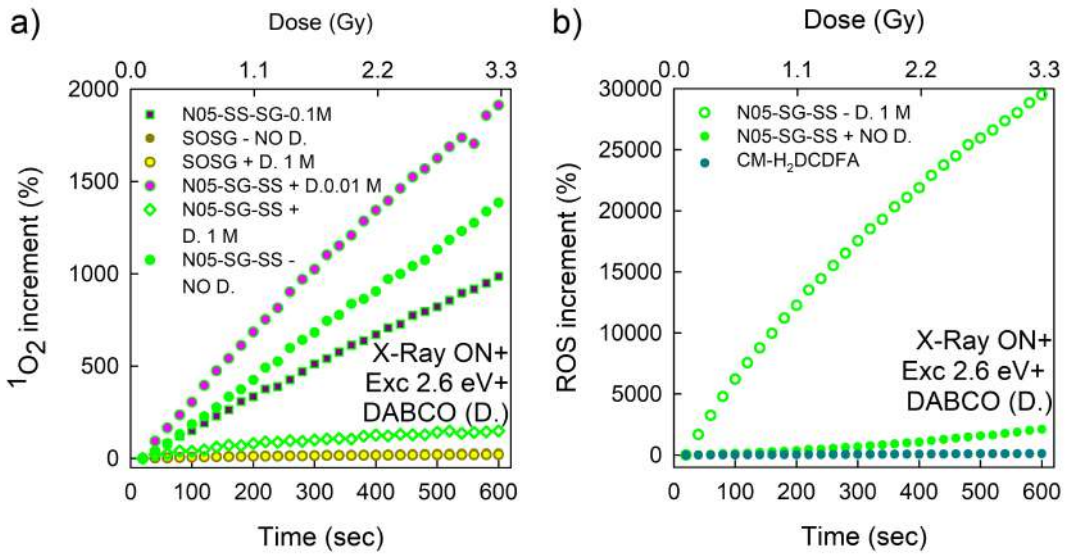

Figure 4.20: Singlet oxygen ($^1O_2$) (**a**) and ROS (**b**) relative increment as a function of time for the probe alone (CM-H_2DCFDA and SOSG, respectively) and for the PBS dispersions of one nanometric ZnO sample (N05-SG-SS) with or without DABCO solutions. All the spectra are recorded in air under both X-Ray exposure and laser excitation at 2.6 eV (to monitor the probe fluorescence). The X-Ray tube is operated at 20 kV and 20 mA and the total accumulated dose is of 3.3 Gy. The measurements performed on each sample in the presence of DABCO are reported in Figure 4.21.

Noticing that 1 M DABCO solution scavenged almost all the generated $^1O_2$ and assuming that the N05-SG-SS radio-catalytic activity is stable, this concentration is selected to test also the CM-H_2DCFDA sensitiveness toward singlet oxygen species (Figure 4.20b and 4.21e): the presence of DABCO increases of about one order of magnitude the measured $^1O_2$ concentration under continuative X-Ray exposure in air with respect to the radio-sensitization effect detected for the ZnO NPs without the quencher. In a previous study, the increase of $^1O_2$ concentration under light excitation in solution containg both $^1O_2$ quenchers and 2',7'-dichlorofluorescin (DCF) moieties has been already observed. [164] The results suggest that $^1O_2$ does not oxidize DCF derivates, but upon chemical reaction with its quenchers, it generates radical oxygen and water derivates, *i.e.* ROS, that in turn activate the DCF luminescence. Hence, this work indicates that DCF-based molecules are efficiently oxidized by ROS, but they are not directly sensitive to singlet oxygen moieties. Consequently, the ROS and $^1O_2$ relative increments (Figure 4.15a and c) can be attributed almost exclusively to free radicals and singlet oxygen, respectively. Further studies on the probes fluorescence response should be performed to evaluate whether ROS or $^1O_2$ are the major products of the radio-catalytic activity in ZnO NPs.

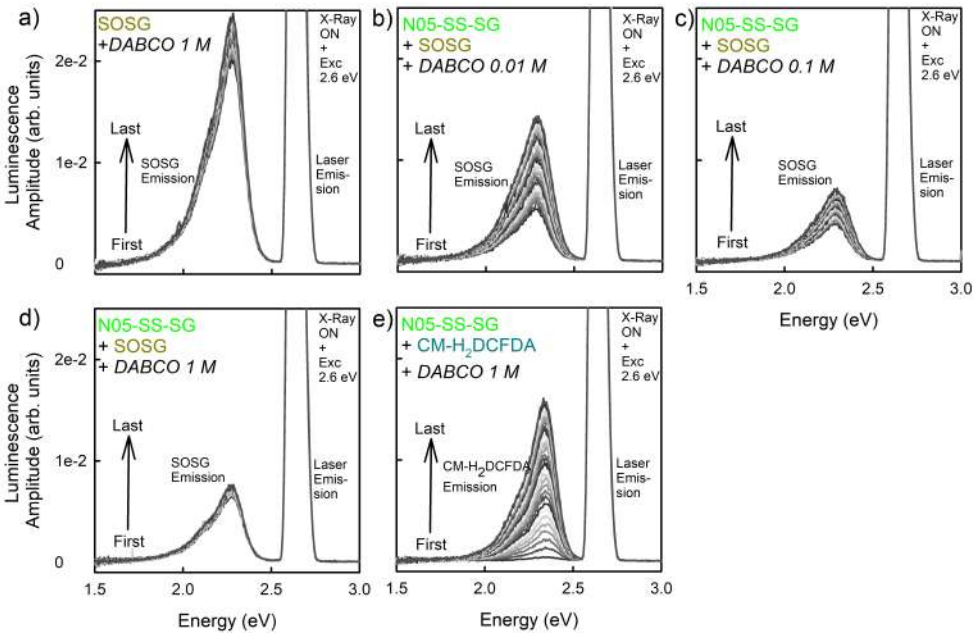

Figure 4.21: Spectra recorded in air, under both X-Ray irradiation and laser excitation at 2.6 eV (to monitor the probe fluorescence) of SOSG alone in 1 M DABCO solution (**a**), of N05-SG-SS in PBS dispersions in the presence of 0.01, 0.1 and 1 M DABCO solutions using SOSG as optical probe (**b,c,d**), and of N05-SG-SS in PBS dispersions in the presence of 1 M DABCO solutions using CM-H_2DCFDA as optical probe, (**e**). For each panel, the arrow shows the evolution of the probe signal and the relative $^1O_2$ or ROS increment is reported in Figure 4.20.

In conclusion, nanometric ZnO systems unveil excellent radio-catalytic properties strongly dependent on the sample surface-to-volume ratio and defectiveness. In particular, the stability and the efficiency of sensitization towards both free radicals and singlet oxygen of the four sets of ZnO NPs upon X-Ray exposure paves the way for their application as active ROS generators in radiotherapy.

4.4 Conclusions

This detailed investigation of ZnO optical and radio-catalytic properties highlights their dependences on nanostructure parameters (particle size, growth conditions, and interfaces). In particular, the main findings are:

- The luminescence spectra of various ZnO systems with different sizes (nanometric, micrometric, and bulk), obtained upon excitation with three photon energies (keV for ionizing radiation, UV and VIS for above and sub-band gap light), exhibit the presence of the same five spectral components: one UV excitonic band, accompanied by four defect-related ones in the visible region.

- The excitation with photons of different energies causes a peculiar activation of optical active centers, and hence impacts on the spectral shapes of its emission. Notably, in the nanometric samples, the excitonic luminescence is enhanced upon X-Ray exposure, whereas the green and blue bands related to defect emissions are promoted by excitation below ZnO band gap.

- ZnO defectiveness is strongly related to its surface properties. Thus, by scaling down the size, several optical and catalytic properties are affected, as disclosed by i) losses in the luminescence efficiency, ii) acceleration of the decay times, iii) a decrease in the intensity ratio between the exciton and defect emissions, iv) an increased sensitiveness of the optical properties to environmental conditions, v) a reduced dependence of the optical properties on the temperature, vi) an improvement of the catalytic performances.

- The growth conditions impact on ZnO morphology leading to the formation of different radiative defect centers and of quenching channels. Consequently, ZnO NPs disclose light outputs with colors spanning from the violet to the red region of the spectrum and catalytic activities with peculiar selectivity and efficiency.

In conclusion, the particle dimensionality and growth conditions strongly influence the NPs final point defects types and concentration that concur in defining the unique and versatile ZnO optical and catalytic properties. Hence, defect engineering strategies, based on the modulation of size, interfaces and synthesis procedures, could offer the opportunity to tune the luminescence and the surface reactivity of ZnO nanoparticles, boosting their applicability in both optics and nanomedicine.

Chapter 5

Porphyrin functionalized ZnO/SiO_2 nanosystems

In the last years, high atomic number and dense NPs able to efficiently interact with ionizing radiation have attracted great interest in the ongoing research of novel cancer treatments with limited side effects and optimized therapeutic outcomes (as mentioned in Section 1.3). In particular, X-PDT is an innovative oncological strategy to treat deep tumours that relies on the activation upon X-Ray exposure of an inorganic/organic nanostructure. Indeed, a key issue in the development of this treatment is the design of efficient and stable nanosystems that combine heavy nanoscintillators, able of down-converting the high energy radiation, with organic moieties, able to use that released energy to trigger the production of cytotoxic species (as presented in sub-Section 1.3.3). An optimized X-PDT agent requires to fulfil several chemical, optical, and biological requirements, that are related to its design, and consequently a definite synthesis strategy is still to be unveiled. In particular, the choice of suitable nanoscintillators and organic molecules and of the functionalization process significantly impacts the final properties of the multicomponent nanosystems and consequently the resultant therapeutic efficiency. In this frame, an accurate comprehension of the interaction mechanisms occurring between the nanoscintillators and the organic molecules upon X-Ray excitation, is pivotal for the rational development of X-PDT agents.

This chapter presents an accurate fundamental study on ZnO based multicomponent nanosystems for possible applications as X-PDT agents. Indeed, ZnO NPs are promising materials thanks to their biocompatibility, their high surface reactivity, and their scintillating properties. In this work, ZnO NPs grown onto either porous or non-porous spherical silica supports are coupled with different

amounts of porphyrin molecules using amino-silane moieties (APTES) as surface ligands. The inorganic/organic components, their relative concentrations and the functionalization process are chosen with the goal to optimize the performances of the final material and to fulfil the X-PDT requirements. Moreover, the synthesis of various multicomponent nanosystems allows both to carefully investigate the role of the organic molecules concentration and spatial distribution on the sample final optical properties, and to analyse the types of interaction mechanisms occurring under light excitation or exposure to X-Ray with various mean beam energies. Additionally, to further investigate the role of energy deposition in the resultant properties of the multicomponent nanosystems, two computational models (on non-porous ZnO/SiO_2 NPs) are developed aiming at discriminating the contribution of SiO_2 and ZnO and at estimating the effect of the X-Ray excitation energy.

First, the design and development of various ZnO/SiO_2 nanosystems functionalized with porphyrin molecules are described. Then, the optical properties measured under either light or ionizing radiation excitation of two selected sets of dye-coupled NPs are discussed in comparison to those of the NPs before the functionalization process and the porphyrin alone. Lastly, the evaluation of the profile of energy deposition in the non-porous ZnO/SiO_2 NPs by a computational analysis is presented.
As a guideline for the reading of this chapter, a schematic description of the herein analysed ZnO-based systems (for synthesis details please refer to sub-Section 3.2.1) is provided in Table 5.1.

Sample	Substrate porosity	ZnO weight percent (wt%)	APTES weight percent (wt%)	Porphyrin weight percent (wt%)	APTES: Porphyrin molar ratio
SS	Yes	-	-	-	-
SS_{np}	No	-	-	-	-
ZS	Yes	10	-	-	-
ZS_{np}	No	6.6	-	-	-
ZS-A	Yes	10	0.2	-	-
ZS-A5	Yes	10	1.0	-	-
ZS-A25	Yes	10	5.0	-	-
ZS_{np}-A	No	6.6	0.2	-	-
ZS-AP-0.1	Yes	10	0.2	0.3	1:0.1
ZS-AP-0.25	Yes	10	0.2	0.7	1:0.25
ZS-AP-0.5	Yes	10	0.2	1.4	1:0.5
ZS-AP-1	Yes	10	0.2	2.7	1:1
ZS-A5P-1	Yes	10	1.0	13.5	1:1
ZS-A25P-1	Yes	10	5.0	67.5	1:1
ZS_{np}-AP-0.1	No	6.6	0.2	0.3	1:0.1
ZS_{np}-AP-1	No	6.6	0.2	2.7	1:1

Table 5.1: Schematic diagram of the investigated samples.

5.1 Nano-agent concept

The design of efficient multicomponent nanosystems for X-PDT requires to accurately select the inorganic and organic moieties and to properly develop the synthesis procedure in order to optimize the final chemical and physical properties of the nano-agent. In particular, the inorganic NPs should be scintillators presenting a RL emission that matches the absorption of fluorescent dyes featuring a high singlet oxygen production yield. Aiming at investigating the use of nanometric ZnO as nanoscintillators for X-PDT, ZnO NPs grown onto highly porous spherical SiO_2 substrates (N05-SG-SS) are selected from the four set of nanosystems investigated in Chapter 4. In this chapter, N05-SG-SS is renamed as ZS to emphasize the following functionalization steps rather than the synthesis route and the substrate shape. Indeed, ZS discloses the highest RL efficiency among the ZnO NPs and its green emission overlaps with the absorption features of porphyrins (as disclosed by Figure 4.1 and 3.13) that are already under study as PSs in PDT due to their high singlet oxygen quantum yield. [70] Moreover, ZS size (the overall diameter is about ∼80 nm, as reported in sub-Section 3.2.3) is reasonable to consider biological applications. Among the porphyrin derivatives, TCPP molecules are chosen as PSs, because their -COOH groups allow to form stable covalent bonds with the amino groups of APTES used as surface ligands for ZS (Figure 3.7).

As a preliminary test of the conceptualized nano-agent design, the RL features of ZS samples, functionalized with various APTES content (ZS-A, ZS-A5, ZS-A25) at which subsequentially TCPP are covalently attached with 1:1 molar ratio (ZS-AP-1, ZS-A5P-1, ZS-A25-P), are investigated. For synthesis details, please refer to sub-Section 3.2.1. The amount of APTES is chosen to explore different loading conditions: by increasing the amino-silane ligands concentration, the APTES coating of the NPs surface ranges from approximately 0.2 to 5 wt% and the porphyrin weight percent varies within more than one order of magnitude (2.9-28.5 wt%). The normalized RL spectra of ZS samples before and after the APTES decoration disclose that the amino-silane moieties do not alter the ZnO luminescence, regardless of their concentration (Figure 5.1a). It is worth noticing that the emission of ZS (former N05-SG-SS) matches the one reported in Figure 4.1. Upon porphyrin functionalization, the ZnO green emission is suppressed in all the dye coupled NPs and the characteristic porphyrin emission at ∼1.7 eV is observed (Figure 5.1b), unveiling that the high Z nanoscintillators promote the PSs activation by radiative and/or non-radiative energy transfer rather than emitting themselves. As mentioned in sub-Section 1.3.3, a good optical interaction

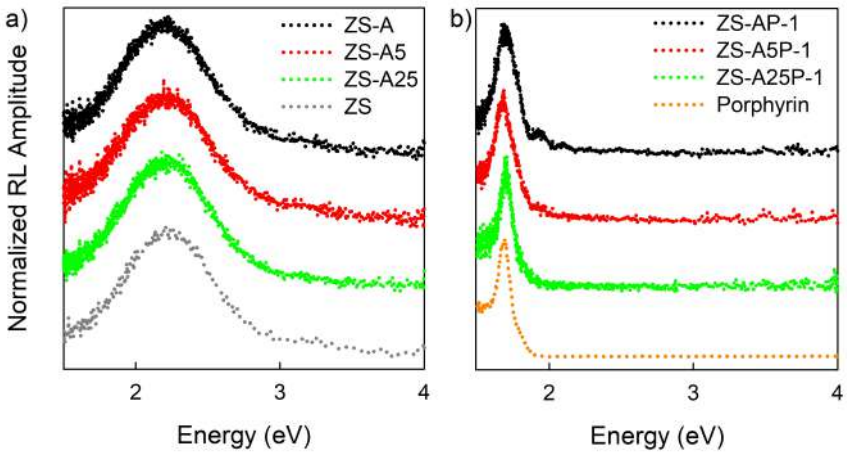

Figure 5.1: Normalized RL spectra of bare ZnO/SiO_2 nanosystems (ZS) and ZS decorated with different contents of amino-silane moieties (**a**) and subsequentially functionalized with porphyrin with molar ratio 1:1 (**b**). In (**b**), the normalized RL spectrum of porphyrin is reported for comparison.

between the nanoscintillators and the dyes under ionizing radiation is necessary for the X-PDT mechanism. Moreover, typically, porphyrin luminescence includes two peaks centred at about 1.9 eV (∼650 nm), due to the Q(0,0) transition from dye monomer, [46] and at 1.7 eV (∼725 nm), due to the Q(0,1) transition, known as J-bands, also associated with J-aggregates formation. [165] The 1.9 eV emission is barely detected in ZS-AP-1, almost negligible in ZS-A5P-1, and absent in both ZS-A25P-1 and porphyrin. Indeed, the occurrence of aggregation in dye molecule powders, on which the RL measurements are performed, is very likely. [80] Nevertheless, these findings reveal that the use of APTES as anchors to distribute small amounts of porphyrin on the nanoscintillators surfaces limits this phenomenon, that is detrimental for the final X-PDT efficiency.

The second preliminary analysis is the evaluation of the stability of dye-coupled ZS samples in biological environment, in order to assess their behaviour in cellular-like conditions. In fact, the porphyrin functionalization step is carried out in DMF, (please refer to sub-Section 3.2.1), but the use of a solvent with a higher polarity as water or PBS may influence the stability of the TCPP bonding to the SiO_2 surface and induce the TCPP release.

Thus, the dye coupled NPs are dispersed in PBS, to mimic the pH of cells, and their absorption spectra are measured before and after an optimized centrifugation process (please refer to sub-Section 3.2.2). Figure 5.2 discloses a drastic reduction of the dyes absorbance, and hence concentration (Equation 3.7), for all the specimens, unveiling that PBS can corrupt the TCPP anchoring to the

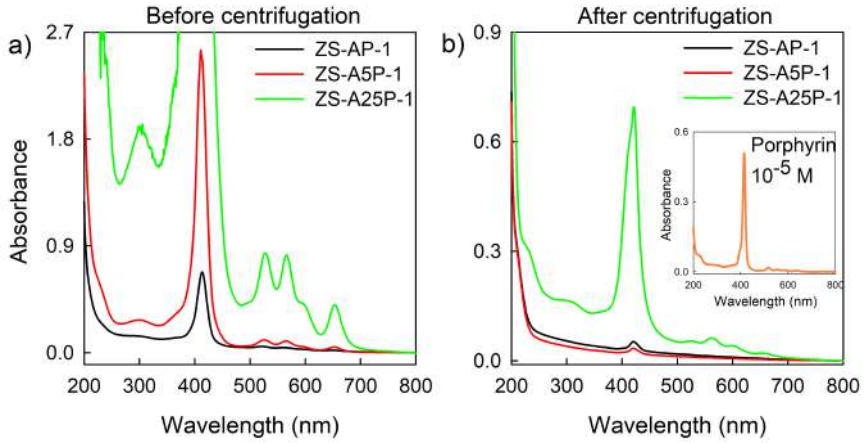

Figure 5.2: Absorbance spectra of porphyrin functionalized ZnO/SiO_2 nanosystems before (**a**) and after (**b**) centrifugation in PBS dispersions.

SiO_2 NPs, most likely the amidic bond between APTES and TCPP. Then, the multicomponent nanosystem with the medium degree of functionalization,*i.e.* ZS-A5P-1, is selected to verify the reproducibility of the centrifugation process and the overall stability of the as-prepared samples: seven different samples (A-G) from three different synthesis batches (Batch 1: A, B, C – Batch 2: D, E – Batch 3: F,G) are tested performing the centrifugation both on the individual sample (Process 1: A, Process 2: B, Process 3: C) and on multiple samples simultaneously (Process 4: D, E – Process 5: F, G). Figure 5.3 shows digital pictures of some of the centrifugated samples, whose colours disclose a great variability (from white to khaki), in comparison to that of the as-synthesized dark brown functionalized NPs, indicating the loss of different quantities of porphyrin throughout the specimens upon centrifugation.The absorption measurements report a different residual amount of porphyrin on each sample (Figure 5.4), which corroborate the assumption that the TCPP anchoring onto SiO_2 in PBS is likely unstable. Consequently, these findings disclose the need to pursue different synthesis protocols in order to improve the stability of the multicomponent nanosystems in the biological environment. For instance, several strategies could be used to stabilize the TCPP bonding to SiO_2 surface throught APTES moieties, as the modifications of the synthesis conditions (temperature and time) as well as of the functionality groups of the silane ligand responsible of the interaction with TCPP.

Despite the need to improve the porphyrin coupled ZnO/SiO_2 nanosystems stability in biological environment, their luminescence features highlight their potentiality as X-PDT agents, since the nanoscintillators efficiently interact with the organic molecules, regardless of their loading content. Moreover, the observed

Figure 5.3: Digital pictures of some samples from different batches of one porphyrin functionalized ZnO/SiO_2 nanosystem (ZS-A5P-1) after centrifugation in PBS dispersions, compared to the sample as synthesized.

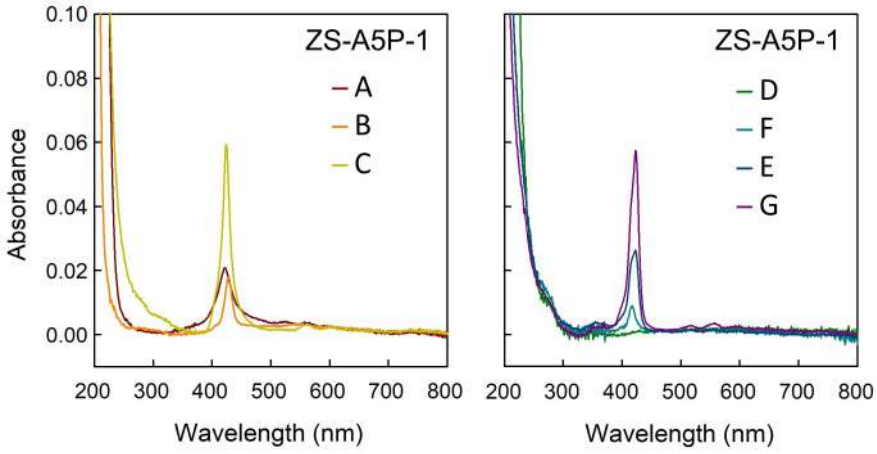

Figure 5.4: Absorbance spectra of seven different samples of one porphyrin functionalized ZnO/SiO_2 nanosystem (ZS-A5P-1) after centrifugation in PBS dispersions.

dependence of optical properties of the dye in the functionalized NPs on its concentration and arrangement is of particular interest for the comprehension of the impact of the nano-agent design on the X-PDT efficiency. Aiming at further investigate this issue and noticing that the most promising sample is ZS-AP-1 due to the lowest occurrence of dye aggregation, nanosystems with a similar content of APTES but a decreasing porphyrin concentration (ZS-AP-0.5, ZS-AP-0.25, ZS-AP-0.1) are realized. In the following, this set of dye coupled NPs is also labelled generically ZS-AP-Y. Furthermore, non-porous SiO_2 NPs of ∼75 nm diameter (SS_{np}) are used as a support for ZnO NPs (ZS_{np}) and then decorated with APTES (ZS_{np}-A) and functionalized with two different porphyrin loading levels (ZS_{np}-AP-1 and ZS_{np}-AP-0.1, also labelled ZS_{np}-AP-Y). The non-porous set of nanosystems is investigated with the goal of evaluating the role of the silica substrate porosity on the ZnO growth and luminescence as well as on the ATPES and TCPP distribution. For synthesis details, please refer to sub-Section 3.2.1; the specimens parameters are listed in Table 5.1. These sets of samples (*i.e.* ZS, ZS-A, ZS-AP-Y, ZS_{np}, ZS_{np}-A and ZS_{np}-AP-Y) are selected for an accurate PL and RL analysis in DMF solutions and as powders, respectively.

5.2 Photoluminescence

Under light excitation, the luminescence features of the single components (*i.e.* the TCPP porphyrin and the porous and non-porous ZnO/SiO_2 nanoscintillators alone and upon APTES decoration) as well as of the dye coupled samples are analysed to investigate the role of nano-agent design, such as substrate porosity and TCPP functionalization, on the final optical properties of the multicomponent nanosystems. The steady-state and time-resolved PL techniques permit to study the occurrence of radiative and/or non-radiative energy transfer (ET) between the inorganic and organic moieties of the TCPP functionalized NPs.

5.2.1 Steady-state excitation-emission luminescence

In this sub-Section, the PL and PLE features of the investigated samples are presented and discussed in relation to their morphology and composition.

PL/PLE properties of the porphyrin

Figure 5.5a displays the optical properties of TCPP, that are in agreement with the literature. [138, 166] The PL of TCPP exhibits both the monomer and J-

aggregates related peaks, at ∼1.9 eV and at ∼1.7 eV, respectively; [46, 165] the PLE features mirror those of the absorption spectrum (Figure 3.13). Notably, at energies above the Soret band, the dye PLE intensity is not null (Inset in Figure 5.5a): in the literature, this effect is attributed to the occurrence of small aggregates, especially dimers and trimers, that alter the dye absorption in the UV region of the spectrum. [82, 84]

The impact of substrate porosity and APTES decoration on PL/PLE properties of ZnO/SiO_2 NPs

Figure 5.5b and 5.5c show the luminescence features of the porous ZS and ZS-A and of their non-porous counterparts, respectively. The PL spectra of ZS (former N05-SG-SS), consistent with that displayed in Figure 4.1, and of ZS_{np} disclose a similar broad emission centred at ∼2.2 eV with a corresponding PLE ranging from 3.5 to 5 eV. However, the high energy PLE band (peaked at ∼4.6 eV) is dominant only in the bare porous nanosystems, hinting a minor modification in the sample absorption mechanism varying the substrate porosity. Moreover, the weak PL signal at ∼1.5 eV detected for the non-porous SiO_2 NPs (Figure 5.5d) indicates that solely ZnO is the optically active material in the ZS_{np}, similarly to the porous specimens case (Figure 4.4). Hence, in agreement with the previous investigation on the optical properties of ZS, former N05-SG-SS, (Section 4.1), for both the porous and non-porous ZnO/SiO_2 nanoscintillators, the green emission from 1.7 to 3 eV is attributable to the same defect species in ZnO. Moreover, the excitation luminescence peaked at ∼3.8 eV is related to ZnO absorption above the band gap, whereas the PLE band above 4 eV is associated to SiO_2 absorption. [167, 168] In the porous samples, ZnO NPs are distributed both inside and outside the support, thus the surface portion of SiO_2 support left exposed is expected to be higher than in the non-porous nanosystems where the ZnO NPs cover almost completely the external silica surfaces.

For both the porous and non-porous nanosystems, no differences are observed in their optical properties upon APTES coating, suggesting that the anchors are not emissive and they do not alter ZnO luminescence.

These findings highlight that, regardless of the substrate porosity and the APTES decoration, the ZnO emission is resonant with the TCPP Q-bands, indicating that the nanoscintillators functionalization with the dye might permit both non-radiative ET and radiative ET, *i.e.* porphyrin re-absorption of ZnO emitted photons. [130]

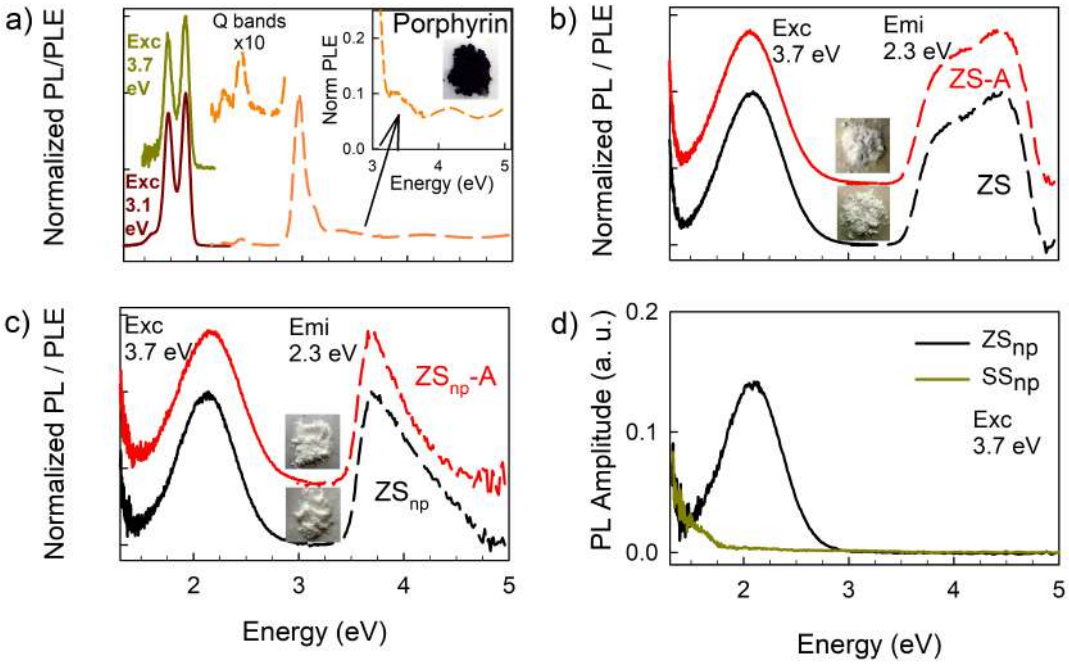

Figure 5.5: **a,b,c**) Normalized steady-state PL (solid lines) and PLE (dashed lines) recorded under CW excitation of the porphyrin (**a**), the porous (**b**) and non-porous (**c**) ZnO/SiO_2 nanosystems alone (ZS, ZS_{np}) and upon APTES decoration (ZS-A, ZS_{np}-A), dispersed in DMF solution. In panel (**a**), enlargements of TCPP PLE between 2.2 and 2.8 eV (Q-bands) and between 3.0 and 5.0 eV are also shown. Insets are digital pictures of the samples as synthesized. **d**) PL spectra of the non-porous silica NPs alone (SS_{np}) and upon the growth of ZnO NPs (ZS_{np}), for comparison.

The impact of porphyrin functionalization on the PL/PLE properties of dye coupled NPs

Figure 5.6 reports the optical properties of ZS-AP-Y and ZS_{np}-AP-Y, disclosing that both PL and PLE spectra present similar features but with different intensity ratios between the porphyrin and ZnO bands for the porous and non-porous NPs. The ZnO emission at 2.3 eV of ZS-AP-Y and ZS_{np}-AP-Y displays the PLE spectrum similar to the one of ZS and ZS_{np}, respectively, related to the ZnO absorption. Additionally, the PLE spectra monitored at 1.9 eV exhibit the typical TCPP Soret band at ∼3 eV and ZnO PLE features at higher energies. By exciting at 3.7 eV (in the absorption region of ZnO), PL spectra of ZS-AP-Y and ZS_{np}-AP-Y present both the ZnO broad band and the TCPP red emission, whose relative intensities decrease as the porphyrin content increases. These findings suggest that, in the functionalized NPs, TCPP emission may be activated by two

concomitant mechanisms: i) the direct excitation of TCPP, able to absorb even photons with energy higher than 3 eV, as Figure 5.5a reveals, and ii) non-radiative and/or radiative ET from the excited ZnO to TCPP.

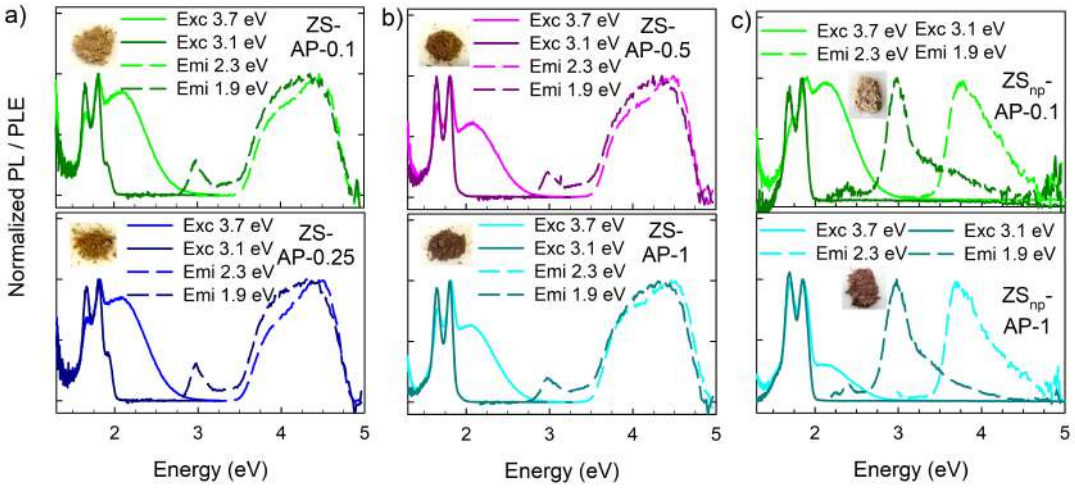

Figure 5.6: **a,b,c**) Normalized steady-state PL (solid lines) and PLE (dashed lines) recorded under CW excitation of the (**a,b**) porous and (**c**) non-porous functionalized nanosystems (ZS-AP-Y, ZS_{np}-AP-Y) dispersed in DMF solution. Insets are digital pictures of the as synthesized samples.

Moreover, PLE spectra of the two non-porous samples disclose that the porphyrin bands are dominant with respect to the ZnO ones while, differently, the opposite relative intensity ratio is observed for the porous sets of NPs. Hence, in ZS_{np}-AP-Y the dye is mainly excited in its Soret band, whereas in ZS-AP-Y the ZnO absorption above band gap prevails. These findings validate the occurrence of a double mechanism in the porphyrin emission triggering and also suggest that such activation may be influenced by the excitation processes of the inorganic NPs, that differs for ZS and ZS_{np}, as discussed above.
By exciting both ZS-AP-Y and ZS_{np}-AP-Y in the TCPP Soret band (at 3.1 eV), only the dye PL, featuring the the emissions at ∼1.7 eV and ∼1.9 eV, is observed. In addition to the characteristic TCPP PL features, a peak centred at ∼2.0 eV is detected in the porous samples with the lowest dye loading (ZS-AP-0.1 and ZS-AP-0.25). This band can be associated to the presence of Zn-TCPP complexes, [169, 170] whose formation can be explained as the release of zinc ions from the highly reactive surface of ZnO NPs and their subsequent coordination with the porphyrin central ring. [166] This additional PL peak is likely present in all samples, but its luminescence is not distinguishable from the typical porphyrin

emissions as their relative intensity decreases.

5.2.2 Time resolved luminescence

In this sub-Section, TRPL and TRES results are reported aiming to investigate the optical interaction mechanism between the inorganic NPs and TCPP, and its dependence on the porphyrin content and spatial arrangement.

The impact of substrate porosity and porphyrin functionalization on the time decay dynamic of ZnO light emission

TRPL measurements performed on the ZnO luminescence of both the porous and non-porous sets of ZnO/SiO_2 nanosystems disclose, among the samples, similar time decay dynamics in the microseconds range, except for a slight acceleration observed in ZS_{np}-AP-1 (Figure 5.7). For all the specimens, the decays of the ZnO emissions are fitted using a three-exponential function with time components ranging from tens of nanoseconds up to few microseconds (Tables 5.2 and Tables 5.3); only for ZS_{np}-AP-1, both the time and relative weight parameters of the slowest component result slightly smaller. It is worth noticing that, since this TRPL analysis is carried out on DMF dispersion, the ZS (former N05-SG-SS) time dynamic (Figure 5.7a, Table 5.3) is a little faster than that observed studying the TRPL on powders (Figure 4.12, Table 4.5), in which the presence of agglomerates can lengthen the emission process. Hence, the ZnO time decay is not affected by the substrate porosity, hinting that the growth of ZnO NPs, either inside and outside the silica matrix, leads to the formation of similar defect centres.

Additionally, ZnO time decay dynamic does not vary significantly upon nanoscintillators functionalization with the dye, indicating that a non-radiate ET between the inorganic and organic components is absent in almost all the TCPP coupled NPs, or very poor in ZS_{np}-AP-1. It is worth recalling that the probability of non-radiative ET depends upon various parameters, such as the extent of the overlap between the emission spectrum of the donor and the absorption spectrum of the acceptor, the quantum yield of the donor, the distance and the relative orientation of the donor and acceptor moieties. [130] Probably, in the herein studied nanosystems, the triggering of non-radiative ET is hindered by the low luminescence efficiency of ZnO NPs (as discussed in sub-Section 4.2.2) and also by the use of ATPES molecules as anchors, that can affect both the distance and the relative orientation between ZnO NPs and the dyes. Since the

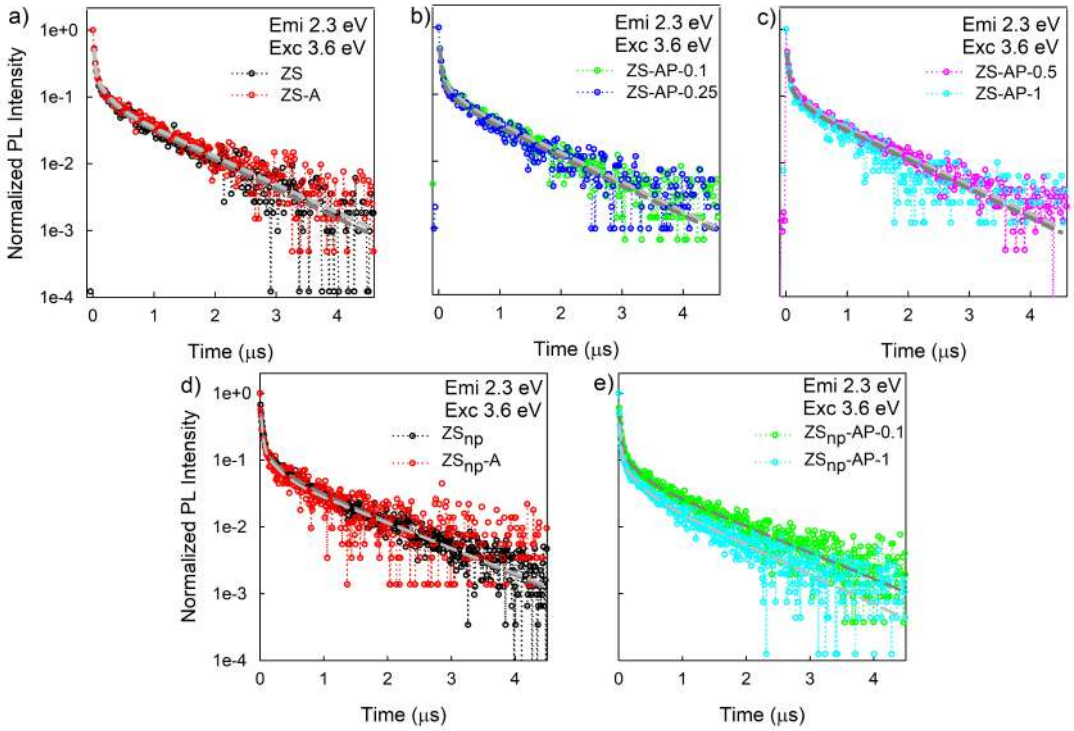

Figure 5.7: TRPL of ZnO emission recorded at 2.3 eV emission under pulsed excitation at 3.6 eV for all the samples. The time decays are fitted as multiexponential functions (dashed lines). The complete sets of parameters used to model the PL decay are reported in Table 5.2 and 5.3.

distribution of APTES may change from the porous and non-porous NPs, also a different spatial distribution of TCPP with respect of ZnO is expected in the two sets of nanosystems. The obtained findings (Figure 5.7) suggest that the surface of non-porous samples presents advantageous functionalization conditions that partially allow the non-radiative ET between donors and acceptors in ZS_{np}-AP-1, in which dye concentration is the highest.

The impact of porphyrin functionalization on the time decay dynamic of its light emission

In all samples, the time decays of TCPP luminescence (Figure 5.8, Table 5.4) feature the porphyrin characteristic decay time component of about 11 ns, in agreement with the literature. [170, 171] Furthermore, in both the porous and non-porous dye coupled nanosystems, an additional fast component of about 2.4 ns with a major relative weight, that increases coherently with the TCCP loading, is detected. The origin of this fast component may be due to Zn-TCPP complexes, whose emission band detected at 2.0 eV (Figure 5.6) displays a time decay of about

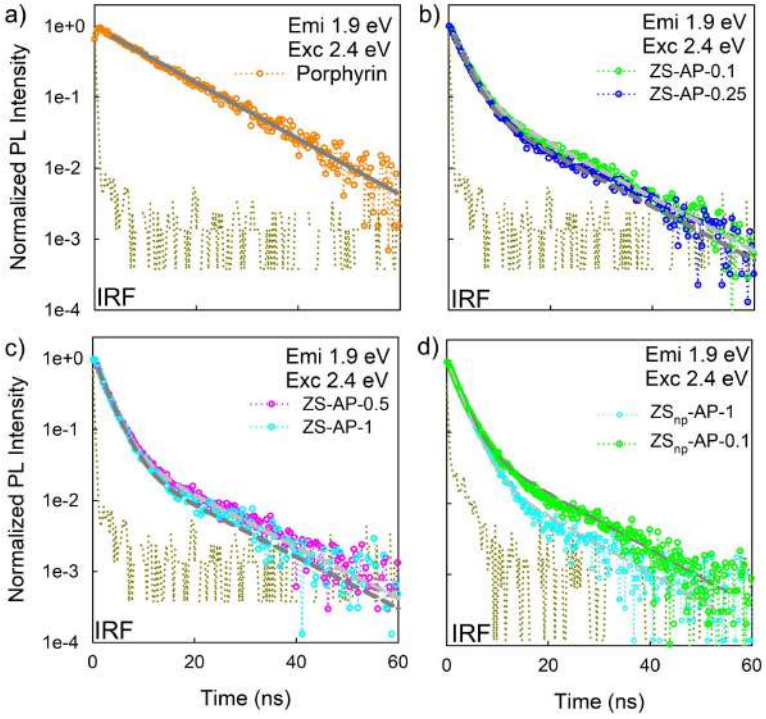

Figure 5.8: TRPL of the porphyrin emission recorded at 1.9 eV under pulsed excitation at 2.4 eV for the TCPP alone and all the dye coupled samples. The time decays are fitted as multiexponential functions (dashed lines). The instrument response function (IRF) is also shown (mustard dotted line). The complete sets of parameters used to fit the PL decay are reported in Table 5.4.

2 ns as reported in the literature. [170, 172] Alternatively, it could be attributed to aggregates species: usually, J-aggregates accelerate the typical porphyrin time dynamic, [83] whereas H-aggregates exhibit a bi-exponential decay trend with both very fast (about 2 ns) and longer (about 10 ns) decay time components. [82] Thus, even if a unique attribution of the observed fast component remains uncertain, its presence clearly reveals the occurrence of dye complexes and/or aggregates, [25, 82, 84] that reduce the TCPP luminescence efficiency and hence its performances as PS. Moreover, the relative weight of the fast component, and consequently the fraction of generated porphyrin complexes and/or aggregates, is similar in the porous and non-porous samples, corroborating that in both sets of NPs the TCPP molecules are present only on the external SiO_2 surfaces.

The impact of porphyrin functionalization on the TRES of dye coupled NPs

Noticing that the TRPL analysis evidences the very different order of magnitude of ZnO and dye luminescence lifetimes, TRES is performed recording the PL

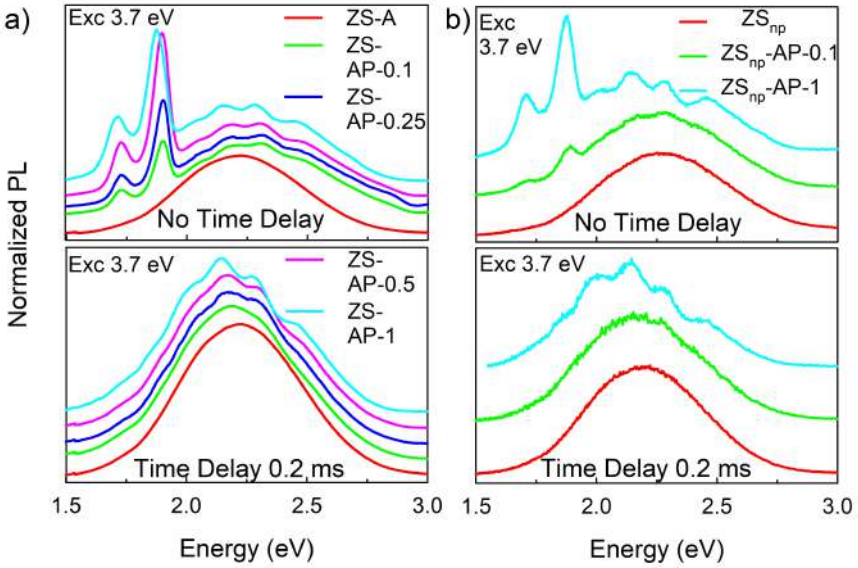

Figure 5.9: Normalized PL spectra of ZS-A and ZS-AP-Y (**a**) and of ZS_{np}-A and ZS_{np}-AP-Y (**b**) dispersed in DMF solution and recorded simultaneously (top) and with 0.2 ms delay (bottom) with respect to the 3.7 eV excitation pulse.

spectra of ZS-A and ZS-AP-Y as well as those of ZS_{np}-A and ZS_{np}-AP-Y with 0 ms (no delay) and 0.2 ms time delay with respect to the 3.7 eV excitation pulse (Figure 5.9), to discriminate the emissions occurring in the nano- and in the milli-seconds time ranges. For all ZS-AP-Y and ZS_{np}-AP-Y samples, the ZnO luminescence displays dips, whose magnitude scales with the loading level, at energies (∼2 eV, ∼2.2 eV, ∼2.4 eV) matching the dye Q-bands. This results unveils the occurrence of radiative ET between the inorganic NPs and the organic molecules. A slight red shift of both porphyrin bands and dips in ZnO emission is observed in the two samples with the highest TCPP content, possibly caused by the presence of a minor fraction of J-aggregates. [80] At variance with the PL spectra displayed in Figure 5.9, those of Figure 5.6 do not show dips in the ZnO luminescence, because in this case a sample holder with a shorter thickness (0.1 cm, with respect to 1 cm of the TRES measurement) and therefore a shorter light path is used, reducing the probability of re-absorption. The dye emission intensity is strong when the signal is collected without delay (Figure 5.9 top panels), whereas it is very weak by introducing a 0.2 ms delay (Figure 5.9 bottom panels). To verify the presence of the porphyrin bands in the PL spectra recorded with 0.2 ms time delay after the lamp shutdown, first derivatives of ZS-AP-Y and ZS_{np}-AP-Y signals are also computed and compared to those of ZS-A, ZS_{np}-A, respectively, and of TCPP (Figure 5.10): a relative minimum at 1.75

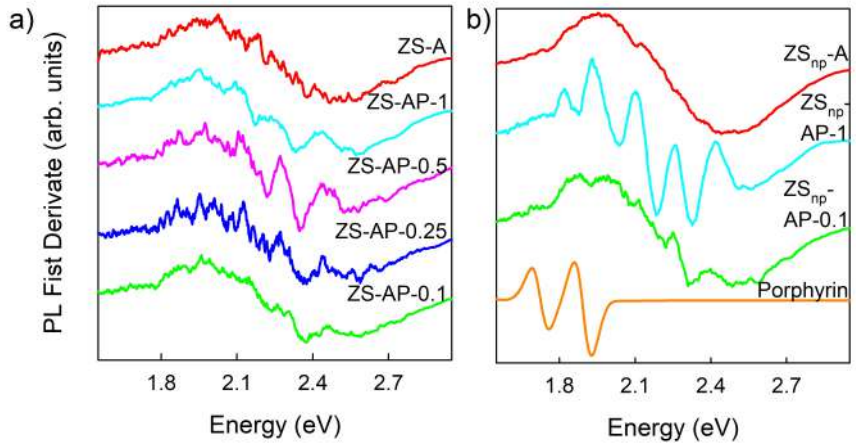

Figure 5.10: First derivatives of normalized PL spectra of ZS-A and ZS-AP-Y (**a**) and ZS_{np}-A and ZS_{np}-AP-Y (**b**) recorded with 0.2 ms delay with respect to the 3.7 eV excitation pulse (reported in Figure 5.9 bottom panels) compared to TCPP.

eV, which is clearly distinguishable in the dye alone, is also present in the dye functionalized samples, validating the occurrence of a poor TCPP luminescence. These findings indicate, that in both the porous and non-porous dye coupled nanosystems, during the excitation at 3.7 eV, the nanoscintillators as well as TCPP molecules are directly and continuously excited by the UV light (Figure 5.9 top panels). Differently, when the excitation source is off and the PL signal is collected after 0.2 ms, the porphyrin luminescence is generated solely by the absorption of photons emitted by ZnO, being the dye decay time much shorter (in the ns range) than the used experimental time delay. The evidence that porphyrin emission intensity is weak in the spectra recorded with 0.2 ms time delay (Figure 5.9 bottom panels) reveals that the efficiency of radiative ET is rather poor.

	ZS	ZS-A	ZS-AP-0.1	ZS-AP-0.25	ZS-AP-0.5	ZS-AP-1
τ_1 (ns)	26±1	23±1	25±1	27±1	27±1	27±2
$Weight_1$ (%)	15	12	12	14	13	14
τ_2 (ns)	190±20	180±20	180±20	200±40	200±30	180±40
$Weight_2$ (%)	16	19	14	13	12	13
τ_3 (ns)	1000±40	1030±40	1000±30	990±50	1020±40	1000±50
$Weight_3$ (%)	69	69	74	73	75	73

Table 5.2: TRPL fit parameters of the ZnO emission recorded at 2.3 eV under pulsed excitation at 3.6 eV for the set of porous ZnO/SiO_2 nanosystems.

	ZS_{np}	ZS_{np}-A	ZS_{np}-AP-0.1	ZS_{np}-AP-1
τ_1 (ns)	28±1	25±1	28±1	24±1
$Weight_1$ (%)	16	14	16	19
τ_2 (ns)	220±20	200±50	220±20	230±20
$Weight_2$ (%)	16	18	18	20
τ_3 (ns)	1080±30	1100±100	1100±40	980±40
$Weight_3$ (%)	68	68	66	61

Table 5.3: TRPL fit parameters of the ZnO emission recorded at 2.3 eV under pulsed excitation at 3.6 eV for the set of non-porous ZnO/SiO_2 nanosystems.

	TCPP	ZS-AP-0.1	ZS-AP-0.25	ZS-AP-0.5	ZS-AP-1	ZS_{np}-AP-0.1	ZS_{np}-AP-1
τ_1 (ns)	-	2.4±0.1	2.5±0.1	2.4±0.1	2.4±0.1	2.3±0.1	2.3±0.1
$Weight_1$ (%)	-	63	70	77	82	71	85
τ_2 (ns)	11±0.1	11.5±0.2	11.5±0.2	12±0.4	12±0.7	11.0±0.4	11.0±0.6
$Weight_2$ (%)	100	37	30	23	18	29	15

Table 5.4: TRPL fit parameters of the porphyrin emission recorded at 1.9 eV under pulsed excitation at 2.4 eV for the TCPP alone and all the dye coupled samples.

5.2.3 Conclusions on photoluminescence

The careful investigation of the steady-state and time resolved photoluminescence properties of the porphyrin alone and of the sets of porous and non-porous NPs reveals the correlations between the nano-agent design and the resultant optical properties of the multicomponent nanosystems. In particular, the main findings are:

- A similar defectiveness occurs in ZnO NPs grown inside and/or outside the silica matrix.
- APTES functionalization does not modify ZnO optical properties.
- Porphyrin aggregates and/or complexes, whose concentration increases coherently with the dye loading level, are present on the inorganic NPs surfaces.
- Under light excitation, the functionalization of the nanoscintillators with the dye enables an optical interaction between the inorganic NPs and the porphyrin mainly by radiative processes, in which ZnO emitted photons are re-absorbed by TCPP molecules.

5.3 Radioluminescence

The optical properties of the porous and non-porous ZnO/SiO_2 NPs together with those of the porphyrin alone are investigated under X-Ray excitation to further analyse their dependence on substrate porosity and of dye functionalization, and to study the interaction mechanisms triggered by the high energy radiation. In fact, upon ionizing radiation exposure, in addition to radiative ET, which is related to optical processes, the deposit of X-Ray energy in the sample surroundings influences the porphyrin sensitization. To further address these topics, in this section, also a mechanical mix (ZS-A+P-0.5), realized by stirring APTES decorated porous nanoscintillators and porphyrins with 1.4 wt% loading, is analysed, aiming at comparing the RL properties of two samples (*i.e.* ZS-AP-0.5 and ZS-A+P-0.5) in which the dye concentration is the same, but its spatial distribution with respect to NPs differs. Indeed, in ZS-AP-0.5, the APTES-TCPP covalent bond on the SiO_2 external surfaces ensures nanometric inter-distances between the inorganic NPs and the dye; on the other hand, in ZS-A+P-0.5, this distance may arbitrarily vary from nano- to micrometres, due to the random distribution of TCPPs in the nanosystems surroundings.

First, the effect of the nano-agent design on the optical features of all the samples is investigated by comparing their RL spectra through an accurate numerical analysis of spectral components. Then, the correlations between the RL intensities of the samples and the morphological parameters as well as the energy of the ionizing radiation are discussed. Lastly, a computational model is developed to estimate the spatial distribution of energy deposition in the non-porous ZnO/SiO_2 nanoscintillators and the outcomes of these simulations are used to improve the interpretation of the experimental results.

5.3.1 Gaussian fit of radioluminescence spectra

In this sub-Section, the RL features of all samples, recorded on powders under irradiation with X-Ray photons with mean beam energy of 6.6 keV, are analysed in relation to their morphology and composition.

The RL spectra of all the herein studied NPs and of the dye alone are reconstructed by a Gaussian deconvolution procedure, whose results are reported in Figures 5.11 and 5.12 and Tables 5.5, 5.6, and 5.7, respectively. As guidelines for the numerical analyses, the following criteria are used: i) to exploit the minor number of bands necessary to obtain a satisfactory spectrum reproduction and ii) to use as starting parameters for ZnO emission those already employed for ZS (former N05-SG-SS) - please refer to sub-Section 4.1.2 - and for the TCPP luminescence those reported in the literature.

The impact of substrate porosity and APTES decoration on the RL spectral components

Both the porous and non-porous nanoscintillators with and without APTES decoration exhibit a ZnO defect related band (centred at ∼2.22 eV with FHWM of ∼0.78 eV) and a ZnO excitonic one (centred at ∼3.15 eV with FHWM of ∼0.57 eV), as displayed in Figures 5.11a-d and Table 5.5. These findings corroborate the fact that both the substrate porosity and the decoration with APTES do not modify the ZnO optical properties. In addition, the RL spectrum of the non-porous silica NPs is recorded: in Figure 5.13 a weak RL signal at about 4 eV is exhibited, that is negligible compared to that of ZS_{np}, confirming that the luminescence of the ZnO/SiO_2 nanosystems is only related to ZnO emissions.

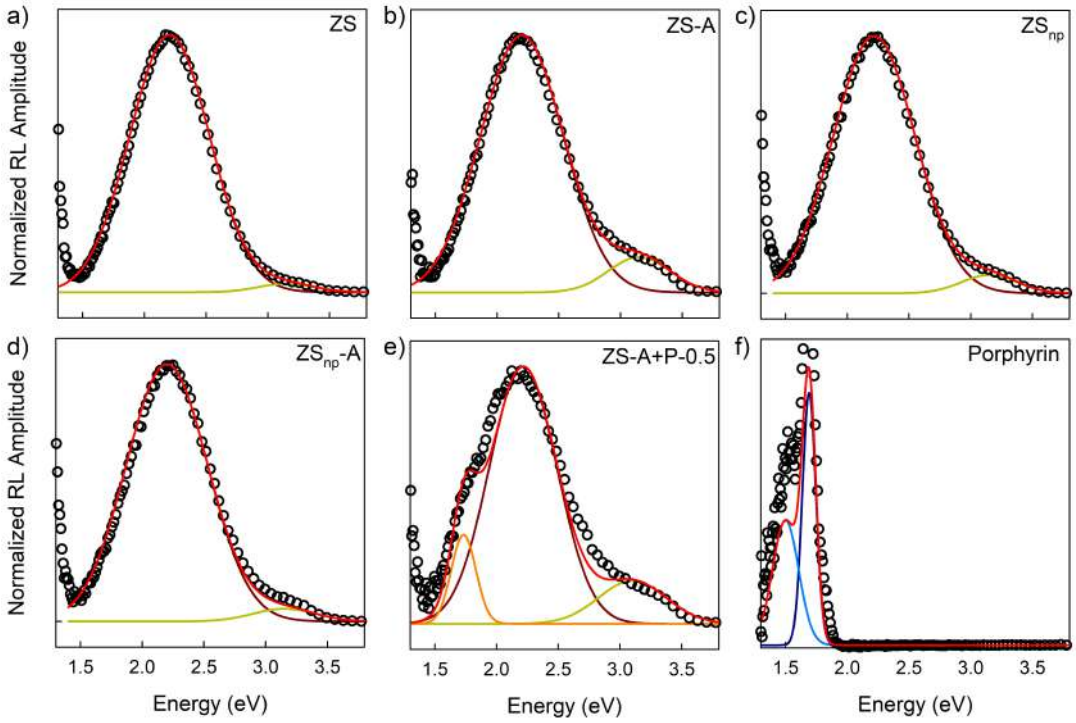

Figure 5.11: Gaussian deconvolution of normalized RL spectra of the porous and non-porous nanoscintillators with and without APTES decoration, of the mechanical mix and of the dye alone. Gaussian components (brown, mustard, orange, light blue, and blue solid lines) obtained by numerical fit are shown together with experimental curves (black empty circle lines). The curve representing the whole numerical fit (red solid line) is superimposed to the experimental data. The sets of all parameters of the deconvolutions are listed in Tables 5.5 and 5.6.

The impact of porphyrin functionalization on the RL spectral components

The Gaussian reconstruction of the mechanical mix (Figure 5.11e, Table 5.5) requires the ZnO defect and excitonic emission bands, that dominate the RL spectrum, together with an additional spectral component associated to the dye luminescence (centred at ∼1.73 eV with FHWM of ∼0.24 eV). Notably, upon the mixing with the dye powders, the FHWM of the ZnO green emission results smaller in ZS-A+P-0.5 (∼0.65 eV) compared to that of ZS-A (∼0.78 eV).
Moreover, the numerical analysis of the luminescence of the TCPP alone (Figure 5.11f, Table 5.6) includes the typical porphyrin J-band (centred at ∼1.69 eV with FHWM of ∼0.13 eV) and an additional one in the red region of the spectrum (centred at ∼1.50 eV with FHWM of ∼0.50 eV), consistently with the aggregation of dye molecules.
Differently, the RL spectra of ZS-AP-Y and ZS$_{np}$-AP-Y disclose both the ZnO

and the TCPP optical features. Indeed, five spectral components are identified by the Gaussian deconvolution (Figure 5.12, Table 5.7): two bands (centred at ∼2.22 eV with FHWM of ∼0.19 eV and at ∼2.48 eV with FHWM of ∼0.34 eV) are related to ZnO emissive defect species and three (centred at ∼1.72 eV with FHWM of ∼0.26 eV, at ∼1.95 eV with FHWM of ∼0.08 eV and at ∼2.06 eV with FHWM of ∼0.15 eV) related to porphyrin luminescence.

The discrepancy between the ZnO defect-related emission bands in the NPs with and without TCPP functionalization can be attributed to the presence of dips matching the porphyrin Q-bands peak energies (at ∼2.2 and ∼2.4 eV), that alter ZnO spectral shape in ZS-AP-Y and ZS_{np}-AP+Y. This result validates the occurrence of radiative ET between the organic and inorganic moieties in the dye coupled NPs even under X-Ray excitation. Moreover, the absence of ZnO excitonic band in the RL spectra of the TCPP functionalized nanosystems can be due to dye re-absorption of ZnO emitted photons.

For the porphyrin emission, the characteristic peak at ∼1.7 eV due to J-aggregates is identified in the mechanical mix as well as in the dye coupled samples, while only ZS-AP-Y and ZS_{np}-AP+Y disclose the monomer and Zn-TCPP complexes related bands, at ∼1.9 and ∼2.0 eV, respectively. Moreover, the TCPP emission intensity increases with the dye loading level and it is higher to that of ZnO for all the porphyrin functionalized NPs; on the other hand, it is rather weak in the mechanical mix. In addition, in all the dye coupled nanoscintillators, the relative intensity ratio of the typical porphyrin emissions (at ∼1.7 eV and at ∼1.9 eV) increases as the TCPP concentration increases, due to a higher probability of J-aggregates formation. [80] These results indicate that the porphyrin luminescence is efficiently sensitized in all the dye functionalized NPs regardless of its concentration and the generation of aggregates, with better performances than in the mechanical mix, in which the dye loading is of 1.4%, as in ZS-AP-0.5 (Figures 5.11e and 5.12). Hence, the controlled anchoring of porphyrin molecules on the nanoscintillators surfaces enables to govern the dye arrangement and spatial distribution, leading to TCPP optical properties similar to those of the single molecule, that are crucial for the interaction between the inorganic and organic moieties in multicomponent nanosystems. Indeed, both radiative ET and the local increment of energy deposition can benefit from the close proximity of properly distributed TCPP molecules and dense luminescent NPs. A detailed investigation on the role played by these two mechanisms is proposed in the sub-Section 5.3.2.

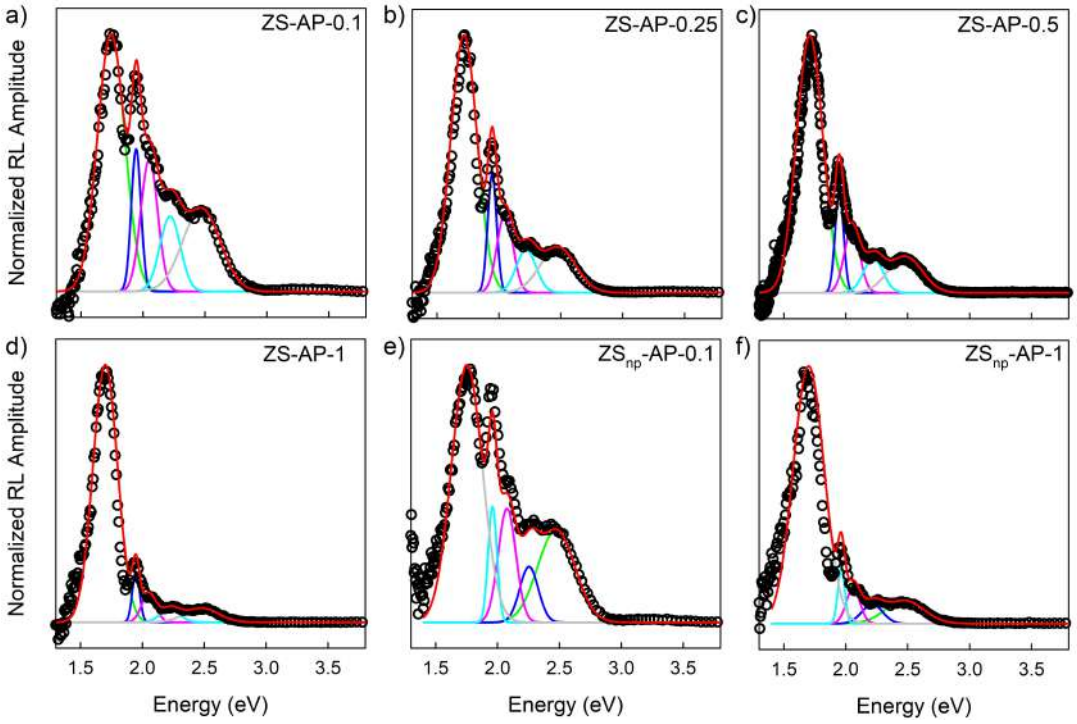

Figure 5.12: Gaussian deconvolution of normalized RL spectra of the porous and non-porous TCPP functionalized nanoscintillators. Gaussian components (brown, mustard, orange, light blue, and blue solid lines) obtained by numerical fit are shown together with experimental curves (black empty circle lines). The curve representing the whole numerical fit (red solid line) is superimposed to the experimental data. The sets of all parameters of the deconvolutions are listed in Table 5.7.

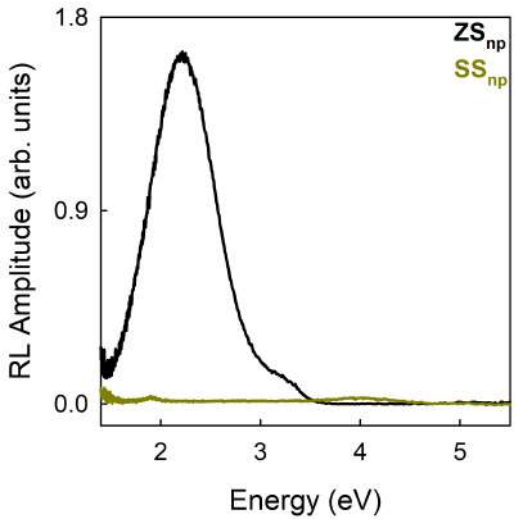

Figure 5.13: RL spectrum recorded under X-Ray excitation of SS_{np} compared to that of ZS_{np}.

		ZS	ZS-A	ZS_{np}	ZS_{np}-A	ZS-A+P-0.5
Band A (brown line)	Energy (eV)	2.25±0.01	2.24±0.01	2.22±0.01	2.20±0.01	2.22±0.01
	FWHM (eV)	0.76±0.01	0.79±0.01	0.78±0.01	0.78±0.01	0.65±0.03
	Weight (%)	98	91	95	96	77
Band B (mustard line)	Energy (eV)	3.15±0.01	3.15±0.03	3.15±0.01	3.15±0.03	3.10±0.05
	FWHM (eV)	0.50±0.10	0.60±0.10	0.54±0.10	0.60±0.10	0.60±0.10
	Weight (%)	2	9	5	4	13
Band C (orange line)	Energy (eV)	-	-	-	-	1.73±0.01
	FWHM (eV)	-	-	-	-	0.24±0.01
	Weight (%)	-	-	-	-	10

Table 5.5: Fit parameters of the Gaussian deconvolution of the RL spectra of the porous and non-porous nanoscintillators with and without APTES decoration, and of the mechanical mix.

		TCPP
Band D (light blue line)	Energy (eV)	1.50±0.01
	FWHM (eV)	0.25±0.01
	Weight (%)	51
Band E (blue line)	Energy (eV)	1.69±0.01
	FWHM (eV)	0.13±0.01
	Weight (%)	49

Table 5.6: Fit parameters of the Gaussian deconvolution of the RL spectrum of the TCPP alone.

		ZS-AP-0.1	ZS-AP-0.25	ZS-AP-0.5	ZS-AP-1	ZS_{np}-AP-0.1	ZS_{np}-AP-0.1
Band F (green line)	Energy (eV)	1.74±0.01	1.72±0.01	1.71±0.01	1.70±0.01	1.75±0.01	1.70±0.01
	FWHM (eV)	0.26±0.01	0.25±0.01	0.21±0.01	0.23±0.01	0.29±0.01	0.29±0.01
	Weight (%)	45	57	63	79	52	78
Band G (blue line)	Energy (eV)	1.94±0.01	1.95±0.01	1.95±0.01	1.95±0.01	1.96±0.01	1.96±0.01
	FWHM (eV)	0.09±0.01	0.08±0.01	0.08±0.01	0.07±0.01	0.08±0.01	0.07±0.02
	Weight (%)	9	10	9	6	7	4
Band H (pink line)	Energy (eV)	2.05±0.01	2.05±0.01	2.05±0.01	2.05±0.02	2.08±0.01	2.06±0.01
	FWHM (eV)	0.16±0.05	0.15±0.05	0.15±0.07	0.14±0.09	0.17±0.07	0.13±0.06
	Weight (%)	15	11	9	6	13	5
Band I (cyan line)	Energy (eV)	2.22±0.03	2.22±0.04	2.22±0.04	2.22±0.07	2.25±0.04	2.22±0.09
	FWHM (eV)	0.19±0.06	0.19±0.09	0.20±0.10	0.20±0.10	0.18±0.09	0.20±0.04
	Weight (%)	11	9	7	3	7	4
Band L (grey line)	Energy (eV)	2.47±0.02	2.48±0.03	2.48±0.04	2.50±0.10	2.47±0.03	2.50±0.10
	FWHM (eV)	0.36±0.03	0.34±0.05	0.32±0.06	0.32±0.09	0.35±0.05	0.37±0.10
	Weight (%)	20	13	12	6	21	9

Table 5.7: Fit parameters of the Gaussian deconvolution of the RL spectra of the porous and non-porous dye functionalized nanoscintillators.

5.3.2 Emission intensities under ionizing radiation

In this section, the absolute RL spectra of all the samples, recorded on powders and at different X-Ray mean beam energies, are reported to investigate the correlations between RL amplitude, the morphological parameters, and the excitation energy.

The impact of substrate porosity on RL efficiency

To test the RL efficiency of the nanoscintillators as synthesized and upon the APTES and TCPP functionalization, four samples are selected, namely ZS, ZS_{np}, ZS-AP-1, and ZS_{np}-AP-1. For each sample, three different aliquots from the same synthesis batch are analysed to verify the experimental reproducibility.

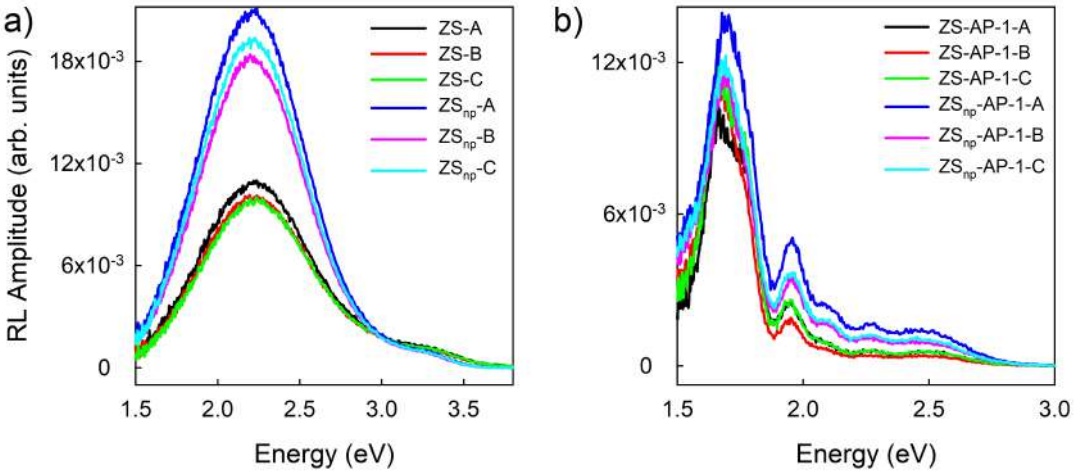

Figure 5.14: RL intensities, recorded upon exposure to X-Ray with mean beam energy of 6.6 keV, of ZS and ZS_{np} (**a**) and of ZS-AP-1 and ZS_{np}-AP-1 (**b**) normalized to the sample weight and to the ZnO content. For each sample, A, B, and C are different aliquots from the same synthesis batch.

The absolute RL intensities of the four chosen NPs, reported in Figure 5.14, disclose that luminescence efficiency of the non-porous samples both before and after APTES-TCPP functionalization is double with respect to that of the porous nanosystems. This result suggests that the optical processes are partially compromised for ZnO NPs grown inside the silica matrix, affecting both its quantum yield and its interaction with the dye. Possibly, in the porous samples, the surfaces of the internally grown ZnO NPs are close or even in contact to those of the SiO_2 pores and consequently the generated excitations may be lost at the interface of the two materials through non radiative recombination mechanisms.

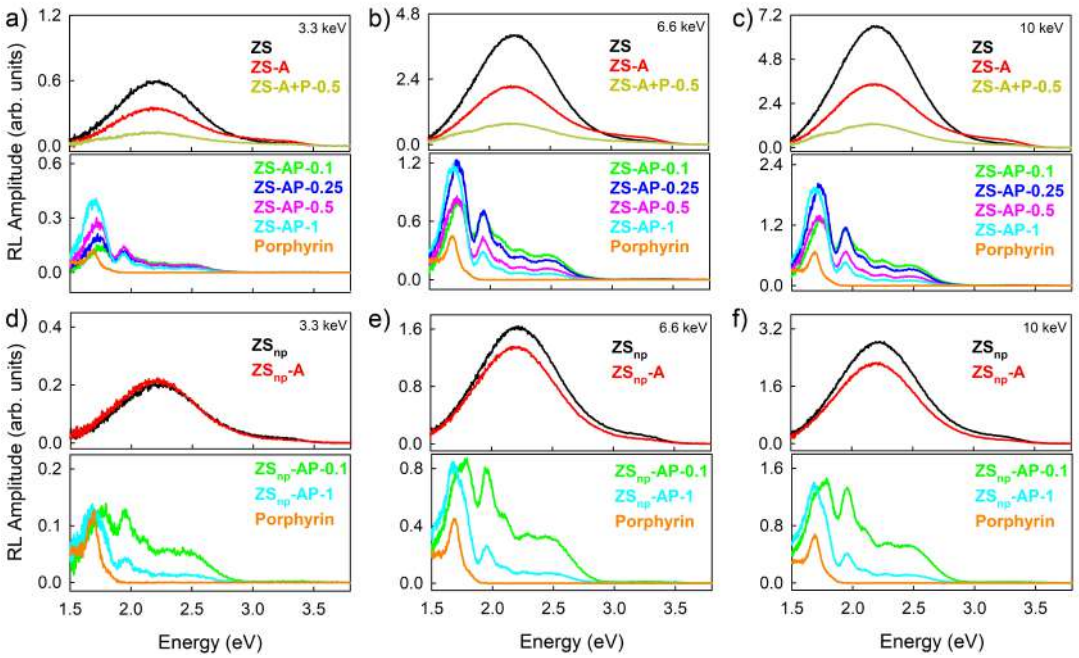

Figure 5.15: RL intensities recorded under X-Ray excitation with beam mean energy of 3.3, 6.6 and 10 keV of the porous (**a-c**) and non-porous (**d-f**) sets of nanosystems. For comparison, also the RL spectra as a function of the excitation energy of the mechanical mix and the porphyrin are reported.

The impact of APTES decoration and porphyrin functionalizazion on RL efficiency

Figure 5.15 displays the RL of the sets of porous and non-porous ZnO/SiO_2 nanosystems, as well as of the mechanical mix and of the porphyrin, as a function of the X-Ray beam energy. All the spectra are collected under the same experimental conditions by only changing the ionizing radiation mean energy, to allow an accurate comparison among their RL amplitudes.

The overall emissions of the mechanical mix as well as of the functionalized nanoscintillators are reduced upon APTES decoration and diminish further by porphyrin addition, for any excitation energy and for both the porous and non-porous supports (Figure 5.15). This finding suggests that new non-radiative recombination centres for the ZnO excitations are generated by the anchoring of APTES on the SiO_2 external surfaces (phenomenon evidenced only in the RL measurements, since no variation in the ZnO time dynamic is observed under light excitation, as shown in Figure 5.7) as well as by the presence of TCPP aggregates and not to the functionalization process itself. The occurrence of additional quenching channels in the dye functionalized samples can affect the ZnO luminescence and hence the efficiency of radiative ET between the inorganic NPs

and the organic molecules. Interestingly, the reduction of the overall efficiency of the nanoscintillators upon APTES anchoring is bigger for the porous samples than for the non-porous ones. This result is in agreement with the hypothesis that the decoration of silica surfaces with APTES is more controlled in the non-porous nanosystems, resulting in a minor occurrence of additional non-radiative centers.

Furthermore, Figure 5.15 shows that the RL of TCPP is generally less intense in the TCPP alone than in the ZS-AP-Y and ZS_{np}-AP-Y, even if their dye content (from 0.1 to wt1%) is two/three orders of magnitude smaller than in the TCPP sample (100%). Differently, in the mechanical mix, the strong overlap between the ZnO and the porphyrin bands negatively affects the analysis of the TCPP emission intensity, proving that the ZnO emission is still dominant in this sample. These findings highlight that the interaction between ionizing radiation and organic molecules is poor because of their low density and low Z atomic number, [73] whereas the triggering of their luminescence is promoted by their proximity to heavy nanoscintillators, [13] whose ability to interact efficiently with X-Ray photons can favour both the radiative ET and the energy release in the dye surroundings. It is worth noticing that in the studied nanosystems, the X-Ray photon energy can be deposited both in ZnO and SiO_2 NPs. In fact, the probability of interaction between matter and ionizing radiation depends on atomic numbers (Z_{Zn}=30, Z_{Si}=14, Z_O=8), on densities (ρ_{ZnO}=5.61 g/cm^3, ρ_{SiO_2}=2.65 g/cm^3), and also on particle dimensions (r_{ZnO} ∼2.5 nm, r_{SS} ∼40 nm, $r_{SS_{np}}$ ∼36 nm). The investigation of the role of SiO_2 and ZnO on the energy deposition in the nanosystems is addressed by the computational analysis presented in Section 5.4.

The impact of X-Ray mean beam energy on RL efficiency

The evolution of the RL properties with the ionizing radiation energy is investigated by performing the Gaussian deconvolutions of all the spectra. The results of the numerical analysis disclose that each sample exhibits the same spectral components identified in the previous spectral reconstruction, regardless of the ionizing radiation energy (Tables 5.5, 5.6, and 5.7). On the other hand, for all the specimens, the RL intensity is enhanced by increasing the energy of the ionizing radiation.

For all the X-Ray beam mean energies, the RL intensities of all TCPP coupled NPs and of the mechanical mix are compared to those of the APTES decorated nanoscintillators (Figure 5.16 and Figure 5.17a). In detail, the integrals of

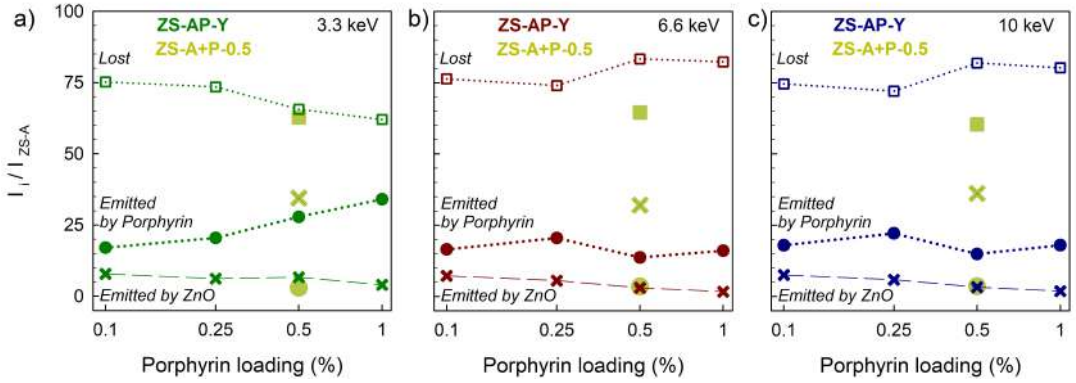

Figure 5.16: Percentage RL intensities dissipated non-radiatively (squares), emitted by porphyrin (circles) or by ZnO (crosses) in the porous dye functionalized nanosystems (in dark green, red or blue) and in the mechanical mix (in lime green) normalized to the total RL intensity of the ATPES decorated NPs (ZS-A) under X-Ray excitation with 3.3, 6.6, and 10 keV mean beam energies (data extracted from Gaussian deconvolutions of RL spectra shown in Figure 5.15a-c.)

Gaussian spectral components, which are proportional to the number of emitted photons, are used to estimate the amount of photons emitted by ZnO (I_{ZnO}) and by porphyrins ($I_{Porphyrin}$) in the dye coupled nanosystems and in the mechanical mix. Furthermore, for all the porphyrin containing samples, it is evaluated the portion of photons dissipated non-radiatively (I_{Lost}) upon TCPP addition with respect to the overall photons emitted by the APTES decorated nanoscintillators. As an example, only for the ZS-AP-Y set, the procedure used to estimate I_{ZnO}, $I_{Porphyrin}$, I_{Lost} is reported:

$$\begin{aligned} I_{ZnO} &= Integral\ of\ Band\ I \\ &+ Integral\ of\ Band\ L \end{aligned}$$

$$\begin{aligned} I_{Porphyrin} &= Integral\ of\ Band\ F \\ &+ Integral\ of\ Band\ G \\ &+ Integral\ of\ Band\ H \end{aligned}$$

$$\begin{aligned} I_{ZS-A} &= Integral\ of\ Band\ A \\ &+ Integral\ of\ Band\ B \end{aligned}$$

$$I_{Lost} = I_{ZS-A} - I_{ZnO} - I_{Porphyrin}$$

For details on the Gaussian spectral components, please refer to Tables 5.5, 5.6, and 5.7.

For all the dye functionalized nanosystems and the mechanical mix, Figures 5.16

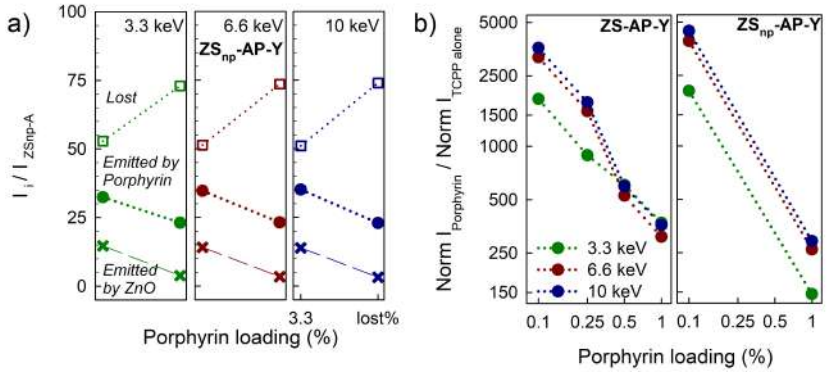

Figure 5.17: **a**) Percentage RL intensities dissipated non-radiatively (squares), emitted by porphyrin (circles) or by ZnO (cross) in the non-porous dye functionalized nanosystems normalized to the total RL intensity of the ATPES decorated NPs (ZS_{np}-A) under X-Ray excitation with beam mean energy of 3.3, 6.6, and 10 keV (data extracted from Gaussian deconvolutions of RL spectra shown in Figure 5.15d-f); (**b**) Normalized RL intensity emitted by the porphyrin in the porous and non-porous dye functionalized nanosystems divided by the normalized RL intensity of the porphyrin alone recorded under X-Ray excitation with beam mean energy of 3.3 keV, 6.6 keV and 10 keV (data extracted from Gaussian deconvolutions of RL spectra Figure 5.15 and normalized to the porphyrin percentage weight present in the sample).

and 5.17a report the percentage RL intensities of the overall ZnO and porphyrin emissions, as well as the fractions of luminescence losses (generally labelled as I_i), all normalized to the total RL intensity of the APTES decorated nanoparticles (I_{ZS-A} or $I_{ZS_{np}-A}$). The data are shown as a function of the porphyrin loading level (displayed in logarithmic scale). Interestingly, independently from the excitation energy, in the all the TCPP functionalized NPs, most of the ZnO luminescence is lost upon functionalization (50-80%), a small fraction is still generated from ZnO (5-15%), and a more intense one is related to porphyrin emission (15-35%). At variance, in the mechanical mix the luminescence losses are conspicuous (60%) but ZnO emission (35%) is much higher than that of the dye (5%). These findings reveal that porphyrin sensitization is promoted by the synergic effect of ionizing radiation and NPs functionalization.

Furthermore, trends of RL intensities for the dye coupled nanosscintillators are similar for the porous NPs at the two highest X-Ray beam mean energies (Figure 5.16b,c) and for the non-porous NPs at all the X-Ray beam mean energies (Figure 5.17a), while it differs only for the porous NPs under ionizing radiation with 3.3 keV mean energy (Figure 5.16a). Solely in this case, the luminescence losses decrease and the porphyrin emission increases with the dye content. This result is consistent with the increase of local energy deposition as the radiation energy

decreases. However, this phenomenon affects only the porous samples and it can be attributed to the different energy release amount and distribution occurring in the two sets of nanosystems under study. The interpretation of these results requires additional studies, especially numerical simulations (refer to sub-Section 1.3.4), on the energy deposition processes in nanometric materials.

The impact of nano-agent design and X-Ray mean beam energy on the sensitization of porphyrin emission

For all the X-Ray beam mean energies, the RL intensities of the TCPP coupled NPs are compared to that of porphyrin alone (Figure 5.17b). In detail, the integrals of Gaussian components are used to compare the porphyrin emission of all the functionalized nanoscintillators ($I_{Porphyrin}$) with that of the dye alone ($I_{TCPP\ alone}$). $I_{Porphyrin}$ and $I_{TCPP\ alone}$ are calculated as the sum of the Gaussian integrals of all the bands attributed to the organic molecules emissions and then normalized to the dye weight percentage in the sample to obtain Norm $I_{Porphyrin}$ and Norm $I_{TCPP\ alone}$, respectively. The used numerical procedure is reported in the following:

$$\begin{aligned} I_{Porphyrin} &= Integral\ of\ Band\ F \\ &+ Integral\ of\ Band\ G \\ &+ Integral\ of\ Band\ H \end{aligned}$$

$$\begin{aligned} I_{TCPP\ alone} &= Integral\ of\ Band\ D \\ &+ Integral\ of\ Band\ E \end{aligned}$$

$$Norm_{I_{Porphyrin}} = \frac{I_{Porphyrin}}{Dye\ wt\%\ in\ the\ functionalized\ NPs}$$

$$Norm_{I_{TCPP\ alone}} = \frac{I_{TCPP\ alone}}{Dye\ wt\%\ in\ the\ TCPP\ alone}$$

For details on the Gaussian spectral components, please refer to Tables 5.5, 5.6, and 5.7. For the three-excitation energies, Figure 5.17b displays the ratio between the normalized RL intensities of porphyrin emissions in the functionalized NPs (Norm $I_{Porphyrin}$) and that of the TCPP alone (Norm I_{TCPP}). The data are shown as a function of the dye loading level (both axes are displayed in logarithmic scale).

Notably, regardless of the porphyrin concentration and of the X-Ray photon mean energy, the proximity of heavy nanoscintillators and dyes molecules promotes an enhancement in TCPP luminescence of about two/three orders of magnitude in

the functionalized NPs, whereas this increment is only of about 30-70% in the mechanical mix (data not shown). For all the ionizing radiation mean energies, the dye sensitization improves by lowering the dye content (Figure 5.17b), further indicating that the higher is the dye content, the higher is the probability of aggregates formation, and the lower the porphyrin luminescence efficiency. Moreover, the triggering of TCPP emission increases coherently with the X-Ray photons mean energy, whatever its loading level, suggesting that the interaction between the inorganic NPs and the ionizing radiation (and consequently the dye luminescence activation) is affected by the energy parameter. However, some discrepancy in the absolute values and in the shapes of the curves are observed upon exposure with ionizing radiation of 3.3 keV in comparison to the findings obtained for the two highest mean beam energy. As already mentioned, these results are related to the amount and spatial distribution of the deposited energy by X-Ray photons in the nanosystems, that both depend on the beam excitation energy and on the morphology parameters of the excited NPs. An interpretation of these data is presented in sub-Section 5.4.2, grounded on a preliminar computational investigation on the energy release of the ionizing radiation in non-porous ZnO/SiO_2 nanosystems.

5.3.3 Conclusions on radioluminescence

In this section, the analysis of the RL spectral shapes and intensities of all the TCPP functionalized nanoscintillators unveils the crucial role of morphological parameters and ionizing radiation energy in determining the final optical properties of the multicomponent nanosystems. In particular, the main findings are:

- The substrate porosity does not influence the ZnO defectiveness and hence its emission properties and its interaction with TCPP molecules; however, the sensitization of porphyrin luminescence results affected by the morphology of the nanosystem.

- The coating of the inorganic NPs with APTES probabily introduces new non-radiative channels for ZnO luminescence.

- The functionalization with porphyrin enables the interaction between the organic and inorganic parts of the multicomponent nanosystems; nevertheless, it creates TCPP aggregates, that generate additional quenching centres and limit the porphyrin luminescence sensitization.

- Under irradiation with X-Ray photons, the enhancement of porphyrin emission is highly efficient, due to the activation of both radiative ET and locally augmented energy deposition mechanisms.

5.4 Computational analysis of the deposited energy

Aiming at deepening the comprehension on the role of the locally augmented energy deposition mechanism in the interaction between the inorganic and organic moieties of the multicomponent nanosystems, the spatial profile of the energy release is evaluated by computational Monte Carlo simulations based on the GEANT4 toolkit and discussed in relation with the results of the RL measurement.
In particular, as model for the analyses, the non-porous ZnO/SiO_2 nanoscintillators (ZS_{np}) are selected, as their geometry is more suitable to be represented by the GEANT4 program, and two different codes are developed to address the complexity of the issue. As already mentioned, the computational analyses have been performed in collaboration with Dr Anne-Laure Bulin of the Synchrotron Radiation for Biomedicine Group at the University of Grenoble-Alpes, INSERM.

5.4.1 Simulations results

To accurately investigate the energy deposition in ZS_{np}, two codes with different geometry parameters (code A and B, respectively) are developed. They allow to discriminate the relative contribution of SiO_2 and ZnO in the energy release process as a function of the energy of the X-Ray beam with only one nanoparticle (code A) or thousands of nanoparticles randomly placed (code B) (for details, please refer to sub-Section 3.2.5). In particular, in code A, the nanosystems geometry is represented with great accuracy but the irradiation conditions are ideal, whereas, in code B, the nanosystems geometry is approximated to match the computational capacity but the used irradiation conditions are similar to the experimental ones (Figure 5.18).
For the simulations performed operating code A, one SiO_2 NP, with a diameter of 80 nm, whose surfaces are covered with an increasing number of ZnO NPs (from 0 to 215 NPs, that is the real ZnO loading on ZS_{np}) is exposed to X-Ray photons with different energy (3.3 / 6.6 /10.0 keV), as shown in Figure 5.18a-b. The used diameters for both SiO_2 and ZnO NPs are equal to the sizes of the silica

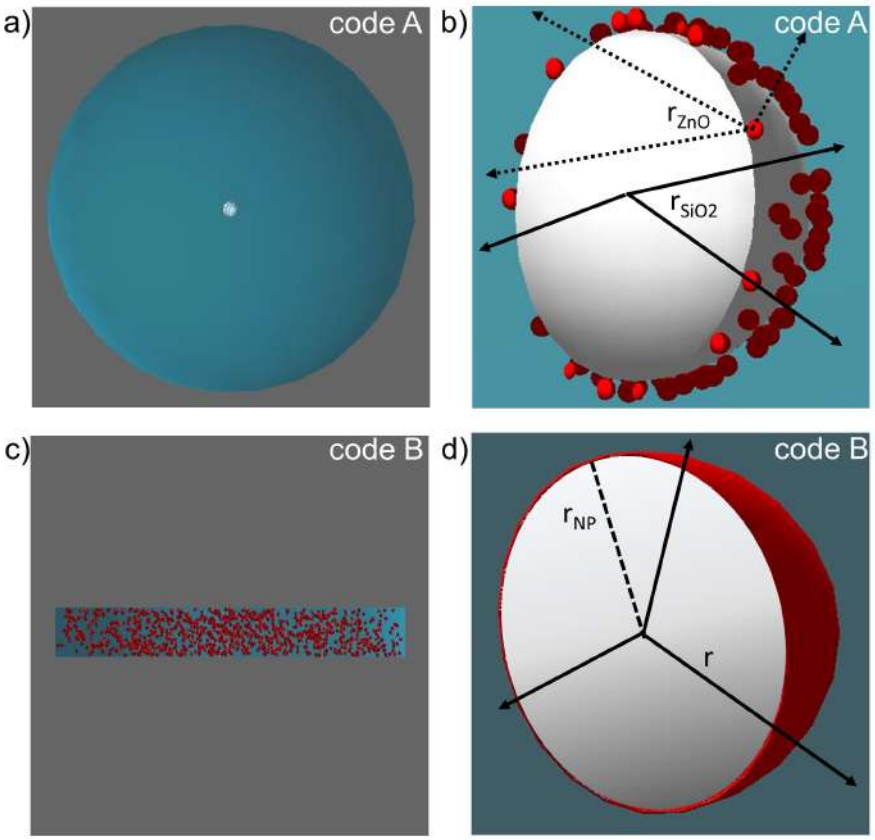

Figure 5.18: Visualization of geometries of the *world*, the *environment*, and the nanosystems for code A (**a-b**) and code B (**c-d**). The *world* is depicted in grey, the *environment* in blue, the SiO_2 in white, and ZnO in red. r_{SiO_2}, r_{ZnO}, r_{NP}, and r are graphical representations of the radial distances used to calculate the spatial profile of energy deposition.

substrate and the ZnO NPs of the ZS_{np} sample. The results obtained by executing code A are reported in Figures 5.19-5.23. Figures 5.19, 5.20, and 5.21 display the spatial profile of the deposited energy in the non-porous nanosystems evaluated both from the centre of the silica (r_{SiO_2}, in panels from a to d) and zinc oxide (r_{ZnO}, in panels from e to g) NPs, for various concentrations of ZnO and several energy of the X-Ray beam. For more clarity, a sketch of the radial distances that were used is depicted in Figure 5.18b. For the keV range, whatever the energy of the X-Ray beam, the data reveal that energy deposition occurs mainly within the first 45 or 85 nm from the SiO$_2$ or ZnO centre, respectively. This result indicates that i) the majority of the ionizing radiation energy is released inside the nanosystem and ii) both SiO$_2$ and ZnO contribute significantly to the process in the used excitation energy range (from 3.3 to 10.0 keV). In particular, the amount of energy deposited in ZnO increases coherently with the number of ZnO NPs placed on the support surfaces.

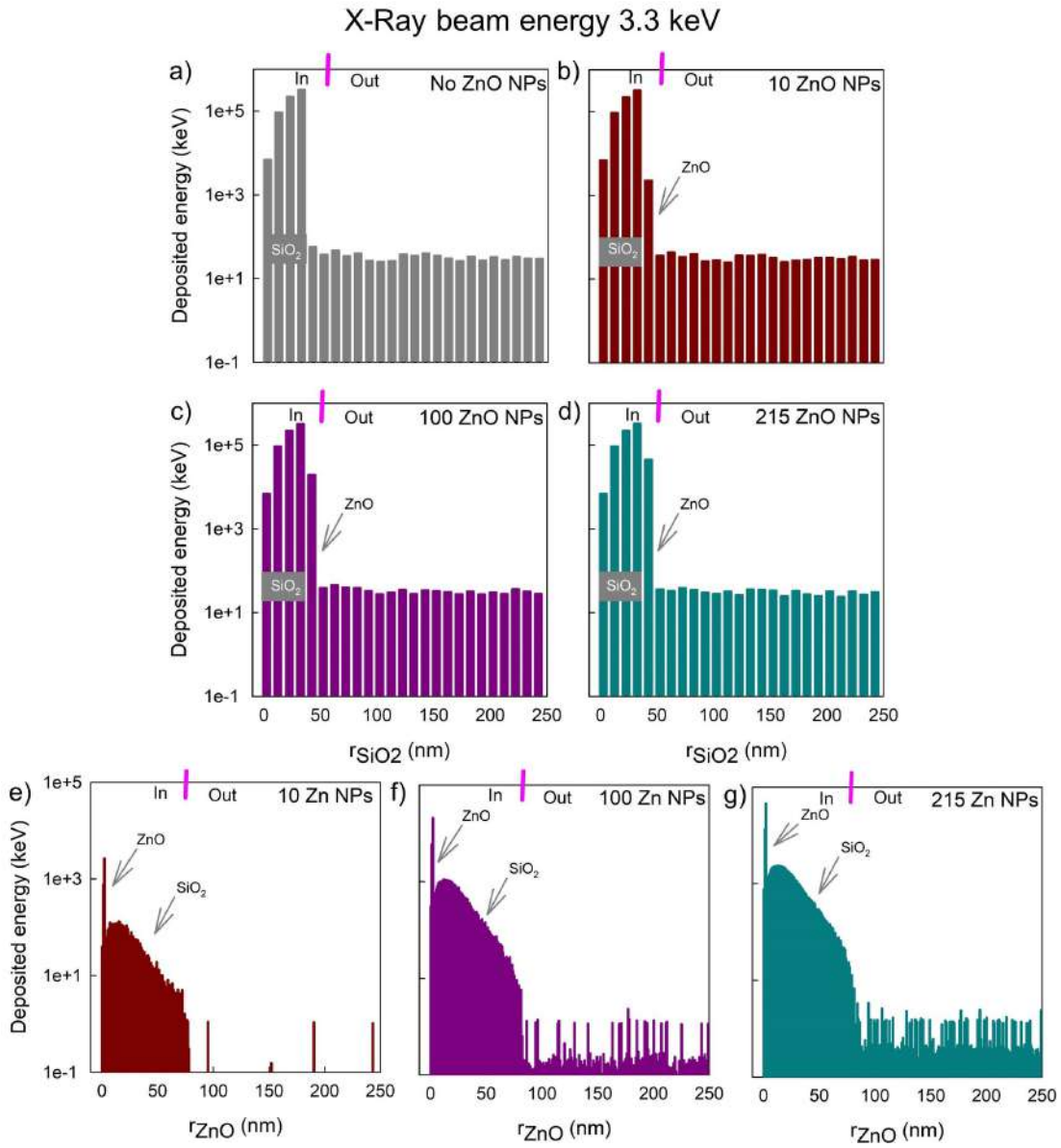

Figure 5.19: Spatial distribution of the energy deposited in one non-porous nanosystem with different ZnO concentrations upon exposure to X-Ray photons with energy of 3.3 keV. The data are reported from both the centre of the SiO_2 NP (r_{SiO_2}, panel **a-d**) and of the ZnO NP (r_{ZnO}, panel **e-g**).

This finding suggests that despite ZnO has reduced dimensions compared to silica, its presence is pivotal to enhance the overall density and atomic number of the nanosystem, and hence the interaction with X-Ray photons. Differently, the overall energy release decreases when the energy of the X Ray beam increases, regardless of the ZnO concentration. This is in agreement with the lower interaction probability between the matter and more energetic photons.

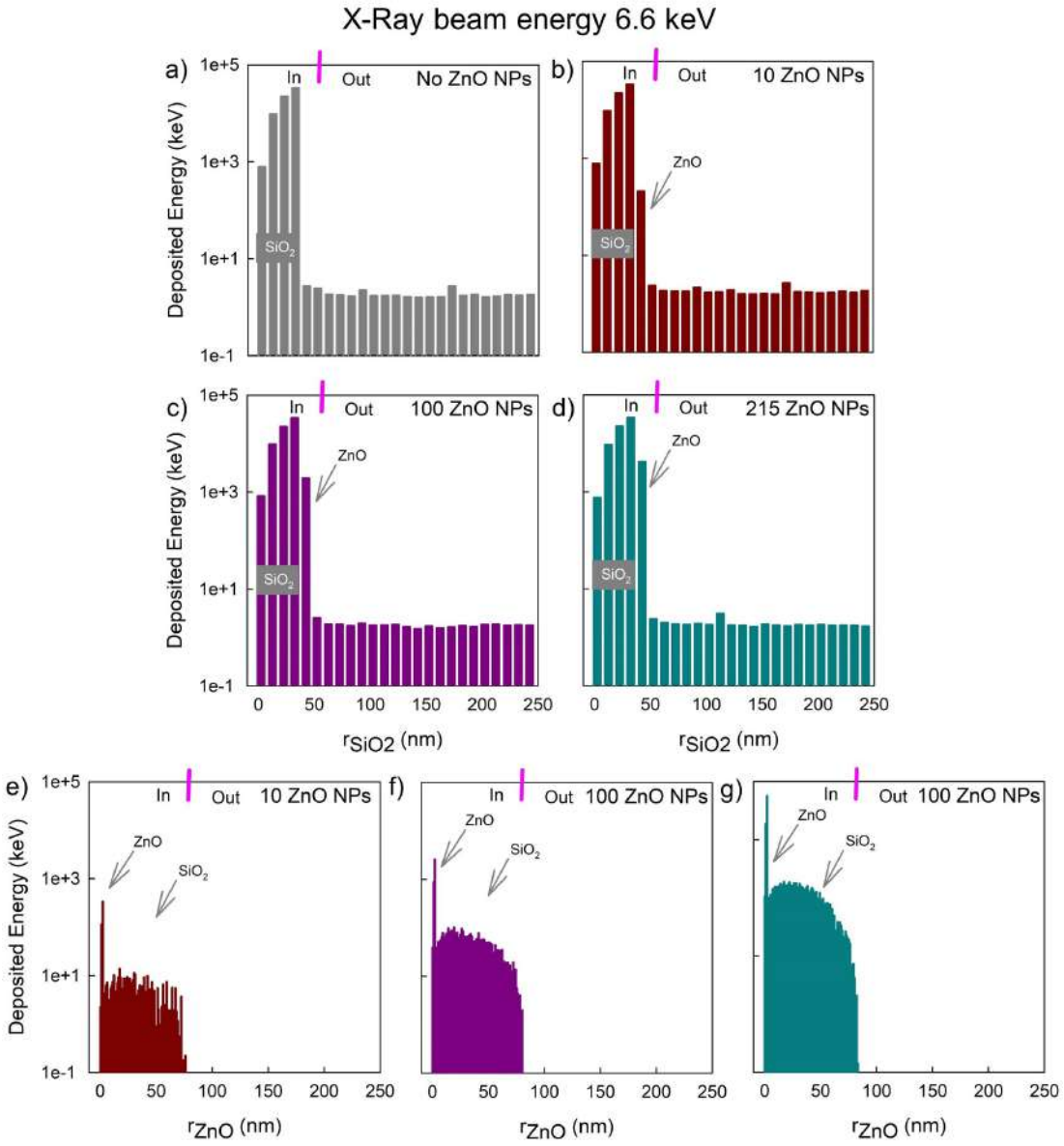

Figure 5.20: Spatial distribution of the energy deposited in one non-porous nanosystem with different ZnO concentrations upon exposure to X-Ray photons with energy of 6.6 keV. The data are reported from both the centre of the SiO_2 NP (r_{SiO_2}, panel **a-d**) and of the ZnO NP (r_{ZnO}, panel **e-g**).

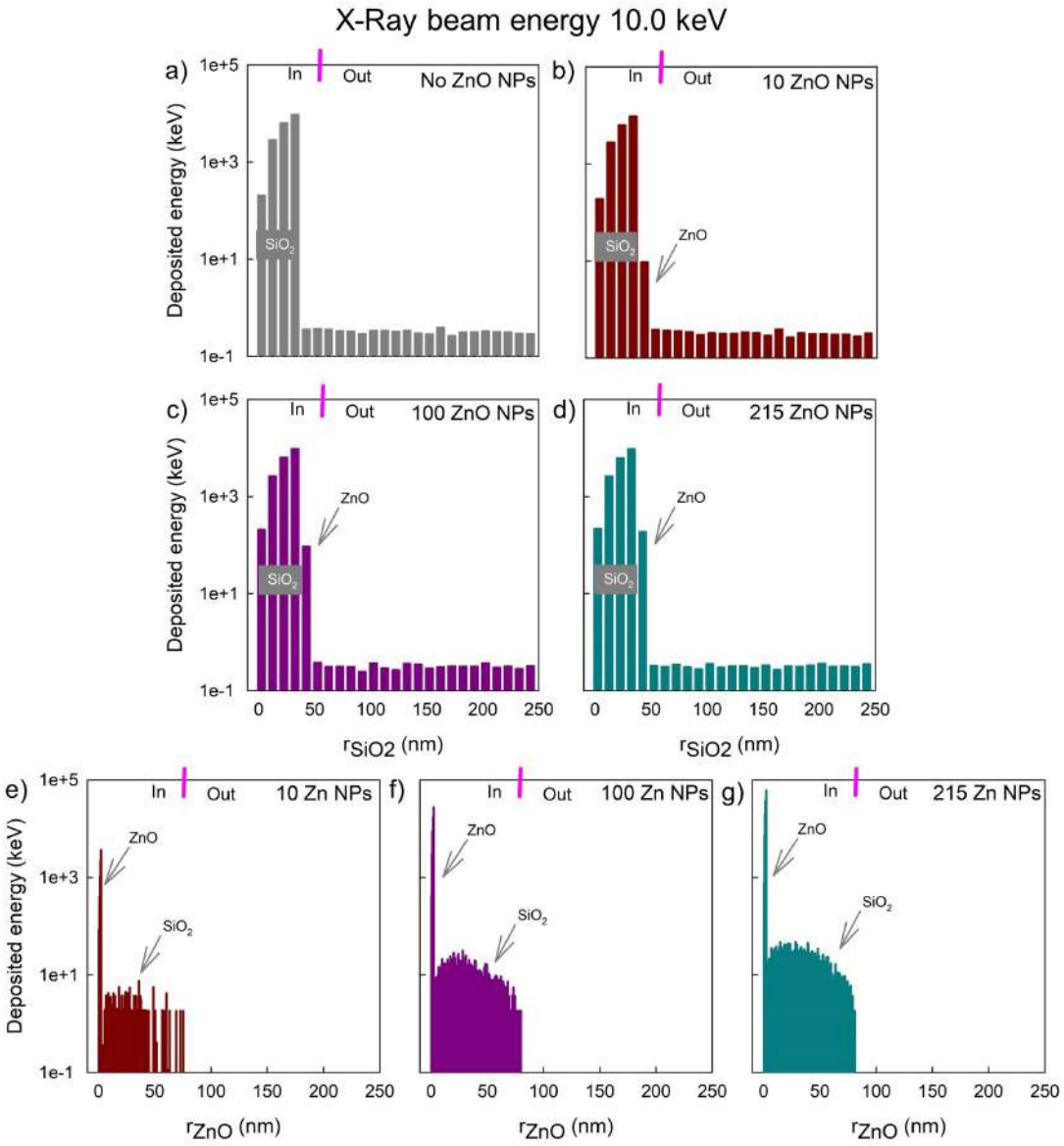

Figure 5.21: Spatial distribution of the energy deposited in one non-porous nanosystem with different ZnO concentrations upon exposure to X-Ray photons with energy of 10.0 keV. The data are reported from both the centre of the SiO_2 NP (r_{SiO_2}, panel **a-d**) and of the ZnO NP (r_{ZnO}, panel **e-g**).

Figures 5.22 and 5.23 report the number of interactions (Nb_{int}) between the matter and ionizing radiation and the estimation of the deposited energy (E_{dep}) in specific volumes (panels a-d). The data are normalized to the total number of incident X-Ray photons, called events (Nb_{events}). Figure 5.23e also shows the percentage of energy deposited in SiO_2, ZnO ($E_{dep\ i}$), or in the total volume ($E_{dep\ tot}$), defined as sum of the two materials (*i.e.* SiO_2 and ZnO NPs) and the environment. The data of Figures 5.22 and 5.23 are reported as functions of the number of ZnO NPs for the three energy of the X-Ray beam. For the keV range, regardless of the energy of the ionizing radiation, the number of interactions and the deposited energy increase in the total volume as well as in the SiO_2, the ZnO, and the environment alone, when the number of ZnO NPs attached to the silica support increases. These findings corroborate the assumption that the presence of ZnO NPs enhances the density and the atomic number of the nanosystems, thus favouring the interactions with ionizing radiations. Moreover, independently of ZnO concentration, the total number of interactions and total deposited energy, as well as the energy released in SiO_2 and in the environment alone (Figures 5.22a,b,d and 5.23a,b,d) decrease as the energy of the X-Ray beam increases. Differently, for ZnO, whatever its concentration, the number of its interactions with the ionizing radiation and also the deposited energy do not vary linearly with the X-Ray energy (Figures 5.22c and 5.23c). More specifically, the number of interactions occurring upon exposure to 10.0 keV X-Ray beam is contained between the number of interactions occurring upon that to 3.3 and 6.6 keV ones. Regarding the deposited energy, the highest amount is released under irradiation of the nanoscintillators with X-Ray photons of 10.0 keV. Usually, the probability of interaction between matter and ionizing radiations and as a consequence, the released energy per interaction, decrease as the photon energy increases (as mentioned in sub-Section 1.3.1). Hence, the results obtained for the total volume, for the SiO_2 and the environment alone are consistent with the theoretical backgrounds. At variance, the behaviour observed for ZnO unveils its ability to interact with ionizing radiations is enhanced upon irradiation with 10 keV X-Ray photons, suggesting the occurrence of an additional process. Indeed, zinc presents the X-Ray absorption edge for the K transitions at 9.66076 keV. [131,173] Consequently, 10.0 keV X-Ray beam is efficiently absorbed by ZnO NPs, leading to the ionization of zinc core shells and subsequent generation of photo- and/or Auger electrons as secondary carries that can afterwards release their energy inside or close to the ZnO NPs.

Moreover, Figure 5.23e clearly demonstrates that for the lowest X-Ray energies

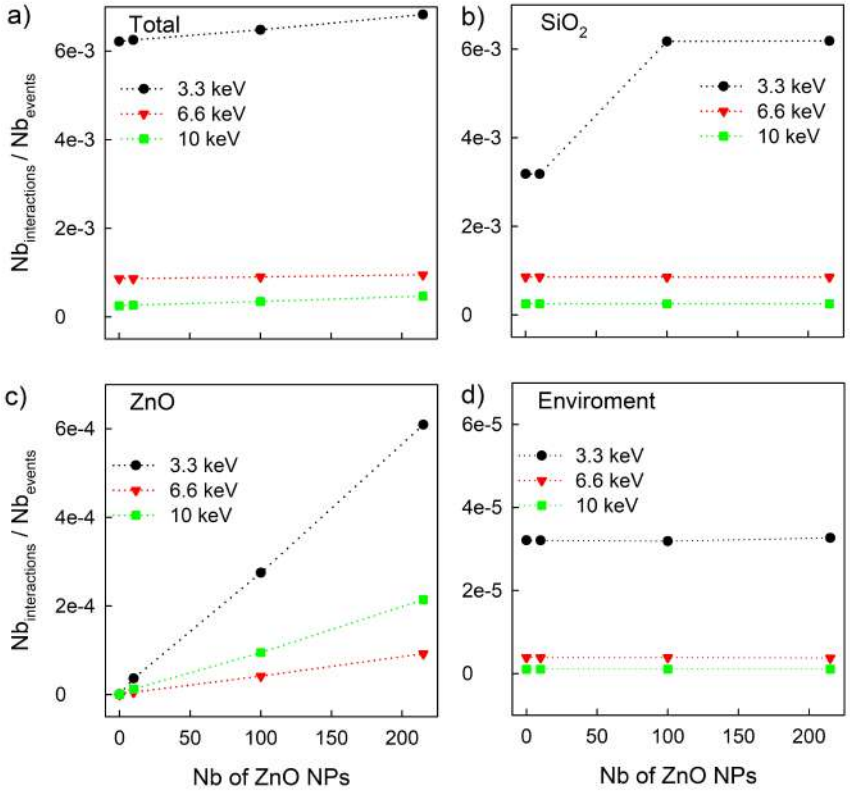

Figure 5.22: Number of interactions between the primary and secondary charges and the total volume (*i.e.* SiO_2, ZnO, and the *environment*) (**a**), the SiO_2 (**b**), the ZnO (**c**), and the *environment* alone (**d**) as a function of the number of ZnO NPs grown onto the silica support. The data are normalized to the total number of incident X-Ray photons (Nb_{events}) and reported for the three energies of the X-Ray beam.

(3.3 keV), the energy is mainly released inside the SiO_2 NP and its contribution to the overall energy deposition slightly decreases by incrementing the number of ZnO NPs onto the non-porous nanosystem. On the contrary, for the highest X-Ray energy (10.0 keV), the energy released in ZnO increases significantly with the concentration of ZnO and its contribution to the overall energy deposition dominates when the number of ZnO NPs is higher than 100. These findings further validate that the presence of ZnO NPs onto the silica support promotes the energy deposition through the increase of the nanoscintillator density and atomic number for all the X-Ray photon energies. It also indicates that the interactions between ZnO and ionizing radiation with energy of 10.0 keV are mainly due to the Zn K-edge absorption at 9.66076 keV [131, 173] that leads to an optimized energy deposition process.

In code B, thousands of nanosystems randomly distributed in the environment are subjected to X-Ray photons of different energy (3.3 / 6.6 / 10.0 keV), as

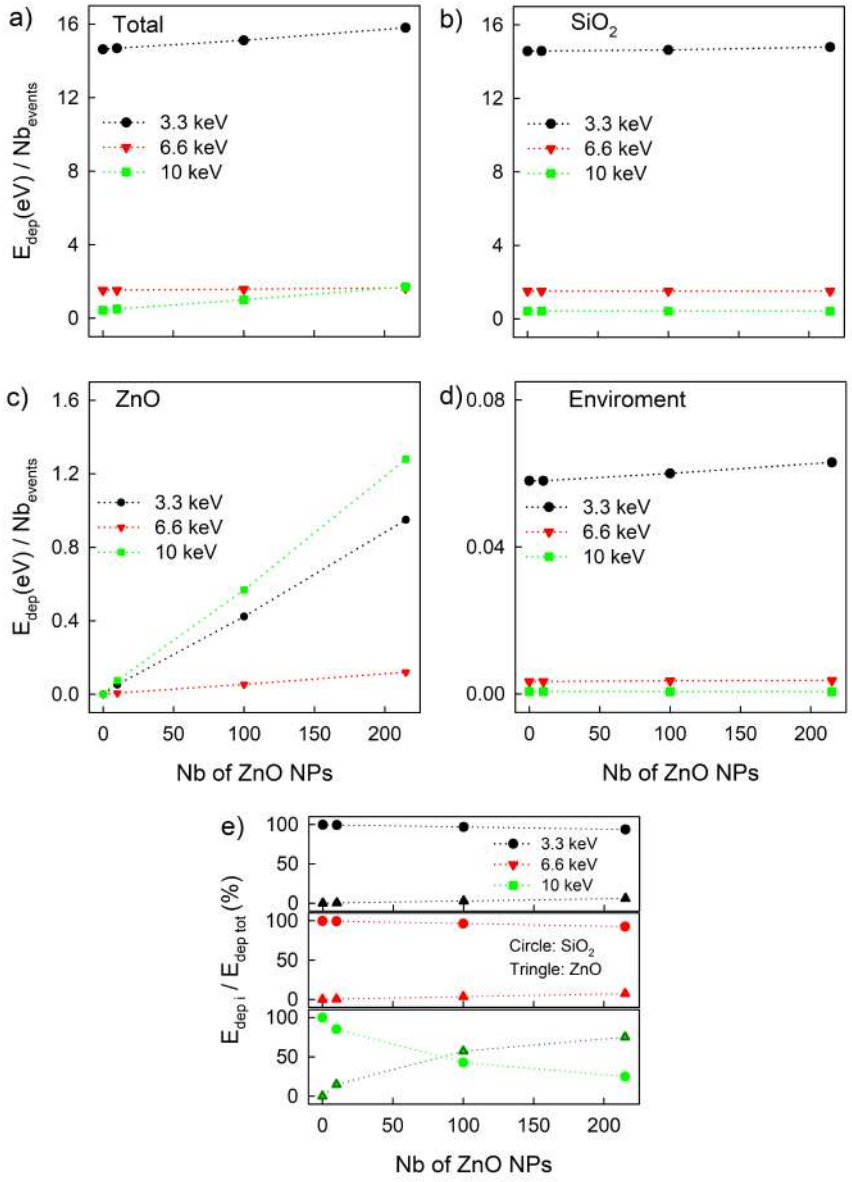

Figure 5.23: **a-d**) Estimation of the energy deposited in the total volume (*i.e.* SiO_2 NP, ZnO, and the *environment*) (**a**), in SiO_2 (**b**), in ZnO (**c**), and in the *environment* alone (**d**) as a function of the number of ZnO nanoparticles grown onto the support. **e**) Percentage fraction of energy deposited in either SiO_2 or ZnO ($E_{dep\ i}$) with respect to the total released energy ($E_{dep\ tot}$). The data are normalized to the total number of incident X-Ray photons (Nb_{events}) and reported for the three X-Ray beam energies.

depicted Figure 5.18c-d. In particular, the nanoscintillators are represented as following: each SiO_2 NP with a diameter of 80 nm, equal to that of the substrate of ZS_{np}, is shelled with a 0.4 nm-thick spherical layer of ZnO. The volume of the shell and therefore its thickness have been calculated to be equivalent to the total volume of 215 ZnO NPs with 5 nm diameter. Figure 5.24 shows the results obtained by operating code B. In detail, panels a-c of Figure 5.24 report, for the three X-Ray beam energies, the spatial distribution of the deposited energy in the non-porous nanosystems as a function of the radial distance from the centre of the approximated NPs (r) normalized to their overall radius (r_{NP}): the short and long range are displayed in the main panels and in the insets, respectively - a graphical representation of the considered distances is depicted in Figure 5.18d.

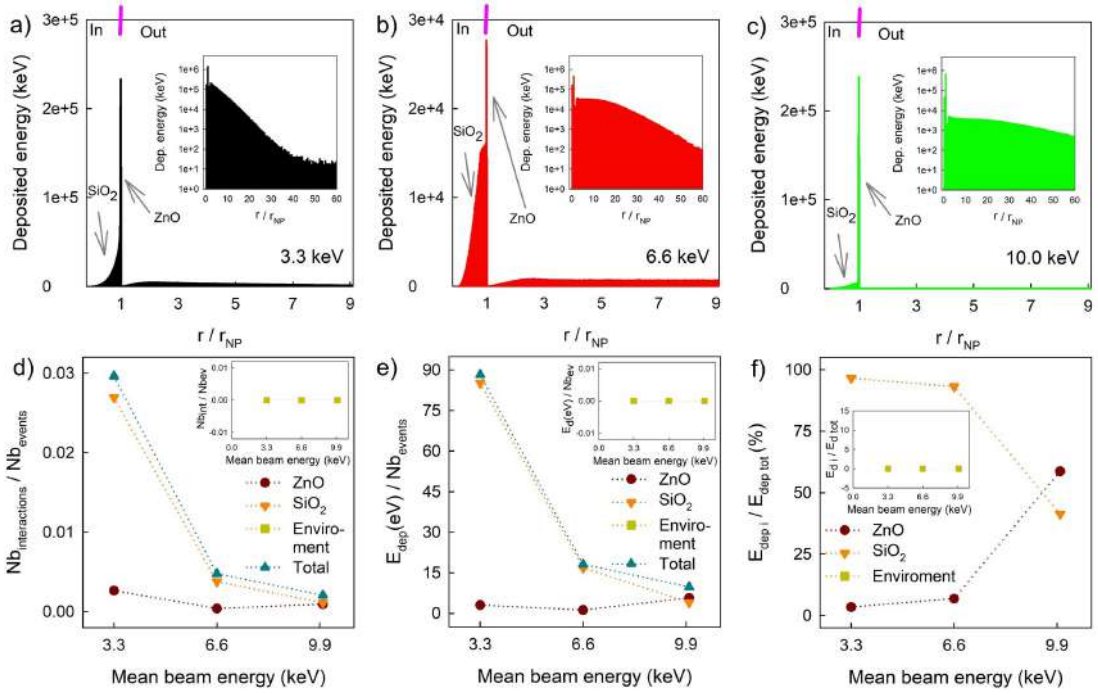

Figure 5.24: **a-c**) Short (main panel) and long (inset) range spatial distribution of the energy deposited in the approximated nanosystems upon exposure to X-Ray photons with energy of 3.3 (**a**) / 6.6 (**b**) / 10.0 (**c**) keV. The data are reported from the centre of the NPs (r) normalized to their overall radius (r_{NP}). **d-f**) Number of interactions between the primary and secondary carries and the matter (**d**), estimation of the energy deposited in specific volumes (**e**), percentage fraction of energy deposited (**f**) in either SiO_2, ZnO, or the *environment* alone ($E_{dep\ i}$) with respect to the total released energy ($E_{dep\ tot}$). From (**d-f**), the data are normalized to the total number of incident X-Ray photons (Nb_{events}) and reported for the three X-Ray beam energies.

These data disclose, in agreement with code A results, that the majority of

the energy is deposited inside the NP with which the incoming photon interacted and that both SiO_2 and ZnO contribute to the energy release process, regardless of the X-Ray energy. It is worth noticing that the amount of deposited energy in the modelled NPs is approximately one order of magnitude smaller upon irradiation with 6.6 keV X-Ray photons compared to irradiations with 3.3 keV or 10 keV ones. This suggests that the interactions between ionizing radiation of 6.6 keV energy and the nanoscintillators are not particularly efficient. Moreover, the profile of energy deposition in the long range broadens when the X-Ray photons energy increases. Probably, this observation is related to the fact that more energetic photons possess higher kinetic energy that allows them to travel longer distances.

Figures 5.24d,e show the number of interactions (Nb_{int}) between the primary and secondary particles and the matter and the evaluation of the deposited energy (E_{dep}) in specific volumes, respectively, both normalized to the total number of incident X-Ray photons, (Nb_{events}). Figure 5.24f presents the ratio (multiplied by a factor of 100) between the energy deposited in either SiO_2, ZnO or the environment alone ($E_{dep\ i}$) and in the total volume ($E_{dep\ tot}$). The data of Figures 5.24d-f are reported as functions of the X-Ray beam energy. These results, also consistent with the findings of code A, disclose that the SiO_2 contribution to the number of interactions and to the energy release decreases when increasing the energy of the ionizing radiation. In addition, these data show that the role of the environment is negligible and that ZnO effect becomes dominant upon exposure with ionizing radiation of 10 keV. Possibly, under excitation with 3.3 keV photons, the energy deposition mostly occurs in SiO_2 because of its medium density, atomic number and large volume compared to those of ZnO. Furthermore, since the probability of interaction is higher for 3.3 keV photons, the total energy released in the nanosystem is significant. At variance, upon excitation with 10 keV photons, the absorption of the ionizing radiation by ZnO NPs is boosted by the zinc absorption K-edge at 9.66076 keV [131, 173] and by their high density and atomic number. Therefore, although their size is small with respect to that of SiO_2, ZnO plays a major role in the energy deposition. Lastly, under excitation with 6.6 keV X-Ray beam, neither the SiO_2 or the ZnO probability of interaction with the ionizing radiation is optimized, leading to a significant decrease in SiO_2 role and to a rather weak ZnO contribution to the total energy release. In accordance with these observations, the total energy released in the nanosystems largely decreases when increasing the X-Ray energy from 3.3 keV to 6.6 keV and slightly decreases when increasing the X-Ray energy from 6.6 keV to 10.0 keV.

This validates that the increment of the ionizing radiation energy reduces the probability of interaction, yet this effect is limited when using 10 keV X-Ray photons. Hence, the results of these simulations indicate that the probability of interaction between non-porous nanoscintillators and ionizing radiation depends on the processes activated by the high energy radiation in SiO_2 and ZnO.

5.4.2 Comparison between computational and experimental results

To understand the role of locally augmented energy deposition in exciting the porphyrin in the functionalized nanoscintillators, the results of the RL measurements performed on non-porous nanosystems are compared to the findings of the computational analysis. In particular, the optical investigation discloses that the overall RL intensities of non-porous nanoscintillators both before and after the functionalization with the organic moieties increase coherently with the X-Ray mean energy (Figure 5.15d-f). Moreover, the Gaussian reconstruction of the RL spectra, recorded as function of the X-Ray photons mean energy, unveils that the higher the mean energy of the ionizing radiation, the higher the porphyrin emission sensitization (Figure 5.17b). At variance, the results of the simulations reveal that the total released energy and the fraction of energy deposited in SiO_2 decrease whereas the amount of energy released in ZnO increases with the X-Ray beam energy (Figures 5.23 and 5.24e,f).
For the two non-porous functionalized nanosystems and each X-Ray mean beam energy, Figure 5.25 shows the experimental porphyrin luminescence enhancement as a function of both the integrated RL intensity of the non-porous nanosystems before the TCPP adding (bottom axis) and the contribution to energy deposition of ZnO (top axis). The TCPP emission boosting is estimated as the ratio between the normalized RL intensities of dye emissions in the functionalized NPs (Norm $I_{Porphyrin}$) and that of the TCPP alone (Norm $I_{TCPP\ alone}$). The fraction of energy deposited in ZnO is evaluated as the ratio, multiplied by a factor of 100, between the energy released in ZnO ($E_{dep\ ZnO}$) and in the non-porous nanosystem together with the environment ($E_{dep\ tot}$). These data highlight that the sensitization of the porphyrin luminescence increases with both the ZS_{np}-A RL intensity (blue curve) and with the fraction of energy deposited in ZnO (red curve) as the X-Ray photons mean energy increments. It is worth noticing that, after the deposition of energy in ZnO, the generated secondary carries can either thermalize in ZnO, leading to its emission and hence radiative ET, or migrate towards the TCPP molecules, releasing small amount of energy in their prox-

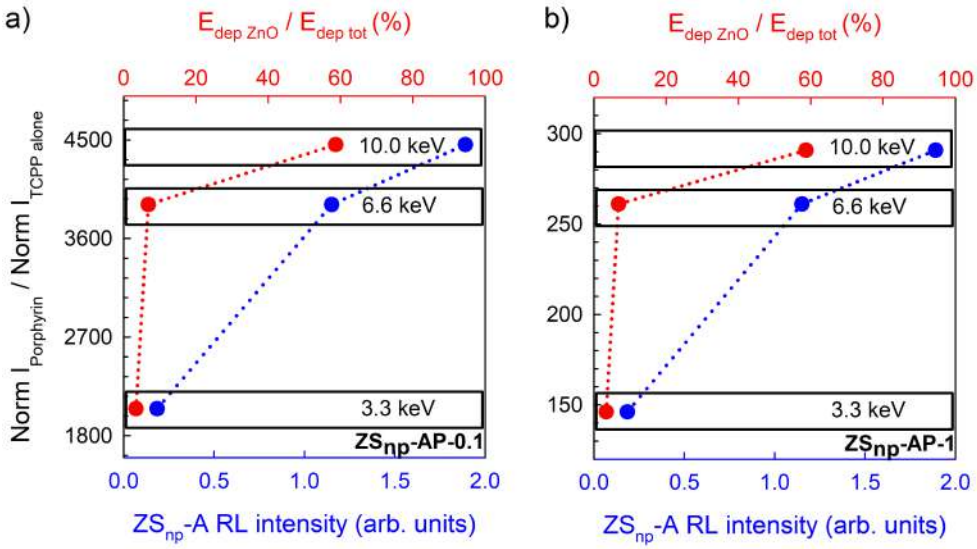

Figure 5.25: Normalized RL intensity emitted by the porphyrin in the non-porous nanosystem (ZS_{np}-AP-0.1 in **a**, ZS_{np}-AP-1 in **b**) divided by the normalized RL intensity of the porphyrin alone recorded upon excitation with X-Ray photons of 3.3 keV, 6.6 keV and 10 keV. The data are extracted from Gaussian deconvolutions of the RL spectra reported in Figure 5.15d-f and normalized to the porphyrin percentage weight present in the sample. The results are plotted as a function of both the overall RL intensity recorded for the non-porous ZnO/SiO_2 nanosystems with APTES decoration (ZS_{np}-A) and the percentage of energy deposited in ZnO ($E_{dep\ ZnO}$) with respect to the total released energy ($E_{dep\ tot}$).

imity and directly exciting them. Hence, since the used computational analysis provides useful information on the energy release but not on the probability of the subsequent excitation/emission processes in the matter, it is not trivial to discriminate the contribution of the two mechanisms, namely radiative ET and locally augmented energy deposition, in activating the porphyrin luminescence. Anyhow, the comparison between the experimental results and the simulations clearly demonstrates the crucial role of ZnO in promoting the porphyrin emission boosting. Indeed, the highest TCPP luminescence enhancement corresponds to the most intense ZnO luminescence and to the biggest amount of energy release in ZnO NPs, which occurs upon X-Ray excitation with a mean beam energy of 10.0 keV, due to the zinc absorption K edge at ∼9.67 keV.

These observations validate that the porphyrin emission is mainly activated by interaction with ZnO NPs while the SiO_2 matrix does not significantly contributes (Figure 5.26), highlighting that, for the two non-porous functionalized nanosystems, the triggering of porphyrin luminescence increases when the fraction of energy released in SiO_2 decreases, unlike ZnO.

In conclusion, this investigation unveils that the synergetic effect of ionizing ra-

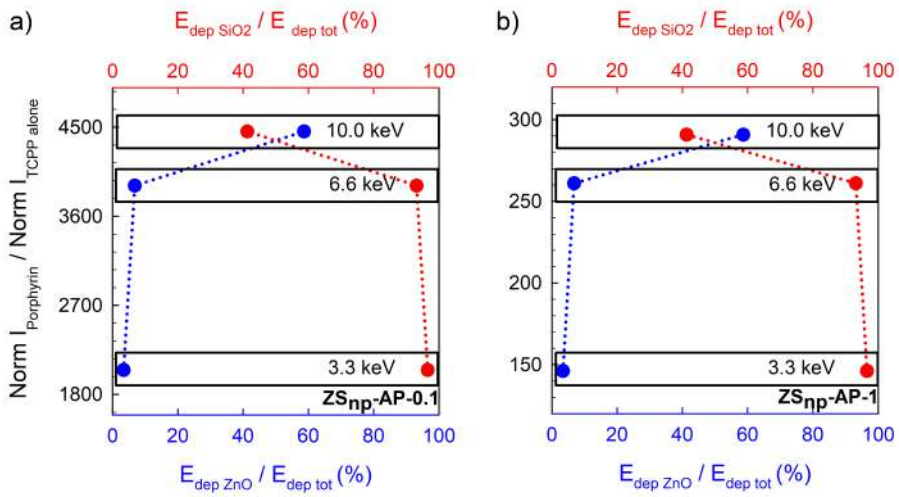

Figure 5.26: Normalized RL intensity emitted by the porphyrin in the non-porous nanosystem (ZS_{np}-AP-0.1 in **a**, ZS_{np}-AP-1 in **b**) divided by the normalized RL intensity of the porphyrin alone recorded upon excitation with X-Ray photons of 3.3 keV, 6.6 keV and 10 keV. The data are extracted from Gaussian deconvolutions of the RL spectra reported in Figure 5.15d-f and normalized to the porphyrin percentage weight present in the sample. The results are plotted as a function of both the percentage fraction of energy deposited in either ZnO ($E_{dep\ ZnO}$) or SiO_2 ($E_{dep\ SiO_2}$) with respect to the total released energy ($E_{dep\ tot}$) estimated for the three X-Ray mean beam energies by the computational analysis operating code B.

diation and proper nano-agent design may be further improved by exploiting the correlations between the X-Ray photon energy beam and the triggered process in the matter. Hence, further fundamental studies on the interaction mechanism occurring between the inorganic nanoscintillators and the organic dyes are of great importance.

5.5 General conclusions

This work on the design, the development and the study of multicomponent nanosystems for X-PDT evidences that its final optimal properties strongly depend on the physical and chemical properties of the inorganic scintillators as well as on the spatial distribution and concentration of the organic dyes. Indeed, the spectroscopic investigation carried out under either light or X-Rays excitation together with the computational studies discloses that:

- The ZnO defectiveness, and hence luminescence features, are not altered by the silica substrate porosity. However, the different morphologies of the two sets of nanosystems lead to discrepancies between their PLE spectra

and to peculiar RL behaviours upon exposure to X-Ray with 3.3 keV mean energy.

- APTES moieties are not luminescent and do not affect the energy position, spectral shape, and decay time of ZnO emission. Nevertheless, they introduce novel quenching channels, observed only upon ionizing radiation excitation.

- The anchoring of TCPP molecules on the ZnO/SiO_2 nanosystems is crucial to promote their interaction, whose underlying mechanisms and efficiency are affected by the formation of porphyrin aggregates, that in turn depends on the dye spatial distribution and loading level.

- Under light excitation, in the multicomponent nanosystems, ZnO NPs are able to trigger the TCPP luminescence only by a radiative energy transfer with a rather poor efficiency. Diffrently, upon ionizing radiation exposure, the porphyrin emission is largely enhanced by both the re-absorption mechanism and the locally augmented energy deposition.

- In the activation of porphyrin emission, ZnO plays a key role at variance with SiO_2, due to its scintillating properties and close proximity to TCPP molecules.

In conclusion, the optical properties, hence X-PDT performances, of the multicomponent nanosystems are strongly correlated to its design. The control of the spatial arrangement and of the concentration of the organic dye on the nanoscintillators is pivotal for optimizing the therapeutic effect of the functionalized nanostructures. Moreover, the comprehension of the processes triggered by the X-Ray photons in nanometric particles and their dependences on the material composition and size as well as on the radiation energy may pave the way for the engineering of NPs for targeted nanomedicine applications.

Conclusions and Perspectives

This PhD thesis addresses the investigation of the optical and catalytic properties of ZnO nanoparticles with different morphologies and functionalization, aiming at proposing them as agents for oncological treatments activated by ionizing radiation.

Indeed, ZnO nanosystems are of great interest for several applications, that include catalysis, sensing, opto-electronics, and medicine, due to their unique surface properties, that are also related to their defectiveness. In this frame, a solid comprehension of the dependence of the ZnO electronic, optical, and scintillation properties, together with its catalytic activity, on the morphology (size, interfaces, growth conditions, surface functionalization) as well as on the external parameters (the environmental conditions and the excitation energy) is pivotal for the engineering of ZnO based nanoparticles for therapeutic purposes.

This work includes i) a detailed study of the optical properties and the catalytic ability to produce cytotoxic species of several ZnO samples with different morphologies and ii) a spectroscopical investigation of the luminescence processes in multicomponent nanosystems, that feature ZnO nanoparticles and porphyrins, supported also by numerical Monte Carlo simulations of the energy deposition in nanosized structures.

First, radioluminescence and photoluminescence techniques are exploited to investigate four types of nanosized ZnO, with different diameters (5 or 22 nm), interfaces (isolated or supported onto highly porous silica NPs), and synthesis procedure (hot injection and sol-gel). In addition, for comparison, a commercial micrometric powder and an industrial bulk crystal are studied. Notably, the numerical analysis of both the radioluminescence and photoluminescence spectra unveils the occurrence of one near-UV excitonic peak $\sim$3.27 eV and four defect-related visible bands at $\sim$1.83 eV, $\sim$2.29 eV, $\sim$2.68 eV and $\sim$3.05 eV, that are identified in all samples. However, the excitation energy, the specimen size, and growth conditions influence the relative weight, the time dynamics, and the temperature dependences of those spectral components, leading to peculiar colour

outputs. Moreover, ZnO nanoparticles with different morphology, and hence defectiveness, exhibit peculiar radio-catalytic properties, further corroborating that the nature and the concentration of points defects influence the efficiency of the ZnO surface catalysis reactions.

This fundamental study on ZnO nanoparticles highlights the importance of governing the defect-related properties to fully exploit the potentiality of nanosized ZnO. Indeed, the possibility of tuning the NPs features by choosing properly the size, the interfaces, and the growth conditions paves the way for the engineering of ZnO nanoparticles not only for opto-electronics and medicine applications, but also in other fields like spintronics and the environment sectors.

Then, the acquired knowledge on the luminescence of ZnO nanoparticles is used as background to design and develop a multicomponent nanosystem for X-Ray induced photodynamic therapy, realized by functionalizing ZnO/SiO_2 nanoparticles with porphyrins. In particular, the analysis of the optical properties of samples with different dye concentrations and substrate porosity enables to clearly unveil the importance of the design of the multicomponent nano-agent to govern the interaction between its organic and inorganic components. In these nanosystems, under light excitation, the achieved spatial distribution between the ZnO nanoparticles and the porphyrin leads to the activation of the dye emission only through a rather weak re-absorption phenomenon. At variance, the triggering of the porphyrin luminescence is efficient upon X-Ray exposure thanks to both radiative energy transfer and, especially, locally augmented energy deposition. Moreover, in agreement with the experimental results, the computational simulation of non-porous nanosystems, evidences the key role of heavy ZnO nanoparticles in favouring the local release of the ionizing radiation energy and in promoting the enhancement of the porphyrin emission.

However, additional studies are required to understand the processes that occur under ionizing radiation excitation in multicomponent nanosized structures and that drive the interaction between the heavy nanoparticles and the surface ligands. For instance, aiming at the application of nanoparticles in the biomedical field, future works may include the investigation of the energy release process in nanometric systems in the biological aqueous environment that mimics the cellular conditions. The accomplishment of these knowledges may represent a significant step forward for the development of efficient and reliable nano-agents for nanomedicine, such as targeted diagnostics and therapies.

Bibliography

[1] Sun, T.; Zhang, Y. S.; Pang, B.; Hyun, D. C.; Yang, M.; Xia, Y. Engineered Nanoparticles for Drug Delivery in Cancer Therapy. Angew. Chemie Int. Ed. 2014, 53(26) 12320-12364. https://doi.org/10.1002/anie.201403036

[2] Khalid, K.; Tan, X.; Mohd Zaid, H. F.; Tao, Y.; Lye Chew, C.; Chu, D.-T.; Lam, M. K.; Ho, Y.-C.; Lim, J. W.; Chin Wei, L. Advanced in Developmental Organic and Inorganic Nanomaterial: A Review. Bioengineered 2020, 11 (1), 328-355. https://doi.org/10.1080/21655979.2020.1736240

[3] Anu Mary Ealia, S.; Saravanakumar, M. P. A Review on the Classification, Characterisation, Synthesis of Nanoparticles and Their Application. IOP Conf. Ser. Mater. Sci. Eng. 2017, 263, 032019. https://doi.org/10.1088/1757-899X/263/3/032019

[4] Yin, Y.; Talapin, D. The Chemistry of Functional Nanomaterials. Chem. Soc. Rev. 2013, 42 (7), 2484. https://doi.org/10.1039/c3cs90011h

[5] Mout, R.; Moyano, D. F.; Rana, S.; Rotello, V. M. Surface Functionalization of Nanoparticles for Nanomedicine. Chem. Soc. Rev. 2012, 41 (7), 2539. https://doi.org/10.1039/c2cs15294k

[6] Dowling, A. P. Development of Nanotechnologies. Mater. Today 2004, 7 (12), 30-35. https://doi.org/10.1016/S1369-7021(04)00628-5

[7] Mobasser, S.; Akbar Firoozi, A. Review of Nanotechnology Applications in Science and Engineering. J. Civ. Eng. Urban. 2016, 6 (4), 84-93. www.ojceu.ir

[8] Chavali, M. S.; Nikolova, M. P. Metal Oxide Nanoparticles and Their Applications in Nanotechnology. SN Appl. Sci. 2019, 1 (6), 607. https://doi.org/10.1007/s42452-019-0592-3

[9] Rizzo, L. Y.; Theek, B.; Storm, G.; Kiessling, F.; Lammers, T. Recent Progress in Nanomedicine: Therapeutic, Diagnostic and Theranostic Applications. Curr. Opin. Biotechnol. 2013, 24 (6), 1159-1166. https://doi.org/10.1016/j.copbio.2013.02.020

[10] Guo-Bin, Z.; Chao-Shu, S.; Zheng-Fu, H.; Jun-Yan, S.; Zhu-Xi, F.; Kirm, M.; Zimmerer, G. Photoluminescent Properties of ZnO Films Deposited on Si Substrates. Chinese Phys. Lett. 2001, 18 (3), 441–442. https://doi.org/10.1088/0256-307X/18/3/344

[11] Perego, J.; Villa, I.; Pedrini, A.; Padovani, E. C.; Crapanzano, R.; Vedda, A.; Dujardin, C.; Bezuidenhout, C. X.; Bracco, S.; Sozzani, P. E.; Comotti, A.; Gironi, L.; Beretta, M.; Salomoni, M.; Kratochwil, N.; Gundacker, S.; Auffray, E.; Meinardi, F.; Monguzzi, A. Composite Fast Scintillators Based on High-Z Fluorescent Metal–Organic Framework Nanocrystals. Nat. Photonics 2021, 15 (5), 393-400. https://doi.org/10.1038/s41566-021-00769-z

[12] Kim, J.; Lee, N.; Hyeon, T. Recent Development of Nanoparticles for Molecular Imaging. Philos. Trans. R. Soc. A Math. Phys. Eng. Sci. 2017, 375 (2107), 20170022. https://doi.org/10.1098/rsta.2017.0022

[13] Juzenas, P.; Chen, W.; Sun, Y.-P.; Coelho, M. A. N.; Generalov, R.; Generalova, N.; Christensen, I. L. Quantum Dots and Nanoparticles for Photodynamic and Radiation Therapies of Cancer. Adv. Drug Deliv. Rev. 2008, 60 (15), 1600-1614. https://doi.org/10.1088/1757-899X/263/3/032019

[14] Park, J. H.; Oh, N. Endocytosis and Exocytosis of Nanoparticles in Mammalian Cells. Int. J. Nanomedicine 2014, 51. https://doi.org/10.2147/IJN.S26592

[15] Doane, T. L.; Burda, C. The Unique Role of Nanoparticles in Nanomedicine: Imaging, Drug Delivery and Therapy. Chem. Soc. Rev. 2012, 41 (7), 2885. https://doi.org/10.1039/c2cs15260f

[16] Larue, L.; Ben Mihoub, A.; Youssef, Z.; Colombeau, L.; Acherar, S.; André, J. C.; Arnoux, P.; Baros, F.; Vermandel, M.; Frochot, C. Using X-Rays in Photodynamic Therapy: An Overview. Photochem. Photobiol. Sci. 2018, 17 (11), 1612-1650. https://doi.org/10.1039/c8pp00112j

[17] Denkova, A. G.; de Kruijff, R. M.; Serra-Crespo, P. Nanocarrier-Mediated Photochemotherapy and Photoradiotherapy. Adv. Healthc. Mater. 2018, 7 (8), 1-21. https://doi.org/10.1002/adhm.201701211

[18] Garibaldi, C.; Jereczek-Fossa, B. A.; Marvaso, G.; Dicuonzo, S.; Rojas, D. P.; Cattani, F.; Starzyńska, A.; Ciardo, D.; Surgo, A.; Leonardi, M. C.; Ricotti, R. Recent Advances in Radiation Oncology. Ecancermedicalscience 2017, 11, 1-19. https://doi.org/10.3332/ecancer.2017.785

[19] Baskar, R.; Lee, K. A.; Yeo, R.; Yeoh, K. W. Cancer and Radiation Therapy: Current Advances and Future Directions. Int. J. Med. Sci. 2012, 9 (3), 193-199. https://doi.org/10.7150/ijms.3635

[20] Ren, X.-D.; Hao, X.-Y.; Li, H.-C.; Ke, M.-R.; Zheng, B.-Y.; Huang, J.-D. Progress in the Development of Nanosensitizers for X-Ray-Induced Photodynamic Therapy. Drug Discov. Today 2018, 23 (10), 1791-1800. https://doi.org/10.1016/j.drudis.2018.05.029

[21] Sun, W.; Zhou, Z.; Pratx, G.; Chen, X.; Chen, H. Nanoscintillator-Mediated X-Ray Induced Photodynamic Therapy for Deep-Seated Tumors: From Concept to Biomedical Applications. Theranostics 2020, 10 (3), 1296-1318. https://doi.org/10.7150/thno.41578

[22] Kuncic, Z.; Lacombe, S. Nanoparticle Radio-Enhancement: Principles, Progress and Application to Cancer Treatment. Phys. Med. Biol. 2018, 63 (2), 02TR01. https://doi.org/10.1088/1361-6560/aa99ce

[23] Król, A.; Pomastowski, P.; Rafińska, K.; Railean-Plugaru, V.; Buszewski, B. Zinc Oxide Nanoparticles: Synthesis, Antiseptic Activity and Toxicity Mechanism. Adv. Colloid Interface Sci. 2017, 249, 37-52. https://doi.org/10.1016/j.cis.2017.07.033

[24] Crapanzano, R.; Secchi, V.; Villa, I. Co-Adjuvant Nanoparticles for Radiotherapy Treatments of Oncological Diseases. Appl. Sci. 2021, 11 (15), 7073. https://doi.org/10.3390/app11157073

[25] Villa, I.; Villa, C.; Crapanzano, R.; Secchi, V.; Taw, M.; Trombetta, E.; Porretti, L.; Brambilla, A.; Campione, M.; Torrente, Y.; Vedda, A.; Monguzzi, A. Functionalized Scintillating Nanotubes for Simultaneous Radio- and Photodynamic Therapy of Cancer. ACS Appl. Mater. Interfaces 2021, 13, 11, 12997-13008 https://doi.org/10.1021/acsami.1c02504

[26] Chen, H.; Wang, G. D.; Chuang, Y. J.; Zhen, Z.; Chen, X.; Biddinger, P.; Hao, Z.; Liu, F.; Shen, B.; Pan, Z.; Xie, J. Nanoscintillator-Mediated X-Ray Inducible Photodynamic Therapy for in Vivo Cancer Treatment. Nano Lett. 2015, 15 (4), 2249-2256. https://doi.org/10.1021/nl504044p

[27] Incerti, S.; Douglass, M.; Penfold, S.; Guatelli, S.; Bezak, E. Review of Geant4-DNA Applications for Micro and Nanoscale Simulations. Phys. Medica 2016, 32 (10), 1187-1200. https://doi.org/10.1016/j.ejmp.2016.09.007

[28] Özgür, Ö.; Alivov, Y. I.; Liu, C.; Teke, A.; Reshchikov, M. A.; Doğan, S.; Avrutin, V.; Cho, S. J.; Morkç, H. A Comprehensive Review of ZnO Materials and Devices. J. Appl. Phys. 2005, 98 (4), 1-103. https://doi.org/10.1063/1.1992666

[29] Djurišić, A. B.; Leung, Y. H. Optical Properties of ZnO Nanostructures. Small 2006, 2 (8-9), 944-961. https://doi.org/10.1002/smll.200600134

[30] Janotti, A.; Van De Walle, C. G. Fundamentals of Zinc Oxide as a Semiconductor. Reports Prog. Phys. 2009, 72 (12). https://doi.org/10.1088/0034-4885/72/12/126501

[31] Klingshirn, C. F. ZnO: Material, Physics and Applications. ChemPhysChem 2007, 8 (6), 782-803. https://doi.org/10.1002/cphc.200700002

[32] Mostoni; Milana; Credico; D'Arienzo; Scotti. Zinc-Based Curing Activators: New Trends for Reducing Zinc Content in Rubber Vulcanization Process. Catalysts 2019, 9 (8), 664. https://doi.org/10.3390/catal9080664

[33] Kumar, R.; Al-Dossary, O.; Kumar, G.; Umar, A. Zinc Oxide Nanostructures for NO_2 Gas-Sensor Applications: A Review. Nano-Micro Lett. 2015, 7 (2), 97-120 https://doi.org/10.1007/s40820-014-0023-3

[34] Mishra, P. K.; Mishra, H.; Ekielski, A.; Talegaonkar, S.; Vaidya, B. Zinc Oxide Nanoparticles: A Promising Nanomaterial for Biomedical Applications. Drug Discov. Today 2017, 22 (12), 1825-1834. https://doi.org/10.1016/j.drudis.2017.08.006

[35] Yanagida, T.; Fujimoto, Y.; Yamanoi, K.; Kano, M.; Wakamiya, A.; Kurosawa, S.; Sarukura, N. Optical and Scintillation Properties of Bulk ZnO

Crystal. Phys. Status Solidi Curr. Top. Solid State Phys. 2012, 9 (12), 2284-2287. https://doi.org/10.1002/pssc.201200176

[36] Zhang, Y.; Ram, M. K.; Stefanakos, E. K.; Goswami, D. Y. Synthesis, Characterization, and Applications of ZnO Nanowires. J. Nanomater. 2012, 2012, 1-22. https://doi.org/10.1155/2012/624520

[37] Rodnyi, P. A.; Khodyuk, I. V. Optical and Luminescence Properties of Zinc Oxide (Review). Opt. Spectrosc. (English Transl. Opt. i Spektrosk. 2011, 111 (5), 776-785. https://doi.org/10.1134/S0030400X11120216

[38] D'Arienzo, M.; Mostoni, S.; Crapanzano, R.; Cepek, C.; Di Credico, B.; Fasoli, M.; Polizzi, S.; Vedda, A.; Villa, I.; Scotti, R. Insight into the Influence of ZnO Defectivity on the Catalytic Generation of Environmentally Persistent Free Radicals in ZnO/SiO_2 Systems. J. Phys. Chem. C 2019, 123 (35), 21651-21661. https://doi.org/10.1021/acs.jpcc.9b06900

[39] Lv, J.; Li, C.; Chai, Z. Defect Luminescence and Its Mediated Physical Properties in ZnO. J. Lumin. 2019, 208 (December 2018), 225-237. https://doi.org/10.1016/j.jlumin.2018.12.050

[40] Xiong, G.; Pal, U.; Serrano, J. G. Correlations among Size, Defects, and Photoluminescence in ZnO Nanoparticles. J. Appl. Phys. 2007, 101 (2). https://doi.org/10.1063/1.2424538

[41] Gbur, T.; Čuba, V.; Múčka, V.; Nikl, M.; Knížek, K.; Pospíšil, M.; Jakubec, I. Photochemical Preparation of ZnO Nanoparticles. J. Nanoparticle Res. 2011, 13 (10), 4529-4537. https://doi.org/10.1007/s11051-011-0407-y

[42] Qi, K.; Cheng, B.; Yu, J.; Ho, W. Review on the Improvement of the Photocatalytic and Antibacterial Activities of ZnO. J. Alloys Compd. 2017, 727, 792-820. https://doi.org/10.1016/j.jallcom.2017.08.142

[43] Baruah, S.; Mahmood, M. A.; Myint, M. T. Z.; Bora, T.; Dutta, J. Enhanced Visible Light Photocatalysis through Fast Crystallization of Zinc Oxide Nanorods. Beilstein J. Nanotechnol. 2010, 1, 14-20. https://doi.org/10.3762/bjnano.1.3

[44] Generalov, R.; Kuan, W. B.; Chen, W.; Kristensen, S.; Juzenas, P. Radiosensitizing Effect of Zinc Oxide and Silica Nanocomposites on Cancer Cells. Colloids Surfaces B Biointerfaces 2015, 129, 79-86.https://doi.org/10.1016/j.colsurfb.2015.03.026

[45] Li, J.; Guo, D.; Wang, X.; Wang, H.; Jiang, H.; Chen, B. The Photodynamic Effect of Different Size ZnO Nanoparticles on Cancer Cell Proliferation In Vitro. Nanoscale Res. Lett. 2010, 5 (6), 1063-1071. https://doi.org/10.1007/s11671-010-9603-4

[46] Procházková, L.; Pelikánová, I. T.; Mihóková, E.; Dědic, R.; Čuba, V. Novel Scintillating Nanocomposite for X-Ray Induced Photodynamic Therapy. Radiat. Meas. 2019, 121 (December 2018), 13-17. https://doi.org/10.1016/j.radmeas.2018.12.008

[47] Bulin, A.-L.; Truillet, C.; Chouikrat, R.; Lux, F.; Frochot, C.; Amans, D.; Ledoux, G.; Tillement, O.; Perriat, P.; Barberi-Heyob, M.; Dujardin, C. X-Ray-Induced Singlet Oxygen Activation with Nanoscintillator-Coupled Porphyrins. J. Phys. Chem. C 2013, 117 (41), 21583-21589. https://doi.org/10.1021/jp4077189

[48] Sadjadpour, S.; Safarian, S.; Zargar, S. J.; Sheibani, N. Antiproliferative Effects of ZnO, ZnO-MTCP, and ZnO-CuMTCP Nanoparticles with Safe Intensity UV and X-Ray Irradiation. Biotechnol. Appl. Biochem. 2016, 63 (1), 113-124. https://doi.org/10.1002/bab.1344

[49] Crapanzano, R.; Villa, I.; Mostoni, S.; D'Arienzo, M.; Di Credico, B.; Fasoli, M.; Scotti, R.; Vedda, A. Morphology Related Defectiveness in Zno Luminescence: From Bulk to Nano-Size. Nanomaterials 2020, 10 (10), 1-19. https://doi.org/10.3390/nano10101983

[50] Park, W.; Shin, H.; Choi, B.; Rhim, W.-K.; Na, K.; Keun Han, D. Advanced Hybrid Nanomaterials for Biomedical Applications. Prog. Mater. Sci. 2020, 114, 100686. https://doi.org/10.1016/j.pmatsci.2020.100686

[51] Romero, G.; Moya, S. E. Synthesis of Organic Nanoparticles; 2012; pp 115-141. https://doi.org/10.1016/B978-0-12-415769-9.00004-2

[52] Willets, K. A.; Van Duyne, R. P. Localized Surface Plasmon Resonance Spectroscopy and Sensing. Annu. Rev. Phys. Chem. 2007, 58 (1), 267-297. https://doi.org/10.1146/annurev.physchem.58.032806.104607

[53] Giner-Casares, J. J.; Henriksen-Lacey, M.; Coronado-Puchau, M.; Liz-Marzán, L. M. Inorganic Nanoparticles for Biomedicine: Where Materials Scientists Meet Medical Research. Mater. Today 2016, 19 (1), 19-28. https://doi.org/10.1016/j.mattod.2015.07.004

[54] Carey, G. H.; Abdelhady, A. L.; Ning, Z.; Thon, S. M.; Bakr, O. M.; Sargent, E. H. Colloidal Quantum Dot Solar Cells. Chem. Rev. 2015, 115 (23), 12732-12763. https://doi.org/10.1021/acs.chemrev.5b00063

[55] Djurišić, A. B.; Chen, X.; Leung, Y. H.; Man Ching Ng, A. ZnO Nanostructures: Growth, Properties and Applications. J. Mater. Chem. 2012, 22 (14), 6526-6535. https://doi.org/10.1039/c2jm15548f

[56] Lu, A.-H.; Salabas, E. L.; Schüth, F. Magnetic Nanoparticles: Synthesis, Protection, Functionalization, and Application. Angew. Chemie Int. Ed. 2007, 46 (8), 1222-1244. https://doi.org/10.1039/c2jm15548f

[57] Shang, L.; Nienhaus, K.; Nienhaus, G. Engineered Nanoparticles Interacting with Cells: Size Matters. J. Nanobiotechnology 2014, 12 (1), 5. https://doi.org/10.1186/1477-3155-12-5

[58] Albanese, A.; Tang, P. S.; Chan, W. C. W. The Effect of Nanoparticle Size, Shape, and Surface Chemistry on Biological Systems. Annu. Rev. Biomed. Eng. 2012, 14 (1), 1-16. https://doi.org/10.1146/annurev-bioeng-071811-150124

[59] Park, J.-H.; Gu, L.; von Maltzahn, G.; Ruoslahti, E.; Bhatia, S. N.; Sailor, M. J. Biodegradable Luminescent Porous Silicon Nanoparticles for in Applications. Nat. Mater. 2009, 8 (4), 331-336. https://doi.org/10.1038/nmat2398

[60] Nune, S. K.; Gunda, P.; Thallapally, P. K.; Lin, Y.-Y.; Laird Forrest, M.; Berkland, C. J. Nanoparticles for Biomedical Imaging. Expert Opin. Drug Deliv. 2009, 6 (11), 1175-1194. https://doi.org/10.1517/17425240903229031

[61] Mahvi, D. A.; Liu, R.; Grinstaff, M. W.; Colson, Y. L.; Raut, C. P. Local Cancer Recurrence: The Realities, Challenges, and Opportunities for New Therapies. CA. Cancer J. Clin. 2018, 68 (6), 488-505. https://doi.org/10.3322/caac.21498

[62] Nurgali, K.; Jagoe, R. T.; Abalo, R. Editorial: Adverse Effects of Cancer Chemotherapy: Anything New to Improve Tolerance and Reduce Sequelae? Front. Pharmacol. 2018, 9. https://doi.org/10.3389/fphar.2018.00245

[63] Park, K. Controlled Drug Delivery Systems: Past Forward and Future Back. J. Control. Release 2014, 190, 3-8. https://doi.org/10.1016/j.jconrel.2014.03.054

[64] Huh, A. J.; Kwon, Y. J. "Nanoantibiotics": A New Paradigm for Treating Infectious Diseases Using Nanomaterials in the Antibiotics Resistant Era. J. Control. Release 2011, 156 (2), 128-145. https://doi.org/10.1016/j.jconrel.2011.07.002

[65] Pokharkar, V.; Bhumkar, D.; Suresh, K.; Shinde, Y.; Gairola, S.; Jadhav, S. S. Gold Nanoparticles as a Potential Carrier for Transmucosal Vaccine Delivery. J. Biomed. Nanotechnol. 2011, 7 (1), 57-59. https://doi.org/10.1166/jbn.2011.1200

[66] Jeong, M.; Park, J.-H. Nanomedicine for the Treatment of Rheumatoid Arthritis. Mol. Pharm. 2021, 18 (2), 539-549. https://doi.org/10.1021/acs.molpharmaceut.0c00295

[67] Beik, J.; Abed, Z.; Ghoreishi, F. S.; Hosseini-Nami, S.; Mehrzadi, S.; Shakeri-Zadeh, A.; Kamrava, S. K. Nanotechnology in Hyperthermia Cancer Therapy: From Fundamental Principles to Advanced Applications. J. Control. Release 2016, 235, 205-221. https://doi.org/10.1016/j.jconrel.2016.05.062

[68] Rajendran, M. Quinones as Photosensitizer for Photodynamic Therapy: ROS Generation, Mechanism and Detection Methods. Photodiagnosis Photodyn. Ther. 2016, 13, 175-187. https://doi.org/10.1016/j.pdpdt.2015.07.177

[69] Mallidi, S.; Anbil, S.; Bulin, A.-L.; Obaid, G.; Ichikawa, M.; Hasan, T. Beyond the Barriers of Light Penetration: Strategies, Perspectives and Possibilities for Photodynamic Therapy. Theranostics 2016, 6 (13), 2458-2487. https://doi.org/10.7150/thno.16183

[70] Lucky, S. S.; Soo, K. C.; Zhang, Y. Nanoparticles in Photodynamic Therapy. Chem. Rev. 2015, 115 (4), 1990-2042. https://doi.org/10.1021/cr5004198

[71] Connell, P. P.; Hellman, S. Advances in Radiotherapy and Implications for the next Century: A Historical Perspective. Cancer Res. 2009, 69 (2), 383-392. https://doi.org/10.1158/0008-5472.CAN-07-6871

[72] Moding, E. J.; Kastan, M. B.; Kirsch, D. G. Strategies for Optimizing the Response of Cancer and Normal Tissues to Radiation. Nat. Rev. Drug Discov. 2013, 12 (7), 526-542. https://doi.org/10.1038/nrd4003

[73] Glenn F. Knoll. Radiation Detection and Measurement. Med. Phys. 1980, 7 (4), 397-398. https://doi.org/10.1118/1.594739

[74] Evans, R. D. The Atomic Nucleus; 1956; Vol. 2. https://doi.org/10.1002/aic.690020327

[75] Buchalska, M.; Łabuz, P.; Bujak, Ł.; Szewczyk, G.; Sarna, T.; Maćkowski, S.; Macyk, W. New Insight into Singlet Oxygen Generation at Surface Modified Nanocrystalline TiO_2 - the Effect of near-Infrared Irradiation. J. Chem. Soc. Dalt. Trans. 2013, 42 (26), 9468-9475. https://doi.org/10.1039/C3DT50399B

[76] Lipovsky, A.; Tzitrinovich, Z.; Friedmann, H.; Applerot, G.; Gedanken, A.; Lubart, R. EPR Study of Visible Light-Induced ROS Generation by Nanoparticles of ZnO. J. Phys. Chem. C 2009, 113 (36), 15997-16001. https://doi.org/10.1021/jp904864g

[77] Molina Higgins, M. C.; Clifford, D. M.; Rojas, J. V. Au@TiO_2 Nanocomposites Synthesized by X-Ray Radiolysis as Potential Radiosensitizers. Appl. Surf. Sci. 2018, 427, 702-710. https://doi.org/10.1016/j.apsusc.2017.08.094

[78] Dujardin, C.; Auffray, E.; Bourret-Courchesne, E.; Dorenbos, P.; Lecoq, P.; Nikl, M.; Vasil'Ev, A. N.; Yoshikawa, A.; Zhu, R. Y. Needs, Trends, and Advances in Inorganic Scintillators. IEEE Trans. Nucl. Sci. 2018, 65 (8), 1977-1997. https://doi.org/10.1109/TNS.2018.2840160

[79] De Luca, G.; Romeo, A.; Villari, V.; Micali, N.; Foltran, I.; Foresti, E.; Lesci, I. G.; Roveri, N.; Zuccheri, T.; Scolaro, L. M. Self-Organizing Functional Materials via Ionic Self Assembly: Porphyrins Hand J-Aggregates on Synthetic Chrysotile Nanotubes. J. Am. Chem. Soc. 2009, 131 (20), 6920-6921. https://doi.org/10.1021/ja901273h

[80] Monguzzi, A.; Lesci, I. G.; Capitani, G. C.; Santo, N.; Roveri, N.; Campione, M. Mineral-Organic Hybrid Nanotubes as Highly Sensitive Solid State Optical Chemical Sensors. Phys. Chem. Chem. Phys. 2014, 16 (6), 2491-2498. https://doi.org/10.1039/c3cp54467b

[81] Bricks, J. L.; Slominskii, Y. L.; Panas, I. D.; Demchenko, A. P. Fluorescent J-Aggregates of Cyanine Dyes: Basic Research and Applications Review. Methods Appl. Fluoresc. 2018, 6 (1). https://doi.org/10.1088/2050-6120/aa8d0d

[82] Maiti, N. C.; Mazumdar, S.; Periasamy, N. J- and H-Aggregates of Porphyrin - Surfactant Complexes: Time-Resolved Fluorescence and Other Spectroscopic Studies. J. Phys. Chem. B 1998, 102 (9), 1528-1538. https://doi.org/10.1021/jp9723372

[83] Villari, V.; Mineo, P.; Scamporrino, E.; Micali, N. Role of the Hydrogen-Bond in Porphyrin J-Aggregates. RSC Adv. 2012, 2 (33), 12989-12998. https://doi.org/10.1039/c2ra22260d

[84] Khairutdinov, R. F.; Serpone, N. Photoluminescence and Transient Spectroscopy of Free Base Porphyrin Aggregates. J. Phys. Chem. B 1999, 103 (5), 761-769 https://doi.org/10.1021/jp980869s

[85] Edouard, M.; Broggio, D.; Prezado, Y.; Estève, F.; Elleaume, H.; Adam, J. F. Treatment Plans Optimization for Contrast-Enhanced Synchrotron Stereotactic Radiotherapy. Med. Phys. 2010, 37 (6Part1), 2445-2456. https://doi.org/10.1118/1.3327455

[86] Bulin, A.-L.; Vasil'ev, A.; Belsky, A.; Amans, D.; Ledoux, G.; Dujardin, C. Modelling Energy Deposition in Nanoscintillators to Predict the Efficiency of the X-Ray-Induced Photodynamic Effect. Nanoscale 2015, 7 (13), 5744-5751. https://doi.org/10.1039/C4NR07444K

[87] Cerrato, E.; Paganini, M. C.; Giamello, E. Photoactivity under Visible Light of Defective ZnO Investigated by EPR Spectroscopy and Photoluminescence. J. Photochem. Photobiol. A Chem. 2020, 397, 112531. https://doi.org/10.1016/j.jphotochem.2020.112531

[88] Sengupta, A.; Sarkar, C. K. Introduction to Nano; Engineering Materials; Springer Berlin Heidelberg: Berlin, Heidelberg, 2015. https://doi.org/10.1007/978-3-662-47314-6

[89] Santos, D. A. A.; Junior, E. A. S.; Macêdo, M. A. Radioluminescence in ZnO. Radiat. Phys. Chem. 2010, 79 (5), 612-614. https://doi.org/10.1016/j.radphyschem.2009.12.008

[90] Demidenko, V. A.; Gorokhova, E. I.; Khodyuk, I. V.; Khristich, O. A.; Mikhrin, S. B.; Rodnyi, P. A. Scintillation Properties of Ceramics Based on Zinc Oxide. Radiat. Meas. 2007, 42 (4-5), 549-552. https://doi.org/10.1016/j.radmeas.2007.01.050

[91] Ajmal, H. M. S.; Khan, F.; Nam, K.; Kim, H. Y.; Kim, S. D. Ultraviolet Photodetection Based on High-Performance Co-Plus-Ni Doped ZnO Nanorods Grown by Hydrothermal Method on Transparent Plastic Substrate. Nanomaterials 2020, 10 (6), 1225. https://doi.org/10.3390/nano10061225

[92] Zu, P.; Tang, Z. K.; Wong, G. K. L.; Kawasaki, M.; Ohtomo, A.; Koinuma, H.; Segawa, Y. Ultraviolet Spontaneous and Stimulated Emissions from ZnO Microcrystallite Thin Films at Room Temperature. Solid State Commun. 1997, 103 (8), 459-463. https://doi.org/10.1016/S0038-1098(97)00216-0

[93] Zhao, X.; Chen, Z.; Luo, Y.; Wang, L. Giant Enhanced Infrared and Orange Emissions of ZnO Nanoparticles Induced by Rich Oxygen Atmosphere. Solid State Commun. 2008, 147 (11-12), 447-451 https://doi.org/10.1016/j.ssc.2008.07.012

[94] Achour, A.; Islam, M.; Vizireanu, S.; Ahmad, I.; Akram, M. A.; Saeed, K.; Dinescu, G.; Pireaux, J. J. Orange/Red Photoluminescence Enhancement upon Sf6 Plasma Treatment of Vertically Aligned Zno Nanorods. Nanomaterials 2019, 9 (5). https://doi.org/10.3390/nano9050794

[95] Vanheusden, K.; Seager, C. H.; Warren, W. L.; Tallant, D. R.; Voigt, J. A. Correlation between Photoluminescence and Oxygen Vacancies in ZnO Phosphors. Appl. Phys. Lett. 1996, 68 (3), 403-405. https://doi.org/10.1063/1.116699

[96] Drouilly, C.; Krafft, J. M.; Averseng, F.; Casale, S.; Bazer-Bachi, D.; Chizallet, C.; Lecocq, V.; Vezin, H.; Lauron-Pernot, H.; Costentin, G. ZnO Oxygen Vacancies Formation and Filling Followed by in Situ Photoluminescence and in Situ EPR. J. Phys. Chem. C 2012, 116 (40), 21297-21307 https://doi.org/10.1021/jp307693y

[97] Kasai, P. H. Electron Spin Resonance Studies of Donors and Acceptors in ZnO. Phys. Rev. 1963, 130 (3), 989-995. https://doi.org/10.1103/PhysRev.130.989

[98] Polarz, S.; Roy, A.; Lehmann, M.; Driess, M.; Kruis, F. E.; Hoffmann, A.; Zimmer, P. Structure-Property-Function Relationships in Nanoscale Oxide Sensors: A Case Study Based on Zinc Oxide. Adv. Funct. Mater. 2007, 17 (8), 1385-1391. https://doi.org/10.1002/adfm.200700139

[99] Buryi, M.; Babin, V.; Chang, Y.-Y.; Remeš, Z.; Mičová, J.; Šimek, D. Influence of Precursor Age on Defect States in ZnO Nanorods. Appl. Surf. Sci. 2020, 525, 146448. https://doi.org/10.1016/j.apsusc.2020.146448

[100] Zhang, M.; Averseng, F.; Krafft, J.-M.; Borghetti, P.; Costentin, G.; Stankic, S. Controlled Formation of Native Defects in Ultrapure ZnO for the Assignment of Green Emissions to Oxygen Vacancies. J. Phys. Chem. C 2020, 124 (23), 12696-12704. https://doi.org/10.1021/acs.jpcc.0c01078

[101] Li, M.; Xing, G.; Xing, G.; Wu, B.; Wu, T.; Zhang, X.; Sum, T. C. Origin of Green Emission and Charge Trapping Dynamics in ZnO Nanowires. Phys. Rev. B - Condens. Matter Mater. Phys. 2013, 87 (11). https://doi.org/10.1103/PhysRevB.87.115309

[102] Zhou, X.; Kuang, Q.; Jiang, Z. Y.; Xie, Z. X.; Xu, T.; Huang, R. Bin; Zheng, L. S. The Origin of Green Emission of ZnO Microcrystallites: Surface-Dependent Light Emission Studied by Cathodoluminescence. J. Phys. Chem. C 2007, 111 (32), 12091-12093. https://doi.org/10.1021/jp071928h

[103] Sekiguchi, T.; Miyashita, S.; Obara, K.; Shishido, T.; Sakagami, N. Hydrothermal Growth of ZnO Single Crystals and Their Optical Characterization. J. Cryst. Growth 2000, 214, 72-76. https://doi.org/10.1016/S0022-0248(00)00065-8

[104] Frodason, Y. K.; Johansen, K. M.; Galeckas, A.; Vines, L. Broad Luminescence from Donor-Complexed LiZn and NaZn Acceptors in ZnO. Phys. Rev. B 2019, 100 (18), 184102. https://doi.org/10.1103/PhysRevB.100.184102

[105] Lyons, J. L.; Alkauskas, A.; Janotti, A.; Van de Walle, C. G. Deep Donor State of the Copper Acceptor as a Source of Green Luminescence in ZnO. Appl. Phys. Lett. 2017, 111 (4), 042101. https://doi.org/10.1063/1.4995404

[106] Cao, B.; Cai, W.; Zeng, H. Temperature-Dependent Shifts of Three Emission Bands for ZnO Nanoneedle Arrays. Appl. Phys. Lett. 2006, 88 (16), 18-21. https://doi.org/10.1063/1.2195694

[107] Han, N. S.; Shim, H. S.; Seo, J. H.; Kim, S. Y.; Park, S. M.; Song, J. K. Defect States of ZnO Nanoparticles: Discrimination by Time-Resolved Photoluminescence Spectroscopy. J. Appl. Phys. 2010, 107 (8). https://doi.org/10.1063/1.3382915

[108] Zeng, H.; Duan, G.; Li, Y.; Yang, S.; Xu, X.; Cai, W. Blue Luminescence of ZnO Nanoparticles Based on Non-Equilibrium Processes: Defect Origins and Emission Controls. Adv. Funct. Mater. 2010, 20 (4), 561-572. https://doi.org/10.1002/adfm.200901884

[109] Villa, I.; Lauria, A.; Moretti, F.; Fasoli, M.; Dujardin, C.; Niederberger, M.; Vedda, A. Radio-Luminescence Spectral Features and Fast Emission in Hafnium Dioxide Nanocrystals. Phys. Chem. Chem. Phys. 2018, 20 (23), 15907-15915. https://doi.org/10.1039/c8cp01230j

[110] Tissue, B. M.; Bihari, B. Lanthanide Luminescence as a Probe of Nanocrystalline Materials. J. Fluoresc. 1998, 8 (4 SPEC.ISS.), 289-294. https://doi.org/10.1023/A:1020508112078

[111] Vistovskyy, V. V.; Zhyshkovych, A. V.; Halyatkin, O. O.; Mitina, N. E.; Zaichenko, A. S.; Rodnyi, P. A.; Vasil'Ev, A. N.; Gektin, A. V.; Voloshinovskii, A. S. The Luminescence of BaF_2 Nanoparticles upon High-Energy Excitation. J. Appl. Phys. 2014, 116 (5). https://doi.org/10.1063/1.4892112

[112] Najib, S.; Bakan, F.; Abdullayeva, N.; Bahariqushchi, R.; Kasap, S.; Franzò, G.; Sankir, M.; Demirci Sankir, N.; Mirabella, S.; Erdem, E. Tailoring Morphology to Control Defect Structures in ZnO Electrodes for High-Performance Supercapacitor Devices. Nanoscale 2020, 12, 16162-16172. https://doi.org/10.1039/D0NR03921G

[113] Zhou, H.; Alves, H.; Hofmann, D. M.; Kriegseis, W.; Meyer, B. K.; Kaczmarczyk, G.; Hoffmann, A. Behind the Weak Excitonic Emission of ZnO Quantum Dots: $ZnO/Zn(OH)_2$ Core-Shell Structure. Appl. Phys. Lett. 2002, 80 (2), 210-212. https://doi.org/10.1063/1.1432763

[114] Liu, F. Z.; Guo, M. Y.; Leung, Y. H.; Ng, A. M. C.; Djurišićc, A. B.; Chan, W. K. Influence of Native Defects on Photocatalytic Activity of ZnO; 2013; pp 75-76. https://doi.org/10.1063/1.4848292

[115] Baruah, S.; Rafique, R.F.; Dutta J. Visible Light Photocatalysis by Tailoring Crystal Defects in Zinc Oxide Nanostructures. Nano 2008, 03 (05). 399-407. https://doi.org/10.1142/S179329200800126X

[116] Ferrari-Lima, A. M.; de Souza, R. P.; Mendes, S. S.; Marques, R. G.; Gimenes, M. L.; Fernandes-Machado, N. R. C. Photodegradation of Benzene, Toluene and Xylenes under Visible Light Applying N-Doped Mixed TiO_2 and ZnO Catalysts. Catal. Today 2015, 241, 40-46. https://doi.org/10.1016/j.cattod.2014.03.042

[117] Youssef, Z.; Vanderesse, R.; Colombeau, L.; Baros, F.; Roques-Carmes, T.; Frochot, C.; Wahab, H.; Toufaily, J.; Hamieh, T.; Acherar, S.; et al. The Application of Titanium Dioxide, Zinc Oxide, Fullerene, and Graphene Nanoparticles in Photodynamic Therapy. Cancer Nanotechnol. 2017, 8 (1), 6. https://doi.org/10.1186/s12645-017-0032-2

[118] Yi, C.; Yu, Z.; Ren, Q.; Liu, X.; Wang, Y.; Sun, X.; Yin, S.; Pan, J.; Huang, X. Nanoscale ZnO-Based Photosensitizers for Photodynamic Therapy. Photodiagnosis Photodyn. Ther. 2020, 30, 101694. https://doi.org/10.1016/j.pdpdt.2020.101694

[119] Meyer, T. J.; Scherzad, A.; Moratin, H.; Gehrke, T. E.; Killisperger, J.; Hagen, R.; Wohlleben, G.; Polat, B.; Dembski, S.; Kleinsasser, N.; et al. The Radiosensitizing Effect of Zinc Oxide Nanoparticles in Sub-Cytotoxic Dosing Is Associated with Oxidative Stress In Vitro. Materials (Basel). 2019, 12 (24), 4062. https://doi.org/10.3390/ma12244062

[120] Zhang, H.; Patel, N.; Xiong, J.; Ding, S. Targeting and Noninvasive Treatment of Hepatocellular Carcinoma in Situ by ZnO Nanorod-Mediated Concurrent Chemoradiotherapy. RSC Adv. 2015, 5 (104), 85720-85729. https://doi.org/10.1039/C5RA16880E

[121] Hariharan, R.; Senthilkumar, S.; Suganthi, A.; Rajarajan, M. Synthesis and Characterization of Doxorubicin Modified ZnO/PEG Nanomaterials and Its Photodynamic Action. J. Photochem. Photobiol. B Biol. 2012, 116, 56-65. https://doi.org/10.1016/j.jphotobiol.2012.08.008

[122] Zhang, H.; Shan, Y.; Dong, L. A Comparison of TiO_2 and ZnO Nanoparticles as Photosensitizers in Photodynamic Therapy for Cancer. J. Biomed. Nanotechnol. 2014, 10 (8), 1450-1457. https://doi.org/10.1166/jbn.2014.1961

[123] Zhang, C.; Zhao, K.; Bu, W.; Ni, D.; Liu, Y.; Feng, J.; Shi, J. Marriage of Scintillator and Semiconductor for Synchronous Radiotherapy and Deep Photodynamic Therapy with Diminished Oxygen Dependence. Angew. Chemie - Int. Ed. 2015, 54 (6), 1770-1774. https://doi.org/10.1002/anie.201408472

[124] Tadiello, L.; D'Arienzo, M.; Di Credico, B.; Hanel, T.; Matejka, L.; Mauri, M.; Morazzoni, F.; Simonutti, R.; Spirkova, M.; Scotti, R. The Filler-Rubber Interface in Styrene Butadiene Nanocomposites with Anisotropic Silica Particles: Morphology and Dynamic Properties. Soft Matter 2015, 11 (20), 4022-4033. https://doi.org/10.1039/C5SM00536A

[125] Scotti, R.; Conzatti, L.; D'Arienzo, M.; Di Credico, B.; Giannini, L.; Hanel, T.; Stagnaro, P.; Susanna, A.; Tadiello, L.; Morazzoni, F. Shape Controlled Spherical (0D) and Rod-like (1D) Silica Nanoparticles in Silica/Styrene Butadiene Rubber Nanocomposites: Role of the Particle Morphology on the Filler Reinforcing Effect. Polymer (Guildf). 2014, 55 (6), 1497-1506. https://doi.org/10.1016/j.polymer.2014.01.025

[126] Susanna, A.; D'Arienzo, M.; Di Credico, B.; Giannini, L.; Hanel, T.; Grandori, R.; Morazzoni, F.; Mostoni, S.; Santambrogio, C.; Scotti, R. Catalytic Effect of ZnO Anchored Silica Nanoparticles on Rubber Vulcanization and Cross-Link Formation. Eur. Polym. J. 2017, 93, 63-74. https://doi.org/10.1016/j.eurpolymj.2017.05.029

[127] Susanna, A.; Armelao, L.; Callone, E.; Dirè, S.; D'Arienzo, M.; Di Credico, B.; Giannini, L.; Hanel, T.; Morazzoni, F.; Scotti, R. ZnO Nanoparticles Anchored to Silica Filler. A Curing Accelerator for Isoprene Rubber Composites. Chem. Eng. J. 2015, 275, 245-252. https://doi.org/10.1016/j.cej.2015.04.017

[128] Cozzoli, P. D.; Snoeck, E.; Garcia, M. A.; Giannini, C.; Guagliardi, A.; Cervellino, A.; Gozzo, F.; Hernando, A.; Achterhold, K.; Ciobanu, N.; Parak, F. G.; Cingolani, R.; Manna, L. Colloidal Synthesis and Characterization of Tetrapod-Shaped Magnetic Nanocrystals. Nano Lett. 2006, 6 (9), 1966-1972. https://doi.org/10.1021/nl061112c

[129] Bu, W.; Chen, Z.; Chen, F.; Shi, J. Oleic Acid/Oleylamine Cooperative-Controlled Crystallization Mechanism for Monodisperse Tetragonal Bipyramid $NaLa(MoO_4)_2$ Nanocrystals. J. Phys. Chem. C 2009, 113 (28), 12176-12185. https://doi.org/10.1021/jp901437a

[130] Lakowicz, J. R. Principles of Fluorescence Spectroscopy, 3th ed.; Springer US: Boston, MA, 2006. https://doi.org/10.1007/978-0-387-46312-4

[131] BEARDEN, J. A. X-Ray Wavelengths. Rev. Mod. Phys. 1967, 39 (1), 78-124. https://doi.org/10.1103/RevModPhys.39.78

[132] Iain Johnson. Molecular Probes Handbook, A Guide to Fluorescent Probes and Labeling Technologies, 11th ed.; Life Technologies, 2010.

[133] Greasley, S. L.; Page, S. J.; Sirovica, S.; Chen, S.; Martin, R. A.; Riveiro, A.; Hanna, J. V.; Porter, A. E.; Jones, J. R. Controlling Particle Size in the Stöber Process and Incorporation of Calcium. J. Colloid Interface Sci. 2016, 469, 213-223. https://doi.org/10.1016/j.jcis.2016.01.065

[134] Solé, J. G.; Bausá, L. E.; Jaque, D. An Introduction to the Optical Spectroscopy of Inorganic Solids; John Wiley & Sons, Ltd: Chichester, UK, 2005. https://doi.org/10.1002/0470016043

[135] Keller, N.; Calik, M.; Sharapa, D.; Soni, H. R.; Zehetmaier, P. M.; Rager, S.; Auras, F.; Jakowetz, A. C.; Görling, A.; Clark, T.; Bein, T. Enforcing Extended Porphyrin J-Aggregate Stacking in Covalent Organic Frameworks. J. Am. Chem. Soc. 2018, 140 (48), 16544-16552. https://doi.org/10.1021/jacs.8b08088

[136] Ahmadi, E.; Ramazani, A.; Hamdi, Z.; Mashhadi-Malekzadeh, A.; Mohamadnia, Z. 5,10,15,20-Tetrakis(4-Carboxyphenyl)Porphyrin Covalently Bound to Nano-Silica Surface: Preparation, Characterization and Chemosensor Application to Detect TNT. Silicon 2015, 7 (4), 323-332. https://doi.org/10.1007/s12633-015-9304-9

[137] Alben, J. O.; Choi, S. S.; Adler, A. D.; Caughey, W. S. Infrared Spectroscopy of Porphyrins. Ann. N. Y. Acad. Sci. 1973, 206 (1 The Chemical), 278-295. https://doi.org/10.1111/j.1749-6632.1973.tb43217.x

[138] Mahajan, P. G.; Dige, N. C.; Vanjare, B. D.; Phull, A. R.; Kim, S. J.; Hong, S. K.; Lee, K. H. Synthesis, Photophysical Properties and Application of New Porphyrin Derivatives for Use in Photodynamic Therapy and Cell

Imaging. J. Fluoresc. 2018, 28 (4), 871-882. https://doi.org/10.1007/s10895-018-2264-x

[139] Snyder, A. W.; Love, J. D. Optical Waveguide Theory; Springer US: Boston, MA, 1984. https://doi.org/10.1007/978-1-4613-2813-1

[140] Williams, F. E.; Eyring, H. The Mechanism of the Luminescence of Solids. J. Chem. Phys. 1947, 15 (5), 289-304. https://doi.org/10.1063/1.1746499

[141] Kumar, N.; Kaur, R.; Mehra, R. M. Photoluminescence Studies in Sol-Gel Derived Zno Films. J. Lumin. 2007, 126 (2), 784-788. https://doi.org/10.1016/j.jlumin.2006.11.012

[142] Fonoberov, V. A.; Alim, K. A.; Balandin, A. A.; Xiu, F.; Liu, J. Photoluminescence Investigation of the Carrier Recombination Processes in ZnO Quantum Dots and Nanocrystals. Phys. Rev. B - Condens. Matter Mater. Phys. 2006, 73 (16), 1-9. https://doi.org/10.1103/PhysRevB.73.165317

[143] Chen, H. I.; Hsiao, J. J.; Fang, C. H.; Jiang, J. A.; Wang, J. C.; Wu, Y. F.; Nee, T. E. Investigation of the Thermal Photocarrier Interaction-Recombination in ZnO Nanostructures Fabricated by the Hydrothermal Method. J. Lumin. 2017, 190 (September 2016), 136-140. https://doi.org/10.1016/j.jlumin.2017.05.020

[144] El Filali, B.; Torchynska, T. V.; Polupan, G.; Shcherbyna, L. Radiative Defects, Emission and Structure of ZnO Nanocrystals Obtained by Electrochemical Method. Mater. Res. Bull. 2017, 85, 161-167. https://doi.org/10.1016/j.materresbull.2016.09.016

[145] Nikl, M. Scintillation Detectors for X-Rays. Meas. Sci. Technol. 2006, 17 (4). https://doi.org/10.1088/0957-0233/17/4/R01

[146] Vedda, A.; Fasoli, M. Tunneling Recombinations in Scintillators, Phosphors, and Dosimeters. Radiat. Meas. 2018, 118, 86-97. https://doi.org/10.1016/j.radmeas.2018.08.003

[147] Djurišić, A. B.; Ng, A. M. C.; Chen, X. Y. ZnO Nanostructures for Optoelectronics: Material Properties and Device Applications. Prog. Quantum Electron. 2010, 34 (4), 191-259. https://doi.org/10.1016/j.pquantelec.2010.04.001

[148] Pozina, G.; Yang, L. L.; Zhao, Q. X.; Hultman, L.; Lagoudakis, P. G. Size Dependent Carrier Recombination in ZnO Nanocrystals. Appl. Phys. Lett. 2010, 97 (13), 1-4. https://doi.org/10.1063/1.3494535

[149] Dujardin, C.; Amans, D.; Belsky, A.; Chaput, F.; Ledoux, G.; Pillonnet, A. Luminescence and Scintillation Properties at the Nanoscale. IEEE Trans. Nucl. Sci. 2010, 57 (3 PART 2), 1348-1354. https://doi.org/10.1109/TNS.2009.2035697

[150] Wilkinson, J.; Ucer, K. B.; Williams, R. T. Picosecond Excitonic Luminescence in ZnO and Other Wide-Gap Semiconductors. Radiat. Meas. 2004, 38 (4-6), 501-505. https://doi.org/10.1016/j.radmeas.2004.01.022

[151] Cui, M.; Zhang, Z.; Wang, Y.; Finch, A.; Townsend, P. D. Temperature Dependence of Bulk Luminescence from ZnO. Luminescence 2018, 33 (4), 654-659. https://doi.org/10.1002/bio.3460

[152] Ji, J.; Colosimo, A. M.; Anwand, W.; Boatner, L. A.; Wagner, A.; Stepanov, P. S.; Trinh, T. T.; Liedke, M. O.; Krause-Rehberg, R.; Cowan, T. E.; Selim, F. A. ZnO Luminescence and Scintillation Studied via Photoexcitation, X-Ray Excitation and Gamma-Induced Positron Spectroscopy. Sci. Rep. 2016, 6 (1), 31238. https://doi.org/10.1038/srep31238

[153] Dell'Orto, E.; Fasoli, M.; Ren, G.; Vedda, A. Defect-Driven Radioluminescence Sensitization in Scintillators: The Case of $Lu_2Si_2O_7$:Pr. J. Phys. Chem. C 2013, 117 (39), 20201-20208. https://doi.org/10.1021/jp407248q

[154] Derenzo, S. E.; Weber, M. J.; Klintenberg, M. K. Temperature Dependence of the Fast, near-Band-Edge Scintillation from CuI, HgI_2, PbI_2, ZnO:Ga and CdS:In. Nucl. Instruments Methods Phys. Res. Sect. A Accel. Spectrometers, Detect. Assoc. Equip. 2002, 486 (1-2), 214-219. https://doi.org/10.1016/S0168-9002(02)00705-2

[155] Van Dijken, A.; Meulenkamp, E. A.; Vanmaekelbergh, D.; Meijerink, A. The Kinetics of the Radiative and Nonradiative Processes in Nanocrystalline ZnO Particles upon Photoexcitation. J. Phys. Chem. B 2000, 104 (8), 1715-1723. https://doi.org/10.1021/jp993327z

[156] Gomes, A.; Fernandes, E.; Lima, J. L. F. C. Fluorescence Probes Used for Detection of Reactive Oxygen Species. J. Biochem. Biophys. Methods 2005, 65 (2-3), 45-80. https://doi.org/10.1016/j.jbbm.2005.10.003

[157] Kim, S.; Fujitsuka, M.; Majima, T. Photochemistry of Singlet Oxygen Sensor Green. J. Phys. Chem. B 2013, 117 (45), 13985-13992. https://doi.org/10.1021/jp406638g

[158] Nosaka, Y.; Nosaka, A. Y. Generation and Detection of Reactive Oxygen Species in Photocatalysis. Chem. Rev. 2017, 117 (17), 11302-11336. https://doi.org/10.1021/acs.chemrev.7b00161

[159] Liu, H.; Carter, P. J. H.; Laan, A. C.; Eelkema, R.; Denkova, A. G. Singlet Oxygen Sensor Green Is Not a Suitable Probe for $^1O_2$ in the Presence of Ionizing Radiation. Sci. Rep. 2019, 9 (1), 8393. https://doi.org/10.1038/s41598-019-44880-2

[160] Zhang, S.-P.; Zhao, J.-Q.; Jiang, L.-J. Photosensitized Formation of Singlet Oxygen by Phycobiliproteins in Neutral Aqueous Solutions. Free Radic. Res. 2000, 33 (5), 489-496. https://doi.org/10.1080/10715760000301031

[161] Ouannes, C.; Wilson, T. Quenching of Singlet Oxygen by Tertiary Aliphatic Amines. Effect of DABCO (1,4-Diazabicyclo[2.2.2]Octane). J. Am. Chem. Soc. 1968, 90 (23), 6527-6528. https://doi.org/10.1021/ja01025a059

[162] Heal, H. G. The Decomposition of Crystalline Sodium Azide by X-Rays. Can. J. Chem. 1953, 31 (12), 1153-1163. https://doi.org/10.1139/v53-149

[163] Kelly, P.; Smith, M. 291. The Radiation Chemistry of Azide Solutions. Part II. The Action of X-Rays (200 Kv) on Deœrated Aqueous Solutions of Sodium Azide in the Presence of Different Organic Solutes. J. Chem. Soc. 1961, 1487-1494. https://doi.org/10.1039/JR9610001487

[164] Bilski, P.; Belanger, A. G.; Chignell, C. F. Photosensitized Oxidation of 2',7'-Dichlorofluorescin: Singlet Oxygen Does Not Contribute to the Formation of Fluorescent Oxidation Product 2',7'-Dichlorofluorescein. Free Radic. Biol. Med. 2002, 33 (7), 938-946.https://doi.org/10.1016/S0891-5849(02)00982-6

[165] Hope, C. K.; Billingsley, K.; De Jong, E. J. De; Higham, S. M. A Preliminary Study of the Effects of PH upon Fluorescence in Suspensions of Prevotella Intermedia. PLoS One 2016, 11 (7). https://doi.org/10.1371/journal.pone.0158835

[166] Zhang, W.; P.C. Lai, E. Fluorescence Detection of Zinc Oxide Nanoparticles in Water Contamination Analysis Based on Surface Reactivity with Porphyrin. AIMS Environ. Sci. 2018, 5 (2), 67-77. https://doi.org/10.3934/environsci.2018.2.67

[167] Optically Active Oxygen-Deficiency-Related Centers in Amorphous Silicon Dioxide. J. Non. Cryst. Solids 1998, 239 (1-3), 16-48 https://doi.org/10.1016/S0022-3093(98)00720-0

[168] Carbonaro, C. M.; Corpino, R.; Ricci, P. C.; Chiriu, D. On the Origin of Blue and UV Emission Bands in Mesoporous Silica. AIP Conference Proceedings 2014, 1624, 15 https://doi.org/10.1063/1.4900451

[169] Pierini, G. D.; Pinto, V. H. A.; Maia, C. G. C.; Fragoso, W. D.; Reboucas, J. S.; Centurión, M. E.; Pistonesi, M. F.; Di Nezio, M. S. A Porphyrin-Based Fluorescence Method for Zinc Determination in Commercial Propolis Extracts without Sample Pretreatment. Luminescence 2017, 32 (7), 1227-1232. https://doi.org/10.1002/bio.3315

[170] Brookfield, R. L.; Ellul, H.; Harriman, A. Luminescence of Porphyrins and Metalloporphyrins IX: Dimerization of Meso-Tetrakis(N-Methyl-4-Pyridyl)-Porphine. J. Photochem. 1985, 31 (1), 97-103. https://doi.org/10.1016/0047-2670(85)85077-2

[171] Gao, Z.; Chen, F.; Li, Y.; Zhang, Y.; Cheng, K.; An, P.; Sun, B. A Small-Sized and Stable 2D Metal-Organic Framework: A Functional Nanoplatform for Effective Photodynamic Therapy. Dalt. Trans. 2019, 48 (45), 16861-16868. https://doi.org/10.1039/c9dt03706c

[172] Liu, J.; Huang, J. W.; Shen, H.; Wang, H.; Yu, H. C.; Ji, L. N. The Synthesis of Two Novel Hybrids Containing a Zinc(II) Porphyrin Unit and a Polypyridyl Ruthenium(II) Complex Unit and Their Photoinduced Intramolecular Electron and Energy Transfer. Dye. Pigment. 2008, 77 (2), 374-379. https://doi.org/10.1016/j.dyepig.2007.06.008

[173] Kraft, S.; Stümpel, J.; Becker, P.; Kuetgens, U. High Resolution X-ray Absorption Spectroscopy with Absolute Energy Calibration for the Determination of Absorption Edge Energies. Rev. Sci. Instrum. 1996, 67 (3), 681-687. https://doi.org/10.1063/1.1146657

Acknowledgments

I would like to express my most sincere gratitude at Professor Anna Vedda, who welcomed me in her research group and guided me during the last three years both professionally and personally. I'm thankful to her for sharing with me her great scientific knowledge and for supporting me with inspiring kindness and patience. Then, I would like to deeply thank Dr Irene Villa for tutoring and teaching me every day with her positive energy and thoughtfulness. She always encouraged me in trying new approaches and improving myself. I would also like to express my gratitude at the other members of the research group, Professor Mauro Fasoli and Dr. Francesca Cova, for their precious help and availability.

I would also like to acknowledge all the scientists that collaborated with me for the PhD project during these years.
A particular thank to Dr Silvia Mostoni, for providing all the nanomaterials with such diligence and for working with me in the comprehensions of their properties. Thanks also at Professor Roberto Scotti, Professor Massimiliano D'Arienzo and Professor Barbara Di Credico for supervising and improving the synthesis procedures.
I would also like to express my gratitude to Roberto Lorenzo e Angelo Monguzzi for their help with the photoluminescence measurements and with their interpretations and for their priceless advices.
I'm also thankful to Chiara Villa and Valeria Secchi for the possibility to take part in exciting biological experiments and for sharing with me their expertise.
My sincere and special thanks to Dr Anne-Laure Bulin for her teaching and assistance with the computational analyses: her patient guidance was precious for me to approach a completely new topic.

I would also like to express my gratitude to all the people and friends that I have met in these years at the University of Milano-Bicocca for sharing the everyday routine filling it with laughs and encouragement.

Lastly, I'm thankful to my big and non-traditional family and to my old and new friends for always believing in me. Deep felt thanks to my grandparents, parents, aunts, uncles, and cousins for giving me continuous support and for listening to my PhD presentations, even if they were not so interesting for them. Special thanks to my partner Gianni that listened to my endless complains and always believed that I could face the difficulties, giving me self-confidence and strength. Sincere thanks to my dear friend Riccardo who lived with me the moments of discouragement and happiness and together with Nicola made me feeling at home.